



**HAL**  
open science

# Linking medicinal cannabis to autotaxin lysophosphatidic acid signalling and development of cannabinoid-inspired inhibitors

Mathias Eymery

► **To cite this version:**

Mathias Eymery. Linking medicinal cannabis to autotaxin lysophosphatidic acid signalling and development of cannabinoid-inspired inhibitors. Structural Biology [q-bio.BM]. Université Grenoble Alpes [2020-..], 2023. English. NNT: 2023GRALV061 . tel-04415112

**HAL Id: tel-04415112**

**<https://theses.hal.science/tel-04415112>**

Submitted on 24 Jan 2024

**HAL** is a multi-disciplinary open access archive for the deposit and dissemination of scientific research documents, whether they are published or not. The documents may come from teaching and research institutions in France or abroad, or from public or private research centers.

L'archive ouverte pluridisciplinaire **HAL**, est destinée au dépôt et à la diffusion de documents scientifiques de niveau recherche, publiés ou non, émanant des établissements d'enseignement et de recherche français ou étrangers, des laboratoires publics ou privés.

THÈSE

Pour obtenir le grade de

**DOCTEUR DE L'UNIVERSITÉ GRENOBLE ALPES**

École doctorale : CSV- Chimie et Sciences du Vivant

Spécialité : Biologie Structurale et Nanobiologie

Unité de recherche : laboratoire européen de biologie moléculaire

**Lien entre le cannabis médicinal et l'axe de signalisation autotaxine acide lysophosphatidique : développement d'inhibiteurs inspirés des cannabinoïdes**

**Linking medicinal cannabis to autotaxin lysophosphatidic acid signalling and development of cannabinoid-inspired inhibitors**

Présentée par :

**Mathias EYMERY**

Direction de thèse :

**Andrew MAC CARTHY**

Directeur de thèse

**Ahcène BOUMENDJEL**

PROFESSEUR DES UNIVERSITES, UGA

Co-directeur de thèse

Rapporteurs :

**Marc LE BORGNE**

PROFESSEUR DES UNIVERSITES, Université de Lyon 1 - Claude Bernard

**Anastassis PERRAKIS**

FULL PROFESSOR, Universiteit Utrecht

Thèse soutenue publiquement le **2 octobre 2023**, devant le jury composé de :

**Wim BURMEISTER**

PROFESSEUR DES UNIVERSITES, Université Grenoble Alpes

Examineur

**Marc LE BORGNE**

PROFESSEUR DES UNIVERSITES, Université de Lyon 1 - Claude Bernard

Rapporteur

**Anastassis PERRAKIS**

FULL PROFESSOR, Universiteit Utrecht

Rapporteur

**Olivier PEYRUCHAUD**

DIRECTEUR DE RECHERCHE, INSERM délégation Auvergne-Rhône-Alpes

Président

**joanna TIMMINS**

DIRECTRICE DE RECHERCHE, CNRS délégation Alpes

Examinatrice

**Ahcène BOUMENDJEL**

PROFESSEUR DES UNIVERSITES, Université Grenoble Alpes

Co-directeur de thèse

Invités :

**Andrew McCarthy**

Docteur en Sciences, European Molecular Biology Laboratory



# Doctoral Thesis

Linking medicinal cannabis to autotaxin–lysophosphatidic acid signalling and development of cannabinoid-inspired inhibitors

By Mathias Christophe Eymery  
02/10/2023

Note:

## Note:

Part of this work has been published in the following articles and patent:

- Eymery MC, McCarthy AA, Hausmann J. Linking medicinal cannabis to autotaxin-lysophosphatidic acid signaling. *Life Sci Alliance*. 2023 Jan 9;6(2):e202201595. doi: 10.26508/lsa.202201595. PMID: 36623871; PMCID: PMC9834664.
- EP22215403.1 filed on 21.12.2022
- Eymery et al. Cannabinoid-inspired inhibitors of Autotaxin. Submitted to *EJ Med Chem*.

## Table of content

<b>NOTE:</b> .....	<b>2</b>
<b>TABLE OF CONTENT</b> .....	<b>3</b>
<b>TABLE OF FIGURES:</b> .....	<b>5</b>
<b>TABLE OF SUPPLEMENTARY FIGURES</b> .....	<b>6</b>
<b>LIST OF TABLES:</b> .....	<b>7</b>
<b>LIST OF SCHEMES:</b> .....	<b>8</b>
<b>ABBREVIATIONS</b> .....	<b>9</b>
<b>1 THESIS SUMMARY</b> .....	<b>11</b>
1.1 RÉSUMÉ EN FRANÇAIS .....	11
1.2 ABSTRACT: .....	13
<b>2 INTRODUCTION</b> .....	<b>15</b>
2.1 THE ENPP2 FAMILY : IMPLICATION IN HUMAN HEALTH AND DISEASES .....	15
2.1.1 <i>General description</i> .....	15
2.1.2 <i>Autotaxin : structural and functional description</i> .....	16
2.1.3 <i>Implication of autotaxin in diseases</i> .....	19
2.1.4 <i>Autotaxin inhibitors</i> .....	24
2.2 LPA RECEPTORS: FUNCTIONAL AND STRUCTURAL DESCRIPTION .....	26
2.3 MEDICINAL CANNABIS AND TETRAHYDROCANNABINOL (THC) .....	28
2.3.1 <i>Description of medicinal cannabis and its components</i> .....	28
2.3.2 <i>Interaction of medicinal cannabis components with human proteins</i> .....	34
2.3.3 <i>Recent advances in medicinal cannabis therapy</i> .....	37
2.4 AIM OF THE PHD THESIS .....	38
<b>3 MATERIALS AND METHODS</b> .....	<b>40</b>
3.1 CHEMISTRY: .....	40
3.1.1 <i>General information</i> .....	40
3.1.2 <i>Compounds synthesis:</i> .....	40
3.2 BIOCHEMISTRY: .....	48
3.2.1 <i>Reagents:</i> .....	48
3.2.2 <i>Autotaxin expression and purification:</i> .....	49
3.2.3 <i>Crystallization, data collection and model building:</i> .....	50
3.2.4 <i>Dose response assay:</i> .....	51
3.2.5 <i>End point assays:</i> .....	53
3.2.6 <i>Mode of inhibition assay:</i> .....	54
	3

## Table of content

3.2.7	<i>Biochemical analysis:</i> .....	54
3.2.8	<i>Choline standard:</i> .....	55
3.2.9	<i>Western blot and SDS Page gel analysis:</i> .....	55
3.2.10	<i>AlphaFold:</i> .....	56
3.2.11	<i>hLPA1 internalization assay:</i> .....	56
3.2.12	<i>CryoEM data collection and processing:</i> .....	58
<b>4</b>	<b>RESULTS</b> .....	<b>60</b>
4.1	AUTOTAXIN EXPRESSION AND PURIFICATION.....	60
4.2	EFFECTS OF MEDICINAL CANNABIS AND ENDOCANNABINOIDS ON ATX.....	61
4.2.1	<i>Inhibition of ATX by various cannabinoids</i> .....	61
4.2.2	<i>Inhibition of of autotaxin by endocannabinoids</i> .....	63
4.2.3	<i>Biochemical characterization of THC and 6a10aTHC with ATX-<math>\beta</math> and ATX-<math>\gamma</math></i> .....	64
4.2.4	<i>Co-crystal structure of ATX-THC</i> .....	67
4.2.5	<i>Co-crystal structure of ATX-6a10aTHC</i> .....	69
4.2.6	<i>Inhibition of LPA1 internalization in Hela cells by THC</i> .....	72
4.3	CANNABINOID-INSPIRED INHIBITORS OF AUTOTAXIN.....	74
4.3.1	<i>Development of new inhibitors:</i> .....	74
4.3.2	<i>From hit to lead :</i> .....	74
4.3.3	<i>Biochemical characterization of cannabinoid-inspired inhibitors:</i> .....	77
4.3.4	<i>Binding interface of cannabinoid-inspired inhibitors and ATX-<math>\gamma</math> structure:</i> .....	78
4.3.5	<i>MEY-003 reduces hLPA1 internalization and is not cytotoxic to HeLa cells.</i> .....	84
4.3.6	<i>Insight into hATX-<math>\gamma</math> structure and biology</i> .....	85
4.4	CRYOEM ANALYSIS OF ATX :.....	87
<b>5</b>	<b>DISCUSSION</b> .....	<b>90</b>
5.1	MEDICINAL CANNABIS INHIBITION OF AUTOTAXIN:.....	90
5.1.1	<i>Mechanisms by which medicinal cannabis might have effect on the ATX-LPA axis: ...</i>	90
5.1.2	<i>Prospective experiments that could be done to investigate the effect of medicinal cannabis on the ATX-LPA axis:</i> .....	92
5.2	DEVELOPMENT OF CANNABINOID-INSPIRED AUTOTAXIN INHIBITORS:.....	93
5.2.1	<i>Structure-activity relationship of cannabinoid-inspired inhibitors:</i> .....	93
5.2.2	<i>Synthesis protocol and prospectives inhibitors:</i> .....	94
5.2.3	<i>Insights into ATX-<math>\gamma</math> structure:</i> .....	96
<b>6</b>	<b>CONCLUSION:</b> .....	<b>98</b>
<b>7</b>	<b>FUTURE AIM OF RESEARCH</b> .....	<b>99</b>
<b>8</b>	<b>REFERENCES:</b> .....	<b>101</b>
<b>9</b>	<b>ACKNOWLEDGEMENTS:</b> .....	<b>115</b>
<b>10</b>	<b>SUPPLEMENTARY DATA</b> .....	<b>117</b>

Table of figures:

## Table of figures:

Figure 1: Autotaxin domain organization, overall structure, and active site.....	17
Figure 2: ATX inhibitors classified according to discrete binding mode.....	24
Figure 3: Summary of LPA receptor signaling pathways activated by autotaxin mediate LPA production and signalling. ....	26
Figure 4: Chemical structures of the main plant cannabinoids .....	32
Figure 5: Chemical structures of human endocannabinoids.....	34
Figure 6: Structure-function of human proteins interacting with cannabinoids and endocannabinoids. ....	35
Figure 7: Representative example of recombinant ATX protein purity and enzymatic assays. ....	60
Figure 8: End point assays of tested compounds with hATX .....	62
Figure 9: Inhibition of hATX- $\beta$ by endocannabinoids at 20 $\mu$ M LPC concentration..	64
Figure 10: Inhibition of hATX by plant-derived THC and synthetic 6a10aTHC.....	66
Figure 11: Enzymatic assay controls.....	67
Figure 12: Electron density and structure of rATX- $\beta$ -THC complex.....	68
Figure 13: Electron density and structure of rATX- $\beta$ -6a10aTHC complex.....	70
Figure 14: Physiological effect of THC on LPA1 receptor internalization .....	73
Figure 15: Inhibition of autotaxin (ATX) by MEY-003. ....	78
Figure 16: MEY-003 binding to hATX- $\gamma$ hydrophobic pocket .....	80
Figure 17: MEY-003-ATX- $\gamma$ interaction analysis using the PLIP server.....	80
Figure 18: MEY-002 and MEY-003 binding to the rATX- $\beta$ hydrophobic pocket.....	81
Figure 19: MEY-003 reduces LPA1 receptor internalization and is not cytotoxic to HeLa cells. ....	85
Figure 20: hATX- $\gamma$ insertion can be cleaved by an unknown protease during protein production. ....	86
Figure 21: Cryo-EM results from Krios dataset analysis.....	88
Figure 23: Discovery of cannabinoid-inspired ATX inhibitors .....	98

## Table of supplementary figures

supplementary 1: Chemical groups of the screened library.....	117
supplementary 2 : <sup>1</sup> H NMR spectra of MEY-001 .....	118
supplementary 3: <sup>19</sup> F NMR spectra of MEY-001 .....	119
supplementary 4: <sup>13</sup> C NMR spectra of MEY-001 .....	120
supplementary 5: ESI of MEY-001 .....	121
supplementary 6: LCMS of MEY-001 .....	122
supplementary 7: <sup>1</sup> H NMR spectra of MEY-002 .....	123
supplementary 8: <sup>13</sup> C NMR spectra of MEY-002.....	124
supplementary 9: ESI of MEY-002 .....	125
supplementary 10: LCMS of MEY-002 .....	126
supplementary 11: <sup>1</sup> H NMR spectra of MEY-003 .....	127
supplementary 12: <sup>13</sup> C NMR spectra of MEY-003.....	128
supplementary 13: ESI of MEY-003 .....	129
supplementary 14: LCMS of MEY-003 .....	130
supplementary 15: <sup>1</sup> H NMR spectra of MEY-005 .....	131
supplementary 16: <sup>13</sup> C NMR spectra of MEY-005.....	132
supplementary 17: ESI of MEY-005 .....	133
supplementary 18: LCMS of MEY-005 .....	134
supplementary 19: <sup>1</sup> H NMR spectra of MEY-007 .....	135
supplementary 20: <sup>13</sup> C NMR spectra of MEY-007 .....	136
supplementary 21: ESI of MEY-007 .....	137
supplementary 22: LCMS of MEY-007 .....	138
supplementary 23: <sup>1</sup> H NMR spectra of MEY-008 .....	139
supplementary 24: <sup>13</sup> C NMR spectra of MEY-008.....	140
supplementary 25: ESI of MEY-008 .....	141
supplementary 26: LCMS of MEY-008 .....	142
supplementary 27: Analogs of MEY-003 bearing an extra hydroxyl group at position 3 of the chromone moiety. are less potent than MEY-003, using the FS3 assay. ....	143
supplementary 28: hATX-γ and hATX-γ N54A N411A have the same catalytic activity towards LPC18:1.....	144
supplementary 29: SEC-MALL curves of rATX .....	145
supplementary 30: SEC-MALLS report of rATX .....	147



List of tables:

supplementary 31 : 3D representation of the interaction of THC(a), 6a10aTHC(b) and MEY-003(c) with surrounding amino acids in ATX hydrophobic pocket ..... 148

List of tables:

Table 1: Crystallographic data collection and refinement statistics for cannabinoid compounds..... 71

Table 2: Crystallographic data collection and refinement statistics for cannabinoid-inspired inhibitors ..... 84

Table 3: Inhibition activity of hits and the lead on hATX- $\beta$  and hATX- $\gamma$  ..... 96

List of schemes:

## List of schemes:

Scheme 1: Synthesis of compounds MEY-001, MEY-002, MEY-005, MEY-007 and MEY-008 .....	43
Scheme 2: Comparison of the ATX- $\beta$ and ATX- $\gamma$ sequences.....	75
Scheme 3: Summary for the discovery process of flavone-derived ATX inhibitors ..	76
Scheme 4: Synthesis of MEY-003. (a) KOH, MeOH, reflux, (b) I <sub>2</sub> , 150 °C, (c) BBr <sub>3</sub> , CH <sub>2</sub> Cl <sub>2</sub> , room temperature.....	76
scheme 5: Chemical groups of the screened library .....	77
Scheme 6: Synthetized and prospective inhibitors .....	95

## Abbreviations

## Abbreviations

<sup>13</sup> C NMR	Carbon-13 nuclear magnetic resonance
<sup>19</sup> F NMR	Fluoride-19 nuclear magnetic resonance
<sup>1</sup> H NMR	hydrogen-1 nuclear magnetic resonance
2-AG	2-Arachidonoylglycerol
6a10aTHC	$\Delta^{6a(10a)}$ -Tetrahydrocannabinol
AEA	Anandamide
ATX	Autotaxin
C-term	C-terminal
CB1	Cannabinoid receptor type 1
CB2	Cannabinoid receptor type 2
CBD	Cannabidiol
CBN	Cannabinol
CryoEM	Cryogenic electron microscopy
ENPP1	Ectonucleotide pyrophosphatase/phosphodiesterase 1
ENPP2	Ectonucleotide pyrophosphatase/phosphodiesterase 2
ESI	Electrospray ionization
FABP5	Fatty Acid Binding Protein 5
GPCR	G-protein-coupled receptors
HEK293	Human embryonic kidney 293 cells,
HEK293 Flp-In	Human embryonic kidney 293 cells flp-in
HeLa	Henrietta Lacks cells
kDa	Kilo Daltons
LCMS	Liquid chromatography–mass spectrometry
LPA	Lysophosphatidic acid
LPAR	Lysophosphatidic acid receptors
LPC	Lysophosphatidylcholine
MicroSEC	Microliter size exclusion chromatography
MW	Molecular weight
MX	Macromolecular crystallography
N-term	N-terminal
NADA	N-Arachidonoyl dopamine
NMR	Nuclear magnetic resonance
PDE	Phosphodiesterase
PhD	Philosophiae doctor

## Abbreviations

PPAR-Gamma	Peroxisome proliferator-activated receptor gamma
SDS-PAGE	Sodium dodecyl sulfate–polyacrylamide gel electrophoresis
SEC	Size exclusion chromatography
SEC-MALS	Size exclusion chromatography with multi-angle static light scattering
SMB	Somatomedin-B-like
THC	Tetrahydrocannabinol
WB	Western blot
XDS	X-ray Detector Software

# 1 Thesis summary

## 1.1 Résumé en français

L'autotaxine (ATX) est une lysophospholipase D de 115-125 kDa impliquée dans une large gamme de processus physiologiques et pathologiques. Cette enzyme fait partie de la famille des ectonucléotides pyrophosphatases/phosphodiesterases et elle est également appelée ENPP2. L'ATX est principalement impliquée dans le métabolisme des phospholipides et la production d'acide lysophosphatidique extracellulaire (LPA) à partir de l'acide lysophosphatidylcholine (LPC). Au moins cinq isoformes humaines ont été découvertes à ce jour. L'isoforme  $\beta$  est la plus abondante. En effet, elle est exprimée dans de nombreux tissus et représente la majorité de l'activité enzymatique de l'autotaxine. Les isoformes  $\alpha$  et  $\epsilon$  sont moins abondantes et se distinguent de l'ATX- $\beta$  par une insertion polybasique de 52 aa. Il manque à l'isoforme delta un exon de 19 tétrapeptides de fonction inconnue. L'ATX- $\gamma$  est spécifique du cerveau et diffère de l'ATX- $\beta$  par une insertion de 25 aa, tandis que son activité est similaire à l'isoforme  $\alpha$ . La structure de l'autotaxine a été largement étudiée avec 51 entrées expérimentales dans la Protein Data Bank à ce jour. Il repose sur (i) deux domaines flexibles de type somatoméline B (SMB), impliqués dans les interactions protéine-protéine, (ii) un domaine phosphodiesterase conservé responsable de l'activité catalytique, et (iii) un domaine nucléase inactif. Les informations structurales sur l'ATX montrent que le site actif contient deux ions zinc, permettant la liaison et le clivage de la lysophosphatidylcholine. Un point majeur de la reconnaissance du substrat par le site actif ATX est la présence d'une poche hydrophobe, permettant l'accommodation du LPA et du LPC.

L'implication de l'ATX dans un large éventail de maladies humaines peut être mise en évidence à la fois par la recherche fondamentale et les essais cliniques. Premièrement, il a été démontré que l'ATX est importante pour la progression du cancer et les métastases car cette enzyme est responsable de la génération de LPA. Le LPA est un facteur de croissance, régulant de nombreuses fonctions cellulaires différentes, dont certaines sont importantes pour les cellules cancéreuses. Notamment, il a été montré que le LPA est un facteur de motilité cellulaire et que

## Thesis summary

l'inhibition de l'ATX entraîne une réduction de l'invasion cellulaire in vitro du fait de la diminution de la concentration de LPA dans les fluides environnants. Des expériences in vivo et des essais cliniques ont montré que les cellules cancéreuses ovariennes produisent des niveaux élevés de LPA, ainsi que d'autres conditions comme la grossesse, les accidents vasculaires cérébraux et le syndrome coronarien aigu. Récemment, la confirmation de l'implication de l'ATX dans les maladies neurologiques a été rapportée. Des études récentes ont en outre montré que les niveaux d'ATX sont liés à des troubles du métabolisme dans la maladie d'Alzheimer, soulignant que l'ATX est un biomarqueur intéressant pour cette pathologie dévastatrice. Les niveaux d'ATX dans le sérum ont été comparés aux données IRM de patients souffrant de cette maladie, montrant que certaines caractéristiques de ce dernier étaient corrélées avec le premier. Les taux sériques d'ATX varient également dans d'autres maladies et conditions physiologiques, ce qui renforce la nécessité d'une régulation fine de la catalyse de l'ATX. Cependant, la concentration systémique de LPA par l'ATX n'est pas un bon biomarqueur car il n'est pas librement disponible dans le sang et incapable de traverser seul les compartiments physiologiques. De plus, les niveaux de LPA ne sont pas nécessairement élevés chez les patients atteints de cancer car la sécrétion et la liaison aux récepteurs sont principalement limitées aux sites tumoraux. De plus, le LPA se lie aux récepteurs exprimés à la surface des cellules. Ces récepteurs ont de nombreuses fonctions, par exemple régulant la survie cellulaire, l'apoptose, la différenciation cellulaire, la transformation maligne et de nombreux autres processus grâce à leur activité de récepteur couplé aux protéines G. Plus précisément, les récepteurs LPA de la famille EDG (LPAR1 à LPAR3) ont été largement étudiés et sont des cibles pharmacologiques majeures. Des récepteurs LPA non-EDG (LPAR4-LPAR6) ont été découverts et des études récentes ont permis de déterminer la structure du LPAR6. Ils ont décrit cette famille de récepteurs comme des cibles médicamenteuses importantes. Ces dernières années, il a été émis l'hypothèse et démontré que l'ATX peut agir non seulement comme une enzyme mais aussi comme un chaperon présentant le LPA à ses récepteurs.

Dans ce contexte, il est d'un grand intérêt de développer des médicaments qui pourraient inhiber sélectivement l'ATX dans son environnement pathologique, sans diminuer les niveaux globaux de LPA dans le sang.

## Thesis summary

Divers inhibiteurs de l'ATX ont déjà été développés et certains font actuellement l'objet d'essais cliniques. Cependant, les composés avec des paramètres pharmacocinétiques satisfaisants et une faible toxicité sont limités. Ainsi, il n'existe toujours pas de médicament approuvé pour les maladies cérébrales liées à l'ATX. De plus, la distribution de l'ATX est spécifique aux tissus et la plupart des recherches se sont concentrées sur les isoformes  $\beta$  et  $\alpha$ . Pour l'ATX- $\gamma$ , vraisemblablement lié à de nombreuses maladies neurologiques, une compréhension plus approfondie est nécessaire pour concevoir et développer des inhibiteurs plus spécifiques de cette isoforme et pour comprendre pleinement son rôle physiopathologique.

Récemment, nous avons découvert que divers cannabinoïdes peuvent agir comme inhibiteurs de l'ATX. En particulier, le THC et le delta 6a,10a-THC réduisent l'activité catalytique de l'ATX en tant qu'inhibiteurs de type mixte à des concentrations de l'ordre du nanomolaire. Les paramètres pharmacocinétiques des cannabinoïdes sont largement étudiés et il existe un consensus sur le fait qu'ils traversent la BHE et se lient aux récepteurs CB1 et CB2, ce qui en fait un point de départ idéal pour inhiber spécifiquement l'ATX dans le cerveau. Bien que les cannabinoïdes se soient révélés être d'excellents inhibiteurs de l'ATX, leurs inconvénients majeurs concernent la réglementation, la législation et l'acceptation par les patients, les rendant moins désirables pour le développement.

L'objectif de notre travail vise le développement d'inhibiteurs efficaces et sélectifs de l'ATX et l'étude des interactions avec le site actif de l'enzyme en utilisant des approches de biologie structurale.

### 1.2 Abstract:

Autotaxin (ATX) is a 115-125 kDa lysophospholipase D involved in a wide range of physiological and pathological processes. This enzyme is a member of the ectonucleotide pyrophosphatase/phosphodiesterase family and is also known as ENPP2. ATX is mainly involved in phospholipid metabolism and the production of extracellular lysophosphatidic acid (LPA) from lysophatidylcholine acid (LPC). The structure of ATX has been extensively studied and is based on (i) two flexible somatomedin B (SMB) domains involved in protein-protein interactions, (ii) a

## Thesis summary

conserved phosphodiesterase domain responsible for catalytic activity, and (iii) an inactive nuclease domain. Structural information on ATX shows that the active site contains two zinc ions, allowing the binding and cleavage of lysophosphatidylcholine. A major feature of substrate recognition by the ATX active site is the presence of a hydrophobic pocket, allowing accommodation of LPC substates and LPA products. The involvement of ATX in a wide range of human diseases has been demonstrated in both basic research and clinical trials. ATX has been shown to be important for cancer progression and metastasis as this enzyme is responsible for the generation of LPA and regulating many different cellular functions, some of which are important for cancer cells. In particular, it has been shown that LPA is a factor in cell motility and that inhibition of ATX leads to a reduction in cell invasion *in vitro* due to a decrease in the concentration of LPA in the surrounding fluids. Various ATX inhibitors have already been developed and some are currently in clinical trials. However, compounds with satisfactory pharmacokinetic parameters and low toxicity are limited and there is still no approved drug for ATX-related brain diseases. Furthermore, the distribution of ATX is tissue specific and most research has focused on the  $\alpha$  and  $\beta$  isoforms. For ATX- $\gamma$ , which is likely to be linked to many neurological diseases, a deeper understanding is needed in order to design and develop more specific inhibitors of this particular isoform, as well as fully understanding its pathophysiological role. In this work I show that ATX is inhibited by various cannabinoids. In particular, tetrahydrocannabinol (THC) and delta 6a,10a-THC reduce the catalytic activity of ATX- $\beta$  and  $\gamma$  isomers as mixed-type inhibitors at nanomolar concentrations. The pharmacokinetics of cannabinoids are widely studied and there is consensus that they cross the blood brain barrier (BBB) to bind Cannabinoid (CB) 1 and 2 receptors, making them an ideal starting point for specifically inhibiting ATX in the brain. Although cannabinoids have proven to be excellent ATX inhibitors, their major drawbacks relate to regulation, legislation and patient acceptance, making them less desirable for development but paving the way towards new cannabinoid-inspired ATX inhibitors. Therefore, we used THC as a basis to explore diverse molecules with partial chemical and structural similarity, particularly those sharing a benzopyrane moiety such as naturally occurring chromones and flavones. The process of screening, hit identification and hit optimization allowed us to identify MEY-003 as a potent and safe inhibitor of ATX. The inhibition profile of MEY-003 was rationalized through advanced structural biology



drug discovery studies. MEY-003 has a unique structure compared to previously published ATX inhibitors that could potentially lead to the development of new drugs targeting the ATX-LPA axis with fewer side effects.

## 2 Introduction

### 2.1 The ENPP2 family : implication in human health and diseases

#### 2.1.1 General description

Autotaxin (ATX) is a 115-125 kDa lysophospholipase D involved in a large range of physiological and pathological processes (1). This enzyme is part of the ectonucleotide pyrophosphatase/phosphodiesterase family and is also referred to as ENPP2. ATX is mainly involved in the phospholipidic metabolism and the production of extracellular lysophosphatidic acid (LPA) from lysophosphatidylcholine acid (LPC) (2). At least five human isoforms have been discovered so far (3). The  $\beta$  isoform is the most abundant, expressed in many tissues and accounting for the majority of ATX activity. The  $\alpha$  and  $\epsilon$  isoforms are less abundant and differ from ATX- $\beta$  by a 52 aa polybasic insertion (4). The ATX delta isoform is missing an exon of 19 tetrapeptides with unknown function (5). ATX- $\gamma$  is brain-specific and differs from ATX- $\beta$  by a 25 aa insertion, while its activity is similar to the  $\beta$  isoform (Figure 1) (3). The ATX structure has been widely studied with 51 experimental entries in the Protein Data Bank to date (6). It relies on (i) two flexible somatomedin B (SMB)-like domains, involved in protein-protein interactions, (ii) a conserved phosphodiesterase domain responsible for catalytic activity, and (iii) an inactive nuclease domain (Figure 1) (7). Structural insights into ATX show that the active site contains two zinc ions, allowing lysophosphatidylcholine binding and cleavage. A major point of substrate recognition by the ATX active site is the presence of a hydrophobic pocket, allowing the accommodation of LPC (7).

The implication of ATX in a large range of human diseases can be highlighted by both fundamental research and clinical trials (2,3,8–10). Firstly, it has been shown that ATX is important for cancer progression and metastasis as this enzyme is responsible for LPA generation (8,9,11–14). LPA is a growth factor, regulating many

## Introduction

different cellular functions, some of which are important for malignant cells. Notably, it has been shown that LPA is a cell motility factor and that inhibiting ATX results in a reduction of *in vitro* cellular invasion through a decrease of LPA concentration in the surrounding fluids (10). *In vivo* experiments and clinical trials showed that ovarian cancer cells produce high levels of LPA, as well as other conditions like during pregnancy (15), stroke (16) and acute coronary syndrome (17). ATX is also necessary for blood vessel formation (18). Recently, the confirmation of ATX's implication in neurological diseases was reported (11,19). Further studies showed that ATX levels are related to metabolism disorders in Alzheimer's disease, highlighting ATX as an interesting biomarker for this devastating pathology (20). ATX levels in the serum were compared to MRI data of patients suffering from this disease, showing that some features of the latter were correlated with the former (20). Serum levels of ATX also vary in other diseases and physiological conditions, which strengthens the need for fine-tuning of ATX catalysis (8). However, systemic LPA generation by ATX is not a good biomarker as it is not freely available in the blood, and unable to cross physiological compartments. In addition, LPA levels are not necessarily elevated in patients with cancer as the secretion and binding is mostly limited to tumor sites (3). Also, LPA binds to receptors expressed at the cell surface. These receptors have many functions, e.g. regulating cell survival, apoptosis, cell differentiation, malignant transformation and many other processes through their G protein-coupled receptor activity (21). More precisely, LPA receptors from the EDG family (LPA<sub>1</sub> to LPA<sub>3</sub>) have been widely studied and are major pharmacological targets. Non-EDG family LPA receptors (LPA<sub>4</sub>-LPA<sub>6</sub>) were reported and recent studies allowed LPA<sub>6</sub> structure determination and described this receptor family as important drug targets (22) (see section 1.3 for more details). In recent years, it has been hypothesized and demonstrated that ATX may act not only as an enzyme but also as a chaperone presenting LPA to its receptors (7,23). In this setting, it is of great interest to develop drugs that could selectively inhibit ATX in its pathological environment, without decreasing the overall levels of LPA in blood.

### 2.1.2 Autotaxin : structural and functional description

## Introduction

As described previously, autotaxin has 4 domains: two N-terminal SMB-like domains, one phosphodiesterase (PDE) domain, which contains the catalytic site and a hydrophobic pocket for substrate binding, and an inactive nuclease (NUC) domain at the C-terminus (figure 1). A lasso linker connects the PDE and NUC domains. In ATX- $\gamma$ , there is an additional 25 AA insertion here, whose function remains unknown.

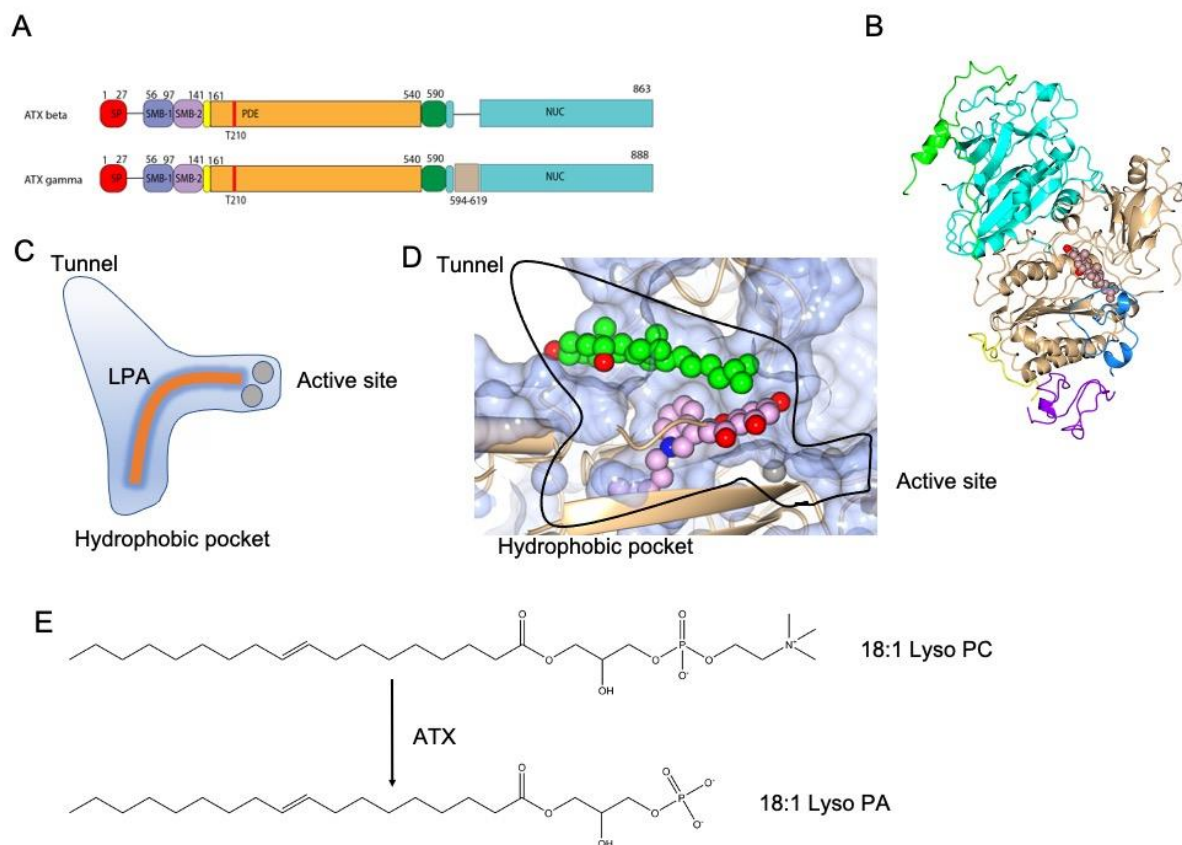


*Figure 1: Autotaxin domain organization, overall structure, and active site.*

(A) Comparison of the ATX- $\beta$  and ATX- $\gamma$  sequences. (B) Overall structure of autotaxin colored by domain. (C) Schematic and (D) structural representation of autotaxin displaying the active site, hydrophobic pocket and substrate exit tunnel. Signal peptide (SP) is colored red; SMB-1 and 2 in blue and magenta, respectively; PDE domain is colored brown with the active site residue T210 highlighted in red; lasso linker is colored green and ATX- $\gamma$  insert in grey; the NUC domain is coloured cyan. (E) Representation of the transformation of Lyso PC (LPC) to Lyso PA (LPA) by ATX.

## Introduction

rATX- $\beta$  has been crystallized in 2011 by Hausmann et al (24,25), allowing structural characterization of ATX. The structures revealed that the central catalytic PDE domain is surrounded by the SMB domains and the NUC domains, leading to extensive interactions. The protein is glycosylated on 3 different amino acids (N53, N410, N524 and for the rATX- $\beta$  isoform), which are important for folding, activity and interdomain interactions (26,27). The lasso loop linking the PDE and the NUC domain is important for the NUC folding, and it is also described that the NUC domain can tightly bind  $\text{Ca}^{2+}$  ions, but the biological importance of such interactions still remains to be determined (7). Concerning the SMB domains, this family is well known to be important for mediating protein-protein interactions and in ATX they closely interact with the PDE catalytic domain. They both share structural features but have different functions due to their interaction regions. SMB-1 is close to the tunnel and is probably related to the substrate tunnel exit. SMB-2 lies more at the surface of the protein and is most likely involved in mediating binding to partner proteins such as integrins (7,24). It has been shown that ATX-integrin binding is involved in platelet activation through an interaction between the SMB-2 domain and the  $\beta 1$  and  $\beta 3$  integrins (24). Concerning the PDE catalytic domain, it is very conserved and similar to the previously solved Nucleotide pyrophosphatase/phosphodiesterase (NPP) (28). The ATX active site is composed of two zinc ions in coordination with three histidine (H315, H359, H474 for rATX and H316, H360, H475 for hATX) and three aspartic acid residue (D171, D311, D358 for rATX and D172, D312, D359 for hATX). The reaction is mediated by a threonine residue (T209 and T210 for rATX and hATX, respectively) that is in the middle of the two zinc ions, allowing the nucleophilic substitution during LPC to LPA transformation (Figure 1E) (23). The shallow groove next to the zinc ions is able to accommodate various nucleotides, and is important for correctly orienting the lipid phosphodiester substrate in the active site by accommodating the glycerol moiety. A deep hydrophobic pocket can be found in ATX (26). This is a unique feature among phospholipases and is not found in ENPP1, from which ATX evolved, most likely after deletion of 18 AA (7). The hydrophobic pocket can accommodate various phospholipids, enabling different conformations depending on their length. Many crystallographic structures with LPA derivatives are available in the PDB (29,30). This hydrophobic pocket is a major drug target in ATX. It is also important to mention the tunnel, which facilitates the LPA substrate to leave the protein after transfer from the active site and

## Introduction

hydrophobic pocket once the choline head group has been cleaved. The tunnel is composed of residues from the PDE catalytic domain and the SMB-1 domain (24). This feature doesn't exist in ENPP1 and might be the consequence of the 18AA deletion that also responsible of the hydrophobic pocket formation (31). Also, many small molecules have been described as interacting with ATX using this product exit tunnel, with one of the best example being steroids binding in the ATX tunnel as published by Perrakis's laboratory (30). Here, rATX- $\beta$  was co-crystallized with 7 $\alpha$ -hydroxycholesterol and the bile salt tauroursodeoxycholate (TUDCA), displaying the structural basis of ATX modulation by endogenous steroids. Although the exact function of this tunnel in ATX is still not fully understood recent advances have shown it's involved in both ATX catalytic activity modulation and presentation to LPA receptors (23).

### 2.1.3 Implication of autotaxin in diseases

ATX has been linked to numerous pathologies due to its implication in many cellular processes. It has been shown that ATX expression is increased in various cancer types and under inflammatory conditions.

#### **Implication in cancer**

Autotaxin was first discovered by Stracke et al in melanoma cells and linked to tumour progression, metastasis and angiogenesis (32). This can easily be explained by the pleiotropic role of LPA in stimulating cell migration and division (26,33). Yang et al reported in 1999 that ATX was overexpressed in non-small-cell lung cancers, with 7 out of the 12 studied cell lines that were positive for ATX overexpression (34). In 2002, Umezu-Goto and co-workers reported that ATX activity was 25 times higher towards LPC than nucleotides, and that ATX induced chemotaxis was enhanced by lysophosphatidylcholine in A-2058 melanoma cells, particularly when treated in presence of LPC (35). They extended their work to several other cancer cell lines, MDA-MB231, CHO-K1, EDG2-RH7777 and RH7777. They found that addition of ATX

## Introduction

and LPC stimulated the cell growth of most cancer cell lines. They also treated cells with increasing doses of LPA, and found a dose dependent induced cell growth (10). From these results, it became clearer that ATX could be a therapeutic target for drug design of anticancer agents. Other cancers that are promoted by ATX include glioblastoma. It has been shown that glioblastoma tumours overexpress LPA receptors and ATX, paving the way to target lysophosphatidic signaling in this deadly disease (36,37).

### **Implication in chronic inflammation**

Many studies have showed that ATX is mediating various effects, in particular vascular homeostasis, platelet aggregation, lymphocytes trafficking, chronic neuropathic pain, bone development and remodelling as well as stem cell renewal (11,38). ATX and LPA have been linked to vascular homeostasis through *in vitro* and *in vivo* studies. *In vitro* studies showed that the ATX/LPA signaling axis is an important mediator for endothelial cells, since it is required for blood vessel formation in mice and zebrafish during development (38,39). ATX/LPA signaling was also shown to be important for the formation and regression of blood vessels in recent publications (40,41). Concerning lymphocytes, ATX/LPA signaling was shown to be an important mediator of their migration in lymphoid organs (42). These effects show that ATX is now an emerging therapeutic target in chronic inflammatory diseases.

### **Implication in obesity and glucose homeostasis**

More than 50 % of LPA is produced by adipocytes and it is known that obesity is a factor in chronic inflammation (43,44). One study showed that serum ATX correlates with insulin resistance and glucose homeostasis, suggesting the ATX/LPA signaling axis could be targeted for insulin resistance (43). Indeed, ATX expression is increased in patients with obesity and impaired glucose tolerance(44). Rancoule et al showed

## Introduction

that injection of exogenous LPA in mice leads to an acute glucose tolerance and insulin impairment, showing a deleterious effect of LPA on glucose regulation (44).

### **Implication in cardiovascular diseases and atherosclerosis**

Since LPA is well known to be involved in angiogenic homeostasis and metabolism regulation, it seems quite logical that the ATX/LPA signaling axis is linked to cardiovascular diseases (45). Recent studies showed that ATX can activate platelets, leading to aggregation, a major cause of stroke (46). Regarding endothelial cells, it has been shown that ATX is implicated in adhesion molecule expression, cytokine expression, as well as migration, proliferation, angiogenesis and vasodilatation (47). The ATX/LPA signaling axis is also involved in smooth muscle cells regulation, in particular cytokine expression, proliferation, migration and vasoconstriction (48). Concerning immune cells linked to cardiovascular diseases, monocytes are activated by the LPA/ATX signaling axis (49). Cytokine expression can also be mediated through LPAR activation as well as lipid uptake (45,50). Implication of the ATX/LPA signaling axis in the development of atherosclerotic plaques is mostly due to a prothrombotic effect arising from platelet aggregation. It is a slowly progressive disease implicating inflammatory processes and vascular remodelling. LPA has been found in the atherosclerotic core, probably locally generated by oxidation of lipoproteins. Localization of ATX at the cell surface is likely to be linked to the inflammatory process found in atherosclerosis, with secretion of pro-inflammatory LPA near the lesion. Implication of the ATX/LPA signaling axis has also been shown in a mouse model, highlighting the importance of LPA1/3 receptors in the physiopathology of atherosclerosis (51).

### **Implication of autotaxin in idiopathic pulmonary fibrosis (IPF)**

IPF is a chronic lung disease with progressive fibrosis in older adults, mostly from 50 years old. It is a relatively rare disease with about 3 million people affected worldwide.

## Introduction

Since it is an idiopathic disease, there is no direct explanation for its' development. Several risk factors have been described in the literature such as smoking, air pollution and some professions exposed to risky factors. It has been shown that ATX levels are high in the bronchoalveolar fluid of patients presenting IPF (52). LPA production is also increased in these patients, leading to multiple activation of LPA receptors (LPARs), and their associated effects, including secretion of pro-inflammatory mediators and fibroblast accumulation (52). It has been shown that an animal model with LPA1 receptor deletion has an attenuated disease development (53). Pharmacological inhibition of LPARs was also successful in reducing disease progression and development (54). Other studies showed that deletion of ATX in bronchial epithelial cells or macrophages reduced disease progression, suggesting that ATX is a putative target for IPF management (55). More evidence for this comes from the study reported by Oikonomoud et al, who showed an increased ATX concentration in the lung tissue of patients presenting IPF (55). For this, they performed an ATX immunostaining of samples from several patients presenting pulmonary diseases. ATX staining was increased in the hyperplastic bronchiolar and alveolar epithelium surrounded by fibroblasts (55). They also showed that pharmacological inhibition of ATX attenuates the development of pulmonary fibrosis in a diseased mouse model using the ATX inhibitor GWJ-A-23, highlighting ATX as a major target for IPF management. Later, Galapagos and Gilead carried out a clinical trial investigating ziritaxestat, an ATX inhibitor, for idiopathic pulmonary fibrosis management. Unfortunately, the clinical trial was stopped due to high toxicity and there is still no efficient drug currently on the market for IPF management.

### **Implication in neurological disorders**

Recent advances have linked ATX to neurological diseases. ATX has been detected in brain tissues and cerebrospinal fluids (56). A specific isoform, ATX- $\gamma$ , is present only in the central nervous system, as mentioned previously (4). LPA dysregulation is known to trigger numerous cell processes and it has also been reported that it might be involved in central and peripheral nervous system disorders such as neuropathic



## Introduction

pain, Alzheimer's disease, glioblastoma multiform, schizophrenia, multiple sclerosis, traumatic brain injuries and many other diseases (56,57).

Kuwajima et al investigated the correlation between LPA and ATX levels with neuropathic pain intensity in humans: they found that higher lysophosphatidic levels are correlated with higher pain symptoms (58). The link between LPA signalling and neurological pain has also been demonstrated by an *in vivo* study reported by Inoue et al. In which they showed that mice lacking LPA1 receptor were not developing neuropathic pain after nerve injury (59).

Concerning Alzheimer's disease, it has been shown that ATX expression and activity dysregulation were linked to the disease (60). Umemura et al published a study where they compared gene expression in the frontal cortex of patients presenting Alzheimer's dementia to a control population. They found that ENPP2 was overexpressed in patients presenting Alzheimer's disease, paving the way of putative new therapeutic targets against this life altering disease (35). Another study reported by McLimans et al (20) showed that ATX levels were higher in patients presenting mild cognitive impairment and Alzheimer's disease. They showed that increased ATX levels were also linked to hypometabolism in the medial temporal lobe and to worst performance on function execution and memory tests (20).

## Introduction

### 2.1.4 Autotaxin inhibitors

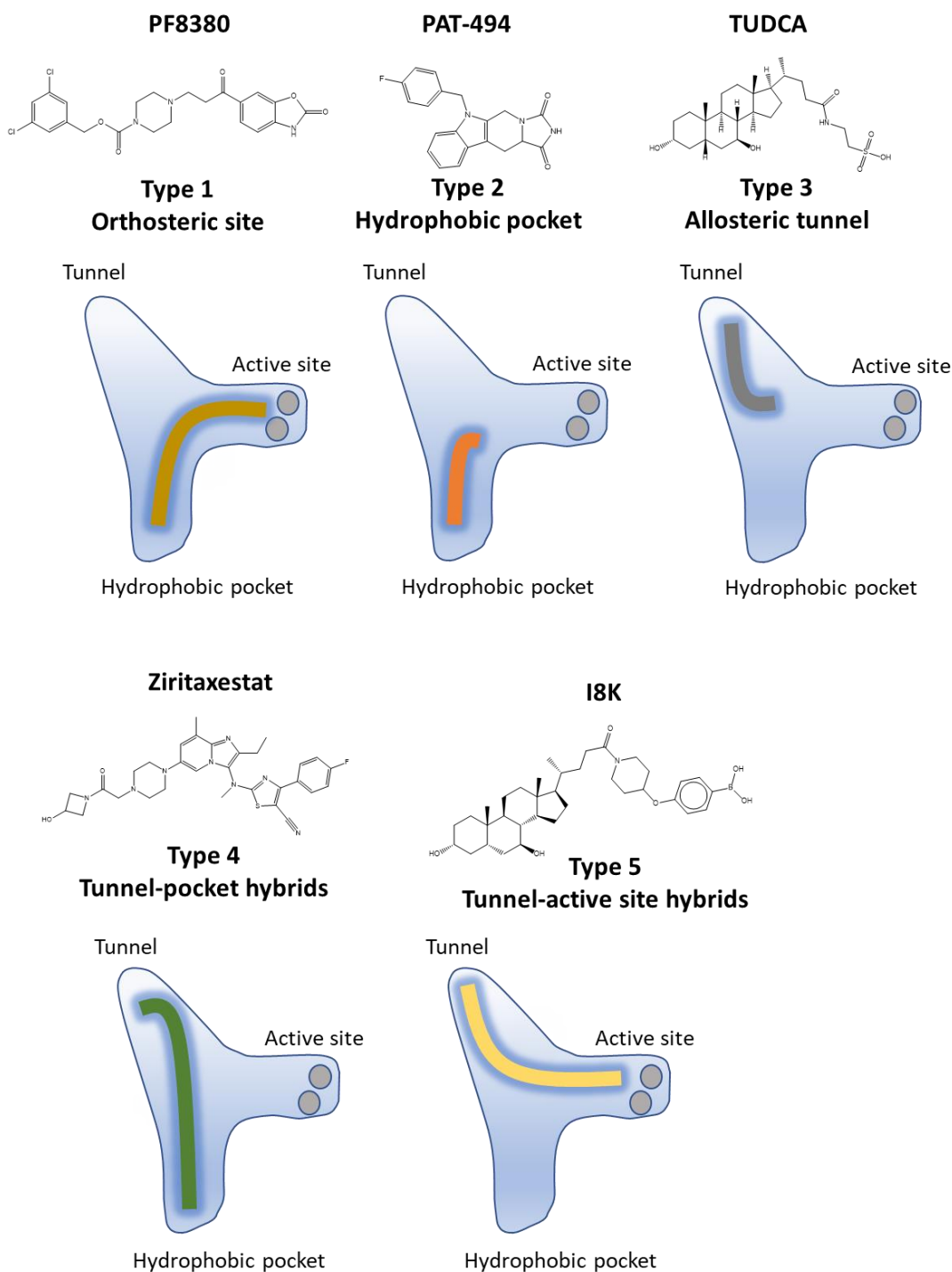


*Figure 2: ATX inhibitors classified according to discrete binding mode.*

*Adapted from Clark et al.*

Many ATX inhibitors have been developed over the last 20 years due to the implication of ATX in many pathologies (2,61). Structural and biochemical studies allowed their

## Introduction

classification according to differences in the binding mode within the active site. To date five different inhibitor types are known and summarised in figure 2 (61,62).

Type 1 inhibitors correspond to the first inhibitors discovered after screening a large library. They mainly form interactions within the active site and hydrophobic pocket, in a similar manner to LPA and LPC. Within this type, the first developed inhibitors were thiazolidinediones, leading to the discovery of HA-155, an inhibitor with a reported  $IC_{50}$  of 5.7 nM. Later, PF8380 was developed by Pfizer with an  $IC_{50}$  of 1.7 nM, and considered as the most potent ATX inhibitor discovered to date (62,63).

Type 2 inhibitors exclusively bind in the hydrophobic pocket and don't interact with the active site. They disturb LPC binding in the active site by occupying the hydrophobic pocket, which is needed to accommodate the LPC and LPA hydrophobic tail. They can offer more selectivity since there is no interaction with the active site zinc ions. The PAT-494 family are good examples of type 2 ATX inhibitors, they have been designed by PharmAkea and they all exhibit an indole moiety, which is important for interaction with the hydrophobic pocket (62,64).

Type 3 inhibitors bind in the tunnel used for product exit, avoiding the LPC entrance on the protein surface, and processing by the active site. These inhibitors are inspired by the observed binding of steroids into the ATX tunnel, shown to be important physiological regulators of ATX activity. An example of a type 3 inhibitor is TUDCA, a physiological inhibitor of ATX (30).

Type 4 inhibitors such as ziritaxestat are tunnel-pocket hybrids. They occupy both the tunnel and hydrophobic pocket, avoiding the LPC substrate entrance on the cell surface and accommodation of the lipophilic tail. They have been discovered by a fusion of type 1 and type 3 inhibitors, or by serendipity followed by screening and optimization, such as the series discovered by Galapagos laboratory (65).

Type 5 inhibitors have only very recently been described by Clark et al. They occupy both the tunnel and the active site, avoiding the both LPC entrance and catalysis. They are steroid-derived hybrids and only two inhibitors of this family are known, with I8K as the more active inhibitor with an  $IC_{50}$  of 30 nM (61) (PDB: 7Z0N).

## 2.2 LPA receptors: functional and structural description

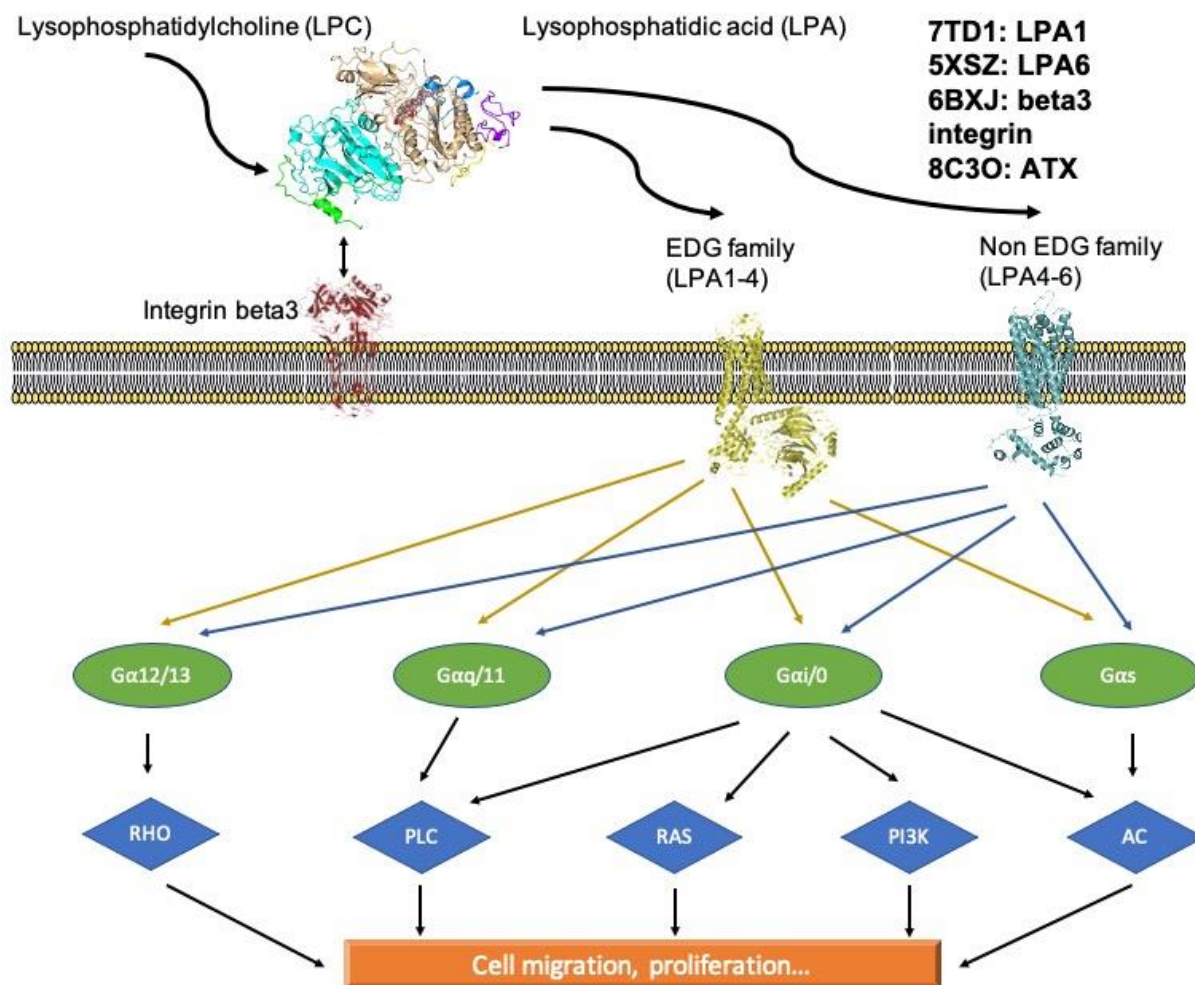


Figure 3: Summary of LPA receptor signaling pathways activated by autotaxin mediate LPA production and signalling.

Adapted from Yung et al.

LPA1 and LPA6 are displayed yellow and cyan, respectively.

To date, six LPA receptors (LPARs) have been described in the literature (figure 3). Historically, LPAR1, 2 and 3 have been classified as part of the endothelial differentiation gene (EDG) family of G protein-coupled receptors (GPCRs). However, not all functions of LPARs could be explained by this subtype of GPCRs. In 2008, researchers at university of Bonn discovered that a new member, LPAR6, was involved in hair loss, paving the way to classification of non-EDG LPARs (63,66–68).

## Introduction

LPAR1 was the first discovered LPA receptor and is the most studied. This 41 kDa protein is essential for embryonic development and *in vivo* mouse studies showed a 50% lethality at birth upon deletion of *Lpar1* encoding for the LPAR1. The deletion of this gene also leads to reduced body size, malformations and neuronal impairments (67). LPAR2 was discovered during an orphan GPCR sequence search and shares a 55% sequence similarity with LPAR1. LPAR2 is mostly expressed in leukocytes and testis, and its activation leads to cell survival and migration. Mice mutants lacking LPAR2 are normal, with no known defects during development (67). LPAR3 is 50 kDa and shares around 50% homology with LPAR1 and LPAR2. This receptor is mostly expressed in the heart, testis, prostate and pancreas. Knock out (KO) LPAR3 mutants have a normal development with the exception of female mice, which experience delayed embryo implantation (67).

LPAR4 is 42 kDa and shares only 20% sequence homology with LPAR1. It is part of the non-EDG family, which includes LPAR5 and 6, and mostly found in the ovary. Mice with deletion of *lpar4* exhibit an increased trabecular bone volume and thickness. They also exhibit pericardial effusions, severe oedema, haemorrhage and dilated vessels. From these results, it seems likely that LPAR4 is involved in osteogenesis (67). LPAR5 shares a 35% homology to LPAR4 and 22% to LPAR1. This receptor is highly expressed in the spleen, heart, small intestine placenta, colon and liver. A possible role of LPAR5 during brain development has been uncovered by Plastira et al (69). Also, LPAR5 has a 10 fold higher affinity to alkyl chains rather than acyl chains 18:1 LPA (66,67). LPAR6 was the last discovered LPA receptor. This receptor has been linked to pattern hair loss and is an emerging target for this disease. Surprisingly, this receptor has a low affinity to LPA and studies show that a 10  $\mu$ M concentration is needed to see any effect, but further studies are needed to understand the physiology of LPAR6 (66,67).

Downstream signaling of the various LPA receptors from both EDG and non-EDG families is complex and involve G-protein coupled receptors. G $\alpha$ 12/13-mediated signaling pathways are responsible for multiple physiological processes, relying on RHO kinase activation, such as embryonic development, cell growth, angiogenesis, platelet activation, immune system and apoptosis (70). This pathway is also involved in several diseases, and acts as a pro oncogenic factor capable of inducing oncogenic

## Introduction

transformation (70). Gαq/11 stimulate the PLC, which is responsible for formation of inositol-1,4,5-trisphosphate (IP3), a second messenger involved in signal transduction and calcium release, in fine activating various calcium-dependent receptors. Functions of this signaling pathway are huge, ranging from cell proliferation to smooth muscle contraction (71). Gαi/o activates PLC, RAS and PI3K downstream signaling. RAS activates several signaling pathways, in particular the Mitogen Activated Protein (MAP-kinase) cascade, which is involved in cell division and growth. This GPCR is also activating the PI3K/AKT/mTOR pathway, also involved in cell proliferation and cancers (72). Finally, Gαs is responsible for the activation of the cAMP-dependent pathway, also involved in many physiological processes such as heart rate regulation and cortisol secretion (73). The difference between EDG and non-EDG LPA receptors comes from a distinct evolution from a common ancestor, leading to a different ligand entry mode and GPCR downstream signaling. Interestingly, Salgado-Polo et al demonstrated that ATX is able to present LPA to the surface of the LPA receptors. They also showed that the ATX-LPA axis is selective over the 6 LPA receptors and has a better affinity towards LPA<sub>4-6</sub> receptors (23). This can be explained by the structural differences between the two LPA receptors families. It is believed that LPA1 binds LPA ligand from the extracellular space, while LPA6 by lateral diffusion, after deposition on the outer lipid bilayer (22,23,74).

## 2.3 Medicinal cannabis and tetrahydrocannabinol (THC)

### 2.3.1 Description of medicinal cannabis and its components

Medicinal cannabis, also called therapeutic cannabis or medical marijuana, refers to *Cannabis sativa*, the botanic name of Chanvre and by extension all the phytocannabinoids used for therapeutic purposes. Up to now, due to the constant evolution of the scientific knowledge in this area, cannabis use is becoming more and more tolerated or even legal in numerous countries such as Belgium, Netherlands, United Kingdom, Canada, Spain and several states in the USA. The use of medicinal cannabis needs either a prescription or medical diagnosis to be legal in most countries. Product distribution is usually under strict laws to avoid misuse of medicinal cannabis, and under the responsibility of the pharmacist.

## Introduction

There is no agreed definition for medicinal cannabis but the Encyclopaedia Britannica proposed the following definition (75):

<< medical cannabis, also called medical marijuana, herbal drug derived from plants of the genus Cannabis that is used as part of the treatment for a specific symptom or disease. Although the term cannabis refers specifically to the plant genus, it is also used interchangeably with marijuana, which describes the crude drug isolated from the plants' leaves and flowers. >>

Historically, cannabis is known from the ancient world. It has been demonstrated that tribes in Romania used Cannabis 5000 years ago. Hui-lin Lin wrote in his article "An Archaeological and Historical Account of Cannabis in China" that medicinal cannabis was probably a very early development even if it started with the use of seeds and fibers as a source of nutriment and clothes. Hui-lin Lin also mentioned that a cannabis plant was painted on the famous Pen-ts'ao Ching herbal, plausibly made by the emperor Shen-nung about 2000 BC. According to this author, this work was based on early traditions passed from ancients and even from prehistoric times (76). It was already stated in Pen-ts'ao Ching herbal that "fruit from the hemp" were leading to hallucinations if taken in excess and making one communicate with the spirits if taken over a long period. It is not surprising that the effects of acute cannabis consumption were already known thousands of years ago. The first testimony of its medicinal use was from the famous physician Hua T'o (117-207 A.D.). He was using a concoction of Cannabis called ma-fei-san. The hemp of the flower was boiled and given to patients with wine, in order to be anesthetized before surgery. This actually makes sense since most of the tetrahydrocannabinolic acid (THC-A) in the plant needs to be converted to tetrahydrocannabinol (THC) in order to be active, this is done by heating the seeds over a certain temperature for couple of minutes before ingesting it. The same chemical reaction happens while smoking, since the cannabis is heated to hundreds of degrees during the process.

Use of cannabis in more recent history can be attributed to Sir William Brooke O'Shaughnessy, who worked in India on various medicinal plants including cannabis

## Introduction

and opium. He tried various mixtures of Hemp on patients suffering from cholera, tetanus and rheumatoid arthritis (77). From there, more and more articles on cannabis plants and their therapeutic properties were published, and it was quite common to use cannabis for therapeutic purposes as a sedative, painkiller or antiemetic until the 1930's.

In 1925, cannabis was added to the list of the narcotic drugs and psychotropic substances (78), reducing the amount imported from producing countries. Then, each country adopted their own, usually restrictive, legislation on cannabis. In 1961, the single convention on Narcotic Drugs was signed within the frame of the United Nations (79). Cannabis was included in table IV, the most restrictive category, leading to extended controls and regulation.

Concerning the molecules in cannabis extract, the most potent one, THC, was isolated by the Israeli chemist Raphael Mechoulam (80) in 1964. He also later discovered endocannabinoids, arachidonylethanolamide and 2-monoglyceride in 1992 and 1995 respectively (81,82). Raphael Mechoulam was one of the pioneers for medicinal cannabis use in more recent history, despite the legal difficulties arising from its listing on table IV scheduled drugs. From the 2000's, researchers and pharmaceutical companies tried to assess its use in human medicines, ranging from pain management to epilepsies. A clinical trial is currently being held in France by the ANSM on patients with specific diseases, including:

- Neuropathic pain not correctly managed by available medicines.
- Severe and pharmaco-resistant epilepsies.
- Cancer symptoms from the disease or therapies.
- Palliative cares.
- Multiple sclerosis and other central nervous system pains.

The results from this study should be available within 2023 and assess the generalization of medicinal cannabis use for patients with specific diseases in France (83).



## Introduction

A difficulty arising from medicinal cannabis is identifying which molecule the patient should be treated with. Indeed, medicinal cannabis is a plant extract and therefore contains a large number of molecules. The most studied ones are called “cannabinoids” that share common structural features (detailed in figure 4). The most famous cannabinoid is delta-9-tetrahydrocannabinol (or for simplicity referred to from here as THC), leading to most of the psychoactive effects of cannabis through CB1 and CB2 receptor binding. Its structure was discovered by Mechoulam et al in 1964, following isolation from hashish (84). A close derivative is delta-8-tetrahydrocannabinol (delta-8-THC), in which only the position of unsaturation 6a-10a on the C ring differs, as shown on figure 4. The THC dibenzopyran numbering is shown in red on figure 4. Delta-9-Tetrahydrocannabinolic acid (THCA) corresponds to the derivative produced by the plant, which is further decarboxylated and activated by heating the leaf before consumption or smoking to lead to THC. Indeed, THCA potency is very low compared to that of THC, at least for the CB1 and CB2 receptor binding potency. Another isomer of THC is Cannabinol (CBN), which differs by the presence of an aromatic ring instead of single unsaturation in the C ring. This derivative is also less active probably due to the higher rigidity of the molecule. Another important class of derivative is represented by cannabidiol (CBD), which is also less potent than THC due to the opening of the B ring. Other derivatives won't be described here but they are widely studied and an abundant literature can be found.

## Introduction

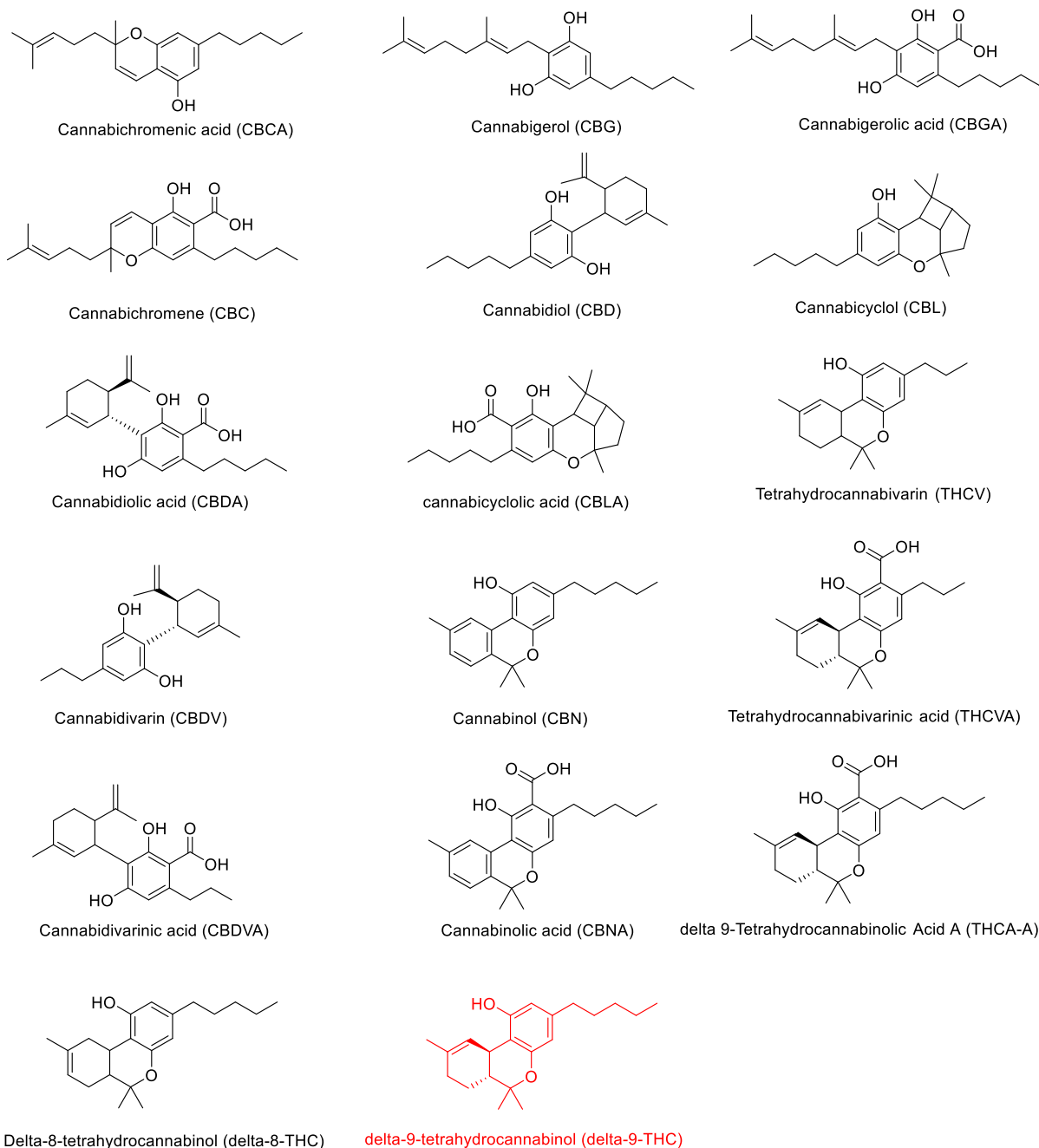


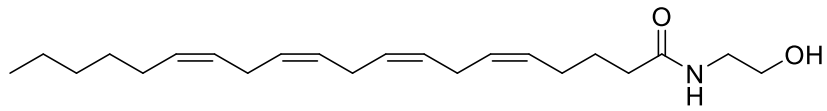
*Figure 4: Chemical structures of the main plant cannabinoids*

As mentioned previously, Raphael Mechoulam discovered other molecules found in the human body, so called "endocannabinoides", because they were identified as the endogenous (or physiological) ligands for the cannabinoid (CB) receptors (82,85). Six molecules have been linked to the endocannabinoid human system to date, namely Anandamide (AEA), 2-Arachidonylglycerol (2-AG), 2-arachidonyl glyceryl ether (2-AEA), N-Arachidonoyl dopamine (NADA), lysophosphatidylinositol and virodhamine. Their chemical structures are displayed in Figure 5 and we can notice some structural

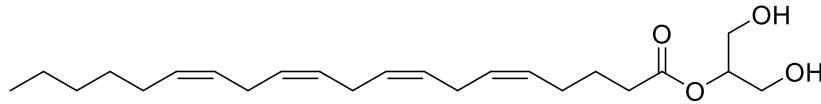
## Introduction

similitudes to LPA, all sharing a long lipophilic tail. Anandamide (AEA)(86) and 2-arachidonoylglycerol (2-AG)(87), which were detected in samples from the brain and intestine, and shown to activate CB<sub>1</sub> and CB<sub>2</sub> with high affinity and efficacy, were subsequently described as endocannabinoids (88) Moreover, enzymes for the biosynthesis and the degradation of endocannabinoids have been discovered, such as N-acetylphosphatidylethanolamine-specific phospholipase D (NAPE-PLD) catalysing the synthesis of anandamide as well as other N-acylethanolamines(89). The fatty acid amines hydrolase (FAAH) catalyzes the degradation of AEA, other N-acylethanolamines and fatty acid primary amides(90). Diacylglycerol lipase  $\alpha$  (DAGL $\alpha$ ) and DAGL $\beta$  generate the formation of 2-AG, as well as other monoacylglycerols(91), and monoacylglycerol lipase (MAGL) catalyzes the breakdown of 2-AG and other monoacylglycerols(92). These breakthroughs accelerated our knowledge about what is nowadays well established as the endocannabinoid system(93). The endocannabinoid system can be further expanded to the endocannabinoidome, a much wider complex network of promiscuous mediators overlapping with other signaling pathways(93). In this context, it has been shown that the enzymatic dephosphorylation of a 2-arachidonoyl species of lysophosphatidic acid (LPA) in the brain of rats generates the formation of 2-AG(94), a process that has later been revealed to depend on lipid phosphate phosphatases(95). From a biomedical point of view, the endocannabinoid system is involved in many physiological processes such as cognition, pain, fertility and appetite. Its effect potentially overlaps with other signaling pathways in regulating processes since CB receptors are also GPCRS.

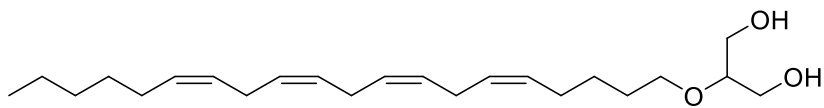
## Introduction



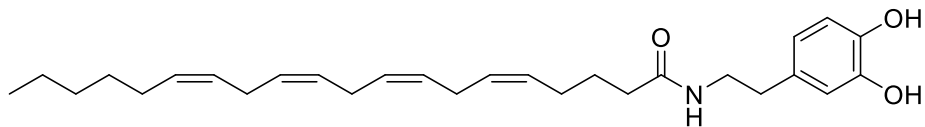
Anandamide (AEA)



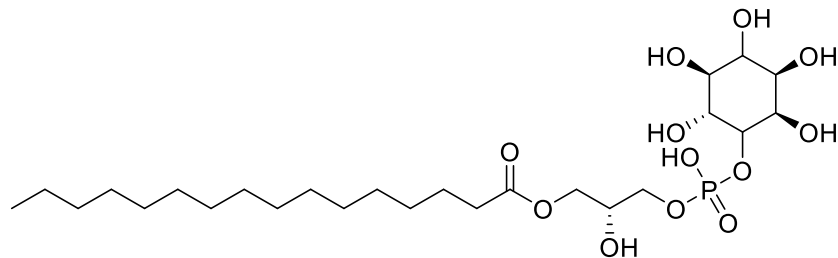
2-Arachidonylglycerol (2-AG)



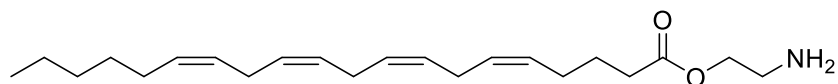
2-Arachidonyl glyceryl ether (2-AEA)



N-Arachidonoyl dopamine (NADA)



Lysophosphatidylinositol



Virodhamine

*Figure 5: Chemical structures of human endocannabinoids*

### 2.3.2 Interaction of medicinal cannabis components with human proteins

## Introduction

Cannabinoid (CB) receptors bind cannabinoids and endocannabinoids with varying affinity. The CB receptors were discovered more than 40 years ago during *in vitro* studies and they are members of the GPCR family (96). Two receptors, CB1 and CB2, have been identified to date. CB1 is one of the most expressed receptors in the brain and responsible of retrograde signalling when bound to any agonist endocannabinoid. This receptor can induce a depolarization of neurons that will reduce GABA mediated neurotransmission. CB2 is expressed in the immune system, in the central nervous system and in the brain. This receptor is involved in the nociception<sup>1</sup> and is responsible for pain relief from cannabinoids. The CB2 receptor is probably involved in many other cellular processes that remain unknown (96,97).

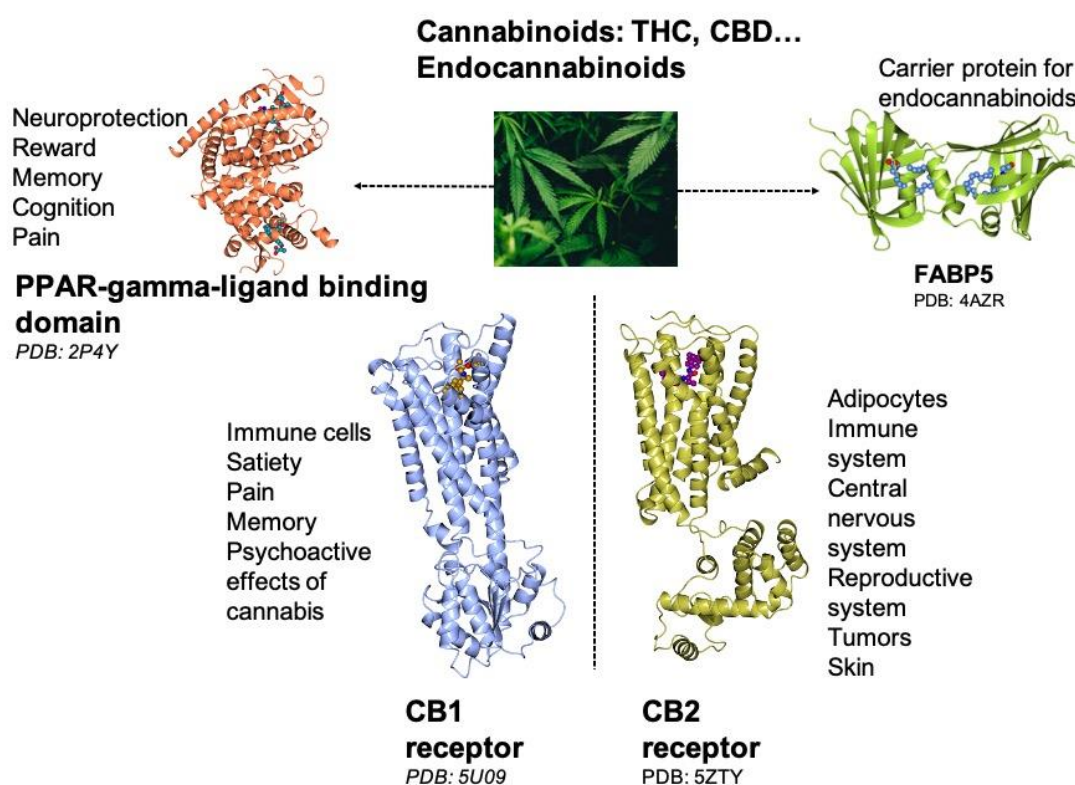


Figure 6: Structure-function of human proteins interacting with cannabinoids and endocannabinoids.

*Cannabis plant picture: courtesy from Matthew Brodeur under Unsplash license for non-commercial use. Link: <https://unsplash.com/photos/qcCPIhhdgTw>*

<sup>1</sup> Nociception refers to the noxious stimulus in vertebrate, such as injuries and temperature extreme leading to what we describe as pain in common parlance.

## Introduction

Both CB1 and CB2 receptor structures were recently solved (figure 6). (98,99). The structures helped understanding CB1 receptor function and signal transduction when bound to cannabinoids and are available from the PDB database (PDB ID: 5U09 and 5TGZ). The CB2 receptor structure was also solved (PDB: 5ZTY) (100), providing structural information on the difference between CB1 and CB2 receptors, helping elucidate the different functions of each receptor and the distinct antagonist-binding mode of the CB2 receptor. CB1 and CB2 receptors share only 44 % homology, but their ligand-binding pockets at orthostatic sites are highly conserved, explaining the binding of similar ligands and the difficulty in designing a selective inhibitor of CB1 or CB2 receptors. Zhi-jie Liu et al have worked extensively on CB1 and CB2 structural determinations and they were able to solve CB receptors in their various states. It is now widely accepted that CB receptors have at least three different functional states: an antagonistic, an intermediate and an activated state, mediating downstream signaling of the receptors (101).

Recent advances in protein crystallography and Cryo-EM deciphered the structure of cannabinoids and endocannabinoids bound to various human proteins such as FABP5, PPAR $\gamma$  and CB1 or 2 receptors (102–105). Yang et Al compared the binding site of both CB1 and CB2 receptors (106). They both share a hydrophobic pocket as a common feature, which can be explained by the cannabinoids and endocannabinoids structures which are highly hydrophobic. The hydrophobic interactions are mediated by a tryptophane and a phenylalanine, which are conserved between CB1 and CB2 receptors. Interestingly, a histine mediating a hydrogen bond is also found in CB1 and CB2 receptors, responsible for the hydrogen bond formation between ligands and receptors. PPAR $\gamma$  binding to cannabinoids have been shown to mediate neuroprotection, reward, memory, cognition and analgesic effects. There is also evidence of PPAR $\gamma$  induced apoptosis during cannabinoid treatment of cancer cell lines. Effects on inflammation, satiety, metabolism and vasorelaxation have also been reported (102). Concerning FABP5, it has been shown that this protein interacts with the endocannabinoid system as a carrier and is indispensable for their transport at central glutamate synapses (103).

### 2.3.3 Recent advances in medicinal cannabis therapy

Hundreds of clinical trials have been conducted in various countries for a large number of diseases such as refractive epilepsy, neuropathic pain, cancer management, multiple sclerosis, anxiety, nausea and anorexia. Despite the huge number of clinical trials held in the world, there has been no clear result as to whether this therapy is effective for the mentioned diseases. Legislation regarding medicinal cannabis is still very restrictive in most of the western countries, and the difficulty in patenting plant cannabinoids is probably a consideration towards investment in clinical trials from the pharmaceutical industry. Most of the current and past clinical trials are led by public agencies with limited numbers of patients, with the aim of making this form of treatment available to patients with late-stage diseases or those recalcitrant to conventional therapies. On the other hand, pharmacokinetics of THC and CBD are widely studied, and numerous data are available assessing their safety (107). However, more clinical trials are needed to assess whether cannabinoid therapy is providing sufficient relief compared to the side effects involved with such treatments. A close monitoring of side effects is also needed during administration since cannabinoids can cause memory impairment, hallucinations, higher risk of psychosis, dizziness and change in mood. Studies have also shown that THC permanently affects brain development, especially when used at a young age, and a recent study highlighted that marijuana was associated with a loss of 8 IQ points if used during adolescence (108,109). Adults do not appear to be concerned by IQ decline if they commenced consumption after brain development was complete. Other side effects have been highlighted in the literature, such as breathing problems and lung cancers due to smoking. This can be avoided by consumption with oral forms of cannabinoids, such as food as the best example, or oil extracts. It is also admitted that cannabis increases the heart rate for several hours after consumption, with a concomitant increased heart attack risk. It is also not safe for pregnant women to consume cannabis since its use has been associated with lower birth weight, and increased risk of brain malformations and other neurological impairments (110). From all this information, a question could arise from the general public. Is cannabis worse than alcohol or tobacco? Why did we legalize use of alcohol and tobacco while cannabis is prohibited in most countries? One of the worst fears from governments and the general public is that cannabis users might use other and

## Introduction

stronger recreational drugs if cannabis is legalized. This has not been demonstrated for the moment but a closer study in regions where cannabis is legal is needed to discern if this is valid. Other countries might also legalize cannabis in the future, but only for therapeutic purposes and from identified prescribers. The medicinal cannabis is mainly sold in pharmacies whose stocks are strictly monitored (111).

All this underscores the need to better understand the interaction of medicinal cannabis constituents with biological targets in order to properly evaluate the therapeutic value of this treatment.

## 2.4 Aim of the PhD thesis

Various ATX inhibitors have already been developed and some are now in clinical trials (2,112–114). However, compounds with satisfactory pharmacokinetic parameters and low toxicity are limited. There still is no approved drug for ATX brain-related diseases. Moreover, ATX distribution is tissue-specific and most of the research has been focused on the  $\alpha$  and  $\beta$  isoforms. For ATX- $\gamma$ , plausibly related to many neurological diseases, a deeper understanding is needed to design and develop more specific inhibitors of this isoform and to fully understand its pathophysiological role. Initial *in silico* studies by Dr. Ulrike Uhrig from the Chemical Biology Core facility at EMBL Heidelberg demonstrated that THC could be a potential inhibitor of ATX. Furthermore, preliminary studies by Jens Hausmann (a former post-doc in the team) confirmed this inhibitory effect. As the pharmacokinetic parameters for cannabinoids are widely studied, and there is a consensus that they cross the BBB and bind to CB1 and CB2 receptors, this could be a viable strategy to specifically inhibit ATX in the brain. However, a major drawback of cannabinoids is their regulation and acceptance by patients, making them less desirable for development. Nevertheless, medicinal cannabis is used more and more to treat neurological diseases, while little is known about the pharmacology behind the therapeutic effects uncovered by recent clinical trials. It is therefore interesting to assess if ATX is important for cannabinoids mode of action to inspire further *in vivo* research.



## Introduction

The first part of the PhD work was therefore to fully characterize the interaction of cannabinoids and endocannabinoids with ATX as well as producing recombinant protein and performing biochemical studies to assess the affinity of cannabinoids toward ATX. Moreover, one of our goals was to decipher the binding interface between THC and ATX using macromolecular crystallography techniques. From these *in vitro* results, a new type of cannabinoid-inspired inhibitors were synthesized and characterized. As there is no regulatory approved ATX inhibitor on the market there is still a need for new ATX inhibitor types that can regulate the ATX-LPA pathway, especially in a tissue or disease specific manner. Cannabinoid chemistry is difficult so we screened compounds sharing similar structural features but that can be plausibly synthesized.

Recent studies have shown that ATX needs to produce LPA close to its cognate LPA signaling receptors. So another part of the PhD project was to develop a protocol for the structural determination of ATX using cryo-EM, opening up the possibility to study ATX signaling study and binding with partner proteins such as integrins.

### 3 Materials and Methods

#### 3.1 Chemistry:

##### 3.1.1 General information

Commercially available reagents and solvents were purchased and used without further purification. Chemical reactions were monitored by thin layer chromatography (plates coated with silica gel 60 F254 from Macherey-Nagel). Chemical products were purified with column chromatography on Silica gel 60 (230-400 mesh from Macherey-Nagel) or by automatic flash chromatography with a Grace device: Reveleris X2. NMR spectra were performed on the NMR-ICMG platform of Grenoble on either a 400 MHz Bruker Avance-400 instrument (400 MHz) or 500 MHz Bruker Avance-500 instrument at room temperature. Chemical shifts ( $\delta$ ) are reported in parts per million (ppm) relative to TMS as internal standard or relative to the solvent [ $^1\text{H}$ :  $\delta(\text{CDCl}_3) = 7.26$  ppm,  $\delta(\text{CD}_3\text{OD}) = 3.31$  ppm  $\delta(\text{DMSO-}d_6) = 2.50$  ppm,  $\delta(\text{acetone-}d_6) = 2.05$  ppm;  $^{13}\text{C}$ :  $\delta(\text{CDCl}_3) = 77.06$  ppm,  $\delta(\text{CD}_3\text{OD}) = 49.03$  ppm,  $\delta(\text{DMSO-}d_6) = 39.53$  ppm,  $\delta(\text{acetone-}d_6) = 29.82$  ppm]. Electrospray ionization (ESI) mass spectra were acquired by the ICMG platform of Grenoble on an Esquire 3000 Plus Bruker Daltonis instrument with a nanospray inlet. Accurate mass measurements (HRMS) were carried out on an ESI/QTOF with the Waters Xevo G2-S QTOF device.

##### 3.1.2 Compounds synthesis:

###### *General protocol for MEY-003:*

This protocol is similar for the various inhibitors synthesized in this compound family. The general protocol described here is for MEY-003 and less details are provided for the compounds (see scheme 1).

*1-N-Pentyl-1H-indole-3-carbaldehyde (2)*: To a stirred suspension of sodium hydride (60% dispersion in mineral oil; 0.413 g, 10.3 mmol) in anhydrous DMF (5 mL), cooled with an ice bath, was added dropwise a solution of 1H-indole-3-carbaldehyde (1) (1 g, 6.89 mmol) in anhydrous DMF (10 mL) over 10 min. After stirring at room temperature for 0.5 h, n-pentyl bromide (1.148 g, 7.6 mmol) was added dropwise over 5 min. After completion of the reaction (TLC), the solution was poured into ice-water. The suspension was stirred for 10 min and extracted with EtOAc. The organic extracts

## Materials and Methods

were combined, washed with brine, dried over anhydrous Na<sub>2</sub>SO<sub>4</sub>, and evaporated under reduced pressure to give a residue that was treated with hexane to remove mineral oil, collected by filtration and dried *in vacuo* to obtain provide compound (**2**) as yellowish solid. (Yield: 1.37 g, 92.6%). The compound was used for the next step without purification.

*(E)-1-(2-Hydroxy-4,6-dimethoxyphenyl)-3-(1-pentyl-1H-indol-3-yl)prop-2-en-1-one* (**3**): Compounds (**1**, 0.819 g, 4.176 mmol) and (**2**, 0.750 g, 3.48 mmol) were dissolved in anhydrous DMF (10 mL) and sodium hydride (60% dispersion in mineral oil; 0.697 g, 17.4 mmol) was added in portions at room temperature. The mixture was stirred for 16 h, poured into cold 1 N HCl solution and an additional 1 N HCl was added until the solution became acidic. The resulting suspension was stirred for 5 min and filtered. Solids were collected and washed with water, then dissolved in dichloromethane, dried over anhydrous Na<sub>2</sub>SO<sub>4</sub>, and concentrated under reduced pressure to give a solid residue which was treated with MeOH to afford compound (**3**) as a yellowish solid (0.69 g, 50.4% yield). <sup>1</sup>H NMR (400 MHz, CDCl<sub>3</sub>) δ ppm 14.87 (s, 1H), 8.12 (d, *J* = 15.5 Hz, 1H), 7.98-8.08 (m, 2H), 7.47 (s, 1H), 7.27-7.43 (m, 3H), 6.12 (d, *J* = 2.3 Hz, 1H), 5.99 (d, *J* = 2.3 Hz, 1H), 5.40 (t, *J* = 6.9 Hz, 1H), 4.24 (t, *J* = 7.0 Hz, 2H), 3.98 (s, 3H), 3.84 (s, 3H), 1.84 (s, 3H), 1.80 (s, 3H). <sup>13</sup>C NMR (100 MHz, CDCl<sub>3</sub>) δ ppm 192.6 (1C), 168.5 (1C), 165.5 (1C), 162.4 (1C), 137.8 (1C), 137.4 (1C), 133.6 (1C), 126.4 (1C), 122.9 (1C), 121.4 (1C), 122.2 (1C), 120.9 (1C), 113.7 (1C), 110.5 (1C), 106.4 (1C), 94.0 (1C), 91.2 (1C), 55.9 (1C), 55.6 (1C), 44.9 (1C), 31.5 (1C), 19.4 (1C), 13.5 (1C). HRMS (m/z): calcd. for C<sub>24</sub>H<sub>27</sub>NO<sub>4</sub> 393.19; found, 394.2606 [M+1].

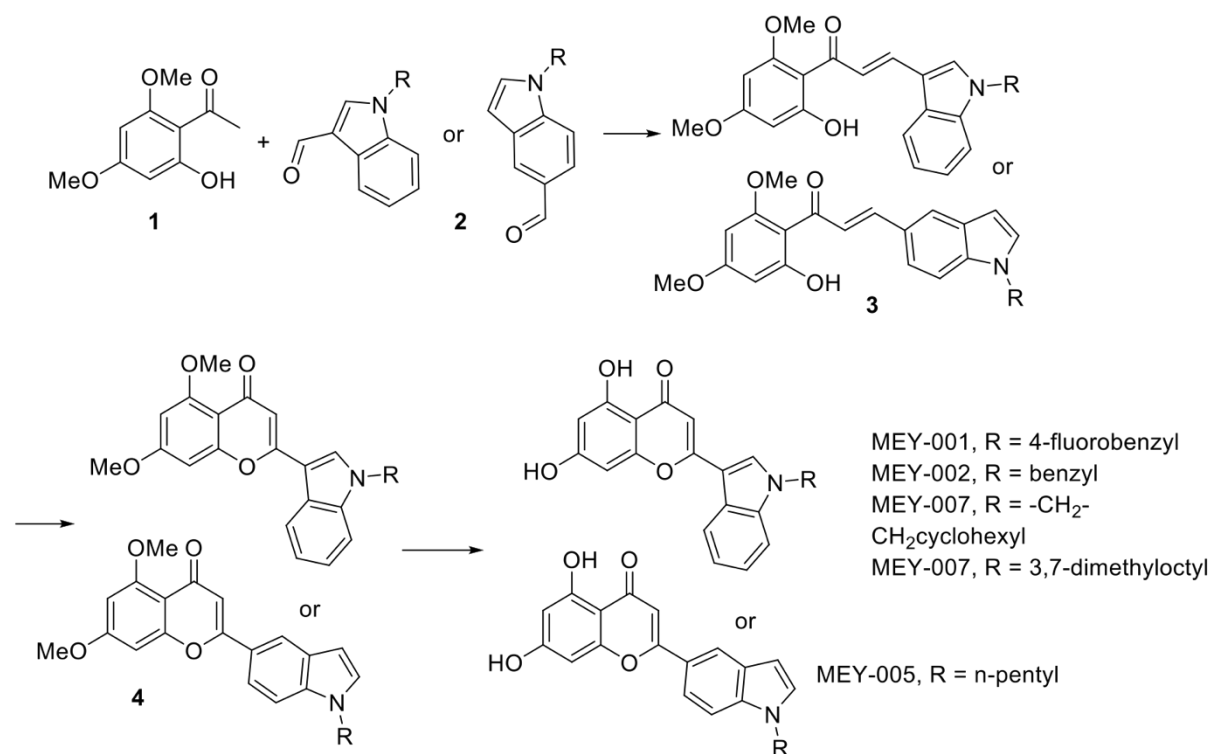
*5,7-Dimethoxy-2-(1-pentyl-1H-indol-3-yl)-4H-chromen-4-one* (**4**). To a solution of compound (**3**) (0.69 g, 1.75 mmol) in DMSO (2 mL) was added a catalytic amount of iodine (0.046 g, 0.18 mmol) and the reaction mixture was heated to 130 °C and stirred for 3 h. The solution was cooled to room temperature and poured into a saturated aqueous sodium thiosulfate solution and the resulting precipitate was filtered, washed with cold water and ether to afford crude compound **4**, which was filtered on a SiO<sub>2</sub> pad using MTBE as eluent. The filtrate was concentrated *in vacuo* to obtain 0.32 g of compound (**4**) as yellowish solid. Yield: 46.4%. <sup>1</sup>H NMR (400 MHz, DMSO-*d*<sub>6</sub>) δ ppm 8.29 (s, 1H), 8.12 (d, *J* = 7.2 Hz, 1H), 8.56 (d, *J* = 7.2 Hz, 1H), 7.24-7.34 (m, 2H), 6.83 (d, *J* = 2.3 Hz, 1H), 6.47-6.51 (m, 2H), 4.87 (d, *t* = 6.9 Hz, 2H), 3.93 (s, 3H), 3.83 (s,

## Materials and Methods

3H), 31.5 (1C), 22.5 (1C), 19.4 (1C), 13.5 (1C).  $^{13}\text{C}$  NMR (100 MHz, DMSO- $d_6$ )  $\delta$  ppm 175.2 (1C), 163.4, 160.2, 159.1, 159.0 (4C), 136.6 (2C)<sub>2C=</sub>, 131.0 (1C), 124.4 (1C), 122.6, 121.6, 120.7 (3C), 111.2 (1C), 108.4 (1C), 106.4 (1C), 96.1 (1C), 93.2 (1C), 56.0 (1C), 56.0 (1C), 44.3 (1C), 31.2 (1C), 23.0 (1C), 19.1 (1C), 13.5 (1C). HRMS ( $m/z$ ): calcd. for  $\text{C}_{24}\text{H}_{25}\text{NO}_4$  391.18; found, 392.1313 [ $\text{M}+1$ ].

*5,7-Dihydroxy-2-(1-pentyl-1H-indol-3-yl)-4H-chromen-4-one (MEY-003)*. A solution of compound (**4**) (0.32 g, 0.817 mmol) in  $\text{CH}_2\text{Cl}_2$  was treated with boron tribromide (2.048 g, 8.17 mmol) at room temperature under an argon atmosphere. The mixture was stirred for 24 h, poured into ice-water and extracted with EtOAc. The organic phase was dried over  $\text{Na}_2\text{SO}_4$  and concentrated under reduced pressure. The residue was purified by preparative HPLC to afford **MEY-003** as a yellowish solid. Yield = 0.0383 g.  $^1\text{H}$  NMR (DMSO- $d_6$ , 500 MHz): 12.51 (1H, s), 10.21 (1H, m), 9.76 (d, 1H), 9.324 (1H, m), 8.95 (2H, m), 8.30 (1H, s), 8.18 (1H, s), 7.84 (1H, s), 5.93 (2H, m), 4.98 (4H, s), 3.48 (2H, m), 2.95 (4H, m).  $^{13}\text{C}$  NMR (DMSO- $d_6$ , 125 MHz): 181.2 (1C), 163.9 (1C), 163.1 (1C), 161.6 (1C), 157.2 (1C), 137.0 (1C), 133.0 (1C), 132.9 (1C), 124.3 (1C), 122.9 (1C), 122.1 (1C), 111.4 (1C), 111.3 (1C), 106.5 (1C), 103.6 (1C), 101.3 (1C), 98.8 (1C), 93.9 (1C), 46.3 (1C), 29.3 (1C), 28.4 (1C), 21.8 (1C), 13.9 (1C). MS (ESI<sup>+</sup>)  $m/z$  364 [ $\text{M}+\text{H}$ ]<sup>+</sup>; (ESI<sup>-</sup>)  $m/z$  362 [ $\text{M}-\text{H}$ ]<sup>-</sup>. HRMS ( $m/z$ ): [ $\text{M} + \text{H}$ ]<sup>+</sup> calcd. for  $\text{C}_{22}\text{H}_{22}\text{NO}_4$  364.1500 ; found, 364.1483. LCMS:  $R_t$  = 15.6 min; [ $\text{M}+1$ ]<sup>+</sup> 364.15, [ $\text{M}-1$ ]<sup>-</sup> 362.00. Purity 95.0% (HPLC).

## Materials and Methods



*Scheme 1: Synthesis of compounds MEY-001, MEY-002, MEY-005, MEY-007 and MEY-008*

*These compounds were synthesized according to the same synthetic scheme for MEY-003 (reported in the thesis)*

*Details for other compounds:*

**2-(1-Benzyl-1H-indol-3-yl)-5,7-dihydroxy-4H-chromen-4-one (MEY-001).** To a stirred suspension of sodium hydride (60% dispersion in mineral oil; 0.413 g, 10.3 mmol) in anhydrous DMF (5 mL), cooled with an ice bath, was added dropwise a solution of 1H-indole-3-carbaldehyde (1 g, 6.89 mmol) in anhydrous DMF (10 mL) over 10 min. After stirring at room temperature for 0.5 h, 4-fluorobenzyl bromide (1.433 g, 7.6 mmol) was added dropwise over 5 min. After completion of the reaction (TLC), the solution was poured into ice-water. The suspension was stirred for 10 min and extracted with EtOAc. The organic extracts were combined, washed with brine, dried over anhydrous Na<sub>2</sub>SO<sub>4</sub>, and evaporated under reduced pressure to give a residue that was treated with hexane to remove mineral oil, collected by filtration and dried *in vacuo* to obtain derivative **2** as a yellowish solid. (Yield: 1.51 g, 86%).

## Materials and Methods

Compound **2** (0.750 g, 2.98 mmol) and 1-(2-hydroxy-4,6-dimethoxyphenyl)ethanone (0.702 g, 3.6 mmol) were dissolved in anhydrous dimethylformamide and sodium hydride (60% dispersion in mineral oil; 0.597 g, 14.9 mmol) was added in portions at room temperature. The mixture was stirred for 16 h, poured into cold 1 N HCl solution and an additional 1 N HCl was added until the solution became acidic. The resulting suspension was stirred for 5 min and filtered. Solids were collected and washed with water, then dissolved in dichloromethane, dried over anhydrous Na<sub>2</sub>SO<sub>4</sub>, and concentrated under reduced pressure to give a solid residue that was treated with MeOH to afford compound **3** as an orange solid. (Yield: 51.5%, 0.68 g).

To a solution of compound **3** (0.68 g, 1.58 mmol) in DMSO (2 mL) was added a catalytic amount of iodine (0.04 g, 0.16 mmol) and the reaction mixture was heated to 130 °C and stirred for 3 h. The solution was cooled to room temperature and poured into a saturated aqueous sodium thiosulfate solution and the resulting precipitate was filtered, washed with cold water and ether to afford crude compound **4**, which was filtered via a SiO<sub>2</sub> pad using MTBE as eluent. The filtrate was concentrated *in vacuo* to obtain compound **4** as a yellowish solid. (Yield: 0.38 g, 56%).

A solution of compound **4** (0.38 g, 0.883 mmol) in CH<sub>2</sub>Cl<sub>2</sub> was treated with BBr<sub>3</sub> (2.212 g, 8.83 mmol) at room temperature under an argon atmosphere. The mixture was stirred for 24 h, poured into ice-water and extracted with EtOAc. The organic phase was dried over Na<sub>2</sub>SO<sub>4</sub> and concentrated under reduced pressure. The residue was purified by preparative HPLC to afford **MEY-001** as a yellowish solid. Yield = 0.0311 g. <sup>1</sup>H NMR (DMSO-*d*<sub>6</sub>, 500 MHz): 13.19 (s, 1H), 10.75 (s, 1H), 8.65 (s, 1H), 8.11 (m, 1H), 7.64 (m, 1H), 7.30 (m, 7H), 6.68 (d, 1H), 6.53 (d, 1H), 6.20 (d, 1H), 5.56 (s, 2H). <sup>13</sup>C NMR (DMSO-*d*<sub>6</sub>, 126 MHz): 181.6, 164.3, 163.2, 162.0, 157.6, 137.4, 137.3, 133.6, 129.19, 128.2, 127.7, 124.8, 123.5, 122.6, 121.2, 112.1, 107.4, 104.0, 102.1, 99.2, 94.2, 50.294. HPLC-MS (ESI+) m/z 402 [M+1]<sup>+</sup>. LCMS: R<sub>t</sub> = 14.6 min; ESI<sup>+</sup> 402.09 [M+1]<sup>+</sup>. Purity 95.0% (HPLC).

**2-(1-(4-Fluorobenzyl)-1H-indol-3-yl)-5,7-dihydroxy-4H-chromen-4-one (MEY-002)**. To a stirred suspension of sodium hydride (60% dispersion in mineral oil; 0.413 g, 10.3 mmol) in anhydrous DMF (5 mL), cooled with an ice bath, was added dropwise a solution of 1H-indole-3-carbaldehyde (1 g, 6.89 mmol) in anhydrous DMF (10 mL)

## Materials and Methods

over 10 min. After stirring at room temperature for 0.5 h, benzyl bromide (1.3 g, 7.6 mmol) was added dropwise over 5 min. After completion of the reaction (TLC), the solution was poured into ice-water. The suspension was stirred for 10 min and extracted with EtOAc. The organic extracts were combined, washed with brine, dried over anhydrous Na<sub>2</sub>SO<sub>4</sub>, and evaporated under reduced pressure to give the residue which was treated with hexane to remove mineral oil, collected by filtration and dried *in vacuo* to obtain compound **2** as a yellowish solid. (Yield: 1.45 g, 89.2%).

Compound **2** (0.750 g, 3.19 mmol) and 1-(2-hydroxy-4,6-dimethoxyphenyl)ethanone (0.751 g, 3.828 mmol) were dissolved in anhydrous DMF and sodium hydride (60% dispersion in mineral oil; 0.639 g, 15.95 mmol) was added in portions at room temperature. The mixture was stirred for 16 h, poured into cold 1 N HCl solution and an additional 1 N HCl was added until the solution became acidic. The resulting suspension was stirred for 5 min and filtered. Solids were collected and washed with water, then dissolved in dichloromethane, dried over anhydrous Na<sub>2</sub>SO<sub>4</sub>, and concentrated under reduced pressure to give a solid residue that was treated with MeOH to afford compound **3** as a yellowish solid. (Yield: 0.73 g, 55.7%).

To a solution of compound **3** (0.73 g, 1.76 mmol) in DMSO (2 mL) was added a catalytic amount of iodine (0.046 g, 0.18 mmol) and the reaction mixture was heated to 130 °C and stirred for 3 h. The solution was cooled to room temperature and poured into a saturated aqueous sodium thiosulfate solution and the resulting precipitate was filtered, washed with cold water and ether to afford crude compound which was filtered via SiO<sub>2</sub> pad using MTBE as eluent. The filtrate was concentrated *in vacuo* to obtain the compound as yellowish solid. (Yield: 0.4 g, 54.8%). A solution of compound **4** (0.4 g, 0.972 mmol) in CH<sub>2</sub>Cl<sub>2</sub> was treated with BBr<sub>3</sub> (2.435 g, 9.72 mmol) at room temperature under an argon atmosphere. The mixture was stirred for 24 h, poured into ice-water and extracted with EtOAc. The organic phase was dried over Na<sub>2</sub>SO<sub>4</sub> and concentrated under reduced pressure. The residue was purified by preparative HPLC to afford **MEY-002** as a yellowish solid. Yield = 0.1222 g. <sup>1</sup>H NMR (DMSO-*d*<sub>6</sub>, 500 MHz): 5.53 (s, 2H), 6.18 (d, 1H, 2.3 Hz), 6.52 (d, 1H, 2.4 Hz), 6.66 (s, 1H), 7.2 (t, 2H, 17 Hz), 7.280 (m, 4H), 7.64 (m, 1H), 8.10 (m, 1H), 8.63 (s, 1H), 10.75 (s, 1H), 13.17 (s, 1H). <sup>19</sup>F NMR (DMSO-*d*<sub>6</sub>, 500 MHz): 114.64 (s, 1F). <sup>13</sup>C NMR (DMSO-*d*<sub>6</sub>, 126 MHz): 48.9, 93.7, 98.5, 101.2, 103.2, 107, 111.7, 115.5, 120.4, 121.6, 122.7, 124.5,

## Materials and Methods

127.0, 127.5, 128.4, 129.0, 132.6, 136.4, 156.7, 160.4, 161.5, 162.5, 162.38, 163.9, 180.9. MS (ESI<sup>+</sup>) m/z 384.07 [M+1]<sup>+</sup>. HPLC-MS: R<sub>t</sub> = 14.6 min; ESI<sup>+</sup> 384.07 [M+1]<sup>+</sup>. Purity 95.0% (HPLC).

**5,7-Dihydroxy-2-(1-pentyl-1H-indol-5-yl)-4H-chromen-4-one (MEY-005).** <sup>1</sup>H NMR (DMSO-*d*<sub>6</sub>, 500 MHz): 10.85 (s, 1H), 8.34 (s, 1H), 7.84 (m, 1H), 7.65 (m, 1H), 7.53 (m, 1H), 6.90 (s, 1H), 6.61 (d, 2H), 6.21 (d, 1H), 4.23 (t, 2H), 1.77 (q, 2H), 1.23 (m, 4H), 0.83 (m, 3H). <sup>13</sup>C NMR (DMSO-*d*<sub>6</sub>, 126 MHz): 181.8, 165.2, 164.21, 161.5, 157.3, 137.7, 130.7, 128.2, 121.4, 119.9, 119.5, 119.4, 110.6, 103.8, 103.4, 102.2, 98.9, 94.0, 45.7, 29.6, 28.445, 21.9, 13.9. MS (ESI<sup>+</sup>) m/z 364 [M+1]<sup>+</sup>, (ESI<sup>-</sup>) m/z 362 [M-1]<sup>-</sup>. HPLC-MS: R<sub>t</sub> = 15.8 min; ESI<sup>+</sup> 364.14 [M+1], ESI<sup>-</sup> [M-1]<sup>-</sup> 362.03. Purity 95.0% (HPLC).

**2-(1-(2-Cyclohexylethyl)-1H-indol-5-yl)-5,7-dihydroxy-4H-chromen-4-one (MEY-007).** To a stirred suspension of sodium hydride (60% dispersion in mineral oil; 16.53 mmol) in anhydrous DMF (10 mL), cooled with an ice bath, was added dropwise a solution of 1H-indole-3-carbaldehyde (2 g, 13.77 mmol) in anhydrous DMF (10 mL) over 10 min. After stirring at room temperature for 0.5 h, (2-bromoethyl)cyclohexane (3.15 g, 16.53 mmol) was added dropwise over 5 min. The reaction mixture was stirred for 16 h at ambient temperature, poured onto water and the solid was collected by filtration. The filter cake was washed with water (100 mL) and dissolved in DCM (100 mL), dried over Na<sub>2</sub>SO<sub>4</sub>, and concentrated *in vacuo* to afford the crude product, which was treated with hexane, the solid was collected by filtration and dried on air to afford compound **2** as a yellow solid. Yield = 2.8 g, 79.64%.

A mixture of compound **2** (2.8 g, 10.96 mmol), 1-(2-hydroxy-4,6-dimethoxyphenyl)ethan-1-one (2.151 g, 10.96 mmol), and piperidine (2.8 g, 32.88 mmol) in EtOH (90 mL) was refluxed overnight. The resulting mixture was cooled to RT, the precipitate formed was collected by filtration and dried *in vacuo* to afford compound **3** as an orange solid. Yield = 3.15 g, 66.31%. To a solution of compound **3** (3.15 g, 7.27 mmol) in DMSO was added a catalytic amount of iodine (0.727 mmol) and the reaction mixture was heated to 130 °C and stirred for 30 min (monitoring by TLC). The solution was cooled to room temperature and poured into a saturated



## Materials and Methods

aqueous sodium thiosulfate solution and the resulting precipitate was filtered, washed with cold water and MTBE to afford pure compound **4** as a brown solid. Yield = 2.4 g, 76.2%.

A solution of compound **4** (0.600 g, 1.4 mmol) in CH<sub>2</sub>Cl<sub>2</sub> was treated with BBr<sub>3</sub> (1 M in anhydrous CH<sub>2</sub>Cl<sub>2</sub>, 14 mmol) at room temperature for 18 h under an argon atmosphere. The solution was poured into ice water and extracted with EtOAc. The organic phase was dried over Na<sub>2</sub>SO<sub>4</sub> and concentrated, and the crude residue was purified by prepHPLC to afford desired **MEY-007** as a yellow solid. Yield = 0.0828 g, 15%. <sup>1</sup>H NMR (DMSO-*d*<sub>6</sub>, 400 MHz): 13.22 (s, 1H), 10.75 (s, 1H), 8.50 (m, 1H), 8.1 (m, 1H), 7.66 (m, 1H), 7.32 (m, 2H), 6.68 (m, 1H), 6.54 (m, 1H), 6.18 (m, 1H), 4.33 (m, 2H), 1.72 (m, 7H), 1.17 (m, 4H), 0.97 (m, 2H). <sup>13</sup>C NMR (DMSO-*d*<sub>6</sub>, 100 MHz): 181.5, 164.3, 162.0, 157.5, 137.2, 133.2, 124.7, 123.3, 122.4, 121.2, 111.7, 106.9, 104.0, 101.7, 99.1, 94.2, 44.7, 37.3, 35.1, 32.9, 26.5, 26.1. MS (ESI<sup>+</sup>) *m/z* 404.28 [M+1]<sup>+</sup>. MS (ESI<sup>-</sup>) *m/z* 402.10 [M-1]<sup>-</sup>. HPLC-MS: *R*<sub>t</sub> = 17.2 min; ESI<sup>+</sup> 404.17 [M+1], ESI<sup>-</sup> [M-1]-402.08. Purity 95.0% (HPLC).

**2-(1-(3,7-Dimethyloctyl)-1H-indol-5-yl)-5,7-dihydroxy-4H-chromen-4-one (MEY-008)**. To a stirred suspension of sodium hydride (60% dispersion in mineral oil; 9.72 mmol) in anhydrous DMF (10 mL), cooled with an ice bath, was added dropwise a solution of 1H-indole-3-carbaldehyde (**1**) (1.176 g, 8.1 mmol) in anhydrous DMF (10 mL) over 10 min. After stirring at room temperature for 0.5 h, 1-bromo-3,7-dimethyloctane (2.15 g, 9.72 mmol) was added dropwise over 5 min. The reaction mixture was stirred for 16 h at ambient temperature, poured onto water and the solid was collected by filtration. The filter cake was washed with water (100 mL) and dissolved in DCM (100 mL), dried over Na<sub>2</sub>SO<sub>4</sub>, and concentrated *in vacuo* to afford the crude product, which was filtered via a SiO<sub>2</sub> pad using hexane as eluent (discarded) followed by MTBE (collected and concentrated *in vacuo*) to obtain compound **2** as an orange oil. Yield = 1.98 g, 85.7%. A mixture of compound **2** (1.98 g, 6.94 mmol), 1-(2-hydroxy-4,6-dimethoxyphenyl)ethan-1-one (1.36 g, 6.94 mmol), and piperidine (1.77 g, 20.82 mmol) in EtOH (70 mL) was refluxed overnight. The resulting mixture was cooled to RT, the precipitate formed was collected by filtration and dried *in vacuo* to afford compound **3** as an orange solid. Yield = 1.6 g, 50.5%.

## Materials and Methods

To a solution of compound **3** (1.6 g, 3.49 mmol) in DMSO was added catalytic amount of iodine (0.349 mmol) and the reaction mixture was heated to 130 °C and stirred for 30 min (monitoring by TLC). The solution was cooled to room temperature and poured into a saturated aqueous sodium thiosulfate solution and the resulting precipitate was filtered, washed with cold water and MTBE to afford pure compound **4** as a brown solid. Yield = 0.65 g, 40.6%. A solution of compound **4** (0.650 g, 1.4 mmol) in CH<sub>2</sub>Cl<sub>2</sub> was treated with BBr<sub>3</sub> (1 M in anhydrous CH<sub>2</sub>Cl<sub>2</sub>, 14 mmol) at room temperature for 18 h under an argon atmosphere. The solution was poured into ice water and extracted with EtOAc. The organic phase was dried over Na<sub>2</sub>SO<sub>4</sub> and concentrated, and the crude residue was purified by prepHPLC to afford desired **MEY-008** as a yellow solid. Yield = 0.1289 g, 22%. <sup>1</sup>H NMR (DMSO-*d*<sub>6</sub>, 400 MHz): 13.21 (s, 1H), 10.72 (s, 1H), 8.50(s,1H), 8.1 (d, 1H), 7.76 (d,1H), 7.30 (m, 1H), 6.65 (s, 1H), 6.52 (d, 1H), 6.19 (d, 1H), 4.30 (m, 2H), 1.88 (m, 1H), 1.65 (m, 1H), 1.2 (m, 10H), 0.90 (d, 3H), 0.80 (d, 6H). <sup>13</sup>C NMR (DMSO-*d*<sub>6</sub>, 100 MHz): 181.56, 164.24, 163.44, 161.98, 157.56, 137.25, 133.27, 124.76, 123.28, 122.43, 121.18, 111.70, 106.94, 104.02, 101.72, 99.15, 94.23, 45.01, 38.99, 36.78, 36.75, 30.26, 27.80, 24.43, 22.97, 22.89, 19.82. MS (ESI<sup>+</sup>) *m/z* 434.31 [M+1]<sup>+</sup>, (ESI<sup>-</sup>) *m/z* 432.16 [M-1]<sup>-</sup>. LCMS: R<sub>t</sub> = 18.9 min; ESI<sup>+</sup> 434.24 [M+1], ESI<sup>-</sup> [M-1]<sup>-</sup> 432.12. HPLC-MS: R<sub>t</sub> = 18.9 min; ESI<sup>+</sup> 434.24 [M+1]<sup>+</sup>, ESI<sup>-</sup> 432.12 [M-1]<sup>-</sup>. Purity 95.0% (HPLC).

### 3.2 Biochemistry:

#### 3.2.1 Reagents:

Opti-MEM (Gibco #31985062) and lipofectamine 3000 (Thermo Scientific™, #L3000001) were used for HEK293 Flp-In and HeLa cell transfections. For protein expression HEK293 Flp-In cells were grown in T300 tissue flasks (TPP, #90301) and roller bottles (Greiner Bio-one, #681070) in DMEM medium (Gibco #12491023) supplemented with FBS (Gibco #A3382101) and L-Glutamine (Gibco #25030-123). For purification, a POROS-20 MC column (Thermo Scientific™ #1542906) and a Superdex 200 increase 10/300 column (GE Healthcare, # GE28-9909-44) were used. For SDS-PAGE and western blot analysis, the following reagents were used: SDS precast gel (Invitrogen #XP04205BOX), InstantBlue Coomassie Protein stain (Abcam, #ab119211), Trans-blot turbo transfer pack (Bio-Rad, #1704158), anti-His tag primary

## Materials and Methods

antibody (Abcam, # ab18184), anti-ATX antibody (Merck, MABT1350-100UG), anti-mouse HRP secondary antibody (Abcam #ab6728), ECL substrate kit (Abcam, #ab133406) and 5% skim milk powder (Millipore, #1.15363.050). For enzymatic reactions a choline quantification kit (AAT Bioquest, #40007) was used with 96 well plates (#3915) from Costar. Reagents included LPC 18:1 (#845875P), LPC 16:0 (#855675C), and LPA 18:1 (#857130C) from Avanti Polar Lipids . For crystallization, NH4I (#AB202711) was ordered from Abcr and NaSCN (#HR2-693) from Hampton Research. For the cell assays, HeLa cells were a gift from the Marcia lab at EMBL Grenoble, fatty acid free Fetal Bovine Serum (FBS), (# A3382101) from Thermo Fisher, anti-HA tag primary antibody (#ab18181) and Alexa-conjugated anti-mouse antibody (#ab ab150113) from Abcam, and Fluoroshield (#F6182-20mL) from Sigma-Aldrich.

### 3.2.2 Autotaxin expression and purification:

A pcDNA5.1 vector containing a glycosylation mutated hATX- $\gamma$  (N54A and N411A) was cloned into HEK293 flp-In cells to generate a stable cell line as previously published for rATX isoform (115). Lipofectamine 3000 was the reagent used to perform the transfection by following the manufacturer's instructions. The same protocol was used to generate a hATX- $\gamma$  cell line expressing the native protein. Native hATX- $\beta$  and rATX producing cell lines were available from Anastassis Perrakis laboratory in the Netherlands (116).

Briefly, cell lines were expanded in 10 T300 flasks before inoculation in 8 roller bottles using DMEM supplemented with 10% FCS and Penicillin/Streptomycin at 37 degrees. After 4 days, the media was switched to DMEM supplemented with 1 % FCS. The media was collected after 4 days of expression and filtered before application on a POROS column for affinity purification using His-Tag selective binding to copper. Samples were eluted in 20 mM HEPES, 150 mM NaCl and 500 mM Imidazole at pH 8. After concentration, the samples were loaded onto a Superdex 10/200 increase gel filtration column and checked for purity using SDS-PAGE gel analysis. Pure fractions were pooled together and further concentrated to 2-3 mg/mL in 50 mM Tris, 150 mM NaCl at pH 8. SEC-MALLS analysis of purified fraction were performed using 50  $\mu$ L of protein solution concentrated to 2-4 mg/mL using the instrument available under the

## Materials and Methods

ISBG consortium. The samples were injected on a Superdex 10/200 GL increase gel-filtration column at a flow rate of 0.5 mL/min at room temperature. The instrument is composed of a Wyatt Dawn Heleos II - Multi-Angle static Light Scattering, a Wyatt Optilab T-rex – Refractometer, a Hitachi Elite LaChrom UV detector L-2400 and a Hitachi Elite LaChrom Pump L-2130. Samples were analyzed for purity, aggregation and MW.

### 3.2.3 Crystallization, data collection and model building:

#### *For cannabinoids:*

Crystallization experiments were performed at 303 K using the hanging-drop vapor diffusion method as previously published (Day et al, 2010). The best crystals were obtained with the rATX construct (3-3.5 mg/ml) after 30 min RT preincubation with 5 mM THC or 5 mM 6a10aTHC dissolved in ethanol. 1  $\mu$ l of the protein solution was then mixed with 1  $\mu$ l of the reservoir solution containing 18-22% (m/v) PEG3350, 0.1-0.3 M NH<sub>4</sub>I and 0.3 M NaSCN. All the crystals were cryoprotected with the addition of 20% (v/v) of glycerol.

X-ray data for THC and 6a10aTHC autotaxin complexes were collected at 100K on EMBL PETRA III beamline P14 and P13 (117), respectively. Crystallographic ATX-THC complex data were acquired using the Global Phasing WFs data collection workflow to maximize the completeness of the P1 dataset. Authorization to collect sample containing THC was granted by the BfArM in Germany. All data were processed with AutoPROC Staraniso (118), which includes XDS (119). Structures were determined by molecular replacement using MRage (120) with the structure of ATX (PDB: 2XR9) as model. Model building was performed using Coot (121), phenix.refine (122), REFMAC5 (123) and PDB-REDO (124). Ligands were drawn with ELBOW (125). Validation of the model was performed with phenix PDB deposition tools, using MolProbability (126). Maps were generated using phenix refine and feature-enhanced map (122). The crystallographic parameters and model quality indicators can be found in Table 1. Structural figures were generated using CCP4mg (127). Structural biology applications used in this project were compiled and configured by SBGrid (128)

## Materials and Methods

### *For cannabinoid-derived inhibitors:*

Trials with full length hATX- $\gamma$  were unsuccessful, probably due to significant glycosylation flexibility. Thus, a hATX- $\gamma$  N54A/N411A mutant construct was designed to retain only one critical glycosylation site for reduced flexibility. Crystallization trials were performed using HTX platform at EMBL Grenoble and crystals were obtained using the previously described conditions for rATX. The best diffracting crystals were obtained in 18-22% PEG3350, 0.1-0.4 M NH<sub>4</sub>I, 0.2-0.4 M NaSCN using the hanging drop method after incubating the protein with 0.2 mM LPA 18:1, 2.5 mM MEY-002 or 2.5 mM MEY-003. Crystals appeared after 2 weeks and were harvested 4-6 weeks after plate set-up. Crystals were flash frozen in liquid nitrogen using 25% glycerol in the mother liquor as a cryoprotectant.

Diffraction data were collected at 100 K at ESRF beamline ID30B using a 13.7 keV beam energy (129,130). The LPA 18:1 complex crystal structure data processing was performed using the Grenades parallelproc pipeline (131) and MEY-003 complex structure was processed using AutoPROC Staraniso (118), both using the XDS software suite (119). Molecular replacement was performed using PHASER (132) as implemented in PHENIX (120) with PDB:4ZG7 as an input model. Model building was iteratively performed using COOT (121), phenix.refine (122) and PDB-redo (124). Ligand restraints were created using ELBOW (125) and PDB validation was performed using MOLPROBILITY (126) before deposition. Maps were generated using phenix.refine and table 1 was generated with PHENIX. Graphical display was drawn with CCP4MG (127). All the mentioned software were managed by the SBgrid application (128).

### 3.2.4 Dose response assay:

#### *For cannabinoids and endocannabinoids:*

ATX phospholipase D activity was measured using choline release from LPC18:1 and LPC 16:0 with a choline quantification kit(133). 30 nM ATX- $\beta$  or  $\gamma$  were incubated with 200  $\mu$ M LPC 18:1 or LPC 16:0 in a final volume of 100  $\mu$ l buffer, which contained 50 mM Tris-HCl (pH 8.5) and 150 mM NaCl. For endocannabinoids, the conditions were identical but with reduced LPC concentrations of 20  $\mu$ M. The LPC solution was

## Materials and Methods

obtained by evaporating a commercial LPC chloroform solution directly in a 1.5 mL Eppendorf under vacuum. The dried LPC was then resuspended in water to obtain the mentioned concentration and incubated at 37 °C on a shaker for 5 to 10 min before addition in the microplate.

The experiment for determining apparent  $EC_{50}$  for various cannabinoids were performed at 37 °C by adding the cannabinoid in a serial 2-fold dilution for each concentration. The cannabinoid solutions were prepared from a stock solution in ethanol or other organic solvents. After initial evaporation and/or dilution to obtain the highest concentration mentioned in the assay figure, a 2-fold dilution was performed in Eppendorf tubes. All the compounds were dissolved in 100% ethanol as a vehicle. For THC and 6a10aTHC the retained 2-fold dilution started at 12.5  $\mu$ M. For CBN, 5-DMHCBD and CBD the starting concentration was 50  $\mu$ M, 150  $\mu$ M and 2 mM, respectively. Released choline was detected and the enzyme activity was determined by measuring fluorescence at  $\lambda_{ex}/\lambda_{em}=540/590$  nm in 96-well plates, every 60 seconds for 50 min minimum using a Clariostar plate reader (BMG Labtech). Initial velocities were taken between 19-31 min after visual inspection. The  $EC_{50}$  values were determined using the non-linear regression analysis method (fit: [inhibitor] vs. response (three parameter)) in Graphpad Prism (GraphPad Software, Inc). Measurements have been performed in triplicate with three different protein preparations.

### *For cannabinoid-inspired inhibitors:*

LPC hydrolysis was detected using choline release assay kit in a 96 well plate format as previously described (116). Briefly, 8  $\mu$ L of amplite red was added to 2 mL of the choline probe before addition of 50  $\mu$ L per reaction well. The assay was performed by adding 30 nM of recombinant hATX- $\gamma$  or hATX- $\beta$  diluted in 50 mM Tris, 150 mM NaCl and 50  $\mu$ M LPC18:1 or 16:0 at pH 8 to the reaction mixture. 2-fold or 3-fold serial dilution of inhibitors were performed using 2% ethanol as a vehicle. LPC was added right before the measurement in order to start the enzymatic reaction. Data acquisition was performed using a Clariostar plate reader (BMG Labtech) with fluorescence

## Materials and Methods

measurement at  $\lambda_{ex}/\lambda_{em}=540/590$  nm every 60 seconds for at least 50 min. Dose-response analyses were performed with Prism (GraphPad, version 9.4.0) after baseline subtraction and normalization.

### 3.2.5 End point assays:

ATX phospholipase D activity was measured using choline release from LPC18:1 and LPC 16:0 with a choline quantification kit(133) (Fig S6D). 30 nM ATX- $\beta$  or  $\gamma$  was incubated with 200  $\mu$ M LPC 18:1 or LPC 16:0 in a final volume of 100  $\mu$ l buffer, which contained 50 mM Tris-HCl (pH 8.5) and 150 mM NaCl. The LPC solution was obtained by evaporating a commercial LPC chloroform solution directly in a 1.5 mL Eppendorf under vacuum. The dried LPC was then resuspended in water to obtain the mentioned concentration and incubated at 37 °C on a shaker for 5 to 10 min before addition in the microplate. The cannabinoids solutions were prepared from a stock solution in ethanol or other organic solvents. After initial evaporation and/or dilution to obtain the highest concentration mentioned in the assay figure, a 2-fold dilution was performed in Eppendorf tubes. All the compounds were dissolved in 100% ethanol as a vehicle.

The experiments for determining relative inhibition for various cannabinoids were performed at 37 °C by adding 10  $\mu$ M of the cannabinoid or endocannabinoid mentioned. Released choline was detected and the enzyme activity was determined by measuring fluorescence at  $\lambda_{ex}/\lambda_{em}=540/590$  nm in 96-well plates, every 60 seconds for 50 min minimum using a Clariostar plate reader (BMG Labtech). Absolute values were taken at 25 min after visual inspection and the 0 min baselines were subtracted to account for compound differences. The relative inhibition values were determined using the normalize method in Graphpad Prism (GraphPad Software, Inc). Measurements have been performed in triplicate with three different protein preparations. All the compounds were controlled for interference of fluorescence and inhibition in the same assay conditions but in the absence of ATX and replacing LPC with choline.

## Materials and Methods

### 3.2.6 Mode of inhibition assay:

#### *For cannabinoids:*

LPC hydrolysis was detected using a choline release assay kit in a 96 well plate format as previously described (116). Briefly, 8  $\mu$ L of amplite red was added to 2mL of the choline probe before addition of 50  $\mu$ L per reaction well. The assay was performed by adding 30 nM recombinant hATX- $\gamma$  diluted in 50 mM Tris, 150 mM NaCl and fixed inhibitor concentrations of 0 nM, 350 nM, 700 nM and 1400 nM THC in 2% ethanol (final concentration in the well). 2-fold serial dilution of LPC18:1 from 500  $\mu$ M was performed using water as a vehicle. LPC was added right before the measurement in order to start the enzymatic reaction. Data acquisition was performed using a Clariostar plate reader (BMG Labtech) with fluorescence measurement at  $\lambda_{ex}/\lambda_{em}=540/590$  nm every 60 seconds for at least 50 min. Mode of inhibition analyses were performed with Prism (GraphPad, version 9.4.0) after baseline subtraction.

#### *For cannabinoid-inspired inhibitors:*

LPC hydrolysis was detected using a choline release assay kit in a 96 well plate format as previously described (116). Briefly, 8  $\mu$ L of amplite red was added to 2mL of the choline probe before addition of 50  $\mu$ L per reaction well. The assay was performed by adding 30 nM recombinant hATX- $\beta$  or hATX- $\gamma$  diluted in 50 mM Tris, 150 mM NaCl and fixed inhibitor concentrations of 0 nM, 187.5 nM, 375 nM and 750 nM MEY-003 in 2% ethanol (final concentration in the well). 3-fold serial dilution of LPC18:1 from 500  $\mu$ M was performed using water as a vehicle. LPC was added right before the measurement in order to start the enzymatic reaction. Data acquisition was performed using a Clariostar plate reader (BMG Labtech) with fluorescence measurement at  $\lambda_{ex}/\lambda_{em}=540/590$  nm every 60 seconds for at least 50 min. Mode of inhibition analyses were performed with Prism (GraphPad, version 9.4.0) after baseline subtraction.

### 3.2.7 Biochemical analysis:



## Materials and Methods

The data analysis was performed with GraphPad (9.4.1). For apparent IC50 determination, fluorescent time points are subtracted from the baseline. From the subtracted results, a linear regression analysis was run on the linear part of the fluorescent curve, between 10 min and 25 min. The linear regression slopes were then plotted and normalized for each inhibitor concentration. A non-linear regression using the following equation was performed with GraphPad in order to calculate the IC50:

$$Y = \text{Bottom} + (\text{Top} - \text{Bottom}) / (1 + (\text{IC}_{50}/X)^{\text{HillSlope}})$$

The EC50 was calculated as the concentration of inhibitor that gives a response halfway between maximal and minimal ATX activity. The SEM of the apparent EC50 was determined by GraphPad as the 95% confidence interval of the mean.

### 3.2.8 Choline standard:

This assay was run, as mentioned in the previous dose response material and methods part, for the LPC that was replaced by the choline standard as mentioned in the manufacturer instructions. The curve obtained was linear, allowing extrapolation of the enzyme activity.

### 3.2.9 Western blot and SDS Page gel analysis:

25  $\mu\text{g}$  of hATX- $\gamma$  or hATX- $\beta$  protein in SDS loading buffer was incubated for 5 minutes at 95 degrees before loading on a 12-well 6-20% SDS page gel (Invitrogen, # XP04200BOX). The gel was run in a chamber filled with SDS running buffer at 225 volts for approximately 45 min. Proteins were detected after staining overnight in Instant-blue.

For western blotting a lower quantity of protein was loaded on a 6-20 % acrylamide SDS-Page gel, typically 25 to 200 ng, and the gel was not stained with Instant-blue. The proteins were transferred onto a nitrocellulose membrane using a Trans-blot turbo

## Materials and Methods

transfer pack. After transfer, the membrane was blocked in 5% skim milk powder in TBST for 1 hr. Then, the primary antibody was diluted 1 to 1/1000 in TBST with 5 % milk and incubated overnight at 4 degrees on the membrane. The blot was then washed three times with TBST and incubated 1 hr with a secondary antibody coupled with a peroxidase in 5% milk in TBST. Before detection, the blot was washed three times with TBST and detection was performed after incubation with the ECL Substrate Kit using the ChemiDoc MP Imaging System (Bio-Rad).

### 3.2.10 AlphaFold:

AlphaFold (134) was run on the hATX- $\gamma$  (Uniprot, Q13822-3) using a locally implemented AlphaFold (version 2.1.0) server installation.

### 3.2.11 hLPA1 internalization assay:

*For cannabinoids:*

The hLPA1 receptor internalization assay was essentially performed as previously described (135). A pRP[Exp]-Puro-CMV>HA/hLPA1 vector coding for full length human LPA1 receptor (UniProt ID: Q92633) with a human influenza hemagglutinin (HA) sequence epitope-tag at the 5'-end of the extracellular domain was designed and maxiprep plasmid DNA was produced commercially (Vector Builder). Vector quality control was done by restriction enzyme analysis and Sanger sequencing.

HeLa cells were grown on coverslips in a 12 well plate format and transfected with HA/hLPA<sub>1</sub> vector in DMEM complete medium with lipofectamine 3000 using 1  $\mu$ g of plasmid DNA, and 3  $\mu$ L of Lipofectamine 3000 per well after complexation in 50  $\mu$ L Opti-MEM, as per the manufacturer's instructions, 48 hours prior to fixation. 8 hours prior to treatment and fixation, the cells were starved in fatty acid free DMEM to avoid hLPA1 activation by serum lipids. Several assays were performed in different conditions before fixation: 30 nM ATX + 150  $\mu$ M LPC 18:1; 30 nM ATX + 150  $\mu$ M LPC

## Materials and Methods

18:1 + 1  $\mu$ M THC; 1  $\mu$ M THC; 1  $\mu$ M LPA 18:1; Untreated (vehicle only); and untransfected: to control specificity of the antibody towards HA tagged hLPA1 receptor. LPC 18:1 and LPA 18:1 were dissolved in fatty acid free FBS with a final concentration in the media of 1%. THC was dissolved in DMSO to a final concentration in the media of 0.025% (v/v) DMSO.

Fixation was carried out by adding paraformaldehyde directly into the media to a final concentration of 3%, and incubating at 37° C for 10 min. Cells were washed 3 times in PBS and membranes were labelled using Wheat Germ Agglutinin, and Alexa Fluor™ 594 Conjugate for 10 min at 5  $\mu$ g/mL in PBS, as per the manufacturer's instructions. Cells were washed three times in PBS, permeabilized using 0.2% tween for 10 min, washed in PBS, and finally blocked with 10% goat serum for 30 min. HA tag was labelled using an anti-HA tag primary antibody at 1/200 dilution in 10% FBS for 1 hour at room temperature followed by PBS wash and secondary staining was done with an anti-mouse antibody, 30 min incubation at 1/500 dilution in 10% FBS. Cells were washed three times and mounted using Fluoroshield mounting. Imaging was performed using a Leica SP5 (X 63 objective). Endosome quantification was done using Fiji analyze particle tools after image thresholding. The number of counted endosomes were normalized over the measuring area to calculate the density per  $\mu$ m<sup>2</sup>. Statistical analysis was performed using paired t-test over 11 images for each condition of ATX-THC-LPC and ATX-LPC in biological triplicate.

### *For cannabinoid-inspired inhibitors:*

The pRP[Exp]-Puro-CMV>HA/hLPA1 vector coding for a human LPA1 cDNA with a hemagglutinin (HA) sequence epitope-tag at the 5'-end of the extracellular domain described above was again used. HeLa cells were plated on CELLSTAR 12 well culture plates and transfected with the HA/hLPA1 vector in DMEM complete medium 48 hours prior to fixation. The transfection was carried out with a lipofectamine 3000 kit using 1  $\mu$ g of DNA, 2  $\mu$ L of P3000 reagent and 3  $\mu$ L of Lipofectamine 3000 per well following complexation in 50  $\mu$ L Opti-MEM as indicated in the manufacturer's instructions. 8 hours prior to treatment and fixation, the cells were starved in FC-DMEM since hLPA1 can be activated by lipids in the serum.

## Materials and Methods

Treatment was performed in the following conditions for 30 min before fixation:

- 30 nM ATX + 200  $\mu$ M LPC 18:1
- 30 nM ATX + 200  $\mu$ M LPC 18:1 + 1  $\mu$ M MEY-003
- 1  $\mu$ M LPA 18:1
- Untransfected: control of the specificity of the antibody towards the HA tagged hLPCAR1 receptor

LPC 18:1 and LPA 18:1 were dissolved in fatty acid free FBS and the final concentration in media was 0.1% FBS. MEY-003 was dissolved in DMSO and the final concentration in media was 0.025% (v/v) DMSO. All conditions received vehicles treatment.

Fixation, HA tag labelling, and mounting was essentially carried out as described above for cannabinoids and imaging was performed on a Leica SP5 (X 63 objective) using the same laser power.

Endosome quantification was performed through particle detection with FIJI. First, the outline of the cell was detected using a low threshold and the FIJI analysis tool with the included attribute. The outline then acted as the ROI for a second step, where a larger secondary threshold in combination with the analyze particle tool identified the number of endosomes inside the cell. The particle analysis tool was configured to detect particles in the size range associated with endosomes (0.06-1.6  $\mu$ M). The endosome count was normalized by dividing by the cell area. Optimal thresholding values were obtained through visual inspection of a sample image. Statistical analysis was performed using paired t-tests over 11 images for each condition of ATX-MEY-003-LPC and ATX-LPC in biological triplicate.

### 3.2.12 CryoEM data collection and processing:

#### *Vitrification:*

Quantifoil R2.2 cu300 grids were glow discharged using a PELCO EasyGlow device at 25 mA and 30 mBar for 20 s. Grid preparation was achieved with a MARK IV

## Materials and Methods

Vitrobot. hATX- $\beta$  concentration was 0.3 mg/mL and 2.5  $\mu$ L was added on one side of the grid. The sample was blotted for 5 s at 4 degrees under 100 % humidity using +10 blot force before vitrification in liquid ethane. Best conditions were identified after initial iterative screening on a Glacios.

### *Data collection:*

The samples were collected at the CM01 beamline at ESRF. The facility is equipped with a TITAN KRIOS microscope (FEI) and a K2 summit electron detector and a GIF energy filter (Gatan) was used, data was collected using the EPU software. The acceleration voltage was 300 keV in EF-TEM mode and data were collected at x105,000 magnification (0.84 Å pixel size). 10,680 movies were collected with a total of 40 e. $\text{\AA}^{-2}$  dose and a defocus from – 0.5 to -4  $\mu$ m.

### *Processing:*

Image processing was done with Cryosparc 4.2.1 (136). Movies were imported, motion-corrected using Patch Motion Correction and CTF estimated using Patch CTF. Movies were curated to remove micrographs with extended motion, bad resolution and contaminations, resulting in the selection of 10,021 movies. Particles were initially picked using a circular blob picker with a minimum particle diameter of 50 Å and a maximum particle diameter of 120 Å. 4,584,107 particles were selected for 2D classification with 100 classes. 49 classes were selected for TOPAZ training and model generation. 8631653 particles were subsequently used for an initial 2D classification and 36 2D classes were selected for subsequent processing ending up with 7297246 particles. Interesting classes were further processed using *ab initio* reconstruction, heterogeneous and homogeneous refinement.

## 4 Results

### 4.1 Autotaxin expression and purification

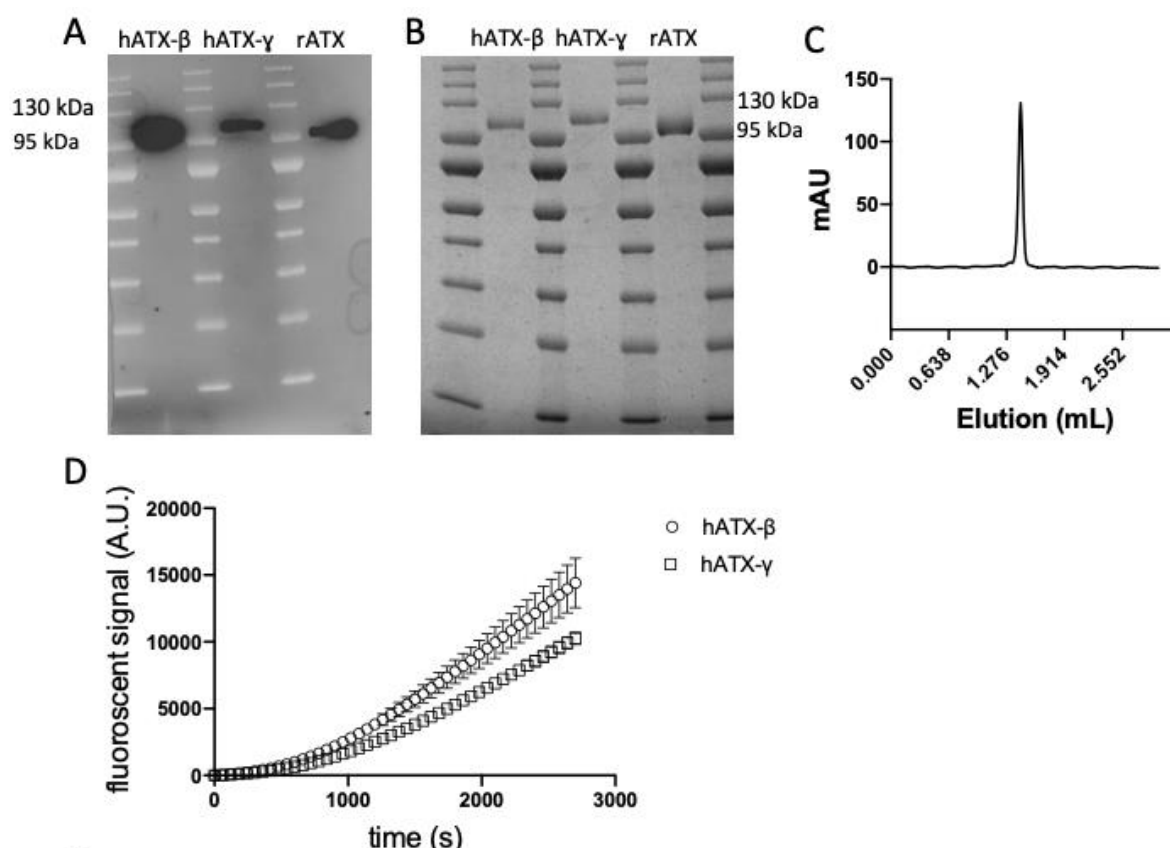


Figure 7: Representative example of recombinant ATX protein purity and enzymatic assays.

(A) Western blot analysis of recombinant proteins hATX- $\beta$ , hATX- $\gamma$  and rATX. (B) SDS-page analysis of recombinant proteins hATX- $\beta$ , hATX- $\gamma$  and rATX showing high purity. (C) Representative analytical microSEC (D) Enzymatic activity comparison between hATX- $\beta$  and hATX- $\gamma$ .

ATX was expressed and purified according to the description provided in the material and method section. Each batch of ATX produced was checked for purity by SDS-PAGE and microSEC for quality control of biochemical experiments. Western blot analysis and mass-spectrometry were performed to confirm protein identity. A SEC-MALLS analysis was also performed to confirm MW, concentration and purity on certain batches.

### 4.2 Effects of medicinal cannabis and endocannabinoids on ATX

#### 4.2.1 Inhibition of ATX by various cannabinoids

First, we set out to confirm and quantify that cannabinoids can bind ATX and modulate its catalytic function. For this we utilized various cannabinoids (Figure 8A) at a fixed concentration of 10  $\mu$ M for each compound with LPC 18:1 (200  $\mu$ M) as substrate in an end-point assay for ATX- $\beta$  (Uniport: Q13822-1) and ATX- $\gamma$  (Uniport: Q13822-3) (Figure 8B and C). The quality of the enzyme assay was confirmed with HA155, a well-documented ATX inhibitor (24,112). The apparent  $IC_{50}$  ( $6 \pm 0.8$  nM) obtained for HA155 is similar in the assay conditions when compared to previous results (137). Additionally, we could exclude an interference of the cannabinoid compounds in the enzymatically coupled assay, as no difference was detectable in the absence of ATX and LPC (Figure 10), when performed in the presence of choline.

We observed a potent inhibition of THC on the catalysis of both ATX isoforms, with > 50% inhibition (Figure 8B and C). Furthermore, 9(R)- $\Delta$ 6a,10a-THC (for simplicity referred to from here as: 6a10aTHC), a derivative of THC that differs only in the position of the double bond in the C-ring compared with THC (Figure 8A) was included in the cannabinoid inhibition screen. Interestingly, this minimal difference caused a further increase in the magnitude of inhibition for both ATX isoforms tested (Figure 8B and C). THCA is a precursor of THC and an active component of medicinal cannabis. It is distinguishable from THC by the presence of a carboxylic group at the A-ring (Figure 8A). THCA also showed an inhibition of the enzymatic activity of both ATX isoforms tested. However, this inhibition is less pronounced, when compared to THC and 6a10aTHC, and did not reach a 50% inhibition magnitude in the assay conditions used (Figure 8B and C).

The next compound tested was cannabidiol (CBD), a non-psychoactive ingredient of medicinal cannabis. CBD is structurally different from THC by an opening of the B-ring. Interestingly, CBD showed only a weak inhibition towards ATX- $\beta$ , and no observable inhibition for ATX- $\gamma$  (Figure 8B and C). 5-DMHCDB is a synthetic CBD

## Results

derivative, which is characterized by the addition of two methyl groups at the beginning of the aliphatic chain and an elongation with a single methyl group at the end of the carbon chain (Figure 1A). These structural modifications remarkably increased the magnitude of inhibition for ATX- $\beta$  and ATX- $\gamma$  (Figure 8B and C).

We also analyzed JWH018 (Figure 8A), which is a synthetic compound investigated as a full agonist for CB1 and CB2 with  $K_i$  values of  $9.0 \pm 8.0$  nM and  $2.9 \pm 2.7$  nM, respectively (138). However, this artificial cannabinoid did not influence the catalytic activity of either ATX  $\beta$  and  $\gamma$  isoforms (Figure 8B and C). To complete the study of cannabinoids' modulation on the enzymatic activity of ATX, we also utilized the endocannabinoids 2-AG and AEA. However, both endocannabinoids did not affect the catalysis of ATX in the applied conditions with 200  $\mu$ M LPC (Fig 8B and C). In this condition, the affinity of autotaxin to endocannabinoids cannot be measured with an inhibition assay. At a lower concentration (20  $\mu$ M) of LPC, we found out that autotaxin activity can be inhibited by endocannabinoids, giving an apparent  $IC_{50}$  in the  $\mu$ M regimen.

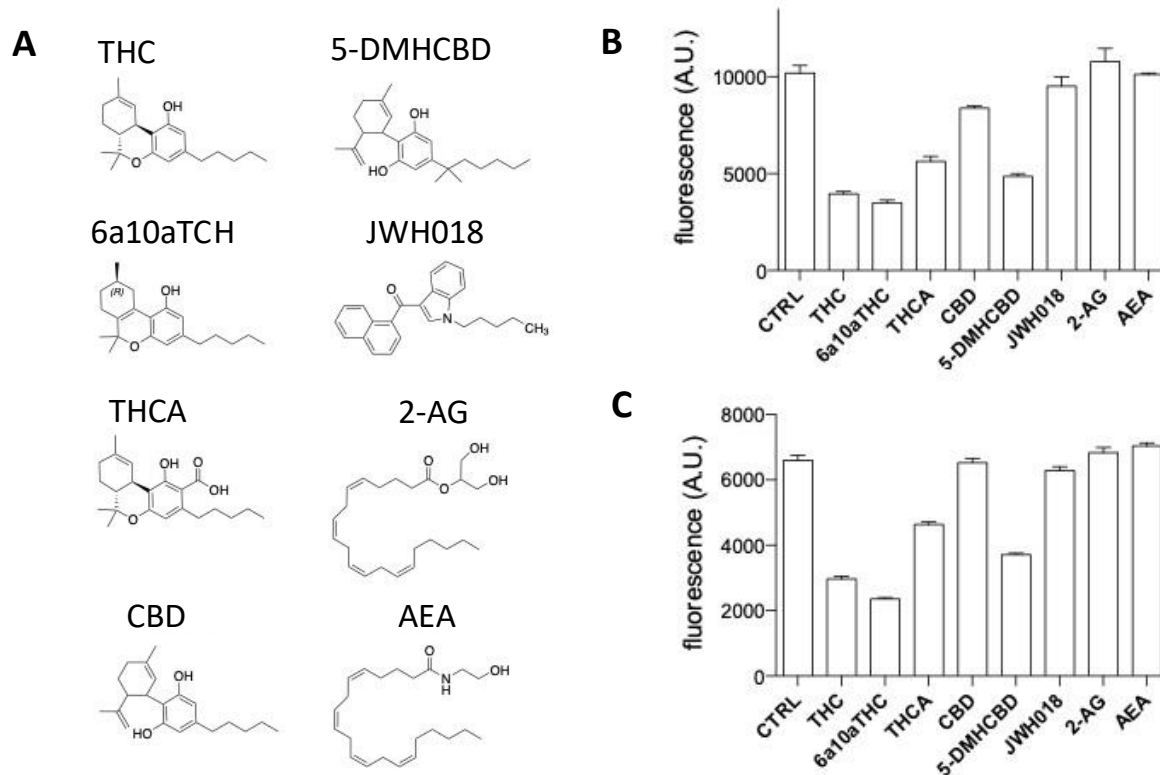


Figure 8: End point assays of tested compounds with hATX



## Results

(A) Chemical representation of  $\Delta^9$ -*trans*-tetrahydrocannabinol (THC), Cannabidiol-dimethylheptyl (5-DMHCBD), 9(R)- $\Delta$ 6a,10a-THC (6a10aTHC), JWH018, Tetrahydrocannabinolic acid (THCA), 2-arachidonoylglycerol (2-AG), Cannabidiol (CBD) and Anandamide (AEA). End-point assay for (B) hATX- $\beta$  and (C) hATX- $\gamma$  inhibition with various cannabinoids and endocannabinoids. All error bars represent the s.e.m (n=3). An activity rate of 99 and 65 mMol end product/mM ATX/min has been found for Figure 8B and C, respectively. ANOVA comparison between CTRL and other conditions showed statistically significant differences for THC, 6a10aTHC, THCA, CBD and 5-DMHCBD for hATX- $\beta$  and hATX- $\gamma$  inhibition (p-value <0.005). hATX was not significantly inhibited by JWH-018, AEA and 2-AG (p-value >0.005).

### 4.2.2 Inhibition of of autotaxin by endocannabinoids

Due to the structural similarity of 2-AG with LPA 20:4 (Figure 8A and 8B), we set out to test the hypothesis that this endocannabinoid might also bind ATX and modulate its catalytic function. Hence, we tried 2-AG (fig. 8b) and AEA (fig. 8c) in biochemical assays with both LPC 16:0 and LPC 18:1 as substrates. Interestingly, we observed a partial inhibition of both endocannabinoids (Figure 9A-D) on the catalysis of rATX- $\beta$  when a LPC concentration of 20  $\mu$ M was used. The apparent EC<sub>50</sub> value for 2-AG is  $4.1 \pm 1.3$   $\mu$ M with LPC 16:0 (Figure 9A) and  $10.6 \pm 2.2$   $\mu$ M with LPC 18:1 (Figure 9B) as substrates, respectively. AEA shows a slightly weaker inhibition with an apparent EC<sub>50</sub> of  $8.1 \pm 2.3$   $\mu$ M with LPC 16:0 (Figure 14C) and  $18.6 \pm 4.5$   $\mu$ M with LPC 18:1 (Figure 14D) as substrates, respectively. 2-AG has a maximal magnitude of inhibition of 65-70% for both substrates and AEA shows a maximal magnitude of inhibition of 55% for LPC 16:0 and 75% for LPC 18:1. However, when repeated using a more physiological LPC concentration of 200  $\mu$ M, little or no inhibition was observed.

## Results

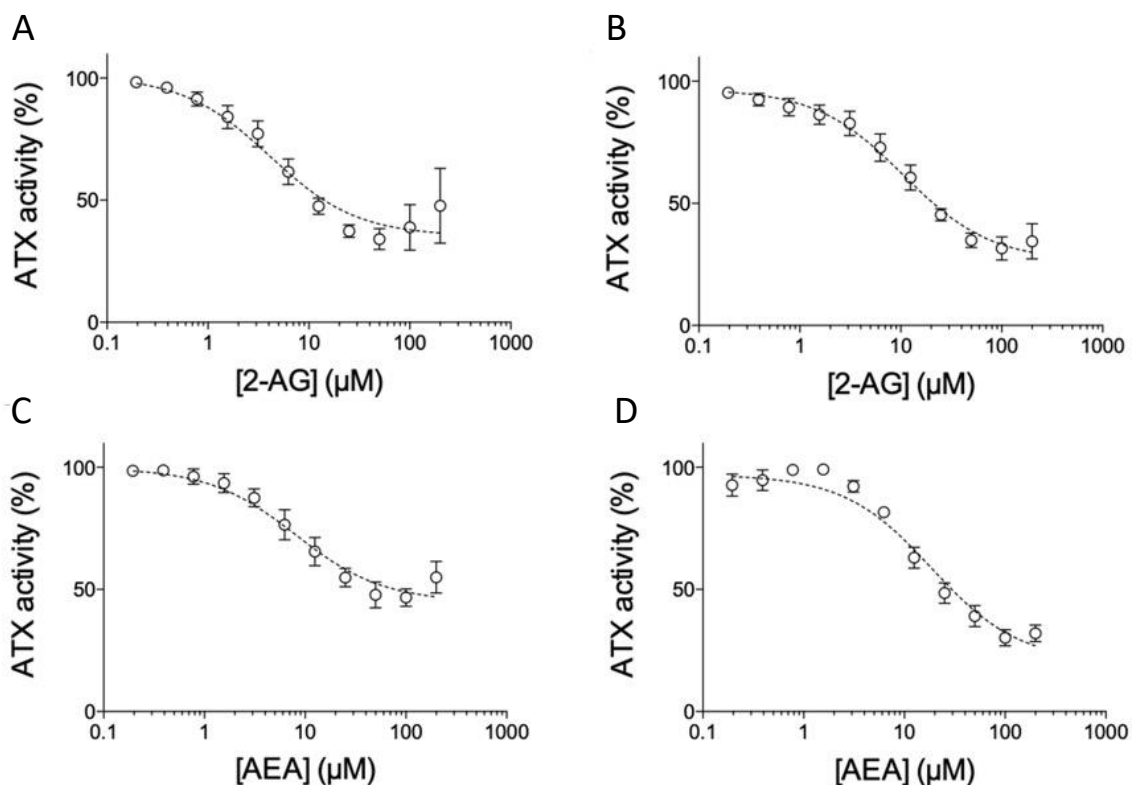


Figure 9: Inhibition of hATX- $\beta$  by endocannabinoids at 20  $\mu$ M LPC concentration.

Dose-response analysis of 2-AG with LPC 16:0 (A) and LPC 18:1 (B), AEA with LPC 16:0 (C) and LPC 18:1 (D). All error bars represent the s.e.m (n=3).

### 4.2.3 Biochemical characterization of THC and 6a10aTHC with ATX- $\beta$ and ATX- $\gamma$

THC and 6a10aTHC were chosen for a detailed biochemical characterization, as they exhibited a maximum magnitude of inhibition >50%, a cut-off criterion selected under the assay conditions used. THC works as a partial inhibitor on the catalysis of both isoforms (Figure 9A and B). The apparent  $EC_{50}$  values of THC with ATX- $\beta$  and LPC 18:1 as substrate is  $1025 \pm 138$  nM, as shown in Figure 9A. The magnitude of inhibition is around 60%. A similar magnitude of inhibition is observed with ATX- $\gamma$ , with an apparent  $EC_{50}$  of  $407 \pm 67$  nM for THC towards this isoform (Figure 9B).

Next, the artificial THC derivative 6a10aTHC was studied. The apparent  $EC_{50}$  value of 6a10aTHC for ATX- $\beta$  is  $844 \pm 178$  nM (Figure 9C), quite comparable to THC. The

## Results

maximum inhibition is marginally increased and appears to be around 75%. 6a10aTHC has the highest potency towards ATX- $\gamma$ , with a determined apparent EC<sub>50</sub> of  $374 \pm 66$  nM (Figure 9D). The magnitude of inhibition is around 70%, which is consistent with ATX- $\beta$ . Overall, 6a10aTHC is the best utilized cannabinoid inhibitor for both isoforms tested with the classical substrate LPC 18:1, and also for LPC 16:0 (Figure 10).

Both THC and 6a10aTHC are structurally close, and show a similar behavior in biochemical assays. Thus, a mode of inhibition analysis was only performed with THC to understand the inhibition mode of these compounds (Figure 9E). The analysis was carried out with 0, 0.35, 0.7 and 1.4  $\mu$ M of THC with geometrically increasing concentrations of LPC 18:1. It revealed that THC functions as a mixed-type inhibitor, which is demonstrated by the decrease of  $V_{max}$  from 8.5 to 7.3, 6.3 and 5.0, respectively, and an increase in  $K_m$  from 10.1 to 19.6, 29.9 and 31.5  $\mu$ M, respectively.

## Results

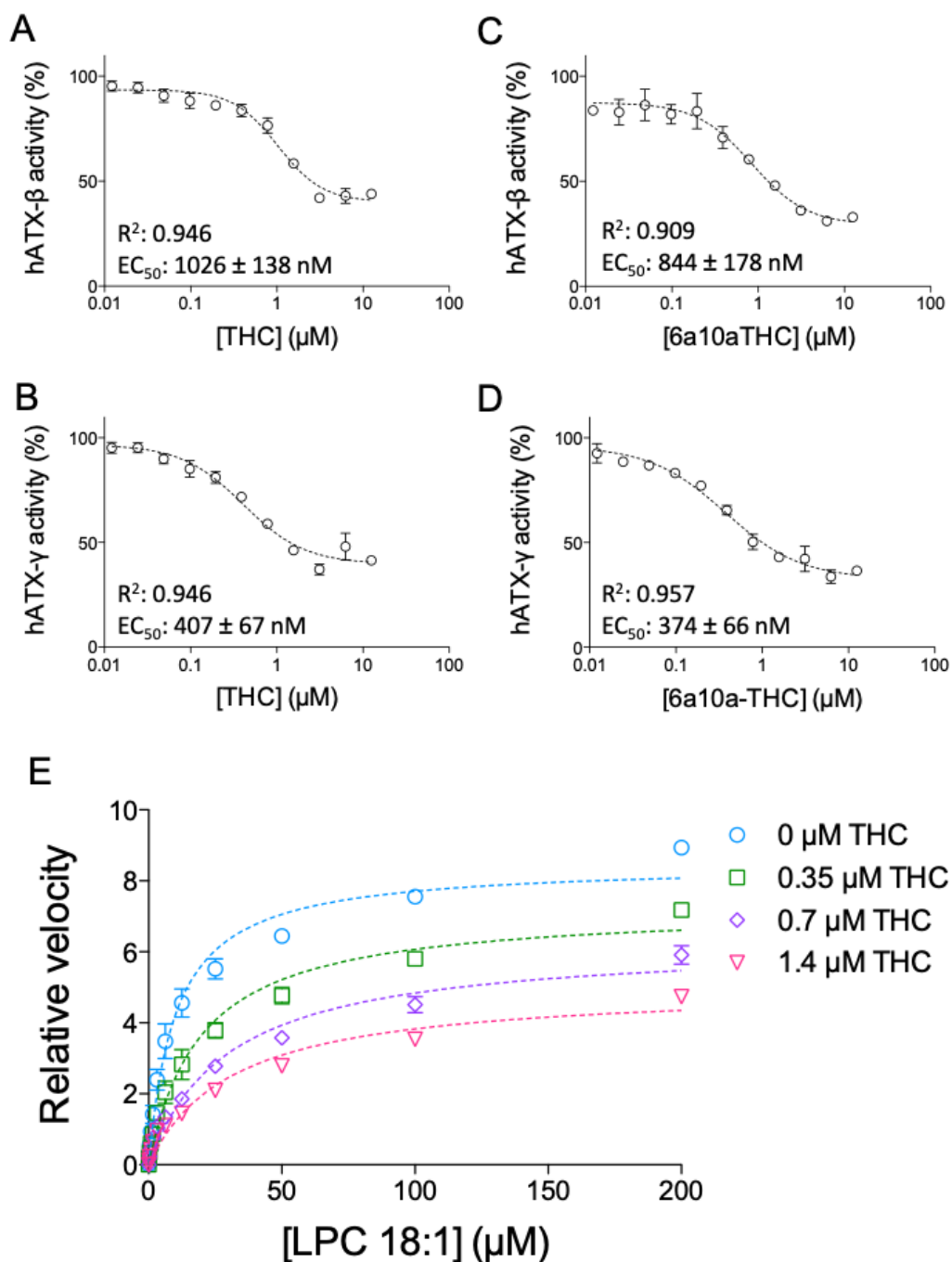


Figure 10: Inhibition of hATX by plant-derived THC and synthetic 6a10aTHC.

Dose-response analysis of (A) hATX-β and (B) hATX-γ with THC and LPC 18:1, (C) hATX-β and (D) hATX-γ with 6a10aTHC and LPC 18:1. (E) Mode of inhibition of THC with hATX-γ indicates a mixed type inhibition. All error bars represent the s.e.m (n=3).

Experiments were controlled with a choline control and a commercial inhibitor as mentioned previously, in order to confirm the good quality of our assays. The  $IC_{50}$  of 6

## Results

nM. found for HA155 corresponds to the one reported for this inhibitor. The cannabinoids and endocannabinoids have no effect on the choline assay itself as shown in Figure 10B, excluding any false positives, and the choline curve was linear, corresponding to the manufacturer assay description.

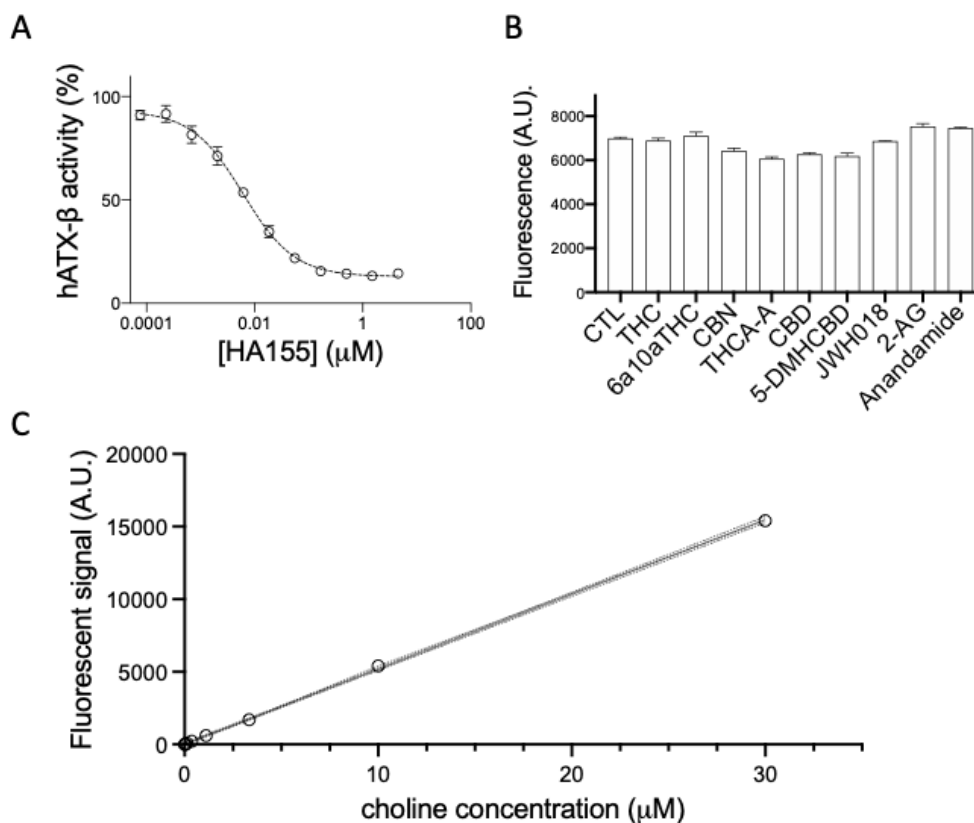


Figure 11: Enzymatic assay controls.

(A) Dose-response analysis of HA155 with LPC 18:1 and hATX-β showing an IC<sub>50</sub> of 6 ± 0.8 nM. (B) Control assay in absence of ATX and replacement of LPC with choline. No interference with the assay was found with the various cannabinoids and endocannabinoids tested. All error bars represent the s.e.m (n=3). (C) Choline standard of the enzymatic assay.

### 4.2.4 Co-crystal structure of ATX-THC

To understand the binding interface between THC and ATX in detail, we expressed and purified a well characterized deglycosylated mutant (rATX N53A, N410A) of the ATX-β from *Rattus norvegicus* (UniProt ID: Q64610-2, rATX-β) (139,140) and co-

## Results

crystallized this with THC. This rATX- $\beta$ -THC structure (PDB ID: 7P4J) was resolved to 1.8 Å resolution with an  $R_{\text{free}}$  of 23.5% (Table 1). Clear residual electron density close to the active site of ATX was observed. Modelling of THC here resulted in a very good fit to this remaining electron density (Figure 11A). rATX- $\beta$  binds THC at the entrance of the hydrophobic pocket with the aliphatic chain pointing into this pocket. The binding of the THC molecule is driven by hydrophobic interactions of the residues I167, F210, L213, L216, W254, F274, Y306 and V365 (Fig 11B), as analyzed by the PLIP server (141). A superposition of the rATX- $\beta$ -THC structure with the rATX- $\beta$ -LPA 18:1 structure (PDB ID: 5DLW) (140) shows that the THC molecule blocks binding of the LPA 18:1 aliphatic chain, while binding to the glycerol backbone and the phosphate group can still occur (Figure 11C).

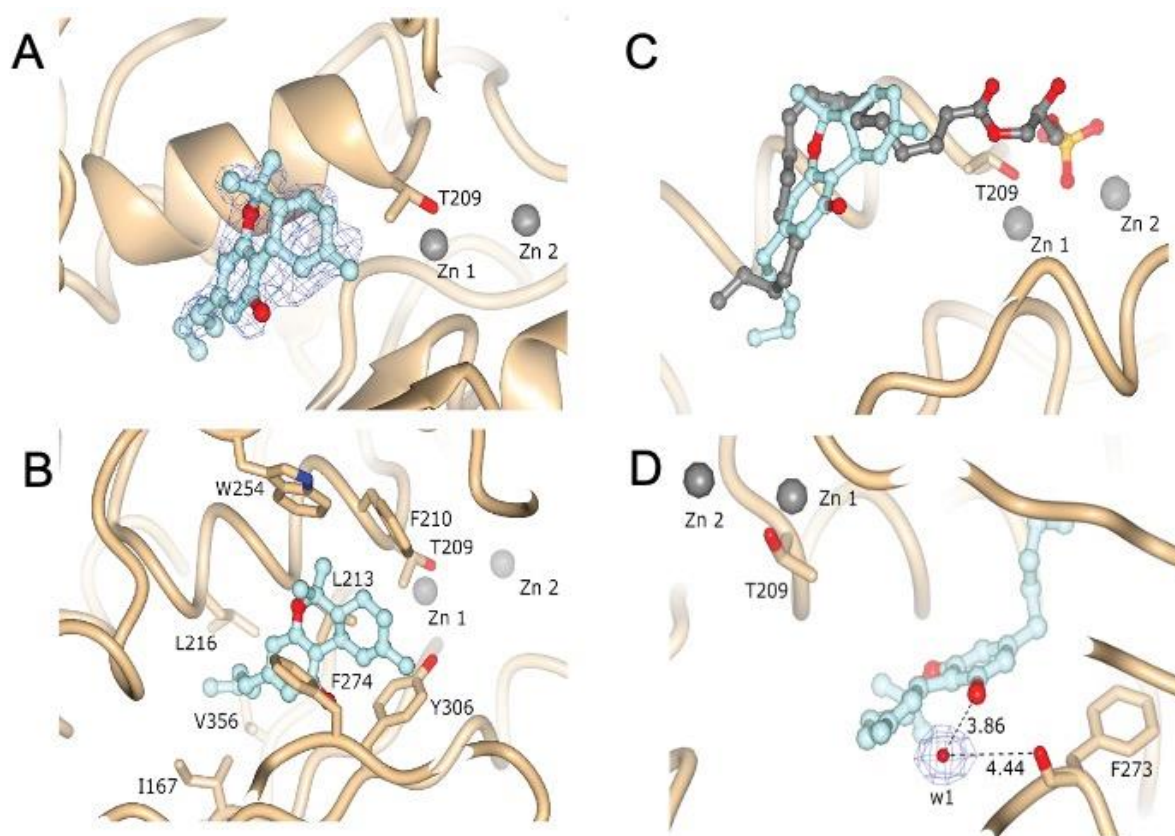


*Figure 12: Electron density and structure of rATX- $\beta$ -THC complex*

(A) Feature Enhanced electron density map before THC placement, contoured at 1 RMSD and represented as a blue wireframe model. (B) Molecular interactions of THC with rATX- $\beta$ . (C) Superposition of rATX- $\beta$  binding to THC (PDB ID: 7P4J) and LPA 18:1 (PDB ID: 5DLW). (D) Water molecule present in the rATX- $\beta$ -THC binding site.

## Results

The distances from the water molecule to the oxygen of THC and carbonyl oxygen of F273 are indicated in Å.

### 4.2.5 Co-crystal structure of ATX-6a10aTHC

We also obtained an rATX- $\beta$ -6a10aTHC structure (PDB ID: 7P4O) to 1.7 Å resolution with an  $R_{\text{free}}$  of 20.6% (Table 1). In this rATX- $\beta$ -6a10aTHC structure, we observed clear residual electron density, which resembles almost perfectly the 6a10aTHC ligand (Figure 12A). The binding of the 6a10aTHC molecule is again mainly accomplished by hydrophobic interactions of the residues I167, F210, L213, W254, F273, F274, Y306 (Figure 12B), as analyzed by the PLIP server (141). Nevertheless, an additional water bridge between the carbonyl of F273 and the THC derivative can be observed (Figure 12C), which could contribute to the increased binding stability of this ligand compared to THC, observed as the lower apparent  $EC_{50}$  for 6a10aTHC. However, a comparable water molecule also exists in the rATX- $\beta$ -THC structure, where the distance of the THC oxygen and carbonyl oxygen of F273 is 4.5 Å, thus above the PLIP server threshold for such an interaction.

The 6a10aTHC ligand in ATX adopts an overall similar binding position to the cannabinoid in the rATX- $\beta$ -THC structure. However, the aliphatic chain of the ligand points in a slightly different direction when compared to THC. Also, noteworthy is that the cyclohexene (C-ring) appears to adopt a different stereoisomeric configuration (Figure 12D) due to the alternate localization of the double bond (Figure 8A).

## Results

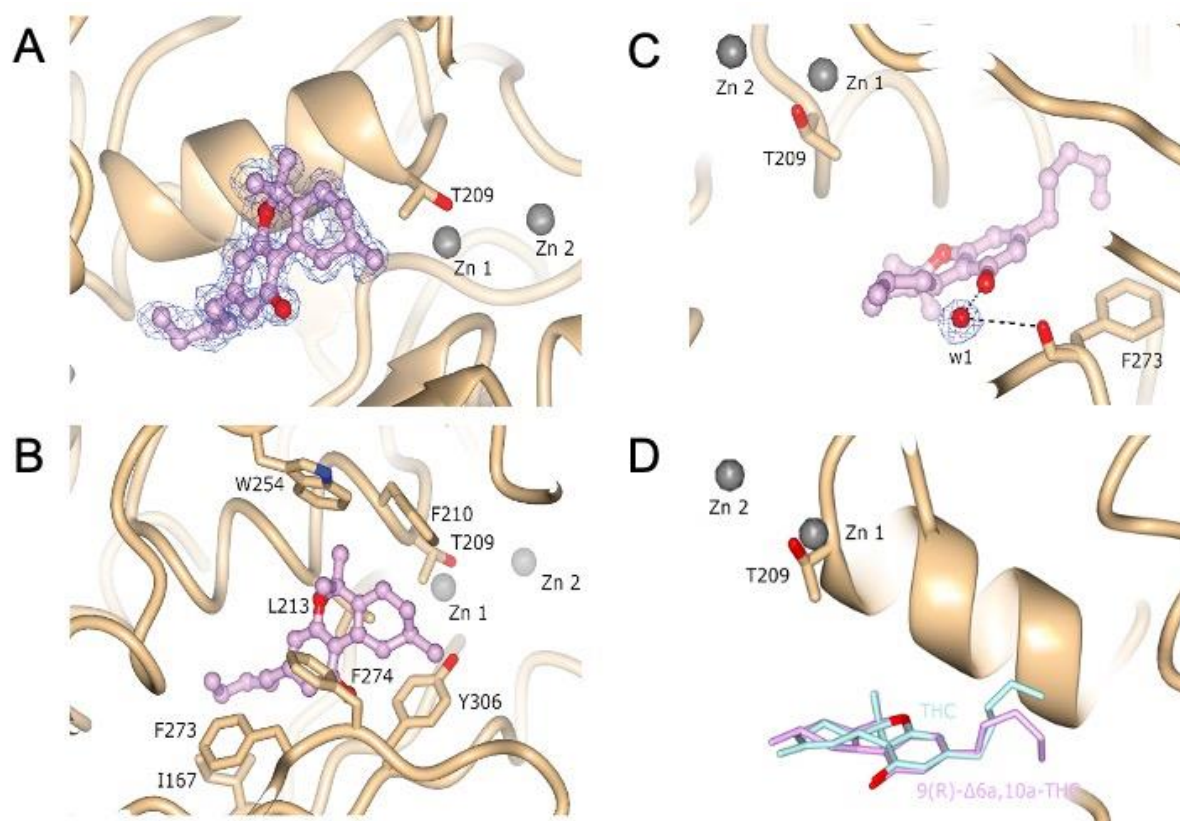


*Figure 13: Electron density and structure of rATX-β-6a10aTHC complex.*

(A) Featured Enhanced electron density map before 6a10aTHC placement, contoured at 1 RMSD and represented as a blue wireframe model. (B) Molecular interactions of 6a10aTHC with rATX-β. (C) Bridging water molecule interaction between 6a10aTHC and carbonyl oxygen of F273. (D) Superposition of the cannabinoids from rATX-β-THC and rATX-β-6a10aTHC. THC and 6a10aTHC are colored turquoise and purple, respectively.



## Results

*Table 1: Crystallographic data collection and refinement statistics for cannabinoid compounds.*

<b>Crystal</b>	<b>ATX-THC</b>	<b>ATX-9(R)-<math>\Delta</math>6a,10a-THC</b>
PDB identifier	7P4J	7P4O
<i>Data collection</i>		
Wavelength (Å)	0.976	1.000
Space group	P1	P1
<i>Cell dimensions</i>		
a, b, c (Å)	53.7 61.0 63.6	53.8 62.4 64.4
$\alpha$ , $\beta$ , $\gamma$ (°)	103.2 97.4 94.2	103.7 98.4 93.4
Resolution (Å)*	61.2-1.8 (1.9-1.8)	53.0-1.7 (1.75-1.7)
No. of reflections	47909 (2395)	85204 (8434)
R <sub>pim</sub> (%)	5.8 (64)	7.25 (63.8)
Completeness (%)		
Spherical	65.9 (13.1)	94.8 (94.2)
Ellipsoidal	91.6 (60.4)	-
Redundancy	9.2 (7.0)	3.5 (3.6)
<i>Refinement</i>		
R <sub>work</sub> (%)	18.69(29.1)	17.10 (21.5)
R <sub>free</sub> (%)	23.5(22.8)	20.60 (25.3)
No. of atoms <sup>†</sup>	6800	6818
Protein+carbohydrates	6230	6244
Ligand+metal ions	163	113
Waters and other ions	407	461
B-factors (Å <sup>2</sup> )		
All	27.5	31.9
Protein+carbohydrates	27.0	31.3
Ligand+metal ions	34.3	42.1
Water and other ions	32.9	36.6
R.m.s. deviations		
Bond lengths (RMS)	0.005	0.007

## Results

Bond angles (RMS)	0.86	0.90
<i>Validation metrics</i>		
Clashscore	6	6
Molprobability	1.63	1.43

---

### 4.2.6 Inhibition of LPA1 internalization in HeLa cells by THC

In order to validate THC can act as an inhibitor in the production of LPA and thus, ATX-LPA signaling in a cellular context, we used an agonist-induced LPA1 receptor internalization as a readout in cultured cell assays (135,142,143). As shown in Figure 5, stimulation of HA/LPA1 transfected HeLa cells with 30 nM ATX, 150  $\mu$ M LPC 18:1, and 1  $\mu$ M THC significantly reduced LPA1 internalization. This observation was only detectable in the presence of ATX and not in control conditions (Figure 13). This is an indirect response to blocking LPA production, which inhibits receptor activation and endocytosis, confirming a more physiological role of THC as a potent inhibitor.

## Results

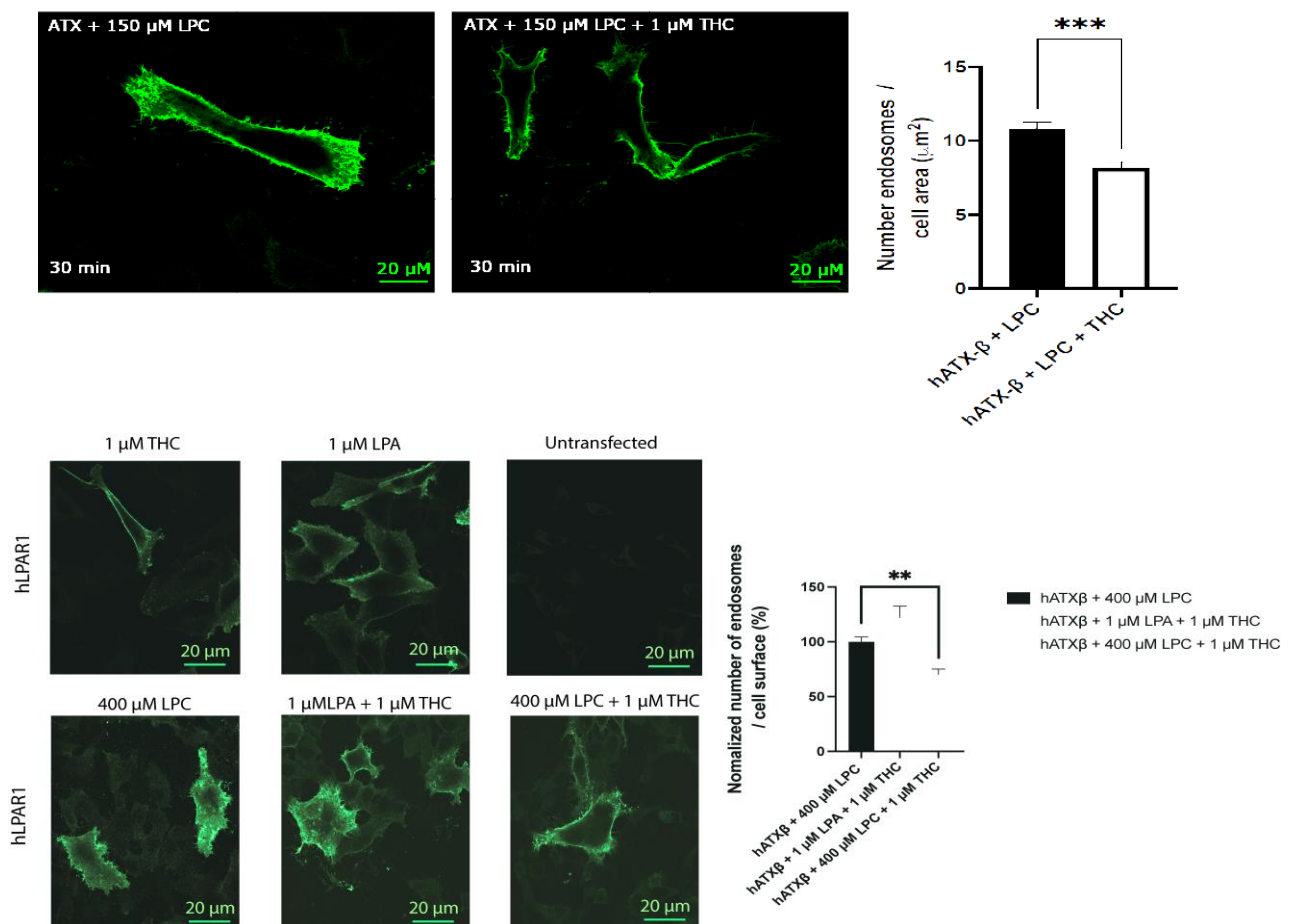


*Figure 14: Physiological effect of THC on LPA<sub>1</sub> receptor internalization*

(A) Quantification of LPA<sub>1</sub> receptor internalization revealed that THC reduced the number of endosomes internalized when compared to untreated condition, paired t-test p-value = 0.0008. All error bars represent the SEM, calculated from 11 images per condition in biological triplicate experiments. (B) Control assays for LPA<sub>1</sub> receptor internalization. No internalization was found using THC alone. LPA treatment of cells led to high LPA<sub>1</sub> receptor internalization, in accordance with previously published results. LPA<sub>1</sub> receptors were internalized in presence of THC, providing evidence for a specific THC mediated effect of the ATX-LPA signaling axis. Inhibition of ATX-LPA signaling by THC is not abolished in the presence of higher LPC concentration (400 μM LPC, p-value= 0.0068). Untransfected cells were not stained using primary and secondary antibody, confirming the specificity of the labelling reagents used. Image analysis was performed with ImageJ using 9 images per condition from 3 experimental replicates.

### 4.3 Cannabinoid-inspired inhibitors of Autotaxin

#### 4.3.1 Development of new inhibitors:

As shown above, it was observed that rATX can be inhibited by various cannabinoids. In particular, THC and delta 6a,10a-THC inhibited hATX as mixed-type inhibitors at nanomolar concentrations. Pharmacokinetic parameters for cannabinoids are widely studied and there is a consensus that they cross the blood brain barrier and bind to CB1 and CB2 receptors, making them an ideal starting point to specifically inhibit ATX in the brain. Although cannabinoids were revealed as excellent ATX inhibitors, their major drawbacks relate to regulations, legislation and acceptance by patients, making them less desirable for development. Because the chemical synthesis of cannabinoid derivatives is not an easy task and legal issues, we decided to pursue a different strategy. Indeed, since most cannabinoids are from natural origin this leaves little room for total synthesis due to low yield process such as photocyclization or isomerization (144). Also, synthetic derivatives are not available freely since they are scheduled compounds, a license needs to be requested from the ANSM before any ordering and for each compound or derivative.

#### 4.3.2 From hit to lead :

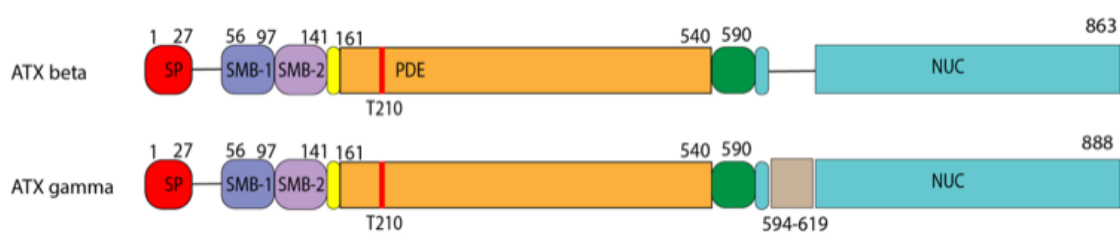
Our strategy was based on the structural similarity between the benzopyran moiety of THC and naturally occurring compounds bearing this chemical entity. Among these compounds, we targeted chromone-bearing derivatives (scheme 3 and 4). This druggable scaffold is known for its therapeutic potential and safety. For this, I tested a library of 80 compounds (available in the Boumendjel lab) bearing a chromone moiety for their inhibitory potential at 1  $\mu$ M (scheme 5).

We observed that molecules bearing an indole linked to a chromone moiety presented potent inhibition against ATX. Following further structure-activity relationship (SAR) studies and optimization, we discovered that compounds having the following substitution pattern tended to exert a high inhibitory effect: (i) the presence of a hydrophobic substituent at the indole nitrogen, and (ii) the presence of two hydroxyls at positions 5/7 of the chromone moiety (scheme 3). Based on these structural requirements, I followed a funnel down approach that led to the identification of MEY-

## Results

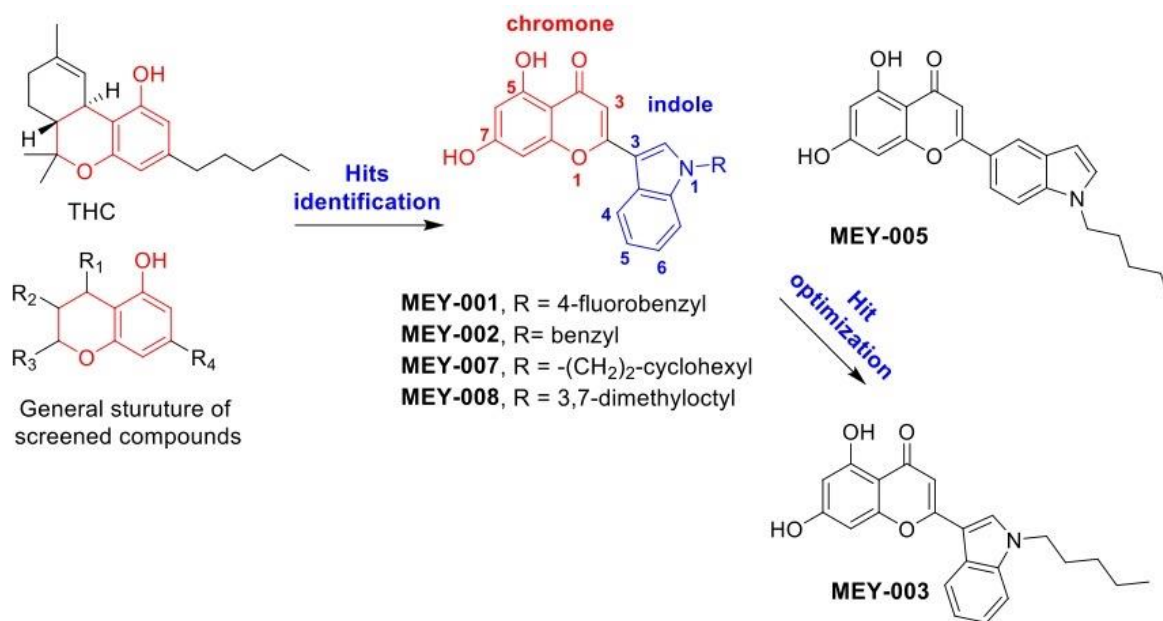
003 as the most active (scheme 3), which was selected for further investigations in this study. It should be highlighted that the site of linkage of chromone and indole moieties is crucial. When the linkage was made through the phenyl ring of the indole moiety, the inhibition activity was severely decreased. Interestingly, the length of hydrophobic carbon chain inducing the highest inhibition activity correlates with the one found in THC. Ramified chains, chains bearing aromatic or saturated rings were dis-advantageous for the inhibition activity as shown by the lower inhibition activity of MEY-007 and MEY-008 compounds.

MEY-003 is synthesized in three steps starting from 2,4-dimethoxy-6-hydroxyacetophenone (1) and N-pentylindol-3-carboxaldehyde (2), as shown in scheme 4. Starting materials (1) and (2) were subjected to a condensation reaction in the presence of potassium hydroxide in methanol to yield diarylpropenone (3) with 65% yield. The latter was submitted to an oxidative-cyclization reaction with iodine at 150 °C to provide chromone derivative (4) with 75% yield. Finally, compound (4) was subjected to BBr<sub>3</sub>-mediated demethylation of methoxy groups to provide the desired compound, MEY-003 with 40% yield. The compound purity and authenticity were attested by HPLC, NMR (<sup>1</sup>H and <sup>13</sup>C) and MS (ESI+) (see supplementary data).

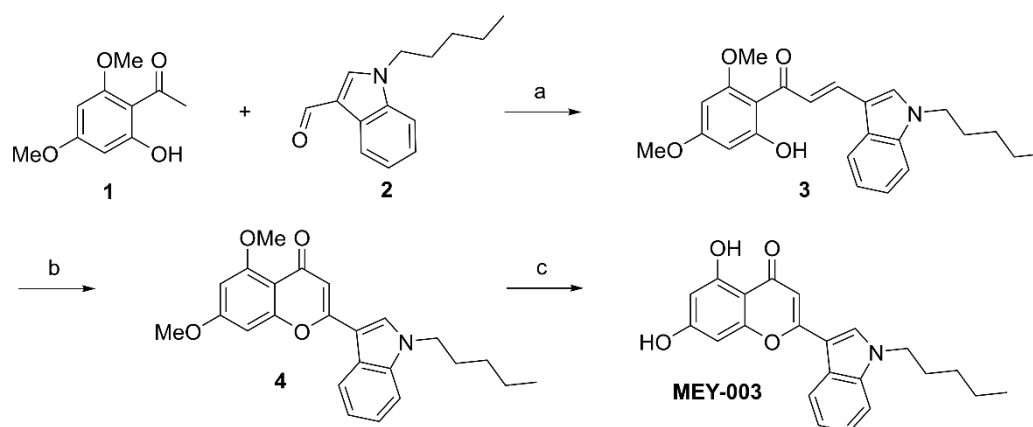


*Scheme 2: Comparison of the ATX- $\beta$  and ATX- $\gamma$  sequences.*

## Results

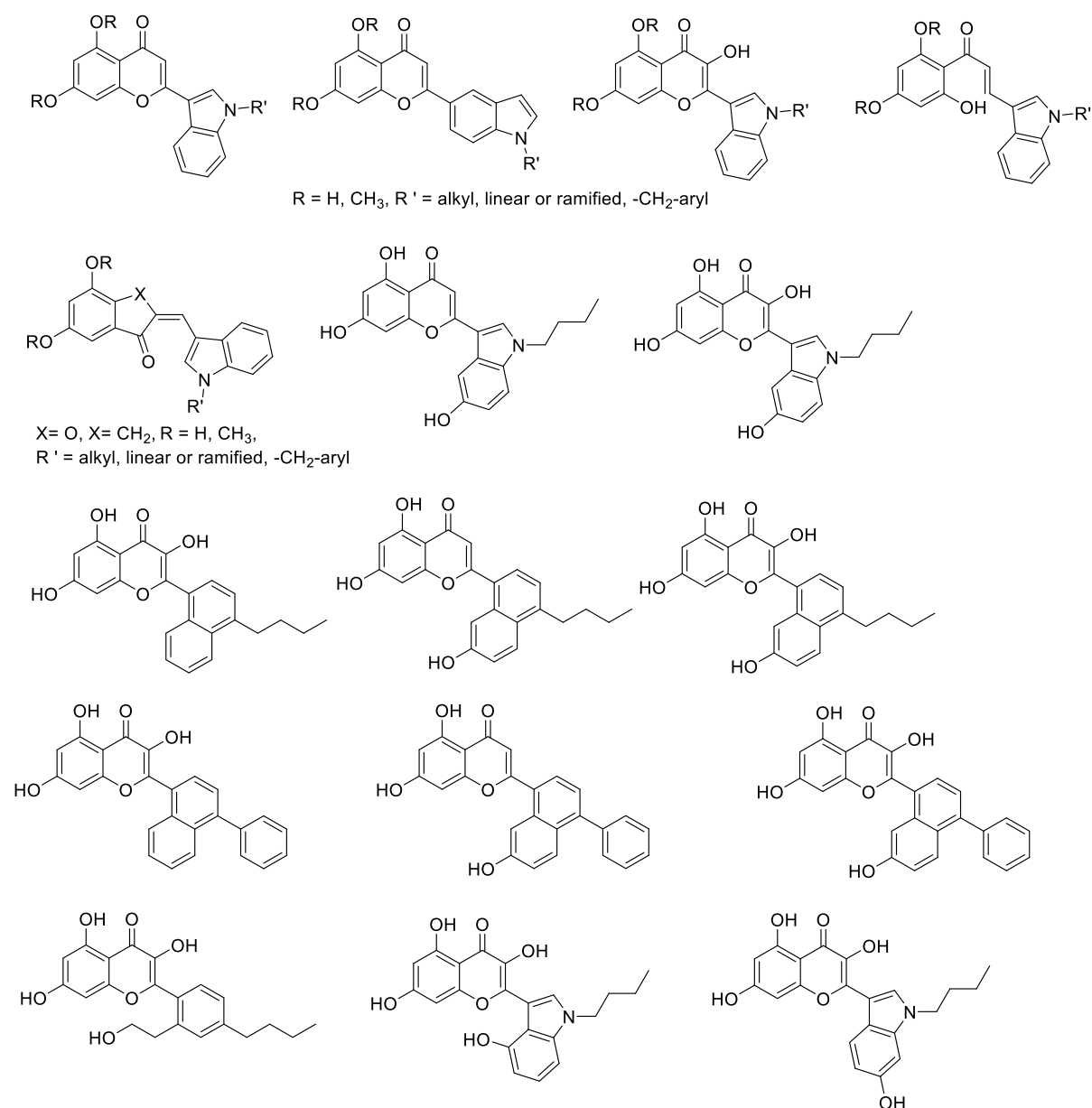


Scheme 3: Summary for the discovery process of flavone-derived ATX inhibitors



Scheme 4: Synthesis of MEY-003. (a) KOH, MeOH, reflux, (b) I<sub>2</sub>, 150 °C, (c) BBr<sub>3</sub>, CH<sub>2</sub>Cl<sub>2</sub>, room temperature.

## Results



*scheme 5: Chemical groups of the screened library*

### 4.3.3 Biochemical characterization of cannabinoid-inspired inhibitors:

As outlined above, emphasis has been put on MEY-003 since it produced the highest inhibition level (Fig 15A-D). EC<sub>50</sub> measurements are described in the experimental section and were adapted from previous work using the choline-release assay (116). Briefly, all the tests were performed in the presence of 30 nM ATX, 50 mM Tris, 150 mM NaCl and 50 μM LPC18:1 or 16:0 at pH 8. The apparent EC<sub>50</sub> with hATX-β and LPC18:1 was 460 nM (350-610 nM) with an inhibition slope of 68% (Figure 15A). The apparent EC<sub>50</sub> with hATX-β and LPC16:0 was 384 nM (360-400 nM), with an inhibition

## Results

slope of 83% (Figure 15C). In order to demonstrate the potency with the cerebral isoform of ATX, the apparent  $EC_{50}$  measurements were repeated using hATX- $\gamma$  with similar assay conditions. Interestingly, the apparent  $EC_{50}$  was slightly higher with LPC18:1, at 1099 nM (925-1317 nM) (Figure 15B), but similar to that previously obtained for hATX- $\beta$  and LPC16:0, with an apparent  $EC_{50}$  of 380 nM (300-460 nM), showing the ability of this compound to inhibit both ATX isoforms at different levels. Additionally, the span of inhibition ranged from 66% to 72% for LPC18:1 and LPC16:0, respectively.

MEY-003 acts as a non-competitive ATX inhibitor. In order to better understand the mode of action of MEY-003, an inhibition assay was run in similar assay conditions using hATX- $\gamma$  and LPC18:1 (Figure 15E). It shows that MEY-003 behaves as a non-competitive inhibitor (apparent  $K_i$  was 432 nM), which is in agreement with structural data (shown later).

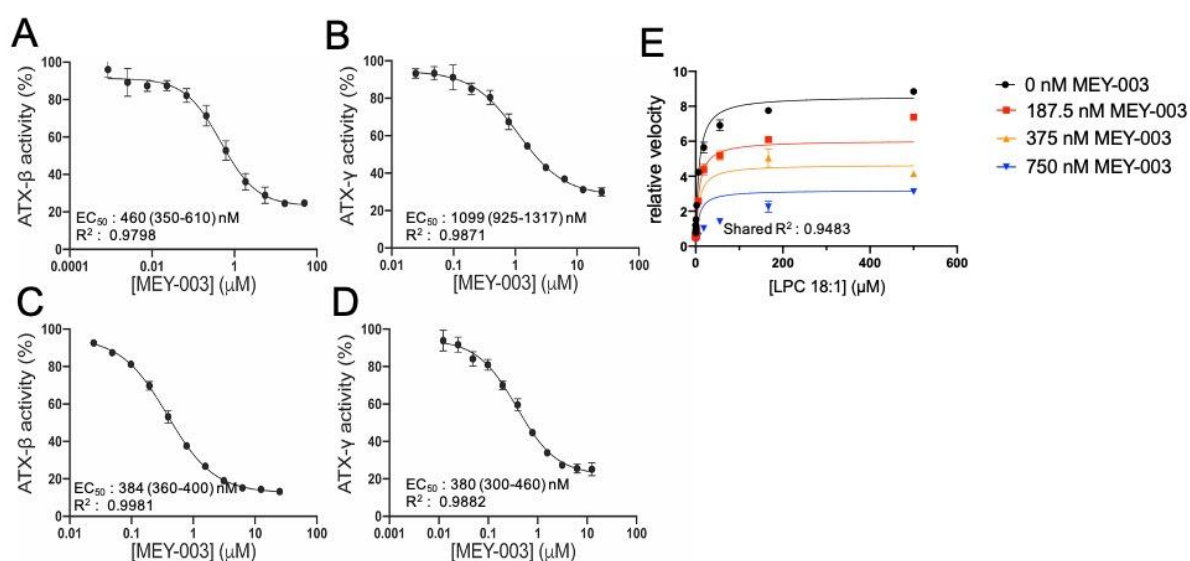


Figure 15: Inhibition of autotaxin (ATX) by MEY-003.

Dose-response analysis of (A) hATX- $\beta$  and (B) hATX- $\gamma$  with LPC18:1 and MEY-003, (C) hATX- $\beta$  and (D) hATX- $\gamma$  with LPC16:0 and MEY-003. (E) The mode of inhibition of MEY-003 with hATX- $\beta$  and LPC18:1 indicates a non-competitive inhibitory activity. All error bars represent the S.E.M. (n=3).

### 4.3.4 Binding interface of cannabinoid-inspired inhibitors and ATX- $\gamma$ structure:



## Results

Human ATX- $\gamma$  has been co-crystallized with MEY-003 and LPA (Figure 16 and table 2). The recombinant N54A/N411A hATX- $\gamma$  mutant was produced and crystallized, as previously reported for other isoforms(25,115). Interestingly, the enzyme was crystallized in the same assay conditions as rat ATX- $\beta$ , with two molecules in the asymmetric unit. The ATX-MEY-003 complex structure allowed the identification of important protein-ligand interactions in the ATX hydrophobic binding pocket using the PLIP (Protein-Ligand Interaction Profiler) server (Figure 17). Most of the interactions are hydrophobic, similar to those observed with THC and rATX- $\beta$ . However, we observed two hydrogen bonds between the main chain amide and carbonyl of W276 to the ketone and a hydroxy group at position 5 of MEY-003, respectively. MEY-003 also forms  $\pi$  stacking interactions between with residues F275 and Y307. These  $\pi$  stacking interactions are probably crucial for orientating MEY-003 within the hydrophobic pocket, since the residue F275 and Y307 can take different orientations in order to accommodate various molecules. These different residue conformations are common in the literature and can be found in various co-structures of ATX (62,145).

The additional  $\pi$  stacking and hydrogen bonds most likely explain the difference in binding between MEY-003 and THC in the ATX- $\gamma$  hydrophobic pocket. Indeed,  $EC_{50}$  comparisons showed that the apparent  $EC_{50}$  of THC is 1026 nM while that of MEY003 with hATX- $\gamma$  and LPC18:1 is 460 nM. A further superposition of hATX- $\gamma$ -MEY-003 and hATX- $\gamma$ -LPA18:1 was carried out (Figure 16 D), showing that the LPA lipophilic tail binds in a similar position to MEY-003 in hATX- $\gamma$ . Additionally, a superposition with the rATX- $\beta$ -THC structure from previous work shows that MEY-003 binds in a similar position, but with a slightly different conformation, to THC (Figure 16e). Interestingly, other ATX inhibitors do not seem to share a similar binding interface. For example, PAT-078, which retains an indole in its structure, does not adopt a similar conformation, at least for the indolic part of the inhibitor (Figure 17C) (PDB: 4ZG6).

## Results

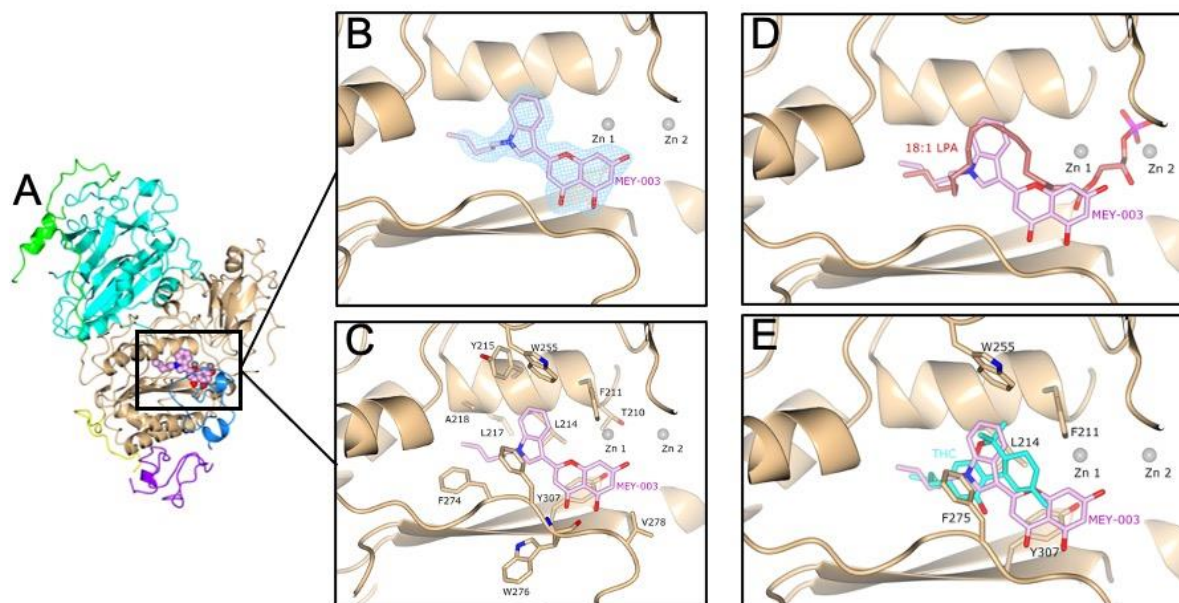


Figure 16: MEY-003 binding to hATX- $\gamma$  hydrophobic pocket

(A) hATX- $\gamma$  overall structure bound with MEY-003 (PDB: 8C3O). Domains are colored according to Figure 1. (B) MEY-003 2FO-FC density at 1 sigma after refinement (PDB: 8C3O). (C) MEY-003 binding interface with hATX- $\gamma$  (PDB: 83CO). (D) Superposition of hATX- $\gamma$ -MEY-003 and hATX- $\gamma$ -LPA (PDB: 8C3O and 8C3P). (E) Superposition of hATX- $\gamma$ -MEY-003 and rATX-THC with main interactions displayed (PDB: 8C3O and 7P4J). To obtain a higher structural resolution, rATX- $\beta$  was co-crystallized with both MEY-003 and MEY-002 (Figure 17).

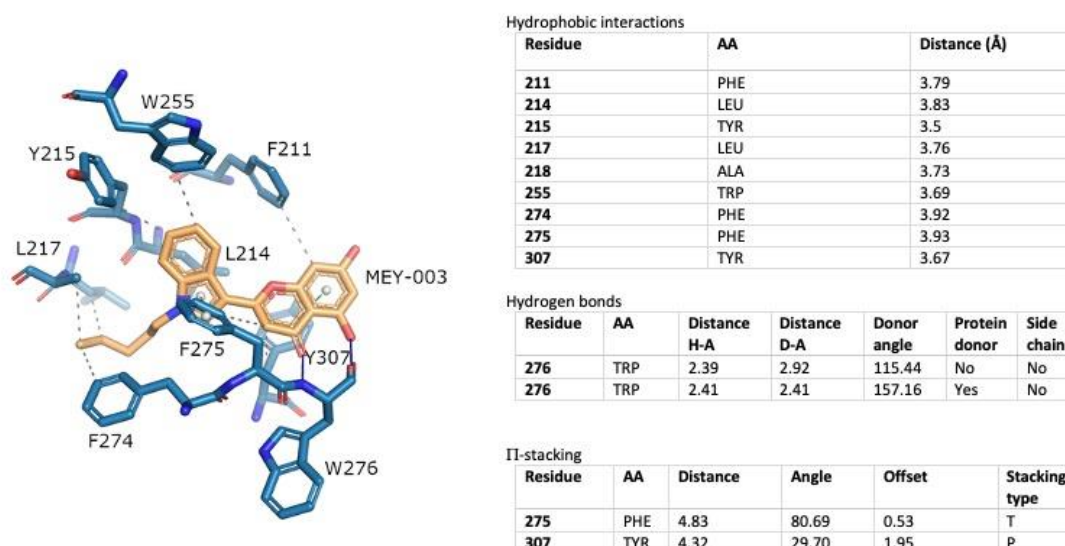


Figure 17: MEY-003-ATX- $\gamma$  interaction analysis using the PLIP server.

## Results

Superposition of both structures showed that the indole can adopt a slightly different conformation in the hydrophobic pocket, relying on the ability of L213 to adopt two different conformations (Figure 17D, E and F). In the MEY-003 bound structure, L213 makes a side-on interaction with the indole while adopting a face-to-face conformation with MEY-002. The MEY-002 bound structure also revealed an important water bridge in the binding interface to mediate interactions with the important active site residues, T209 and D171, that bind the Zn ions (Figure 17D). This water bridge is probably relevant for MEY-003 as well, but this is likely only visible in the MEY-002-rATX- $\beta$  co-structure due to the higher resolution obtained (1.9 vs 2.5 Å) (PDB: 8C4W). This might also explain the observed non-competitive inhibition of hATX- $\gamma$  by MEY-003 (Figure 15e). This new flavone-derived inhibitor could be classified as a type 2 inhibitor since it binds in the hydrophobic pocket. However, this new family does not completely overlap with corresponding type 2 inhibitors like PAT-078 (Figure 17C) (PDB: 4ZG6). Partial overlap with type 1 inhibitors such as HA-155 (Figure 17C) (PDB: 2XRG) shows that flavone-derived inhibitors can be classified as type 2-like inhibitors, with indirect interactions with the active site through a water bridge.

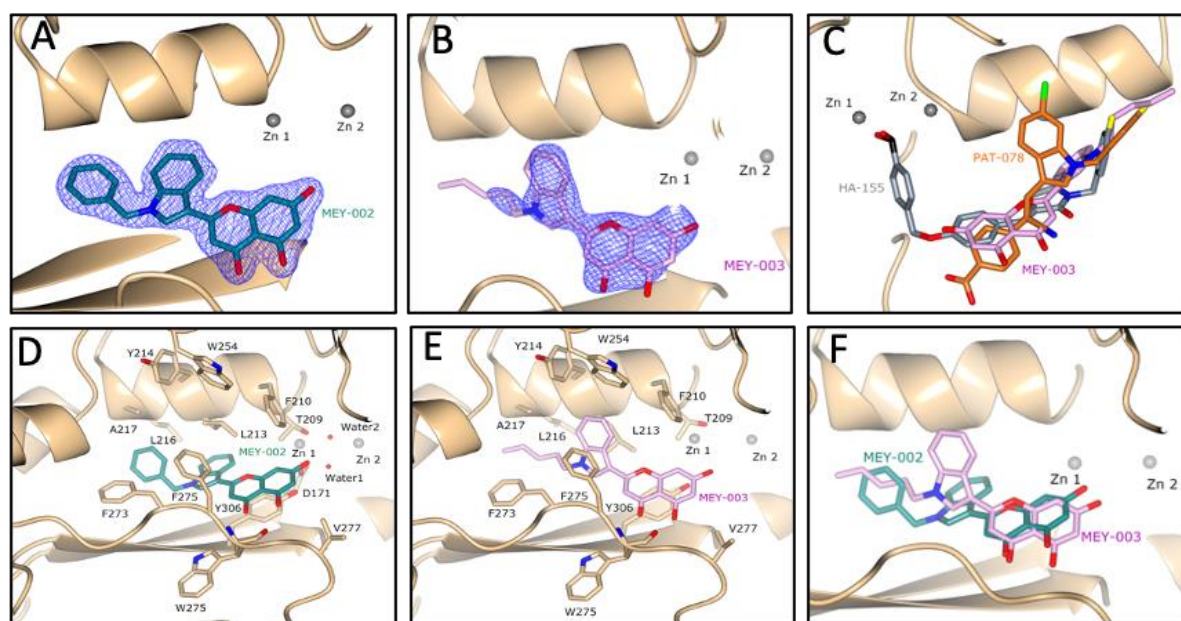


Figure 18: MEY-002 and MEY-003 binding to the rATX- $\beta$  hydrophobic pocket.

(A) MEY-002 2Fo-Fc density at 1 sigma after refinement (PDB: 8C4W). (B) MEY-003 2Fo-Fc density at 1 sigma after refinement (PDB: 8C7R). (C) Superposition of inhibitors HA-155, PAT-078 and MEY-003 (PDB: 2XRG, 4ZG6 and 8C7R). (D) MEY-

## Results

002 binding interface with rATX- $\beta$  (PDB:8C4W). (E) MEY-003 binding interface with rATX- $\beta$  (PDB: 8C7R). (F) Superposition of rATX- $\beta$ -MEY-002 and rATX- $\beta$ -MEY-003 (PDB: 8C4W and 8C7R).

## Results

Crystal	ATX- $\gamma$ -MEY-003	ATX- $\gamma$ -18:1 LPA	rATX-MEY-002	rATX-MEY-003
PDB identifier	8C3O	8C3P	8C4W	8C7R
<i>Data collection</i>				
Wavelength (Å)	0.976	0.976	0.976	0.976
Space group	P 1 21 1	P 1 21 1	P1	P1
<i>Cell dimensions</i>				
a, b, c (Å)	53.9 288.4 57	53.9 57.2 287.9	53.2 62.8 70.1	53.529 61.843 63.850
$\alpha, \beta, \gamma$ (°)	90 90.1 90	90 92.7 90	98.9 106.5 99.5	104.012 98.426 93.267
Resolution (Å)*	53.5 - 2.4 (2.5 - 2.4)	53.8 - 2.3 (2.4 - 2.3)	47.6-1.9 (1.979-1.945)	43.6-2.5 (2.573 -2.50)
CC <sub>1/2</sub>	0.95 (0.68)	0.97 (0.45)	0.99 (0.852)	0.99 (0.509)
Average I/ $\sigma$ I	3.58 (1.5)	6.66 (1.1)	9.3	6.7
Completeness (%)				
Spherical	70.10 (17.0)	98.76 (89.28)	97.2	98.2
Ellipsoidal	90.2 (47.0)	-	-	-
Redundancy	1.9 (1.9)	2.0 (1.9)	3.3 (3.3)	3.4 (3.5)
<i>Refinement</i>				
Resolution (Å)	53.5-2.4	53.8-2.3	47.6-1.9	43.6-2.5
No. of reflections	43828 (112)	69936 (6235)	59934(3012)	25651 (1302)
R <sub>pim</sub> (%)	14 (46)	9 (58)	5 (37)	5.6 (24)
R <sub>work</sub> (%)	0.17 (0.26)	0.22 (0.31)	0.19 (0.23)	0.20(0.26)
R <sub>free</sub> (%)	0.24 (0.17)	0.28 (0.4)	0.23 (0.30)	0.25 (0.30)
<i>No. of atoms<sup>†</sup></i>				
Protein+carbohydrates	12726	12531	6287	6383
Ligand+metal ions	252	225	25	17
Waters and others	49	510	318	94
<i>B-factors (Å<sup>2</sup>)</i>				
All	29.05	42.72	38.46	44.14
Protein+carbohydrates	28.91	42.75	38.69	44.22
Ligand+metal ions	38.50	50.11	38.27	47.83
Water and other	16.85	38.65	33.87	35.55
R.m.s. deviations				

## Results

Bond lengths (RMS)	0.024	0.003	0.42	0.007
Bond angles (RMS)	1.2	0.55	0.63	0.90
<i>Validation metrics</i>				
Clashscore	6.3	9.44	10.78	9.05
MolProbability	1.61	2.29	2.32	1.97

*Table 2: Crystallographic data collection and refinement statistics for cannabinoid-inspired inhibitors*

### 4.3.5 MEY-003 reduces hLPA1 internalization and is not cytotoxic to HeLa cells.

Previous studies have shown that ATX activity is required to trigger LPA receptor internalization (23). It has also been demonstrated that ATX is responsible for LPA presentation towards receptors by acting as a chaperone (23). In this study, we confirmed that MEY-003 is able to reduce LPA1 receptor internalization in HeLa cells after treatment with LPC and hATX- $\beta$ . LPA1 internalization was reduced by approximately 47% (Figure 19A), showing that MEY-003 significantly blocks LPA signaling through ATX inhibition. Moreover, further *in vitro* assays showed that MEY-003 is non cytotoxic after prolonged treatment (up to 8 hours) at 100  $\mu$ M. The same assay performed on MEY-002 also showed no cytotoxicity effects (Figure 19B).

## Results

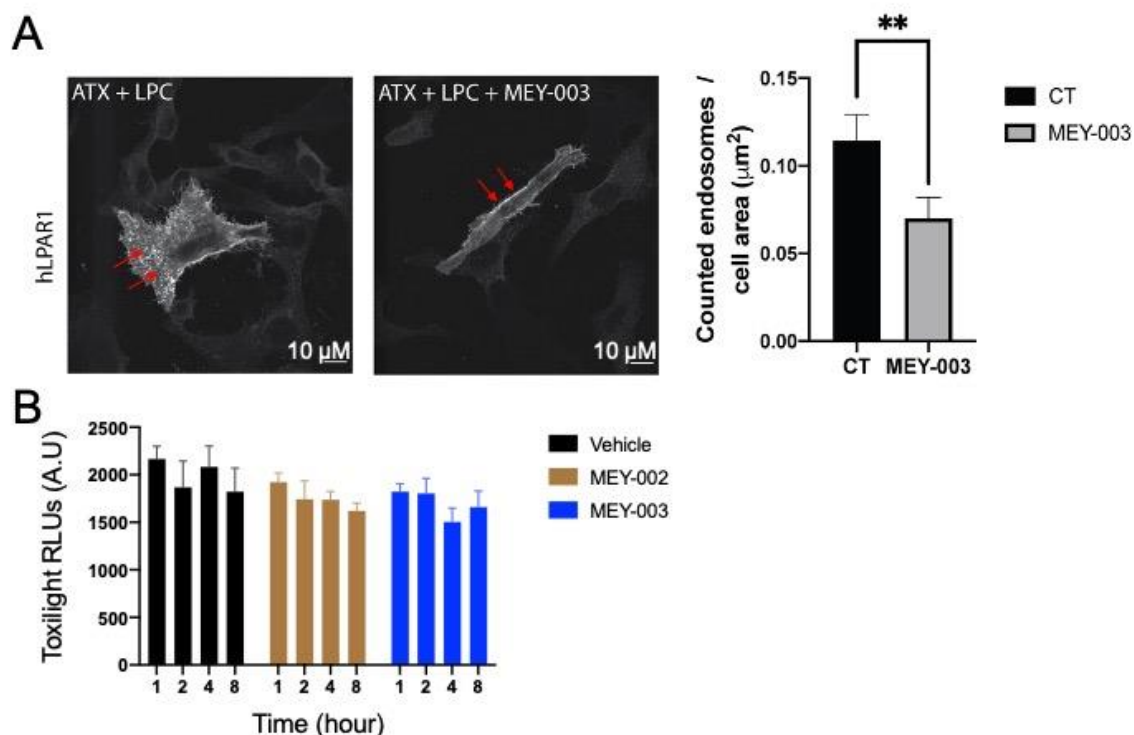


*Figure 19: MEY-003 reduces LPA1 receptor internalization and is not cytotoxic to HeLa cells.*

(A) Cells were treated with hATX- $\beta$  and LPC with or without MEY-003 addition. After treatment, cells were fixed and stained using an anti-HA tag antibody. 17 and 15 images were acquired in biological triplicate for hATX- $\beta$  + LPC + MEY-003 and hATX- $\beta$  + LPC, respectively, using a LEICA micro-scope at 63X magnification. Red arrows point to LPA1 receptor hypersignal. Receptor internalization was quantified with Fiji with a paired t-test p-value = 0.0078. (B) Cells were incubated with 100  $\mu$ M of MEY-003 or MEY-002 for 1 to 8 hours. Cytotoxicity detection was performed using Toxilight assay. All error bars represent S.E.M. (n=3) in biological triplicate.

### 4.3.6 Insight into hATX- $\gamma$ structure and biology

As far as I'm aware the hATX- $\gamma$  structure presented here is the first solved structure of the neuronal isoform. A superposition of hATX- $\beta$  (PDB: 4ZG7) and hATX- $\gamma$  (PDB: 8C3O) results in a RMSD of 0.56 Å for 775 C-alpha atoms, confirming that hATX- $\gamma$  is very similar to hATX- $\beta$  in structure, despite a 25AA insertion. This insertion was not visible by X-ray crystallography due to its high flexibility, confirming an alphafold prediction (Figure 20). The function of this hATX- $\gamma$  brain-specific insertion remains

## Results

unknown. However, similar to ATX- $\alpha$ , it appears that ATX- $\gamma$  is also cleaved in the insertion region, shown by a WB, with two fragments around 70 and 34 kDa visible. This polybasic insertion in hATX- $\gamma$  does not contain a particular furin cleavage site, such as that observed in ATX- $\alpha$  (146), and more research will be required to try and identify the protease involved.

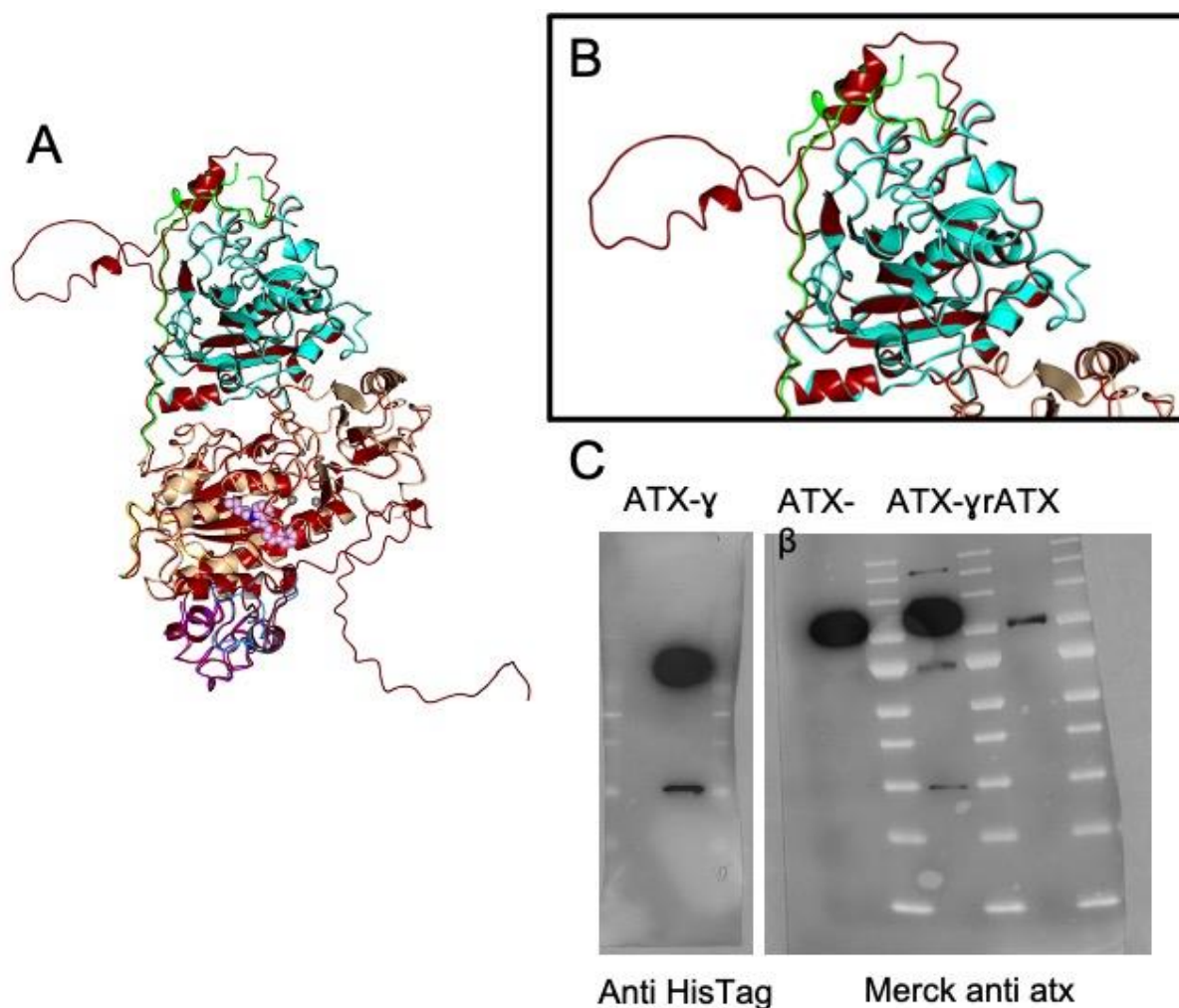


*Figure 20: hATX- $\gamma$  insertion can be cleaved by an unknown protease during protein production.*

A) superposition of hATX- $\gamma$  crystal structure (83CO) and an AlphaFold prediction (coloured in red). Superposition of both model and experimentally determined structure show a high similarity, apart from flexible regions not observed in the crystal structure. B) A zoom in of the hATX- $\gamma$  insertion. C) Western blot showing cleavage of hATX- $\gamma$ . This cleavage is not observed in hATX- $\beta$  and rATX- $\beta$  under similar conditions.



### 4.4 CryoEM analysis of ATX :

Structures of hATX- $\beta$  and rATX- $\beta$  have been extensively studied by X-ray crystallography, either alone or in complex with various molecules (substrates and inhibitors). Here, we report the first hATX- $\gamma$  structure in complex with cannabinoid-inspired inhibitors. However, while ATX is known to bind integrins at the cell surface, specifically those containing  $\beta 1$  and  $\beta 3$  (24), the molecular details of this interaction is still unknown. Recently, it has been shown that ATX can act as a LPA chaperone, presenting it to LPA receptors, presumably through indirect integrin mediated binding at the cell surface(23). ATX contains two SMB domains that were shown to mediate interaction with integrins (24). These domains are quite flexible in ATX and it's likely that they can adopt different conformations to facilitate binding with integrins at the cell surface . In order to study possible ATX interactions with binding partners at a later time I initiated a preliminary characterization of hATX- $\beta$  alone.

## Results

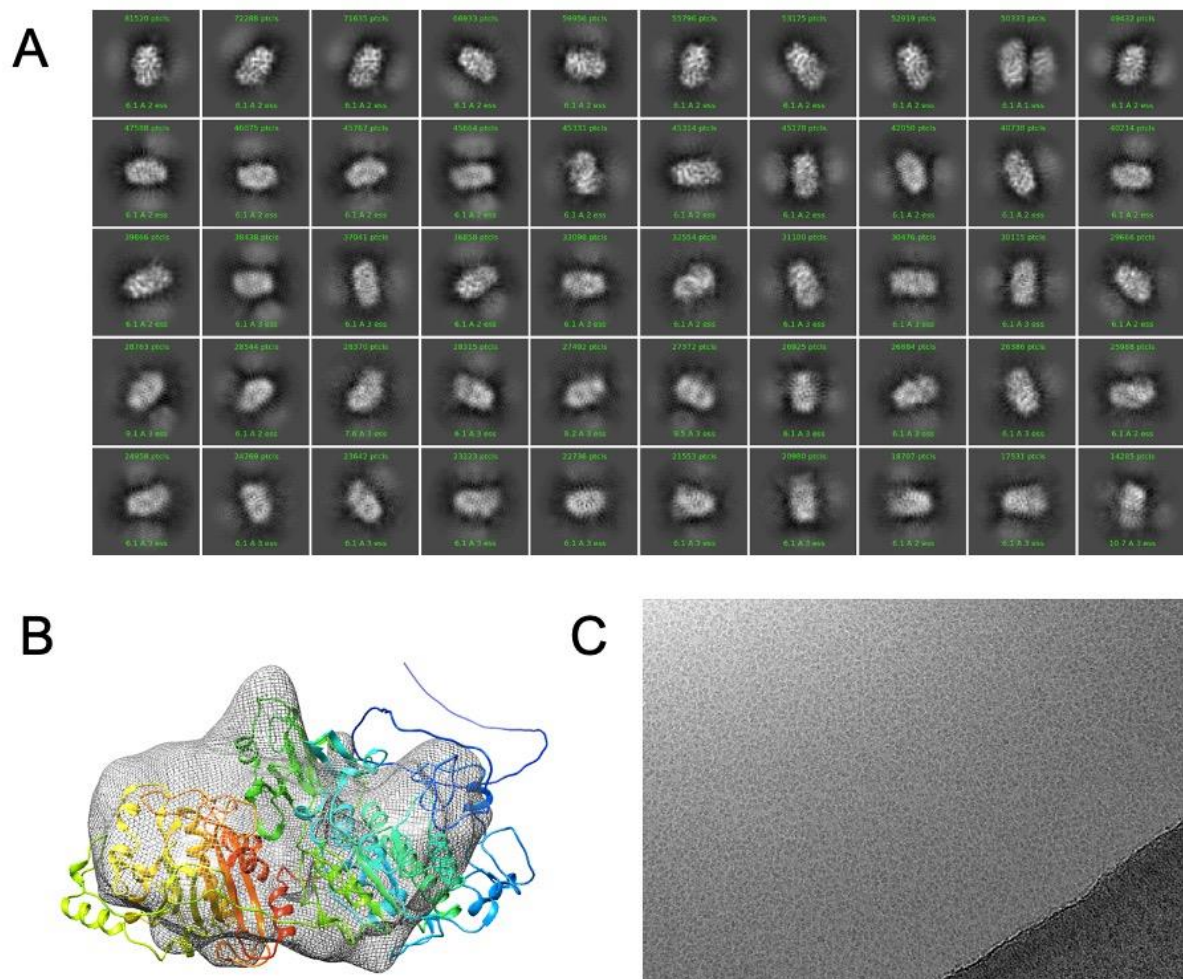


Figure 21: Cryo-EM results from Krios dataset analysis.

(a) 2D classification using CryoSPARC. 1,884,621 particles were extracted using the Topaz tool in CryoSPARC and separated into 50 classes. (b) *ab initio* model after 2D classification and particle selection. (c) Micrographs after CTF and motion correction.

After screening on a Galcios microscope, we selected the best grid(s) for a large data collection on CM01 at the ESRF. However, the flexibility of hATX- $\beta$  resulted in many 2D classes and despite many efforts, we were unable to produce a high quality *ab initio* structure from this Krios dataset (Figure 21A). The overall shape of ATX from the 2D classes can be distinguished, but *ab initio* processing of these data using different protocols always resulted in a map of very low quality, lacking of any recognizable 3D structures and some parts of the protein were even lacking (Figure 21B). Particles are clearly visible on the micrographs but the relatively small size of the protein (~100 kDa)

## Results

combined with particles orientation preferences makes ATX a difficult case to study by Cryo-EM. Perhaps further development of both data collection protocols and processing software will eventually allow a full 3D reconstruction of ATX structure by Cryo-EM in the future. It would be interesting to collect a tilted dataset to improve 2D classes and further processing. Another possibility would be to isolate a larger complex of ATX with a rigid partner, but this is challenging since ATX only weakly binds to physiological partners. Otherwise, it is maybe possible to express an ATX chimera with a fusion protein or to develop a nanobody targeting ATX in order to increase the particle size.

## 5 Discussion

### 5.1 Medicinal cannabis inhibition of autotaxin:

Medicinal cannabis has been approved as a therapeutic agent by local authorities in an increasing number of states all over the world. Even though great progress in the molecular basis of medicinal cannabis therapy has been achieved over the last decades, the pleiotropic effects have been insufficiently characterized to date. In this work, a potent *in vitro* inhibition of various cannabinoids, such as THC, on the catalysis of ATX with different substrates (LPC 16:0 and LPC 18:1) and isoforms has been established. Based on these investigations, it has been provided evidence that THC can potently modulate LPA signaling.

#### 5.1.1 Mechanisms by which medicinal cannabis might have effect on the ATX-LPA axis:

In most studies attempting to address the pharmacological aspects of medicinal cannabis, the administration has been performed via smoking. In this context, the first body fluid that encounters THC is the saliva. The mean concentration of THC in this oral fluid has been detected with up to 4167 ng/ml (13  $\mu$ M) in a radioimmunoassay (147,148). Interestingly, LPA is present in saliva (149) and ATX expression can be detected in salivary gland tissue (150), suggesting that ATX-LPA signaling may be reduced by THC *in vivo*. Furthermore, the deposition of THC in oral fluid reflects a similar time course in plasma after smoked cannabis administration (151). Serum concentrations of THC show a wide inter-individual difference, between 59-421 ng/ml after a 49.1 mg THC dose, which equals 190 nM to 1.3  $\mu$ M of THC (152). The observed mean THC peak in this study for a 69.4 mg THC dose was 190.4 ng/ml (SD=106.8), which is in the range of the apparent EC<sub>50</sub> determined during our studies.

## Discussion

95-97% of THC is bound to plasma proteins and data suggest that ATX might function as a carrier for THC in plasma. Determination of the binding affinity of ATX for THC was extensively tried with various techniques, such as isothermal titration calorimetry and nuclear magnetic resonance, however these approaches were unsuccessful due to the hydrophobic nature of the cannabinoid ligand.

Recently, the potential use of medicinal cannabis in tissue fibrosis has been proposed (153). In this regard, it is noteworthy to mention the role of ATX in idiopathic pulmonary fibrosis (IPF). Several inhibitors targeting ATX are under clinical investigations for their therapeutic use against IPF (154). However, the ISABELA study (clinical phase 3 investigation) of the most advanced molecule targeting ATX, Ziritaxestat (Glp1690) from Galapagos N.V, was discontinued due to risk-benefit concerns. It is tempting to speculate, that a full ATX inhibitor, which reduces LPA levels to almost zero, causes many systemic unwanted side effects, as the ATX-LPA signaling axis is pivotal under physiological conditions. In this context, our observation that THC is a partial inhibitor of ATX is of great interest, because this molecule is an FDA approved drug, which reduces LPA levels incompletely. Moreover, the fact that THC can cross the blood-brain-barrier makes it an attractive candidate to manipulate neuronal diseases, where the brain-specific isoform of ATX is involved. As mentioned before, THC and medicinal cannabis have been investigated in many pathologies such as pain and fibromyalgia (155,156).

Additionally, glaucoma is the leading cause of irreversible blindness worldwide (157). Glaucoma is characterized by elevated intraocular pressure (IOP) levels and medicinal cannabis is being used to treat this pathology, however the therapeutic mechanism is not completely known. Interestingly, in recent years it has been discovered that aqueous humor samples of patients suffering from primary open angle glaucoma have elevated levels of ATX, LPC and LPA (158). Moreover, pharmacological inhibition of ATX lowered IOP in rabbits (159). Our data may explain the molecular basis for the therapeutic effect of medical cannabis in glaucoma patients, as THC could feasibly reduce the formation of LPA by inhibiting the enzymatic activity of ATX.

My observation that ATX can be partially inhibited by endocannabinoids at lower LPC concentrations is also potentially interesting. While LPC concentration levels in plasma have been well characterised similar quantitative values in cerebrospinal fluids are lacking as far as I'm aware. Moreover, LPA is known to be both, a biosynthetic

## Discussion

precursor and a metabolic product of 2-AG (94) and can therefore be considered part of the endocannabinoidome (160). This opens new avenues for the study of possible interactions between the endocannabinoid system and the ATX-LPA signaling axis. The data also suggests that there might be a direct functional involvement of major components of medicinal cannabis therapy in ATX-LPA signaling.

### 5.1.2 Prospective experiments that could be done to investigate the effect of medicinal cannabis on the ATX-LPA axis:

As previously described, medicinal cannabis showed can effect various pathology without a clear answer on the mode of action. Ideally, to show if medicinal cannabis and particularly THC has an effect on whole blood LPA concentration, the easiest would be to compare the patient LPA levels before and after starting a treatment involving cannabinoids. It is possible to measure LPA levels by mass spectrometry and to compare these results (63). LPA levels are not very stable and depend on many factors. It would be important to exclude in such studies patients presenting metabolic disorders and those overweight (161). The blood drawing should also be done systematically in the morning. Another possibility, would be to perform a simple pharmacokinetics study by measuring LPA levels at different time points after administration of cannabinoids over hundred of minutes. This kind of study could also be performed in animals, but since the evaluation only requires small quantities of blood this type of analyses could be done on human during a clinical trial.

In conclusion, the results of the study warrants further research into the pleiotropic effects of medicinal cannabis in the context of ATX-LPA signaling, while also providing a promising starting point for such research lines. Furthermore, this work also provides a scaffold for the design of new inhibitors for further studies of the ATX-LPA signaling axis, and suggests a new way to intervene in ATX-LPA signaling-mediated pathologies with THC.

### 5.2 Development of cannabinoid-inspired autotaxin inhibitors:

The plant *Cannabis sativa* (Marijuana) has been used in medicinal context for millenniums and still attracts interest due to the biological activity of its metabolites, known as cannabinoids (a group of C<sub>21</sub> terpenophenolic compounds). The most abundant among them is  $\Delta^9$ -tetrahydrocannabinol (THC). Marijuana-derived drugs, and especially those derived from THC have been developed but their therapeutic/psychotropic balance was frequently criticized. In this study, we have used the general chemical structure of THC that showed an inhibition activity against ATX as a basis to screen chemical libraries sharing some structural similarities with THC, but derived from different secondary metabolites. Hence, following the screening of a chemical library of compounds bearing the benzopyranone moiety and the optimization of these selected hits, we identified the compound MEY-003, which is derived from a hybrid system bearing both chromone and indole scaffolds as a potent inhibitor of ATX.

#### 5.2.1 Structure-activity relationship of cannabinoid-inspired inhibitors:

We discussed previously the possibility of synthesizing different inhibitors with similar scaffold but with a different substitution on the indole. We also investigated the possibility of modifications directly on the chromone part of the molecule but this led to inactive or very weak inhibitors, especially when the hydroxy were methylated. It seems that having two hydrogen donors is extremely important for the activity of the molecule and then this part cannot be easily modified. We also tried to skip the cyclisation part leading to uncyclized compounds : almost no inhibitory activity was detected for these derivatives. It seems that an intact chromone-indole scaffold is needed for satisfactory autotaxin inhibition. Concerning the indole substitution, it was quite surprising to see that more lipophilic substitution were not necessarily leading to higher inhibition. In particular for the benzyl derivative MEY-002 and the cyclohexyl derivative MEY-007 were not improving the activity. Concerning MEY-008, the dimethyloctyl substituted derivative, the drop in activity was even more surprising since this substitution was improving the activity of CBD (CBD-DMH derivative). Finally, it is





## Discussion

### *Scheme 6: Synthesized and prospective inhibitors*

Synthesized inhibitors are drawn before the dash line and prospective inhibitors that could be synthesized are represented after the dash line.

As shown on scheme 6 more than 6 inhibitors sharing a similar scaffold have been synthesized and displayed various inhibition to ATX as summarized in table 3. The easiest modification is to replace the indole substituent by another, leading to many possibilities. We know that changing the orientation of the indole is not favorable to the inhibition: this can be explained by the discrete binding of the indole in the hydrophobic pocket. The ATX hydrophobic pocket is also not able to accommodate any indole substituent, in particular if they are voluminous. It seems quite easy to try an inhibitor bearing bigger indole substituents such as a heptane or an octane hydrophobic chain. Another possibility might be smaller heterocycles such as thiophene or furane. A benzyl substituent did not result in higher inhibition, in this case it might be interesting in this case to increase the linker by one carbon in order to improve the flexibility and final position in the hydrophobic pocket. Benzyl substitution is also possible by adding alkyl chains or other substituents on the aromatic ring. Flavone and indole derivatives are widely found natural phytochemicals and, to the best of our knowledge, this study is the first to report a highly effective inhibitor of ATX derived from two entities frequently found in natural products. Chromones and indoles are two prominent scaffolds largely investigated for their therapeutic potential and the management of major chronic diseases, including neurodegenerative diseases, cancer, diabetes, infection and inflammation (162,163). In latter contexts, many clinically approved drugs contain one of these two entities (162). Therefore, the combination of a chromone and an indole, two druggable scaffolds, in the same entity may offer diverse advantages for the development of MEY-003 as a drug candidate that targets ATX-related diseases.

From an organic chemist point of view, synthesis of such inhibitor is doable but some part of the protocol could be improved or modified. As mentioned earlier in scheme 1, the first step is a condensation of an indole derivative and acetophenone. This reaction is easily performed with the addition of sodium hydride or under basic conditions. The next step consists of an oxidation-cyclisation, leading to more impurities and lower yield.

## Discussion

This part of the reaction could be improved by switching to other catalyst like palladium or by performing a one step condensation and cyclisation. The main advantage of Iodide being a green catalyst leading to less pollution. Concerning the last step, the demethylation, it is difficult to find an alternative to BBr<sub>3</sub>. Other Lewis' acid could be tried but they will likely lead to the same results, with many impurities in the final product. Another direction for the synthesis development would be to switch to different protector for the hydroxy.

*Table 3: Inhibition activity of hits and the lead on hATX-β and hATX-γ.*

Compound	IC <sub>50</sub> hATX-β (μM)		IC <sub>50</sub> hATX-γ (nM)	
	LPC18:1	LPC16:0	LPC18:1	LPC16:0
MEY-001	1.40 (0.9-1.8)	1.20 (0.31-1.970)	3.8(2.2-9.3)	2.4 (1.9-2.3)
MEY-002	0.82 (0.7-0.96)	0.88 (0.6-1.08)	1.25 (0.99-1.65)	0.81 (0.61-1)
MEY-003	0.46 (0.35-0.61)	0.384 (0.36-0.4)	1.099 (0.925-1.317)	0.38 (0.3-4.6)
MEY-005	> 5	> 5	> 5	> 5
MEY-007	< 20%*	< 20%*	-	-
MEY-008	NA**	NA**	-	-

\* at 1 micromolar concentration; \*\* Not Active. Value shows 95% CI (profile likelihood)

### 5.2.3 Insights into ATX-γ structure:

hATX-β and hATX-γ are essentially identical. The structure of hATX-γ in complex with its natural end-product LPA18:1 and MEY-003 have been determined at a resolution of 2.4 and 2.3 Å, respectively. The results highlight that hATX-γ shares a very similar structural organization with hATX-β, as deduced from superposition with the PDB: 4ZG7 (64), resulting in an RMSD of 0.56 Å for 775 aligned C<sub>α</sub> atoms. The deglycosylated mutant used for crystallization did not lead to a significant activity

## Discussion

difference when compared to wild-type hATX- $\gamma$  (figure 20). One major difference between the brain-specific hATX- $\gamma$  and hATX- $\beta$  is the presence of a 25 aa insertion at position 593 (EAETRKFRGSRNENKENINGNFEPRK), leading to a flexible loop at the surface of hATX- $\gamma$ . The function of this modification is unknown and specific to the brain isoform. Up to now, there is no evidence that proteolytic cleavage of this loop is related to neurological, psychiatric and neoplastic diseases (19,20,164). In this study, we also observed that hATX- $\gamma$  can be cleaved (Supplementary Material 6c), resulting in a fragment of ~34 kDa that corresponds to a C-terminal region cleavage at this insertion. Further experiments would be needed to understand which enzyme is responsible for cleaving hATX- $\gamma$  and if this is biologically relevant.

Conclusion:

## 6 Conclusion:

We recently reported that THC is a potent ATX inhibitor (116). Due to its psychotropic effect, legislation, and non-acceptance by society, this marijuana-derived compound is unlikely to be used in clinical settings for the management of ATX-related disorders. Nevertheless, more research is also needed to assess if cannabinoids can significantly inhibit the ATX-LPA axis *in vivo*.

Therefore, THC has been used as a basis to explore diverse molecules with partial chemical and structural similarity, particularly those sharing a benzopyrane moiety such as naturally occurring chromones and flavones. The process of screening, hit identification and optimization allowed us to identify MEY-003 as a potent and safe inhibitor of ATX. The inhibition profile of MEY-003 was rationalized through advanced structural biology drug discovery studies. MEY-003 has a unique structure compared to previously published ATX inhibitors that could potentially lead to the development of new drugs targeting the ATX-LPA axis with fewer side effects.

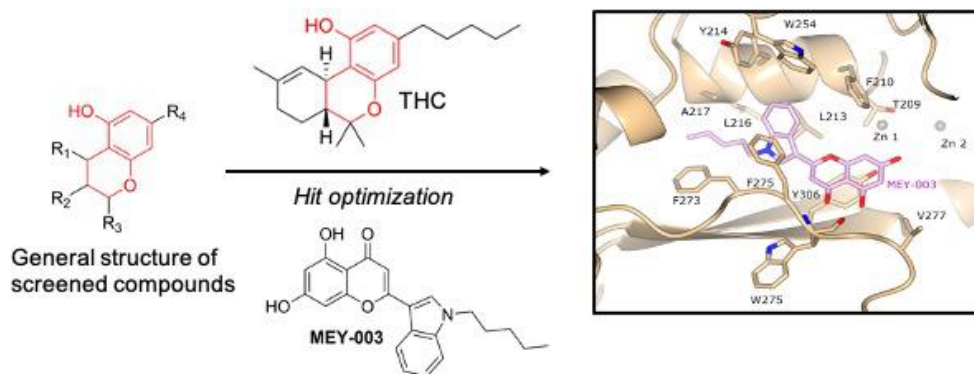


Figure 22: Discovery of cannabinoid-inspired ATX inhibitors

## 7 Future aim of research

Many ATX inhibitors have been developed over the years but not one has achieved regulatory approval to date.. As mentioned before, the inhibitors developed by Galapagos for IPF failed in Phase 2/3 due to their potential toxicity. This is likely due to the numerous effects of ATX on the body and the necessity to target autotaxin catalysis at the site of disease rather than system wide. The pharmacokinetics of the inhibitor might also be an issue due to the high turnover of ATX in the blood stream (3,165). Indeed, inhibitors might need to be taken several times a day to maintain ATX inhibition and subsequent LPA reduction. Our cannabinoid inspired inhibitors might be interesting from this point of view, since their lipidic structure allows potential storage in fatty tissues and maintenance of a limited inhibition following inhibitor intake (166). In this setting, we propose to continue the work on new inhibitors development from the initial lead, MEY003, and to test them on animal models. It is also of great interest to measure LPA levels of patients treated with medicinal cannabis and asses if the inhibition of ATX is significant in vivo, and remains over a long period. Since some of the therapeutic effects of THC might come from the inhibition of ATX, more experiments are needed to investigate this option. For example, it would be interesting to monitor the number of crises of an epilepsy animal model presenting an inducible ATX knock out, and verifying if the number of crises is lower when the ATX is knocked out.

A pharmacokinetics experiment could be done on animals with the developed inhibitor MEY-003. LPA and inhibitor concentration could be monitored upon injection of different MEY-003 doses. This kind of experiment has been done on different ATX inhibitors successfully, such as PF8380 (63). In the meantime, it is also interesting to test the potential autotaxin inhibition in vivo with blood from healthy donors using the same choline release assay as previously described in the materials and methods section for initial investigations. Inflammation, IPF and epilepsy animal model could be used to provide potential therapeutic applications of this new inhibitor family.

Concerning the ATX cryo-EM structure, it seems challenging to solve it at the moment but improvement in both data collection protocols and processing softwares might lead to new possibilities in this rapidly growing field. It might also be possible to solve a

## Future aim of research

complex structure of ATX and a binding partner in order to stabilize the domains and increase the particle size, leading to easier processing. Cryo-EM structures of ATX could allow a better understanding of the catalytic process. Indeed, if the ATX structure is solved using cryo-EM, the sample preparation could include different states of the protein by freezing the sample grids at different time points or in different conditions before and after LPC supplementation. ATX could be trapped in different conformations and unveil the exact molecular processes behind LPC catalysis. Co-structures with large binding partners such as integrins might allow new insight into ATX cell surface interaction and LPA release close to LPA receptors (23,167–169). The molecular basis of ATX-Integrins interaction would be of interest since little is known for the moment, apart from the fact that integrin signalling cross-talks with many other signalling pathways' (170,171).

From an X-ray crystallography perspective, recent developments of software and data acquisition allowed SSX measurements on low symmetry protein crystals at the ESRF (129,172,173). We could acquire multiple datasets at room temperature and eventually perform time resolved experiments to understand the exact molecular basis behind substrate binding and processing. Since ATX is crystalizing in the P1 space group, this is also challenging from a methodical point of view.

## References:

### 8 References:

1. Ninou I, Magkrioti C, Aidinis V. Autotaxin in Pathophysiology and Pulmonary Fibrosis. *Front Med*. 2018 Jun 13;5:180.
2. Castagna D, Budd DC, Macdonald SJF, Jamieson C, Watson AJB. Development of Autotaxin Inhibitors: An Overview of the Patent and Primary Literature: Miniperspective. *Journal of Medicinal Chemistry*. 2016 Jun 23;59(12):5604–21.
3. Ninou I, Magkrioti C, Aidinis V. Autotaxin in Pathophysiology and Pulmonary Fibrosis. *Frontiers in Medicine*. 2018 Jun 13;5.
4. Giganti A, Rodriguez M, Fould B, Moulharat N, Cogé F, Chomarat P, et al. Murine and Human Autotaxin  $\alpha$ ,  $\beta$ , and  $\gamma$  Isoforms. *Journal of Biological Chemistry*. 2008 Mar;283(12):7776–89.
5. Hashimoto T, Okudaira S, Igarashi K, Hama K, Yatomi Y, Aoki J. Identification and biochemical characterization of a novel autotaxin isoform, ATX , with a four-amino acid deletion. *Journal of Biochemistry*. 2012 Jan 1;151(1):89–97.
6. RCSB Protein Data Bank - RCSB PDB [Internet]. [cited 2017 Dec 9]. Available from: <http://www.rcsb.org/pdb/home/home.do>
7. Moolenaar WH, Perrakis A. Insights into autotaxin: how to produce and present a lipid mediator. *Nat Rev Mol Cell Biol*. 2011 Oct;12(10):674–9.
8. Gotoh M, Fujiwara Y, Yue J, Liu J, Lee S, Fells J, et al. Controlling cancer through the autotaxin–lysophosphatidic acid receptor axis. *Biochemical Society Transactions*. 2012 Feb 1;40(1):31–6.
9. Lee D, Suh DS, Lee SC, Tigyi GJ, Kim JH. Role of autotaxin in cancer stem cells. *Cancer and Metastasis Reviews*. 2018 Sep;37(2–3):509–18.
10. Umezu-Goto M, Kishi Y, Taira A, Hama K, Dohmae N, Takio K, et al. Autotaxin has lysophospholipase D activity leading to tumor cell growth and motility by lysophosphatidic acid production. *The Journal of Cell Biology*. 2002 Jul 22;158(2):227–33.
11. Valdés-Rives SA, González-Arenas A. Autotaxin-Lysophosphatidic Acid: From Inflammation to Cancer Development. *Mediators of Inflammation*. 2017;2017:1–15.
12. Nakanaga K, Hama K, Aoki J. Autotaxin--an LPA producing enzyme with diverse functions. *Journal of Biochemistry*. 2010 Jul 1;148(1):13–24.
13. Benesch MGK, Ko YM, McMullen TPW, Brindley DN. Autotaxin in the crosshairs: Taking aim at cancer and other inflammatory conditions. *FEBS Letters*. 2014 Aug 19;588(16):2712–27.

## References:

14. Wu JM, Xu Y, Skill NJ, Sheng H, Zhao Z, Yu M, et al. Autotaxin expression and its connection with the TNF- $\alpha$ -NF- $\kappa$ B axis in human hepatocellular carcinoma. 2010;
15. Willier S, Butt E, Grunewald TGP. Lysophosphatidic acid (LPA) signalling in cell migration and cancer invasion: A focussed review and analysis of LPA receptor gene expression on the basis of more than 1700 cancer microarrays: Role of LPA in cell migration and cancer metastasis. *Biol Cell*. 2013 Aug;105(8):317–33.
16. Achón Buil B, Rust R. Preserving stroke penumbra by targeting lipid signalling. *Journal of Cerebral Blood Flow & Metabolism*. 2023 Jan;43(1):167–9.
17. Dohi T, Miyauchi K, Ohkawa R, Nakamura K, Kishimoto T, Miyazaki T, et al. Increased circulating plasma lysophosphatidic acid in patients with acute coronary syndrome. *Clinica Chimica Acta*. 2012 Jan 18;413(1):207–12.
18. Van Meeteren LA, Ruurs P, Stortelers C, Bouwman P, Van Rooijen MA, Pradère JP, et al. Autotaxin, a Secreted Lysophospholipase D, Is Essential for Blood Vessel Formation during Development. *Molecular and Cellular Biology*. 2006 Jul 1;26(13):5015–22.
19. Herr DR, Chew WS, Satish RL, Ong WY. Pleiotropic Roles of Autotaxin in the Nervous System Present Opportunities for the Development of Novel Therapeutics for Neurological Diseases. *Molecular Neurobiology*. 2020 Jan 1;57(1):372–92.
20. for the Alzheimer's Disease Neuroimaging Initiative, McLimans KE, Willette AA. Autotaxin is Related to Metabolic Dysfunction and Predicts Alzheimer's Disease Outcomes. *JAD*. 2017 Jan 12;56(1):403–13.
21. Tigyi G. Aiming drug discovery at lysophosphatidic acid targets: Novel LPA targets. *British Journal of Pharmacology*. 2010 Sep;161(2):241–70.
22. Taniguchi R, Inoue A, Sayama M, Uwamizu A, Yamashita K, Hirata K, et al. Structural insights into ligand recognition by the lysophosphatidic acid receptor LPA6. *Nature*. 2017 Aug;548(7667):356–60.
23. Salgado-Polo F, Borza R, Matsoukas MT, Marsais F, Jagerschmidt C, Waeckel L, et al. Autotaxin facilitates selective LPA receptor signaling. *Cell Chemical Biology*. 2023 Jan;30(1):69-84.e14.
24. Hausmann J, Kamtekar S, Christodoulou E, Day JE, Wu T, Fulkerson Z, et al. Structural basis of substrate discrimination and integrin binding by autotaxin. *Nature Structural & Molecular Biology*. 2011 Feb;18(2):198–204.
25. Day JE, Hall T, Pegg LE, Benson TE, Hausmann J, Kamtekar S. Crystallization and preliminary X-ray diffraction analysis of rat autotaxin. *Acta Crystallographica Section F Structural Biology and Crystallization Communications*. 2010 Sep 1;66(9):1127–9.



## References:

26. Jankowski M. Autotaxin: Its Role in Biology of Melanoma Cells and as a Pharmacological Target. *Enzyme Research*. 2011 Mar 8;2011:1–5.
27. Jansen S, Callewaert N, Dewerte I, Andries M, Ceulemans H, Bollen M. An Essential Oligomannosidic Glycan Chain in the Catalytic Domain of Autotaxin, a Secreted Lysophospholipase-D. *Journal of Biological Chemistry*. 2007 Apr;282(15):11084–91.
28. Zalatan JG, Fenn TD, Brunger AT, Herschlag D. Structural and Functional Comparisons of Nucleotide Pyrophosphatase/Phosphodiesterase and Alkaline Phosphatase: Implications for Mechanism and Evolution. *Biochemistry*. 2006 Aug 1;45(32):9788–803.
29. Nishimasu H, Okudaira S, Hama K, Mihara E, Dohmae N, Inoue A, et al. Crystal structure of autotaxin and insight into GPCR activation by lipid mediators. *Nat Struct Mol Biol*. 2011 Feb;18(2):205–12.
30. Keune WJ, Hausmann J, Bolier R, Tolenaars D, Kremer A, Heidebrecht T, et al. Steroid binding to Autotaxin links bile salts and lysophosphatidic acid signalling. *Nat Commun*. 2016;7:11248–11248.
31. Perrakis A, Moolenaar WH. Autotaxin: structure-function and signaling. *Journal of Lipid Research*. 2014 Jun;55(6):1010–8.
32. Stracke ML, Krutzsch HC, Unsworth EJ, Arestad A, Cioce V, Schiffmann E, et al. Identification, purification, and partial sequence analysis of autotaxin, a novel motility-stimulating protein. *Journal of Biological Chemistry*. 1992 Feb;267(4):2524–9.
33. Brindley DN, Lin FT, Tigyi GJ. Role of the autotaxin–lysophosphatidate axis in cancer resistance to chemotherapy and radiotherapy. *Biochimica et Biophysica Acta (BBA) - Molecular and Cell Biology of Lipids*. 2013 Jan;1831(1):74–85.
34. Yang Y, Mou L jun, Liu N, Tsao MS. Autotaxin Expression in Non–Small-Cell Lung Cancer. *Am J Respir Cell Mol Biol*. 1999 Aug 1;21(2):216–22.
35. Umemura K, Yamashita N, Yu X, Arima K, Asada T, Makifuchi T, et al. Autotaxin expression is enhanced in frontal cortex of Alzheimer-type dementia patients. *Neuroscience Letters*. 2006 May;400(1–2):97–100.
36. Kishi Y, Okudaira S, Tanaka M, Hama K, Shida D, Kitayama J, et al. Autotaxin Is Overexpressed in Glioblastoma Multiforme and Contributes to Cell Motility of Glioblastoma by Converting Lysophosphatidylcholine TO Lysophosphatidic Acid. *Journal of Biological Chemistry*. 2006 Jun;281(25):17492–500.
37. Hoelzinger DB, Nakada M, Demuth T, Rosensteel T, Reavie LB, Berens ME. Autotaxin: a secreted autocrine/paracrine factor that promotes glioma invasion. *J Neurooncol*. 2008 Feb;86(3):297–309.

## References:

38. Magkrioti C, Galaris A, Kanellopoulou P, Stylianaki EA, Kaffe E, Aidinis V. Autotaxin and chronic inflammatory diseases. *Journal of Autoimmunity*. 2019 Nov;104:102327.
39. Kazlauskas A. Lysophosphatidic acid contributes to angiogenic homeostasis. *Experimental Cell Research*. 2015 May;333(2):166–70.
40. Im E, Motiejunaite R, Aranda J, Park EY, Federico L, Kim T im, et al. Phospholipase C $\beta$  Activation Drives Increased Production of Autotaxin in Endothelial Cells and Lysophosphatidic Acid-Dependent Regression $\square$ . *MOL CELL BIOL*. 2010;30.
41. Nam SW, Clair T, Campo CK, Lee HY, Liotta LA, Stracke ML. Autotaxin (ATX), a potent tumor motogen, augments invasive and metastatic potential of ras-transformed cells. *Oncogene*. 2000 Jan 13;19(2):241–7.
42. Knowlden S, Georas SN. The Autotaxin–LPA Axis Emerges as a Novel Regulator of Lymphocyte Homing and Inflammation. *The Journal of Immunology*. 2014 Feb 1;192(3):851–7.
43. Reeves VL, Trybula JS, Wills RC, Goodpaster BH, Dubé JJ, Kienesberger PC, et al. Serum Autotaxin/ENPP2 correlates with insulin resistance in older humans with obesity: Serum Autotaxin and Insulin Resistance. *Obesity*. 2015 Dec;23(12):2371–6.
44. Rancoule C, Dusaulcy R, Tréguer K, Grès S, Attané C, Saulnier-Blache JS. Involvement of autotaxin/lysophosphatidic acid signaling in obesity and impaired glucose homeostasis. *Biochimie*. 2014 Jan;96:140–3.
45. Zhao Y, Hasse S, Zhao C, Bourgoin SG. Targeting the autotaxin – Lysophosphatidic acid receptor axis in cardiovascular diseases. *Biochemical Pharmacology*. 2019 Jun;164:74–81.
46. Retzer M, Essler M. Lysophosphatidic acid-induced platelet shape change proceeds via Rho/Rho kinase-mediated myosin light-chain and moesin phosphorylation. *Cellular Signalling*. 2000 Oct;12(9–10):645–8.
47. Lin CI, Chen CN, Lin PW, Chang KJ, Hsieh FJ, Lee H. Lysophosphatidic acid regulates inflammation-related genes in human endothelial cells through LPA1 and LPA3. *Biochemical and Biophysical Research Communications*. 2007 Nov;363(4):1001–8.
48. Hao F, Tan M, Wu DD, Xu X, Cui MZ. LPA induces IL-6 secretion from aortic smooth muscle cells via an LPA1-regulated, PKC-dependent, and p38 $\gamma$ -mediated pathway. 2010;298.
49. Fueller M, Wang DA, Tigyi G, Siess W. Activation of human monocytic cells by lysophosphatidic acid and sphingosine-1-phosphate. *Cellular Signalling*. 2003 Apr;15(4):367–75.

## References:

50. Chang CL, Hsu HY, Lin HY, Chiang W, Lee H. Lysophosphatidic acid-induced oxidized low-density lipoprotein uptake is class A scavenger receptor-dependent in macrophages. *Prostaglandins & Other Lipid Mediators*. 2008 Dec;87(1–4):20–5.
51. Zhou Z, Subramanian P, Sevilimis G, Globke B, Soehnlein O, Karshovska E, et al. Lipoprotein-Derived Lysophosphatidic Acid Promotes Atherosclerosis by Releasing CXCL1 from the Endothelium. *Cell Metabolism*. 2011 May;13(5):592–600.
52. Isshiki T, Shimizu H, Sakamoto S, Yamasaki A, Miyoshi S, Nakamura Y, et al. Serum autotaxin levels in chronic disease and acute exacerbation of fibrosing interstitial lung disease. *ERJ Open Res*. 2022 Apr;8(2):00683–2021.
53. Funke M, Zhao Z, Xu Y, Chun J, Tager AM. The Lysophosphatidic Acid Receptor LPA<sub>1</sub> Promotes Epithelial Cell Apoptosis after Lung Injury. *Am J Respir Cell Mol Biol*. 2012 Mar;46(3):355–64.
54. Decato BE, Leeming DJ, Sand JMB, Fischer A, Du S, Palmer SM, et al. LPA1 antagonist BMS-986020 changes collagen dynamics and exerts antifibrotic effects in vitro and in patients with idiopathic pulmonary fibrosis. *Respir Res*. 2022 Dec;23(1):61.
55. Oikonomou N, Mouratis MA, Tzouveleki A, Kaffe E, Valavanis C, Vilaras G, et al. Pulmonary Autotaxin Expression Contributes to the Pathogenesis of Pulmonary Fibrosis. *Am J Respir Cell Mol Biol*. 2012 Nov;47(5):566–74.
56. Fotopoulou S, Oikonomou N, Grigorieva E, Nikitopoulou I, Pappas T, Thanassopoulou A, et al. ATX expression and LPA signalling are vital for the development of the nervous system. *Developmental Biology*. 2010 Mar;339(2):451–64.
57. Savaskan NE, Rocha L, Kotter MR, Baer A, Lubec G, van Meeteren LA, et al. Autotaxin (NPP-2) in the brain: cell type-specific expression and regulation during development and after neurotrauma. *Cell Mol Life Sci*. 2007 Jan;64(2):230–43.
58. Kuwajima K, Sumitani M, Kurano M, Kano K, Nishikawa M, Uranbileg B, et al. Lysophosphatidic acid is associated with neuropathic pain intensity in humans: An exploratory study. Ikeda K, editor. *PLoS ONE*. 2018 Nov 8;13(11):e0207310.
59. Inoue M, Rashid MH, Fujita R, Contos JJA, Chun J, Ueda H. Initiation of neuropathic pain requires lysophosphatidic acid receptor signaling. *Nat Med*. 2004 Jul;10(7):712–8.
60. Ramesh S, Govindarajulu M, Suppiramaniam V, Moore T, Dhanasekaran M. Autotaxin–Lysophosphatidic Acid Signaling in Alzheimer’s Disease. *IJMS*. 2018 Jun 21;19(7):1827.
61. Clark JM, Salgado-Polo F, Macdonald SJF, Barrett TN, Perrakis A, Jamieson C. Structure-Based Design of a Novel Class of Autotaxin Inhibitors Based on Endogenous Allosteric Modulators. *J Med Chem*. 2022 Apr 28;65(8):6338–51.

## References:

62. Salgado-Polo F, Perrakis A. The Structural Binding Mode of the Four Autotaxin Inhibitor Types that Differentially Affect Catalytic and Non-Catalytic Functions. *Cancers*. 2019 Oct 16;11(10):1577.
63. Gierse J, Thorarensen A, Beltey K, Bradshaw-Pierce E, Cortes-Burgos L, Hall T, et al. A Novel Autotaxin Inhibitor Reduces Lysophosphatidic Acid Levels in Plasma and the Site of Inflammation. *J Pharmacol Exp Ther*. 2010 Jul;334(1):310–7.
64. Stein AJ, Bain G, Prodanovich P, Santini AM, Darlington J, Stelzer NMP, et al. Structural Basis for Inhibition of Human Autotaxin by Four Potent Compounds with Distinct Modes of Binding. *Molecular Pharmacology*. 2015 Dec;88(6):982–92.
65. Desroy N, Housseman C, Bock X, Joncour A, Bienvenu N, Cherel L, et al. Discovery of 2-[[2-Ethyl-6-[4-[2-(3-hydroxyazetidin-1-yl)-2-oxo-ethyl]piperazin-1-yl]-8-methyl-imidazo[1,2-a]pyridin-3-yl]-methyl-amino]-4-(4-fluorophenyl)thiazole-5-carbonitrile (GLPG1690), a First-in-Class Autotaxin Inhibitor Undergoing Clinical Evaluation for the Treatment of Idiopathic Pulmonary Fibrosis. :48.
66. Yanagida K, Kurikawa Y, Shimizu T, Ishii S. Current progress in non-Edg family LPA receptor research. *Biochimica et Biophysica Acta (BBA) - Molecular and Cell Biology of Lipids*. 2013 Jan;1831(1):33–41.
67. Yung YC, Stoddard NC, Chun J. LPA receptor signaling: pharmacology, physiology, and pathophysiology. *Journal of Lipid Research*. 2014 Jul;55(7):1192–214.
68. An S, Bleu T, Hallmark OG, Goetzl EJ. Characterization of a Novel Subtype of Human G Protein-coupled Receptor for Lysophosphatidic Acid. *Journal of Biological Chemistry*. 1998 Apr;273(14):7906–10.
69. Plastira I, Joshi L, Bernhart E, Schoene J, Specker E, Nazare M, et al. Small-Molecule Lysophosphatidic Acid Receptor 5 (LPA5) Antagonists: Versatile Pharmacological Tools to Regulate Inflammatory Signaling in BV-2 Microglia Cells. *Front Cell Neurosci*. 2019 Nov 29;13:531.
70. Suzuki N, Hajicek N, Kozasa T. Regulation and Physiological Functions of G12/13-Mediated Signaling Pathways. *Neurosignals*. 2009;17(1):55–70.
71. Umemori H, Inoue T, Kume S, Sekiyama N, Nagao M, Itoh H, et al. Activation of the G Protein Gq/11 Through Tyrosine Phosphorylation of the  $\alpha$  Subunit. *Science*. 1997 Jun 20;276(5320):1878–81.
72. Jiang M, Bajpayee NS. Molecular Mechanisms of Go Signaling. *Neurosignals*. 2009;17(1):23–41.
73. Jeong Y, Chung KY. Structural and Functional Implication of Natural Variants of Gas. *IJMS*. 2023 Feb 17;24(4):4064.

## References:

74. Chrencik JE, Roth CB, Terakado M, Kurata H, Omi R, Kihara Y, et al. Crystal Structure of Antagonist Bound Human Lysophosphatidic Acid Receptor 1. *Cell*. 2015 Jun;161(7):1633–43.
75. Medical cannabis | Definition, Types, Uses, & Facts | Britannica [Internet]. [cited 2023 Jan 26]. Available from: <https://www.britannica.com/science/medical-cannabis>
76. Li HL. An archaeological and historical account of cannabis in China. *Econ Bot*. 1973 Oct;28(4):437–48.
77. O'Shaughnessy WB. On the Preparations of the Indian Hemp, or Gunjah. *Prov Med J Retrospect Med Sci*. 1843 Feb 4;5(123):363–9.
78. United Nations Treaty Collection [Internet]. [cited 2023 Jan 26]. Available from: [https://treaties.un.org/pages/ViewDetailsIV.aspx?src=TREATY&mtdsg\\_no=VI-2&chapter=6&Temp=mtdsg4&clang=\\_fr](https://treaties.un.org/pages/ViewDetailsIV.aspx?src=TREATY&mtdsg_no=VI-2&chapter=6&Temp=mtdsg4&clang=_fr)
79. United Nations : Office on Drugs and Crime [Internet]. [cited 2023 Jan 26]. Single Convention on Narcotic Drugs. Available from: <http://www.unodc.org/unodc/en/treaties/single-convention.html>
80. Gaoni Y, Mechoulam R. ACS Publications. American Chemical Society; 2002 [cited 2023 Jan 26]. Isolation, Structure, and Partial Synthesis of an Active Constituent of Hashish. Available from: <https://pubs.acs.org/doi/pdf/10.1021/ja01062a046>
81. Devane WA, Hanuš L, Breuer A, Pertwee RG, Stevenson LA, Griffin G, et al. Isolation and Structure of a Brain Constituent That Binds to the Cannabinoid Receptor. *Science*. 1992 Dec 18;258(5090):1946–9.
82. Mechoulam R, Ben-Shabat S, Hanus L, Ligumsky M, Kaminski NE, Schatz AR, et al. Identification of an endogenous 2-monoglyceride, present in canine gut, that binds to cannabinoid receptors. *Biochemical Pharmacology*. 1995 Jun;50(1):83–90.
83. Dossier thématique - Cadre et mise en oeuvre de l'expérimentati - ANSM [Internet]. [cited 2023 Feb 2]. Available from: <https://ansm.sante.fr/dossiers-thematiques/cannabis-a-usage-medical/cadre-et-mise-en-oeuvre-de-lexperimentation-du-cannabis-medical>
84. Crocq MA. History of cannabis and the endocannabinoid system. *Dialogues in Clinical Neuroscience*. 2020 Sep 30;22(3):223–8.
85. Mechoulam R, Hanuš L. A historical overview of chemical research on cannabinoids. *Chemistry and Physics of Lipids*. 2000 Nov;108(1–2):1–13.
86. Devane W, Hanus L, Breuer A, Pertwee R, Stevenson L, Griffin G, et al. Isolation and structure of a brain constituent that binds to the cannabinoid receptor. *Science*. 1992 Dec 18;258(5090):1946–9.

## References:

87. Sugiura T, Kondo S, Sukagawa A, Nakane S, Shinoda A, Itoh K, et al. 2-Arachidonoylglycerol: A Possible Endogenous Cannabinoid Receptor Ligand in Brain. *Biochemical and Biophysical Research Communications*. 1995 Oct;215(1):89–97.
88. Di Marzo V, Fontana A. Anandamide, an endogenous cannabinomimetic eicosanoid: 'Killing two birds with one stone.' *Prostaglandins, Leukotrienes and Essential Fatty Acids*. 1995 Jul;53(1):1–11.
89. Okamoto Y, Morishita J, Tsuboi K, Tonai T, Ueda N. Molecular Characterization of a Phospholipase D Generating Anandamide and Its Congeners. *Journal of Biological Chemistry*. 2004 Feb;279(7):5298–305.
90. Cravatt BF, Giang DK, Mayfield SP, Boger DL, Lerner RA, Gilula NB. Molecular characterization of an enzyme that degrades neuromodulatory fatty-acid amides. *Nature*. 1996 Nov;384(6604):83–7.
91. Bisogno T, Howell F, Williams G, Minassi A, Cascio MG, Ligresti A, et al. Cloning of the first sn1-DAG lipases points to the spatial and temporal regulation of endocannabinoid signaling in the brain. *Journal of Cell Biology*. 2003 Nov 10;163(3):463–8.
92. Dinh TP, Carpenter D, Leslie FM, Freund TF, Katona I, Sensi SL, et al. Brain monoglyceride lipase participating in endocannabinoid inactivation. *Proceedings of the National Academy of Sciences*. 2002 Aug 6;99(16):10819–24.
93. Cristino L, Bisogno T, Di Marzo V. Cannabinoids and the expanded endocannabinoid system in neurological disorders. *Nat Rev Neurol*. 2020 Jan;16(1):9–29.
94. Nakane S, Oka S, Arai S, Waku K, Ishima Y, Tokumura A, et al. 2-Arachidonoyl-sn-glycero-3-phosphate, an arachidonic acid-containing lysophosphatidic acid: occurrence and rapid enzymatic conversion to 2-arachidonoyl-sn-glycerol, a cannabinoid receptor ligand, in rat brain. *Archives of Biochemistry and Biophysics*. 2002 Jun;402(1):51–8.
95. Aaltonen N, Lehtonen M, Varonen K, Gotteris GA, Laitinen JT. Lipid phosphate phosphatase inhibitors locally amplify lysophosphatidic acid LPA1 receptor signalling in rat brain cryosections without affecting global LPA degradation. *BMC Pharmacol*. 2012 Dec;12(1):7.
96. Elphick MR, Egertova M. The neurobiology and evolution of cannabinoid signalling. *Phil Trans R Soc Lond B*. 2001 Mar 29;356(1407):381–408.
97. Ameri A. The effects of cannabinoids on the brain. *Progress in Neurobiology*. 1999 Jul;58(4):315–48.
98. Hua T, Vemuri K, Pu M, Qu L, Han GW, Wu Y, et al. Crystal Structure of the Human Cannabinoid Receptor CB1. *Cell*. 2016 Oct;167(3):750-762.e14.

## References:

99. Shao Z, Yin J, Chapman K, Grzemska M, Clark L, Wang J, et al. High-resolution crystal structure of the human CB1 cannabinoid receptor. *Nature*. 2016 Dec;540(7634):602–6.
100. Li X, Hua T, Vemuri K, Ho JH, Wu Y, Wu L, et al. Crystal Structure of the Human Cannabinoid Receptor CB2. *Cell*. 2019 Jan;176(3):459-467.e13.
101. Huang S, Xiao P, Sun J. Structural basis of signaling of cannabinoids receptors: paving a way for rational drug design in controlling multiple neurological and immune diseases. *Sig Transduct Target Ther*. 2020 Jul 21;5(1):127.
102. O'Sullivan SE. An update on PPAR activation by cannabinoids: Cannabinoids and PPARs. *British Journal of Pharmacology*. 2016 Jun;173(12):1899–910.
103. Haj-Dahmane S, Shen RY, Elmes MW, Studholme K, Kanjiya MP, Bogdan D, et al. Fatty-acid-binding protein 5 controls retrograde endocannabinoid signaling at central glutamate synapses. *Proc Natl Acad Sci USA*. 2018 Mar 27;115(13):3482–7.
104. Sanson B, Wang T, Sun J, Wang L, Kaczocha M, Ojima I, et al. Crystallographic study of FABP5 as an intracellular endocannabinoid transporter. *Acta Crystallogr D Biol Crystallogr*. 2014 Feb 1;70(2):290–8.
105. Ambrosio ALB, Dias SMG, Polikarpov I, Zurier RB, Burstein SH, Garratt RC. Ajulemic Acid, a Synthetic Nonpsychoactive Cannabinoid Acid, Bound to the Ligand Binding Domain of the Human Peroxisome Proliferator-activated Receptor  $\gamma$ . *Journal of Biological Chemistry*. 2007 Jun;282(25):18625–33.
106. Yang JF, Williams AH, Penthala NR, Prather PL, Crooks PA, Zhan CG. Binding Modes and Selectivity of Cannabinoid 1 (CB1) and Cannabinoid 2 (CB2) Receptor Ligands. *ACS Chem Neurosci*. 2020 Oct 21;11(20):3455–63.
107. Baratta F, Pignata I, Ravetto Enri L, Brusa P. Cannabis for Medical Use: Analysis of Recent Clinical Trials in View of Current Legislation. *Front Pharmacol*. 2022 May 25;13:888903.
108. Meier MH, Caspi A, Ambler A, Harrington H, Houts R, Keefe RSE, et al. Persistent cannabis users show neuropsychological decline from childhood to midlife. *Proc Natl Acad Sci USA* [Internet]. 2012 Oct 2 [cited 2023 Feb 17];109(40). Available from: <https://pnas.org/doi/full/10.1073/pnas.1206820109>
109. Jackson NJ, Isen JD, Khoddam R, Irons D, Tuvblad C, Iacono WG, et al. Impact of adolescent marijuana use on intelligence: Results from two longitudinal twin studies. *Proc Natl Acad Sci USA* [Internet]. 2016 Feb 2 [cited 2023 Feb 17];113(5). Available from: <https://pnas.org/doi/full/10.1073/pnas.1516648113>
110. Volkow ND, Compton WM, Wargo EM. The Risks of Marijuana Use During Pregnancy. *JAMA*. 2017 Jan 10;317(2):129.

## References:

111. Hall WD, Lynskey M. Is cannabis a gateway drug? Testing hypotheses about the relationship between cannabis use and the use of other illicit drugs. *Drug and Alcohol Review*. 2005 Jan;24(1):39–48.
112. Albers HMHG, Hendrickx LJD, van Tol RJP, Hausmann J, Perrakis A, Ovaa H. Structure-Based Design of Novel Boronic Acid-Based Inhibitors of Autotaxin. *Journal of Medicinal Chemistry*. 2011 Jul 14;54(13):4619–26.
113. Keune WJ, Potjewyd F, Heidebrecht T, Salgado-Polo F, Macdonald SJF, Chelvarajan L, et al. Rational Design of Autotaxin Inhibitors by Structural Evolution of Endogenous Modulators. *Journal of Medicinal Chemistry*. 2017 Mar 9;60(5):2006–17.
114. Miller LM, Keune WJ, Castagna D, Young LC, Duffy EL, Potjewyd F, et al. Structure–Activity Relationships of Small Molecule Autotaxin Inhibitors with a Discrete Binding Mode. *Journal of Medicinal Chemistry*. 2017 Jan 26;60(2):722–48.
115. Hausmann J, Christodoulou E, Kasiem M, De Marco V, van Meeteren LA, Moolenaar WH, et al. Mammalian cell expression, purification, crystallization and microcrystal data collection of autotaxin/ENPP2, a secreted mammalian glycoprotein. *Acta Crystallogr F Struct Biol Cryst Commun*. 2010 Sep 1;66(9):1130–5.
116. Eymery MC, McCarthy AA, Hausmann J. Linking medicinal cannabis to autotaxin–lysophosphatidic acid signaling. *Life Science Alliance*. 2023 Feb;6(2):e202201595.
117. Cianci M, Bourenkov G, Pompidor G, Karpics I, Kallio J, Bento I, et al. P13, the EMBL macromolecular crystallography beamline at the low-emittance PETRA III ring for high- and low-energy phasing with variable beam focusing. *J Synchrotron Rad*. 2017 Jan 1;24(1):323–32.
118. Vonrhein C, Flensburg C, Keller P, Sharff A, Smart O, Paciorek W, et al. Data processing and analysis with the *autoPROC* toolbox. *Acta Crystallogr D Biol Crystallogr*. 2011 Apr 1;67(4):293–302.
119. Kabsch W. *XDS*. *Acta Crystallographica Section D Biological Crystallography*. 2010 Feb 1;66(2):125–32.
120. Adams PD, Afonine PV, Bunkóczi G, Chen VB, Davis IW, Echols N, et al. *PHENIX*: a comprehensive Python-based system for macromolecular structure solution. *Acta Crystallographica Section D Biological Crystallography*. 2010 Feb 1;66(2):213–21.
121. Emsley P, Cowtan K. *Coot*: model-building tools for molecular graphics. *Acta Crystallogr D Biol Crystallogr*. 2004 Dec 1;60(12):2126–32.
122. Afonine PV, Grosse-Kunstleve RW, Echols N, Headd JJ, Moriarty NW, Mustyakimov M, et al. Towards automated crystallographic structure refinement with *phenix.refine*. *Acta Crystallogr D Biol Crystallogr*. 2012 Apr 1;68(4):352–67.



## References:

123. Murshudov GN, Skubák P, Lebedev AA, Pannu NS, Steiner RA, Nicholls RA, et al. *REFMAC 5 for the refinement of macromolecular crystal structures*. Acta Crystallogr D Biol Crystallogr. 2011 Apr 1;67(4):355–67.
124. Joosten RP, Salzemann J, Bloch V, Stockinger H, Berglund AC, Blanchet C, et al. *PDB\_REDO: automated re-refinement of X-ray structure models in the PDB*. J Appl Crystallogr. 2009 Jun 1;42(3):376–84.
125. Moriarty NW, Grosse-Kunstleve RW, Adams PD. *electronic Ligand Builder and Optimization Workbench ( eLBOW )*: a tool for ligand coordinate and restraint generation. Acta Crystallogr D Biol Crystallogr. 2009 Oct 1;65(10):1074–80.
126. Williams CJ, Headd JJ, Moriarty NW, Prisant MG, Videau LL, Deis LN, et al. *MolProbity: More and better reference data for improved all-atom structure validation: PROTEIN SCIENCE.ORG*. Protein Science. 2018 Jan;27(1):293–315.
127. McNicholas S, Potterton E, Wilson KS, Noble MEM. *Presenting your structures: the CCP 4 mg molecular-graphics software*. Acta Crystallogr D Biol Crystallogr. 2011 Apr 1;67(4):386–94.
128. Morin A, Eisenbraun B, Key J, Sanschagrín PC, Timony MA, Ottaviano M, et al. *Collaboration gets the most out of software*. eLife. 2013 Sep 10;2:e01456.
129. McCarthy AA, Barrett R, Beteva A, Caserotto H, Dobias F, Felisaz F, et al. *ID30B – a versatile beamline for macromolecular crystallography experiments at the ESRF*. J Synchrotron Rad. 2018 Jul 1;25(4):1249–60.
130. Mueller-Dieckmann C, Bowler MW, Carpentier P, Flot D, McCarthy AA, Nanao MH, et al. *The status of the macromolecular crystallography beamlines at the European Synchrotron Radiation Facility*. Eur Phys J Plus. 2015 Apr;130(4):70.
131. Monaco S, Gordon E, Bowler MW, Delagenière S, Guijarro M, Spruce D, et al. *Automatic processing of macromolecular crystallography X-ray diffraction data at the ESRF*. J Appl Crystallogr. 2013 Jun 1;46(3):804–10.
132. McCoy AJ. *Solving structures of protein complexes by molecular replacement with Phaser*. Acta Crystallogr D Biol Crystallogr. 2007 Jan 1;63(1):32–41.
133. Hausmann J, Keune WJ, Hipgrave Ederveen AL, van Zeijl L, Joosten RP, Perrakis A. *Structural snapshots of the catalytic cycle of the phosphodiesterase Autotaxin*. Journal of Structural Biology. 2016 Aug;195(2):199–206.
134. Jumper J, Evans R, Pritzel A, Green T, Figurnov M, Ronneberger O, et al. *Highly accurate protein structure prediction with AlphaFold*. Nature. 2021 Aug 26;596(7873):583–9.
135. Lee CW, Rivera R, Dubin AE, Chun J. *LPA(4)/GPR23 is a lysophosphatidic acid (LPA) receptor utilizing G(s)-, G(q)/G(i)-mediated calcium signaling and G(12/13)-mediated Rho activation*. J Biol Chem. 2007 Feb 16;282(7):4310–7.

## References:

136. Punjani A, Rubinstein JL, Fleet DJ, Brubaker MA. cryoSPARC: algorithms for rapid unsupervised cryo-EM structure determination. *Nat Methods*. 2017 Mar;14(3):290–6.
137. Albers HMG, Hendrickx LJD, van Tol RJP, Hausmann J, Perrakis A, Ova H. Structure-based design of novel boronic acid-based inhibitors of autotaxin. *J Med Chem*. 2011 Jul 14;54(13):4619–26.
138. Aung MM, Griffin G, Huffman JW, Wu M, Keel C, Yang B, et al. Influence of the N-1 alkyl chain length of cannabimimetic indoles upon CB(1) and CB(2) receptor binding. *Drug Alcohol Depend*. 2000 Aug 1;60(2):133–40.
139. Hausmann J, Kamtekar S, Christodoulou E, Day JE, Wu T, Fulkerson Z, et al. Structural basis of substrate discrimination and integrin binding by autotaxin. *Nat Struct Mol Biol*. 2011 Feb;18(2):198–204.
140. Keune WJ, Hausmann J, Bolier R, Tolenaars D, Kremer A, Heidebrecht T, et al. Steroid binding to Autotaxin links bile salts and lysophosphatidic acid signalling. *Nat Commun*. 2016 Sep;7(1):11248.
141. Adasme MF, Linnemann KL, Bolz SN, Kaiser F, Salentin S, Haupt VJ, et al. PLIP 2021: expanding the scope of the protein–ligand interaction profiler to DNA and RNA. *Nucleic Acids Research*. 2021 May 5;gkab294.
142. Lee CW, Rivera R, Gardell S, Dubin AE, Chun J. GPR92 as a new G12/13- and Gq-coupled lysophosphatidic acid receptor that increases cAMP, LPA5. *J Biol Chem*. 2006 Aug 18;281(33):23589–97.
143. Murph MM, Scaccia LA, Volpicelli LA, Radhakrishna H. Agonist-induced endocytosis of lysophosphatidic acid-coupled LPA1/EDG-2 receptors via a dynamin2- and Rab5-dependent pathway. *J Cell Sci*. 2003 May 15;116(Pt 10):1969–80.
144. Duggan PJ. The Chemistry of Cannabis and Cannabinoids. *Aust J Chem*. 2021 Mar 18;74(6):369–87.
145. Jones SB, Pfeifer LA, Bleisch TJ, Beauchamp TJ, Durbin JD, Klimkowski VJ, et al. Novel Autotaxin Inhibitors for the Treatment of Osteoarthritis Pain: Lead Optimization via Structure-Based Drug Design. *ACS Med Chem Lett*. 2016 Sep 8;7(9):857–61.
146. Houben AJS, van Wijk XMR, van Meeteren LA, van Zeijl L, van de Westerlo EMA, Hausmann J, et al. The Polybasic Insertion in Autotaxin  $\alpha$  Confers Specific Binding to Heparin and Cell Surface Heparan Sulfate Proteoglycans. *Journal of Biological Chemistry*. 2013 Jan;288(1):510–9.
147. Huestis MA, Cone EJ. Relationship of Delta 9-tetrahydrocannabinol concentrations in oral fluid and plasma after controlled administration of smoked cannabis. *J Anal Toxicol*. 2004 Sep;28(6):394–9.

## References:

148. MacCallum CA, Russo EB. Practical considerations in medical cannabis administration and dosing. *European Journal of Internal Medicine*. 2018 Mar;49:12–9.
149. Sugiura T, Nakane S, Kishimoto S, Waku K, Yoshioka Y, Tokumura A. Lysophosphatidic acid, a growth factor-like lipid, in the saliva. *J Lipid Res*. 2002 Dec;43(12):2049–55.
150. Maruya SI, Kim HW, Weber RS, Lee JJ, Kies M, Luna MA, et al. Gene expression screening of salivary gland neoplasms: molecular markers of potential histogenetic and clinical significance. *J Mol Diagn*. 2004 Aug;6(3):180–90.
151. Huestis MA, Cone EJ. Relationship of Delta 9-tetrahydrocannabinol concentrations in oral fluid and plasma after controlled administration of smoked cannabis. *J Anal Toxicol*. 2004 Sep;28(6):394–9.
152. Hunault CC, Mensinga TT, de Vries I, Kelholt-Dijkman HH, Hoek J, Kruidenier M, et al. Delta-9-tetrahydrocannabinol (THC) serum concentrations and pharmacological effects in males after smoking a combination of tobacco and cannabis containing up to 69 mg THC. *Psychopharmacology (Berl)*. 2008 Dec;201(2):171–81.
153. Pryimak N, Zaiachuk M, Kovalchuk O, Kovalchuk I. The Potential Use of Cannabis in Tissue Fibrosis. *Front Cell Dev Biol*. 2021;9:715380.
154. Zulfikar S, Mulholland S, Adamali H, Barratt SL. Inhibitors of the Autotaxin-Lysophosphatidic Acid Axis and Their Potential in the Treatment of Interstitial Lung Disease: Current Perspectives. *Clin Pharmacol*. 2020;12:97–108.
155. Bridgeman MB, Abazia DT. *Medicinal Cannabis: History, Pharmacology, And Implications for the Acute Care Setting*.
156. Sagy I, Bar-Lev Schleider L, Abu-Shakra M, Novack V. Safety and Efficacy of Medical Cannabis in Fibromyalgia. *JCM*. 2019 Jun 5;8(6):807.
157. Tham YC, Li X, Wong TY, Quigley HA, Aung T, Cheng CY. Global Prevalence of Glaucoma and Projections of Glaucoma Burden through 2040. *Ophthalmology*. 2014 Nov;121(11):2081–90.
158. Ho LTY, Osterwald A, Ruf I, Hunziker D, Mattei P, Challa P, et al. Role of the autotaxin-lysophosphatidic acid axis in glaucoma, aqueous humor drainage and fibrogenic activity. *Biochimica et Biophysica Acta (BBA) - Molecular Basis of Disease*. 2020 Jan;1866(1):165560.
159. Iyer P, Lalane R, Morris C, Challa P, Vann R, Rao PV. Autotaxin-Lysophosphatidic Acid Axis Is a Novel Molecular Target for Lowering Intraocular Pressure. Khan AU, editor. *PLoS ONE*. 2012 Aug 20;7(8):e42627.
160. Di Marzo V. New approaches and challenges to targeting the endocannabinoid system. *Nat Rev Drug Discov*. 2018 Sep;17(9):623–39.

## References:

161. Michalczyk A, Budkowska M, Dołęgowska B, Chlubek D, Safranow K. Lysophosphatidic acid plasma concentrations in healthy subjects: circadian rhythm and associations with demographic, anthropometric and biochemical parameters. *Lipids Health Dis.* 2017 Dec;16(1):140.
162. Reis J, Gaspar A, Milhazes N, Borges F. Chromone as a Privileged Scaffold in Drug Discovery: Recent Advances: Miniperspective. *Journal of Medicinal Chemistry.* 2017 Oct 12;60(19):7941–57.
163. Eymery M, Tran-Nguyen VK, Boumendjel A. Diversity-Oriented Synthesis: Amino Acetophenones as Building Blocks for the Synthesis of Natural Product Analogs. *Pharmaceuticals.* 2021 Nov;14(11):1127.
164. Herr DR, Ong JHJ, Ong WY. Potential Therapeutic Applications for Inhibitors of Autotaxin, a Bioactive Lipid-Producing Lysophospholipase D, in Disorders Affecting the Nervous System. *ACS Chemical Neuroscience.* 2018 Mar 21;9(3):398–400.
165. Helmer E, Willson A, Brearley C, Westerhof M, Delage S, Shaw I, et al. Pharmacokinetics and Metabolism of Ziritaxestat (GLPG1690) in Healthy Male Volunteers Following Intravenous and Oral Administration. *Clinical Pharm in Drug Dev.* 2022 Feb;11(2):246–56.
166. Grotenhermen F. Pharmacokinetics and Pharmacodynamics of Cannabinoids. *Clin Pharmacokinet.*
167. Chen M, O'Connor KL. Integrin  $\alpha 6 \beta 4$  promotes expression of autotaxin/ENPP2 autocrine motility factor in breast carcinoma cells.
168. Fulkerson Z, Wu T, Sunkara M, Kooi CV, Morris AJ, Smyth SS. Binding of Autotaxin to Integrins Localizes Lysophosphatidic Acid Production to Platelets and Mammalian Cells. *Journal of Biological Chemistry.* 2011 Oct;286(40):34654–63.
169. Leblanc R, Lee SC, David M, Bordet JC, Norman DD, Patil R, et al. Interaction of platelet-derived autotaxin with tumor integrin  $\alpha V \beta 3$  controls metastasis of breast cancer cells to bone. 2014;124(20).
170. Campbell ID, Humphries MJ. Integrin Structure, Activation, and Interactions. *Cold Spring Harbor Perspectives in Biology.* 2011 Mar 1;3(3):a004994–a004994.
171. Humphries MJ. Integrin Structure. *Biochemical Society Transactions.* 2000;28.
172. Coquelle N, Brewster AS, Kapp U, Shilova A, Weinhausen B, Burghammer M, et al. Raster-scanning serial protein crystallography using micro- and nano-focused synchrotron beams. *Acta Crystallographica Section D Biological Crystallography.* 2015 May 1;71(5):1184–96.
173. Rossmann MG. Serial crystallography using synchrotron radiation. *IUCrJ.* 2014 Mar 1;1(2):84–6.

Acknowledgements:

## 9 Acknowledgements:

First of all, I would like to thank Dr Andrew McCarthy for supervising and supporting me during the four years of my PhD. I couldn't have hoped for a better supervisor. I have had the opportunity to become a scientist and work on many challenging projects. Andrew also taught me structural biology techniques with a lot of patience and freedom. This allowed me to grow as a scientist.

I am also grateful to Pr Ahcene Boumendjel for being my mentor for all these years. I could learn organic chemistry and develop my research in his lab. This project would not have been possible without your kindness and support, for which I am very grateful to you.

I would also like to thank Dr Jens Hausmann. He taught me many aspects of autotaxin research. Without your input and preliminary results, this thesis would not have been possible.

I would also like to thank all the TAC members for their guidance and their support : Dr José Márquez and Dr Christian Löw.

I would also like to thank my doctoral examining committee: Pr Anastassis (Tassos) Perrakis, Pr Marc Le Borgne, Pr Wilhelm Burmeister, Dr Olivier Peyruchaud and Dr Joanna Timmins. I am very happy that you have agreed to evaluate my thesis.

I am also grateful to all my colleagues for their support during my PhD studies. In particular, I would like to thank the laboratory support: Audrey, Sylvie and Laetitia were very helpful. I would also like to thank Angélique and Sarah who helped me whenever I needed it. I would like to thank Jennyfer for helping me with all the orders I needed to make during the PhD. I also want to thank the whole administrative team for helping me, in particular Valérie, Elise and Mylène. I am also grateful to the researchers at EMBL Grenoble, especially Dr Shibom Basu. I met you four years ago and you introduced me to SSX. I am also grateful to Dr Sarah Schneider for her training in cryo-EM and to Martin Pelosse for his support in cell culture. I'd also like to thank Dr Caroline Mas for helping me with biophysical methods.

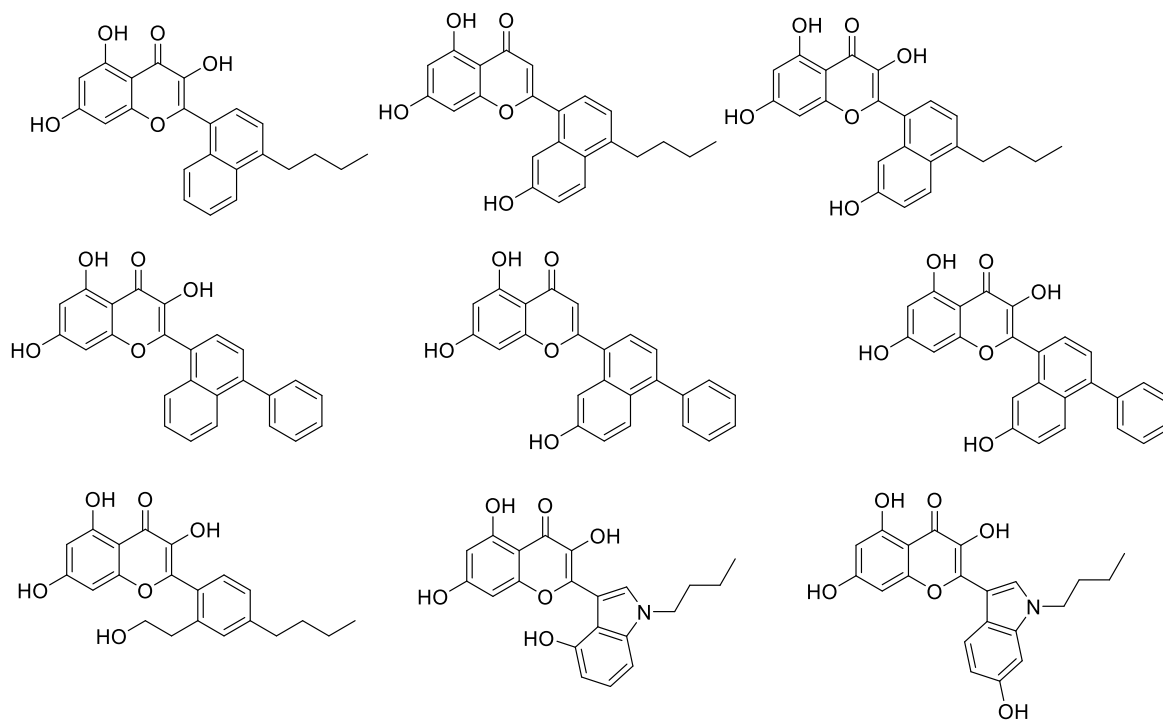
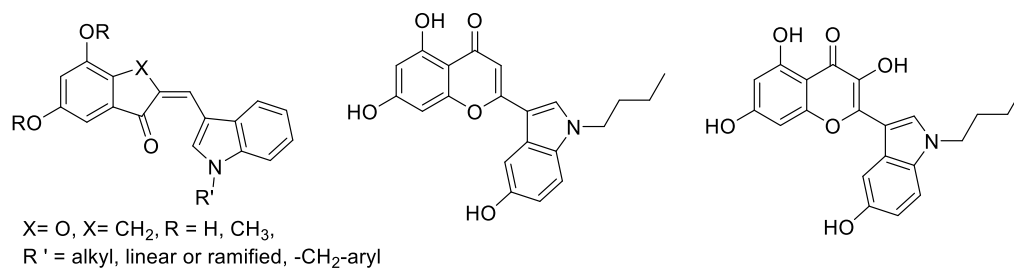
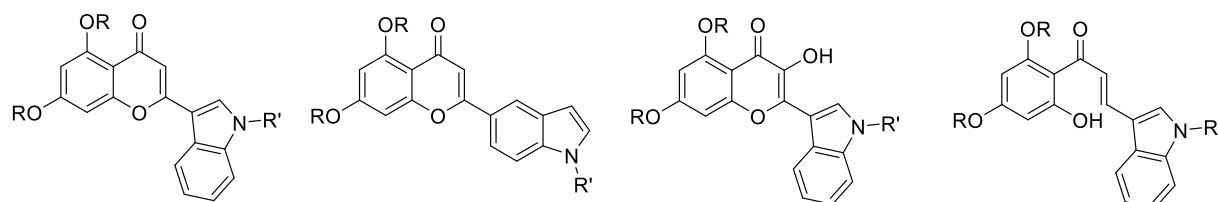
## Acknowledgements:

I'd also like to thank all the PhD students and postdocs at EMBL Grenoble, in particular Simonne, Nicolas and Jill for helping me.

Finally, I would like to thank my parents and my family for supporting me throughout my long and difficult studies. Without their help it would not have been possible.

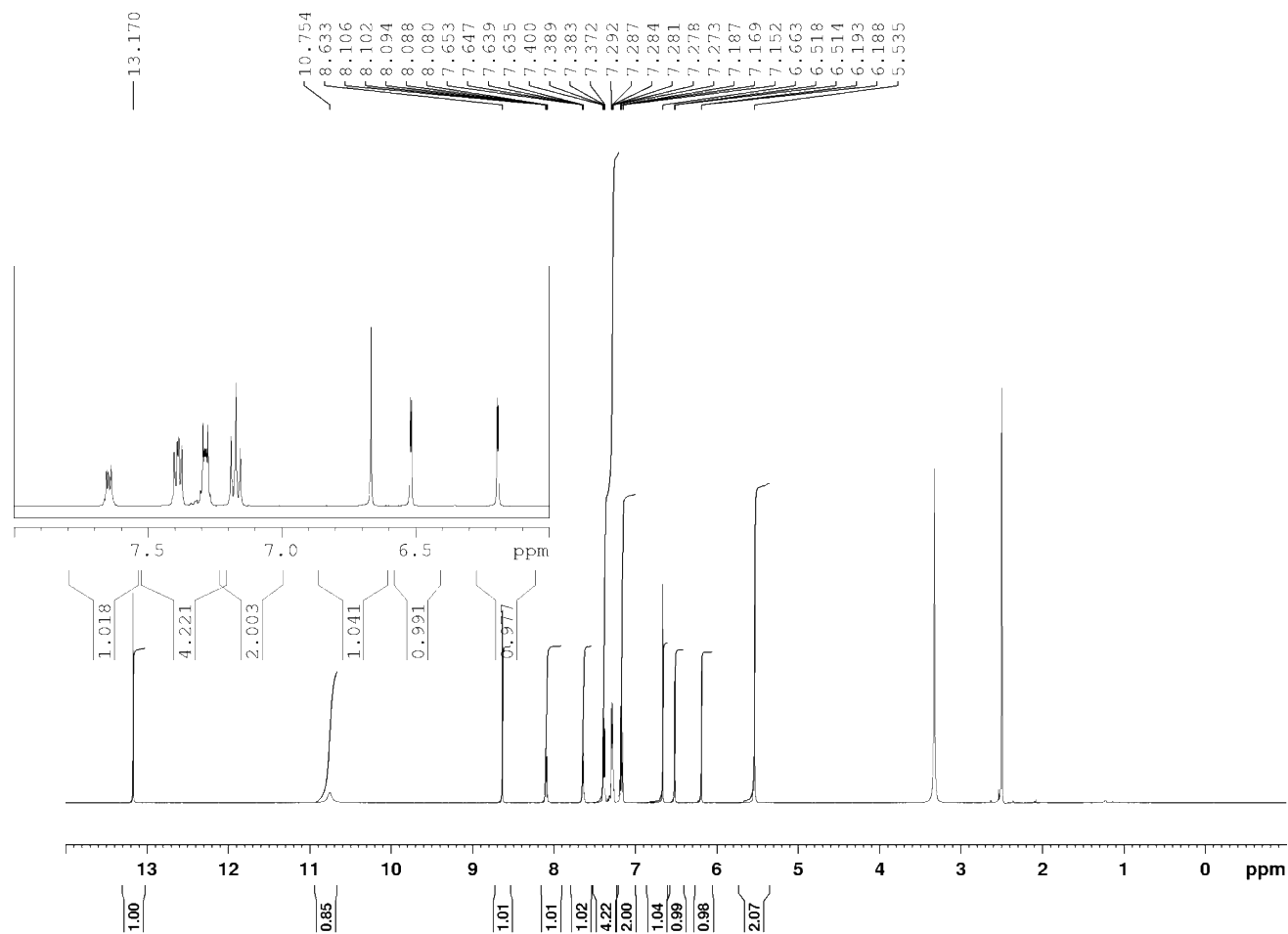
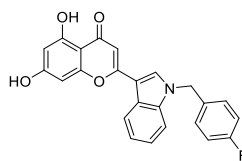
I would also like to thank my friends who have helped me to enjoy my journey as a PhD student in spite of all the difficulties.

## 10 Supplementary data

*supplementary 1: Chemical groups of the screened library*

Supplementary data

**MEY-001**

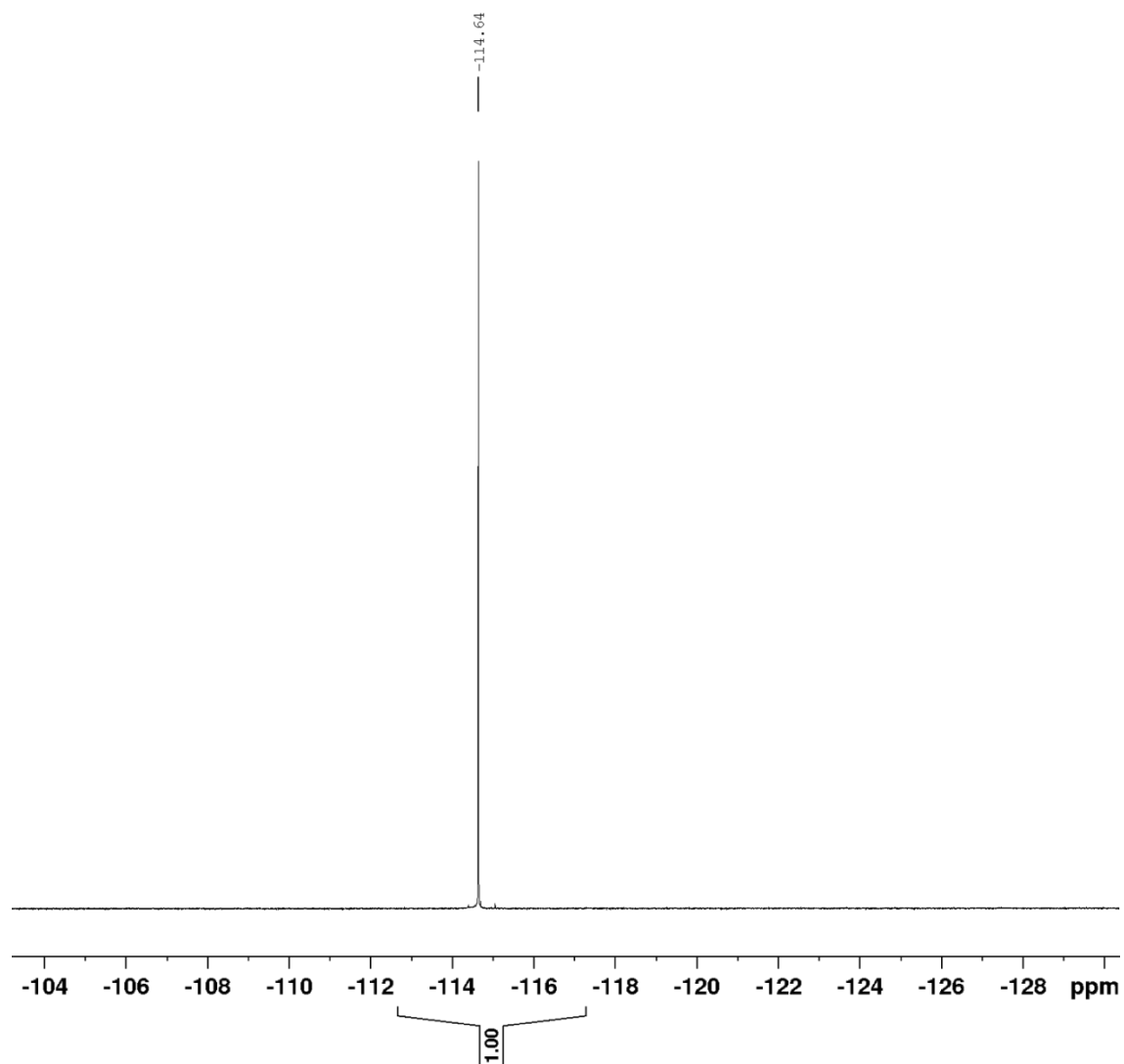


supplementary 2 :  $^1\text{H}$  NMR spectra of MEY-001

$^1\text{H}$  NMR (DMSO- $d_6$ , 500 MHz): 5.535 (s, 2H), 6.188 (d, 1H, 2.34Hz), 6.518 (d, 1H, 2.42Hz), 6.663 (s, 1H), 7.169 (t, 2H, 17Hz), 7.280 (m, 4H), 7.638 (m, 1H), 8.094 (m, 1H), 8.633 (s, 1H), 10.754 (s, 1H), 13.170 (s, 1H)



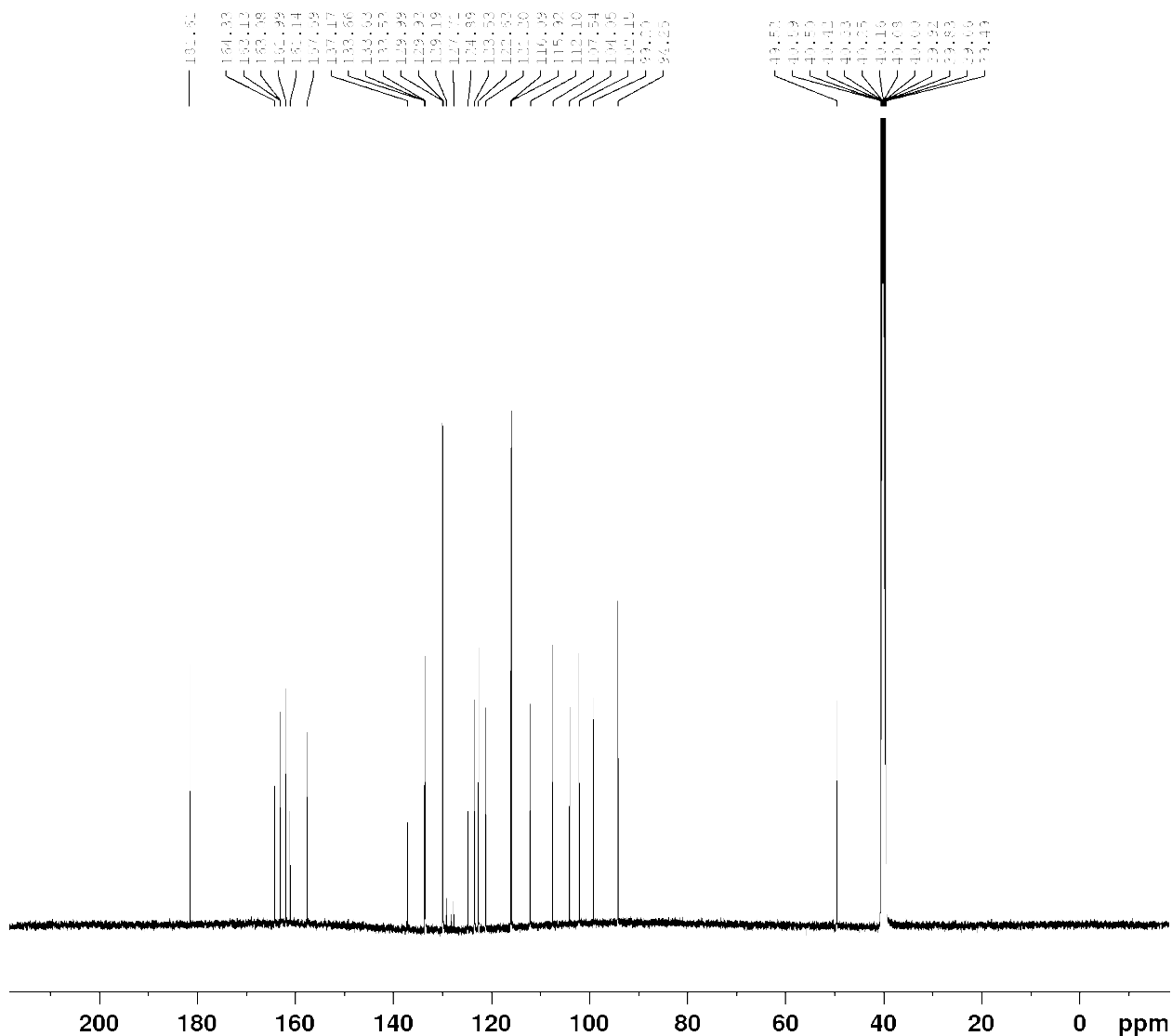
Supplementary data



supplementary 3:  $^{19}\text{F}$  NMR spectra of MEY-001

$^{19}\text{F}$  NMR (DMSO- $d_6$ , 500 MHz): 114.64 (s, 1F)

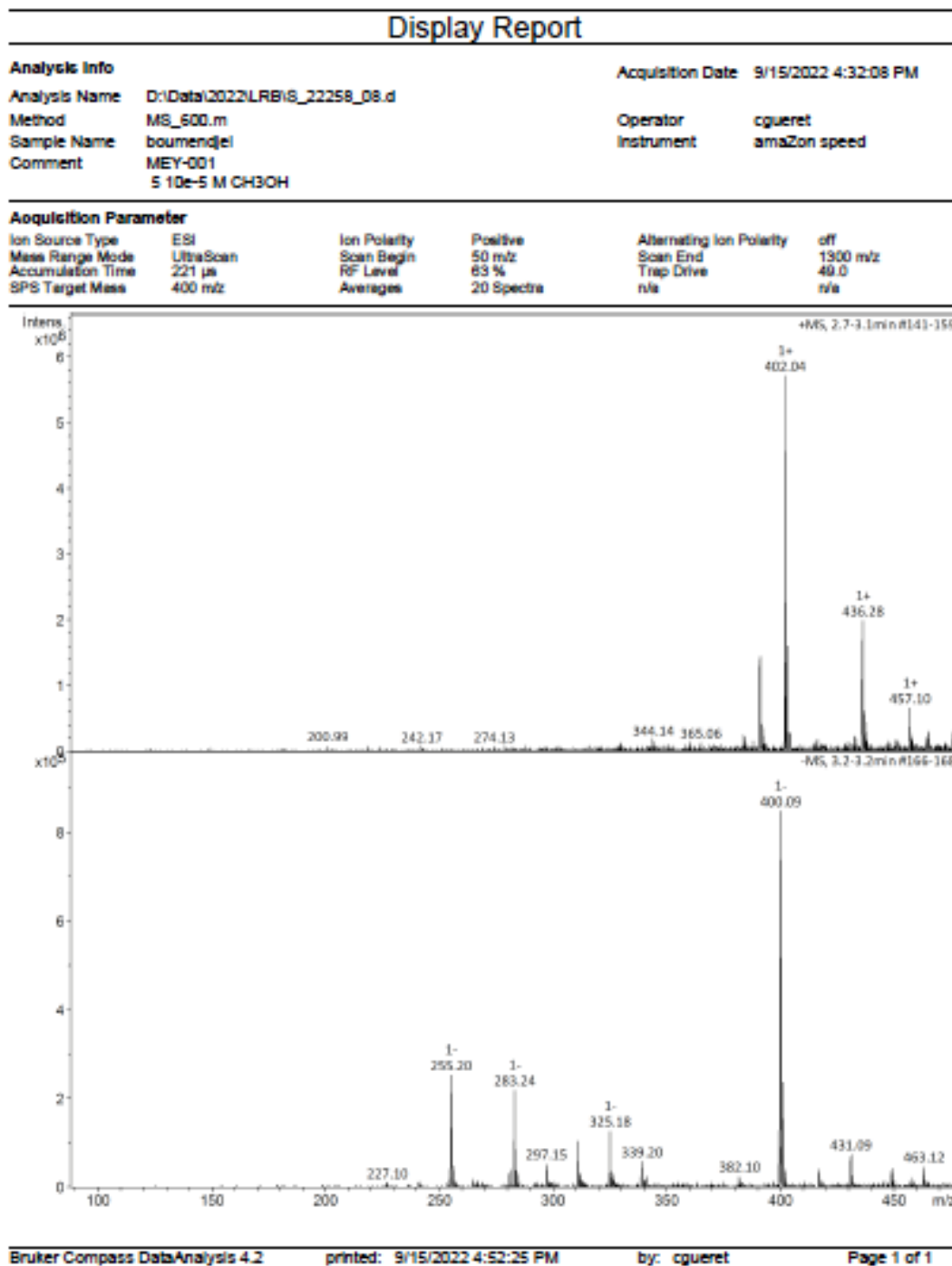
## Supplementary data



### supplementary 4: $^{13}\text{C}$ NMR spectra of MEY-001

$^{13}\text{C}$  NMR (DMSO- $d_6$ , 126 MHz): 48.9, 93.7, 98.5, 101.2, 103.2, 107, 111.7, 115.5, 120.4, 121.6, 122.7, 124.5, 127, 127.53, 128.44, 129, 132.6, 136.4, 156.7, 160.4, 161.5, 162.5, 162.38, 163.9, 180.9

Supplementary data



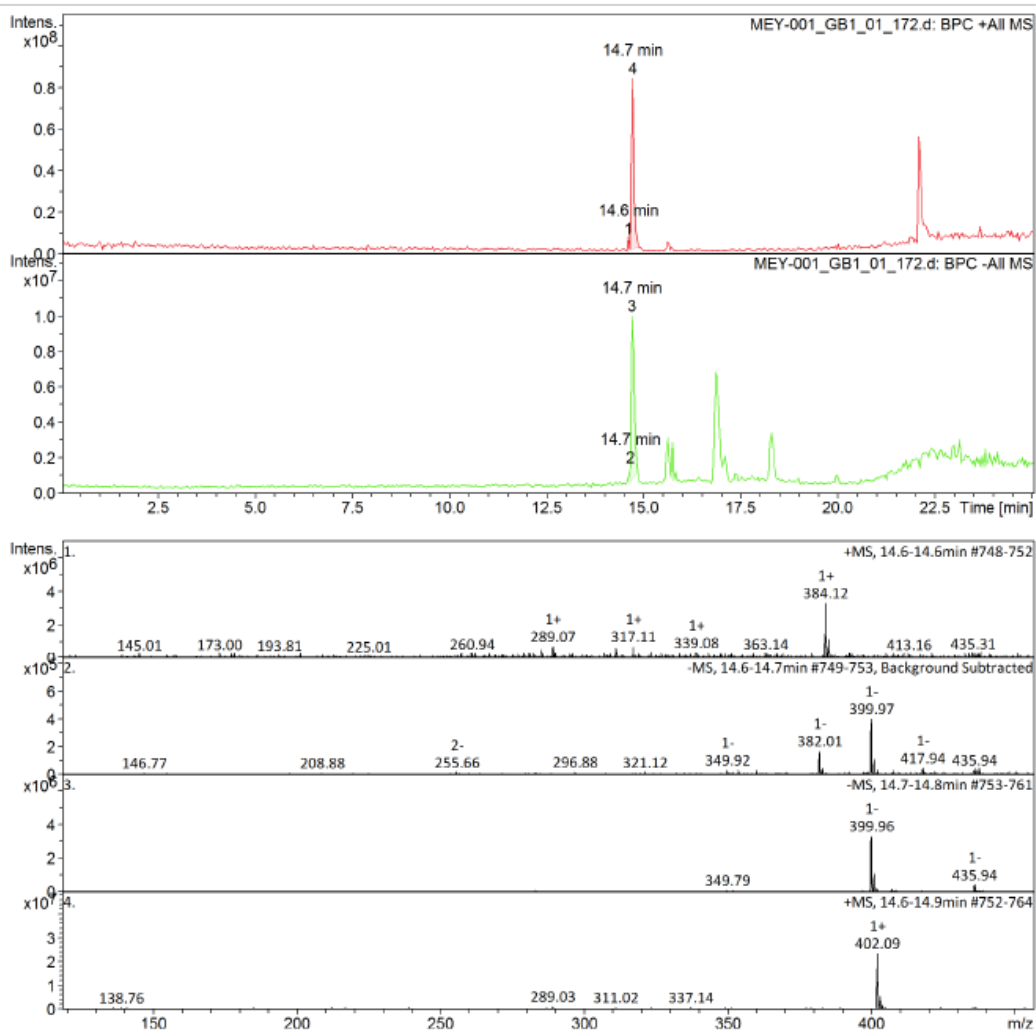
supplementary 5: ESI of MEY-001

LRMS (ESI+) m/z 402  $[M+H]^+$ . LRMS (ESI-) m/z 400  $[M-H]^-$ . Theoretical MW: 401.39 g/mol

### Display Report

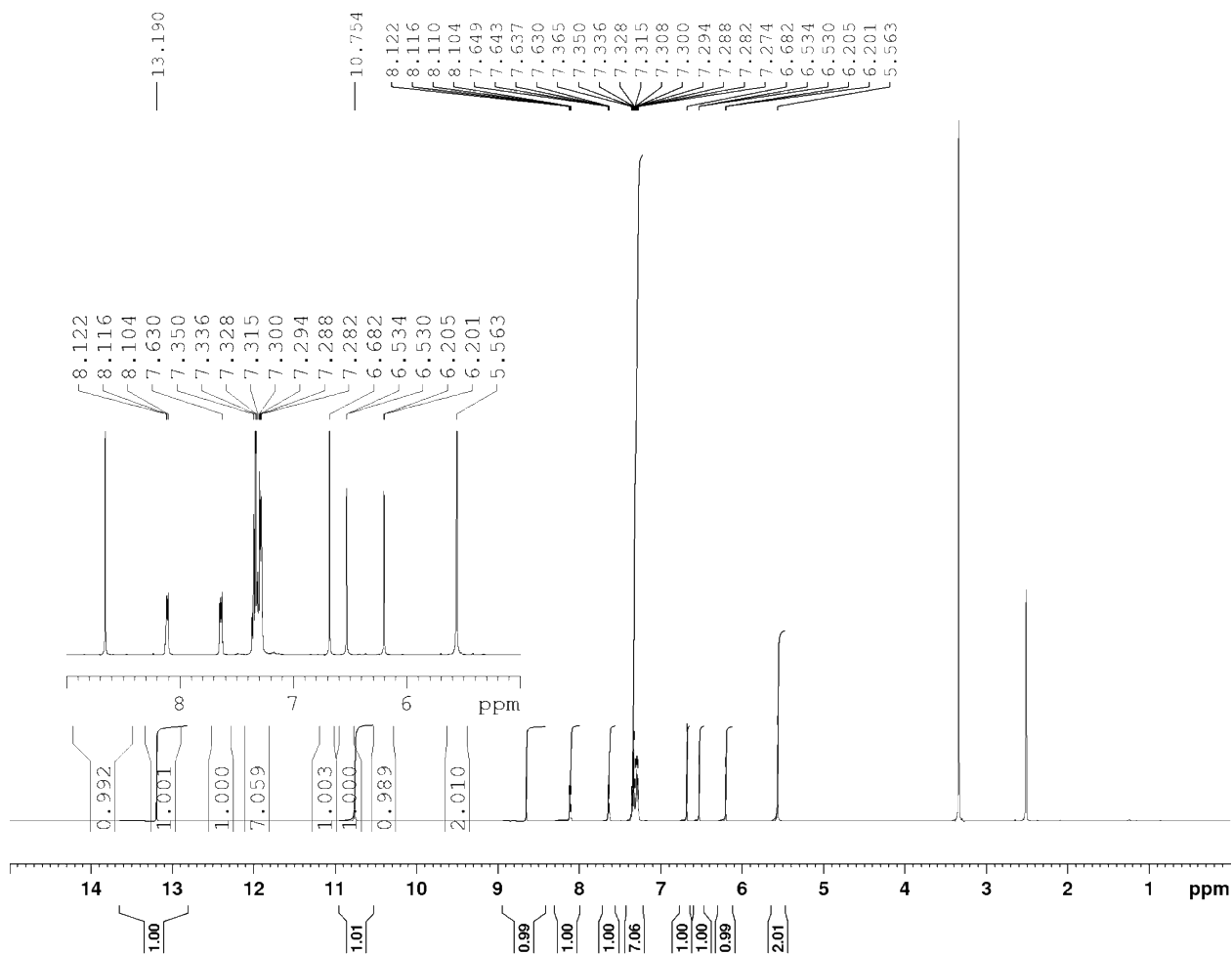
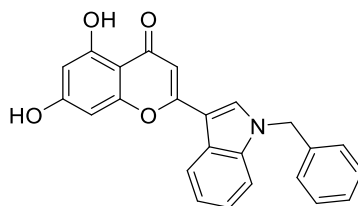
<b>Analysis Info</b>		Acquisition Date	4/6/2023 2:42:18 PM
Analysis Name	D:\Data\2023\DPMMMEY-001_GB1_01_172.d	Operator	cgueret
Method	172.m	Instrument	amaZon speed
Sample Name	MEY-001		
Comment	5 10e-4 M CH2Cl2		

<b>Acquisition Parameter</b>					
Ion Source Type	ESI	Ion Polarity	Negative	Alternating Ion Polarity	on
Mass Range Mode	UltraScan	Scan Begin	50 m/z	Scan End	1000 m/z
Accumulation Time	3836 $\mu$ s	RF Level	63 %	Trap Drive	53.2
SPS Target Mass	400 m/z	Averages	10 Spectra	n/a	n/a



Supplementary data

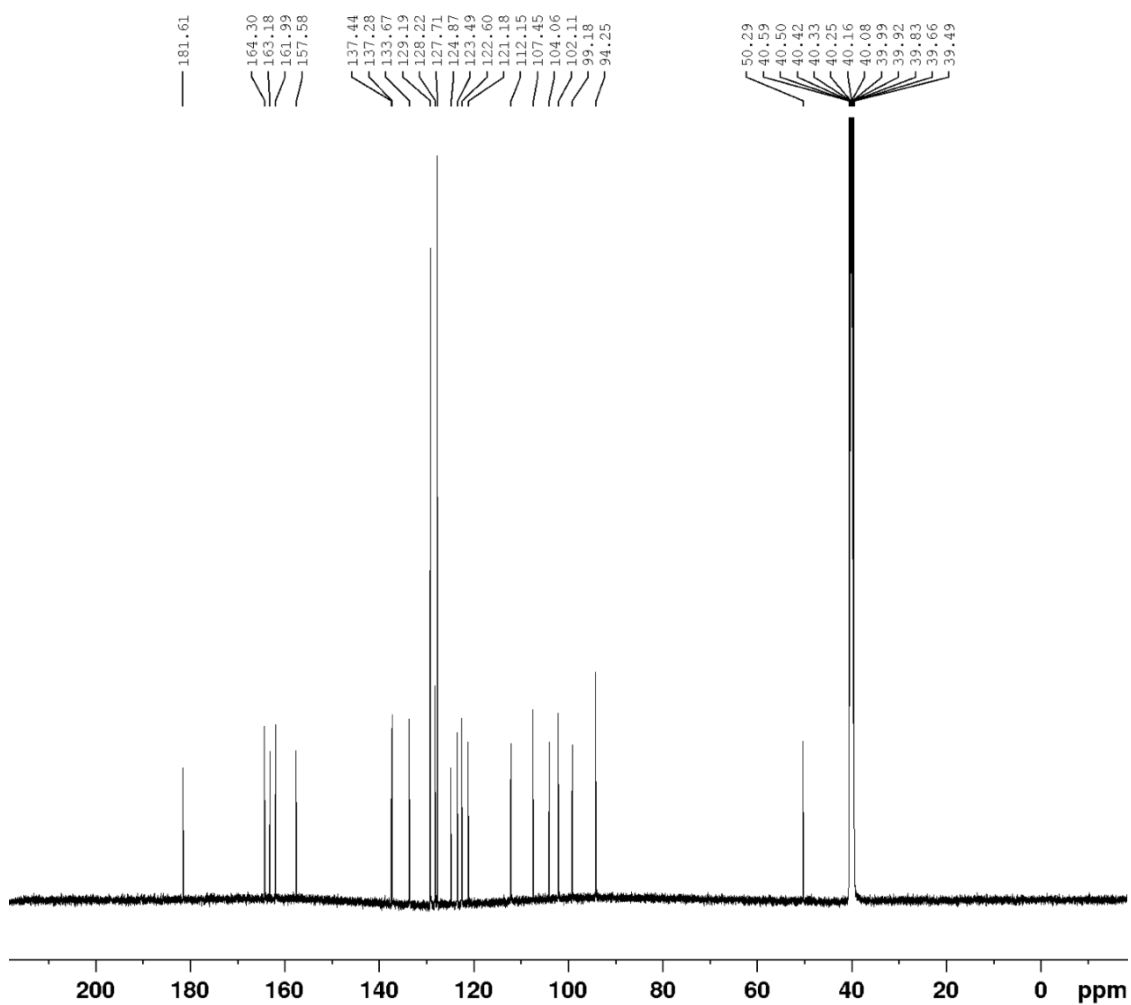
MEY-002



supplementary 7:  $^1\text{H}$  NMR spectra of MEY-002

$^1\text{H}$  NMR (DMSO- $d_6$ , 500 MHz): 13.19 (s, 1H), 10.75 (s, 1H), 8.65 (s, 1H), 8.109 (m, 1H), 7.642 (m, 1H), 7.307 (m, 7H), 6.682 (d, 1H), 6.534 (d, 1H), 6.205 (d, 1H), 5.563 (s, 2H)

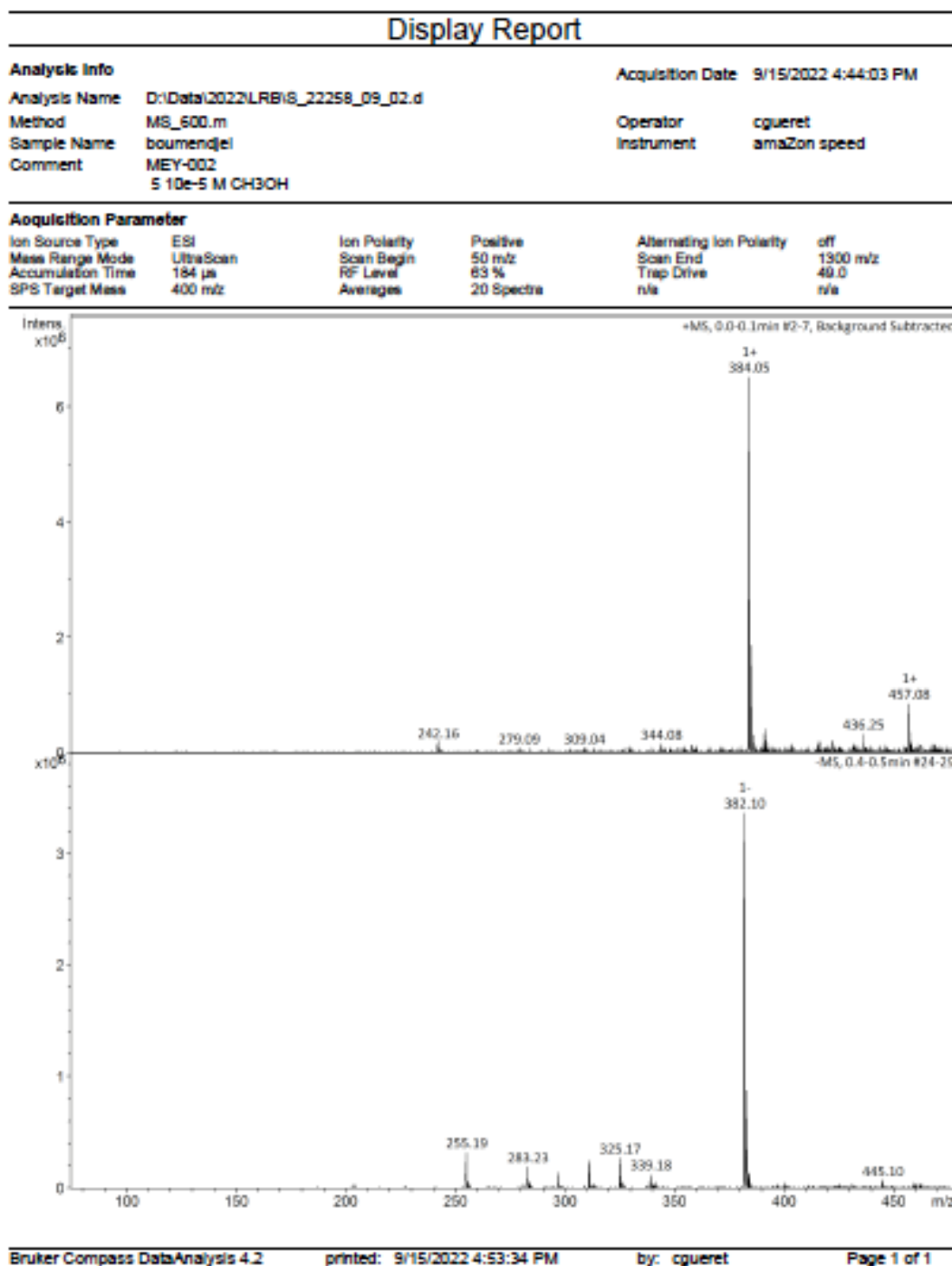
## Supplementary data



supplementary 8:  $^{13}\text{C}$  NMR spectra of MEY-002

$^{13}\text{C}$  NMR (DMSO- $d_6$ , 126 MHz): 181.610, 164.303, 163.184, 161.987, 157.585, 137.443, 137.283, 133.617, 129.189, 128.2155, 127.714, 124.869, 123.491, 122.599, 121.179, 112.146, 107.450, 104.060, 102.107, 99.183, 94.253, 50.294

Supplementary data



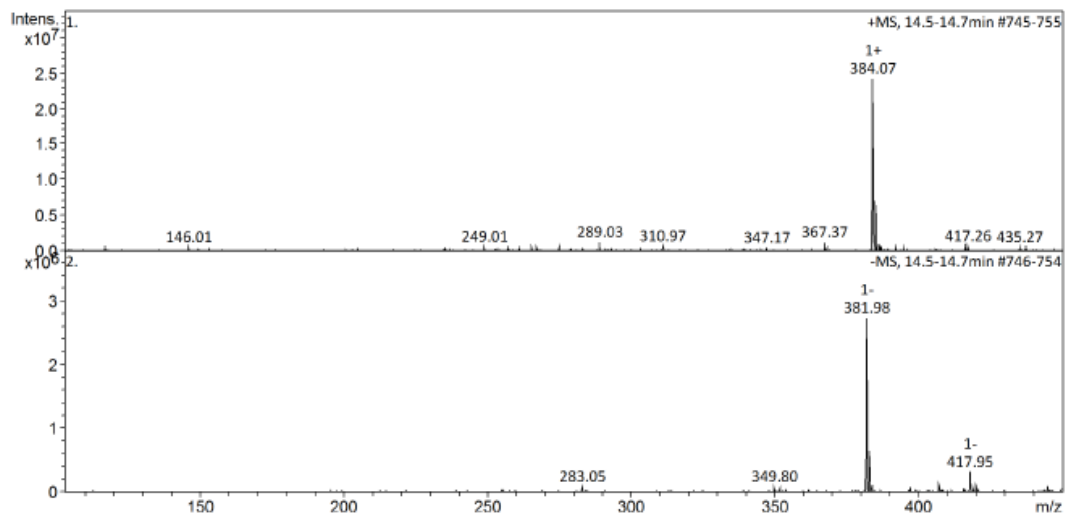
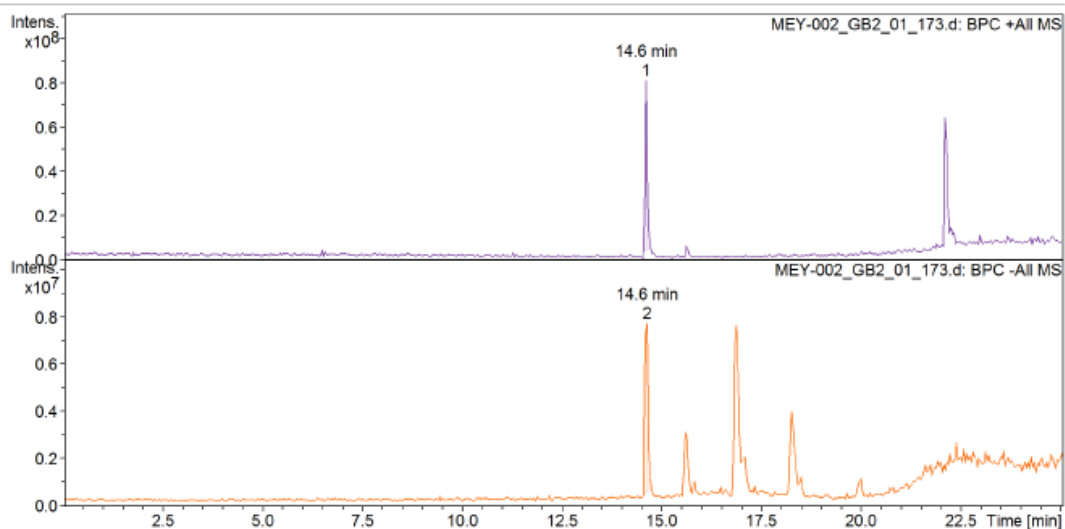
supplementary 9: ESI of MEY-002

LRMS (ESI+) m/z 384 [M+H]<sup>+</sup>. LRMS (ESI-) m/z 382 [M-H]<sup>-</sup>. Theoretical MW : 383.4 g/mol

### Display Report

<b>Analysis Info</b>		Acquisition Date	4/6/2023 3:15:09 PM
Analysis Name	D:\Data\2023\DPMMMEY-002_GB2_01_173.d	Operator	cgueret
Method	173.m	Instrument	amaZon speed
Sample Name	MEY-002		
Comment	5 10e-4 M CH2Cl2		

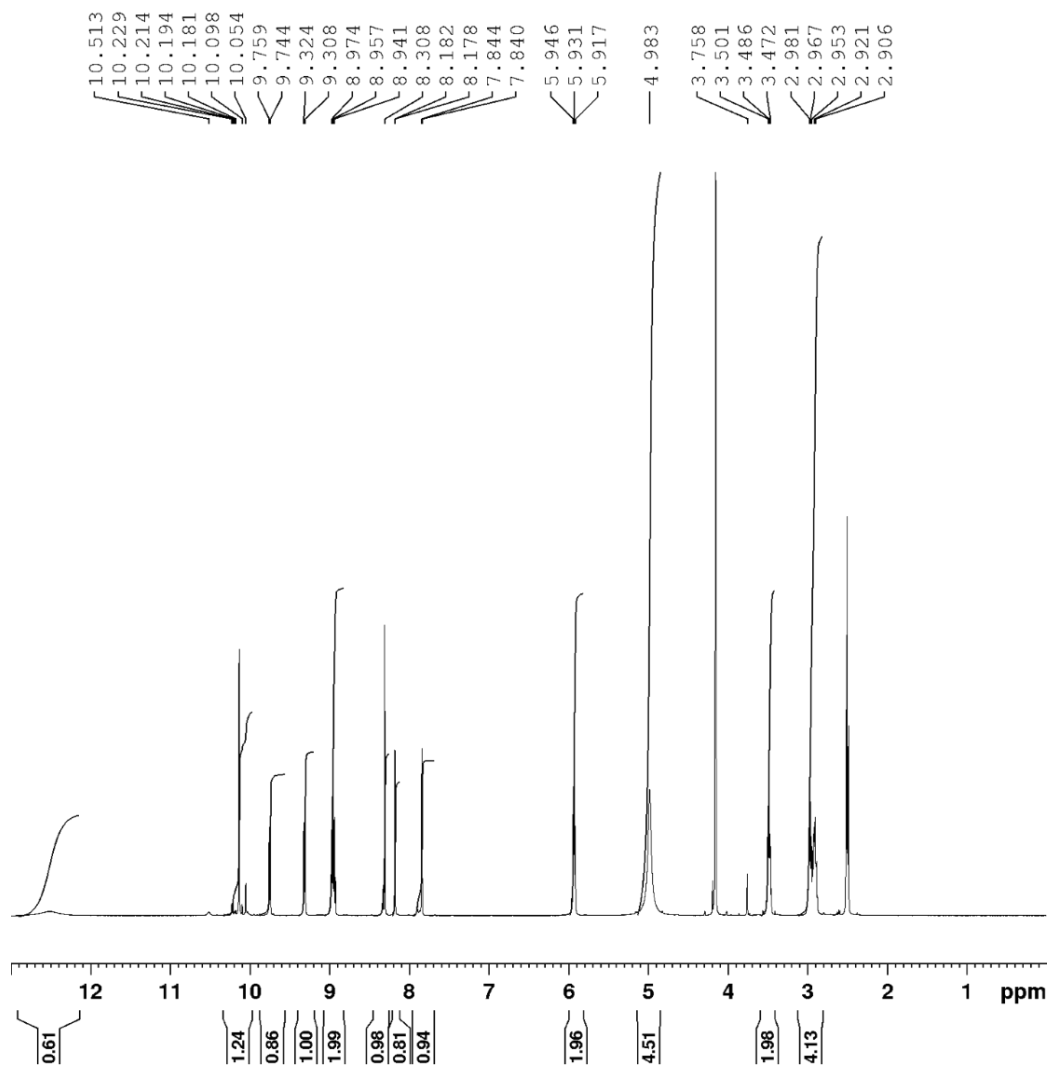
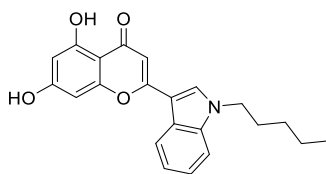
<b>Acquisition Parameter</b>					
Ion Source Type	ESI	Ion Polarity	Positive	Alternating Ion Polarity	on
Mass Range Mode	UltraScan	Scan Begin	50 m/z	Scan End	1000 m/z
Accumulation Time	486 $\mu$ s	RF Level	63 %	Trap Drive	49.0
SPS Target Mass	400 m/z	Averages	10 Spectra		n/a





Supplementary data

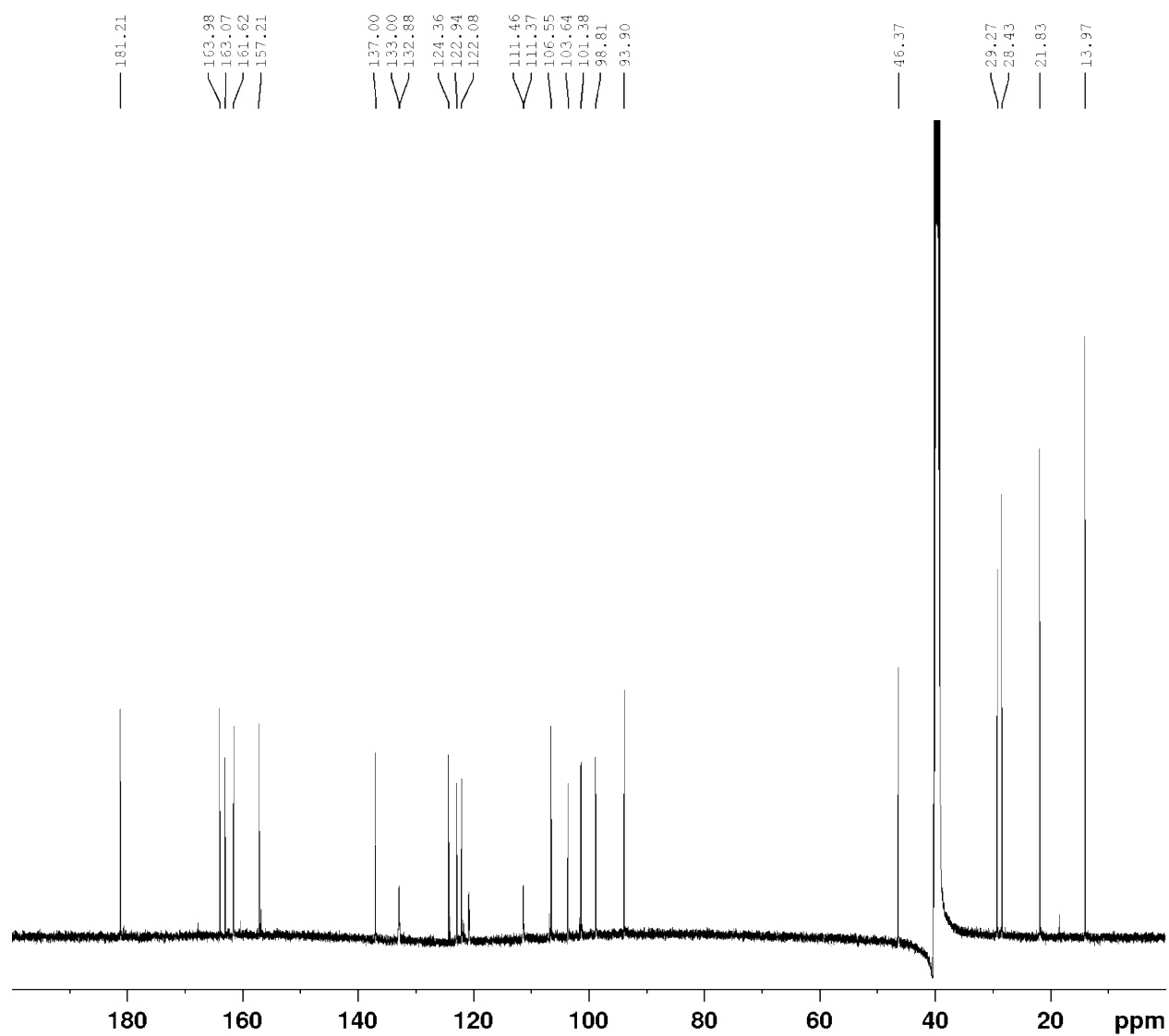
MEY-003



supplementary 11:  $^1\text{H}$  NMR spectra of MEY-003

$^1\text{H}$  NMR (DMSO- $d_6$ , 500 MHz): 12.511 (1H, s), 10.213 (1H, m), 9.759 (d, 1H), 9.324 (1H, m), 8.956 (2H, m), 8.307 (1H, s), 8.182 (1H, s), 7.843 (1H, s), 5.931 (2H, m), 4.9834 (4H, s), 3.486 (2H, m), 2.953 (4H, m)

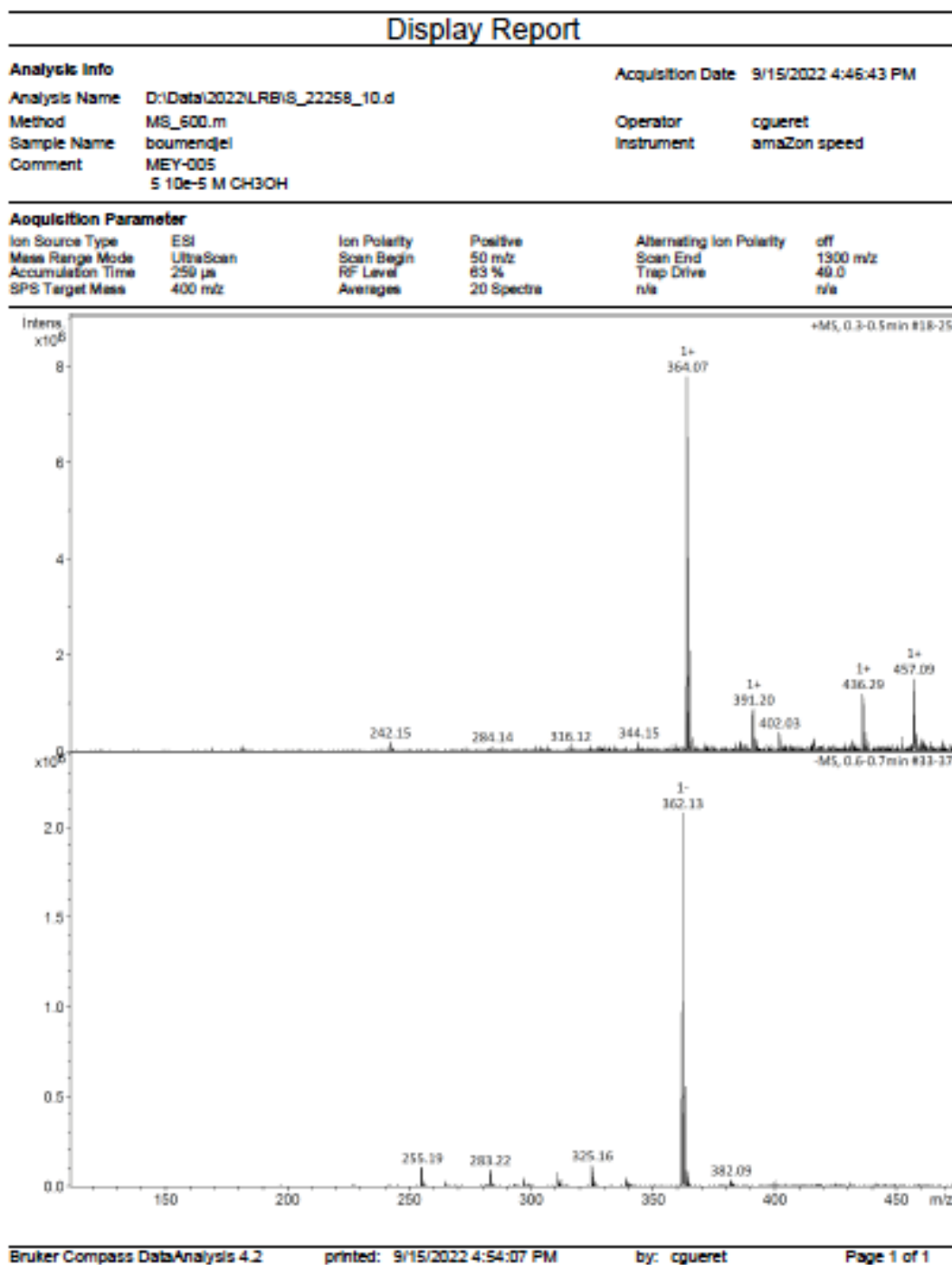
## Supplementary data



supplementary 12:  $^{13}\text{C}$  NMR spectra of MEY-003

$^{13}\text{C}$  NMR (DMSO- $d_6$ , 126 MHz): 181.206, 163.976, 163.067, 161.623, 157.211, 137.000, 133.001, 132.877, 124.357, 122.936, 122.079, 111.461, 111.365, 106.550, 103.642, 101.378, 98.814, 93.895, 46.370, 29.270, 28.431, 21.828, 13.964

Supplementary data



supplementary 13: ESI of MEY-003

LRMS (ESI+) m/z 364  $[M+H]^+$ . LRMS (ESI-) m/z 362  $[M-H]^-$ . Theoretical MW: 363.41 g/mol

# Supplementary data

## Display Report

### Analysis Info

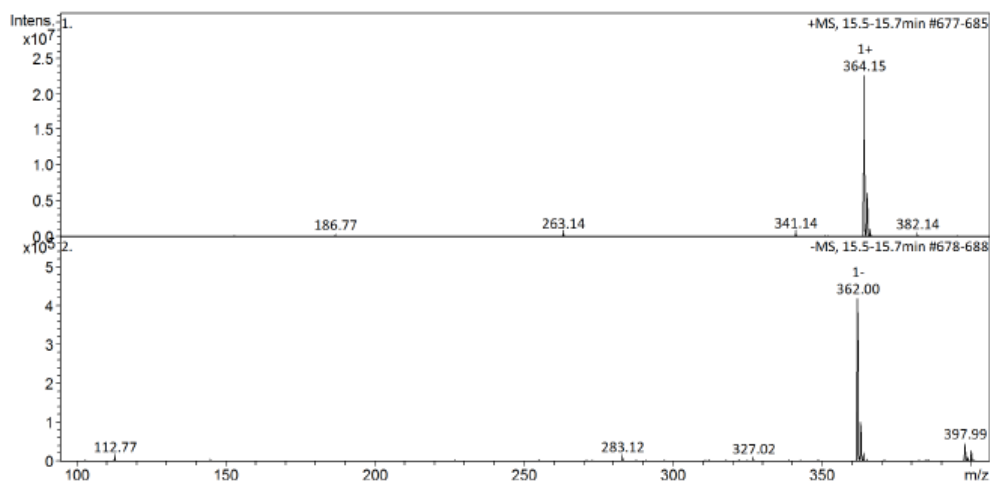
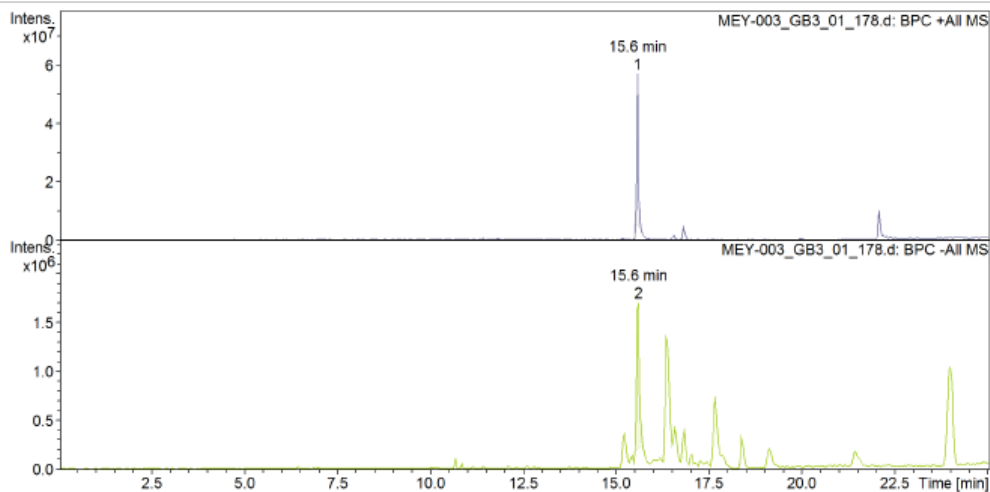
Analysis Name D:\Data\2023\DPMMEY-003\_GB3\_01\_178.d  
Method 178.m  
Sample Name MEY-003  
Comment 5 10e-4 M CH2Cl2

Acquisition Date 4/7/2023 11:11:03 AM

Operator cgueret  
Instrument amaZon speed

### Acquisition Parameter

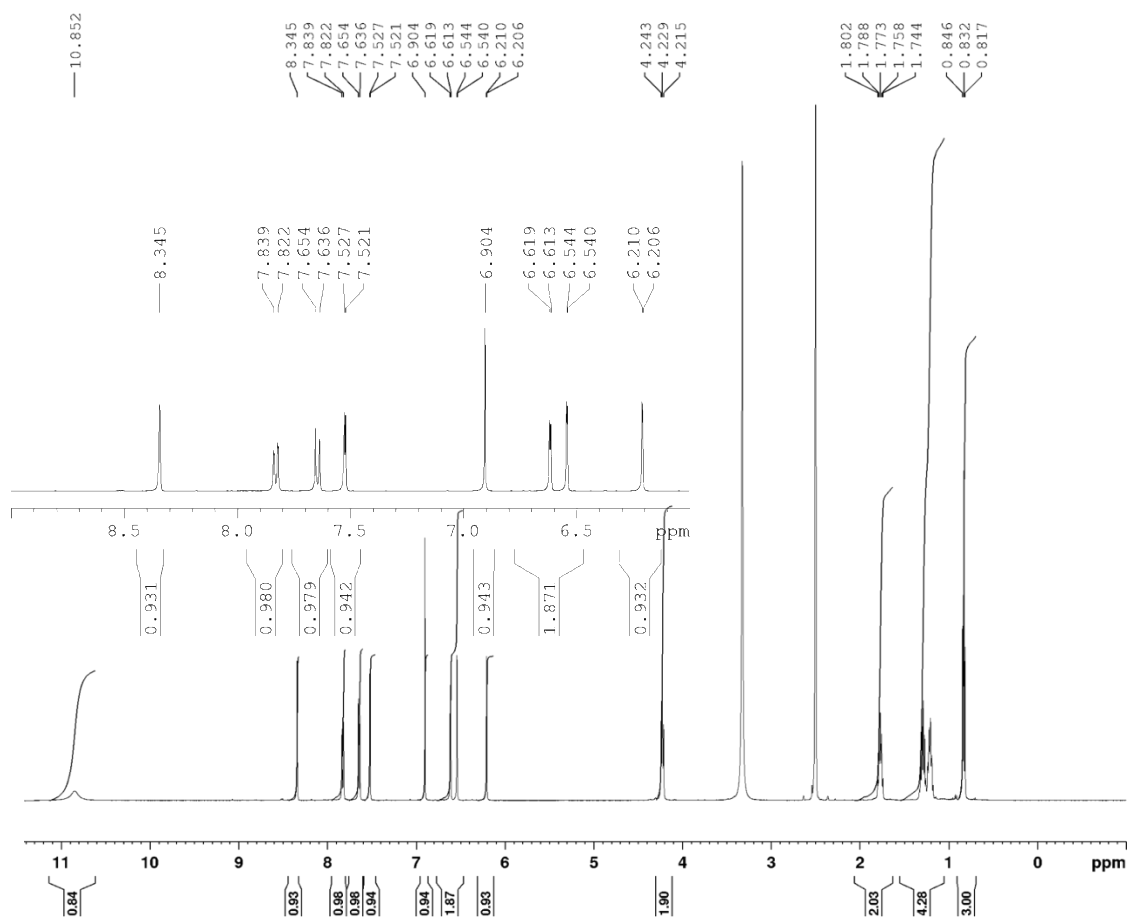
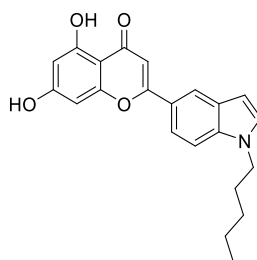
Ion Source Type	ESI	Ion Polarity	Positive	Alternating Ion Polarity	on
Mass Range Mode	UltraScan	Scan Begin	50 m/z	Scan End	1000 m/z
Accumulation Time	7019 $\mu$ s	RF Level	83 %	Trap Drive	49.0
SPS Target Mass	400 m/z	Averages	10 Spectra	n/a	n/a



supplementary 14: LCMS of MEY-003

Supplementary data

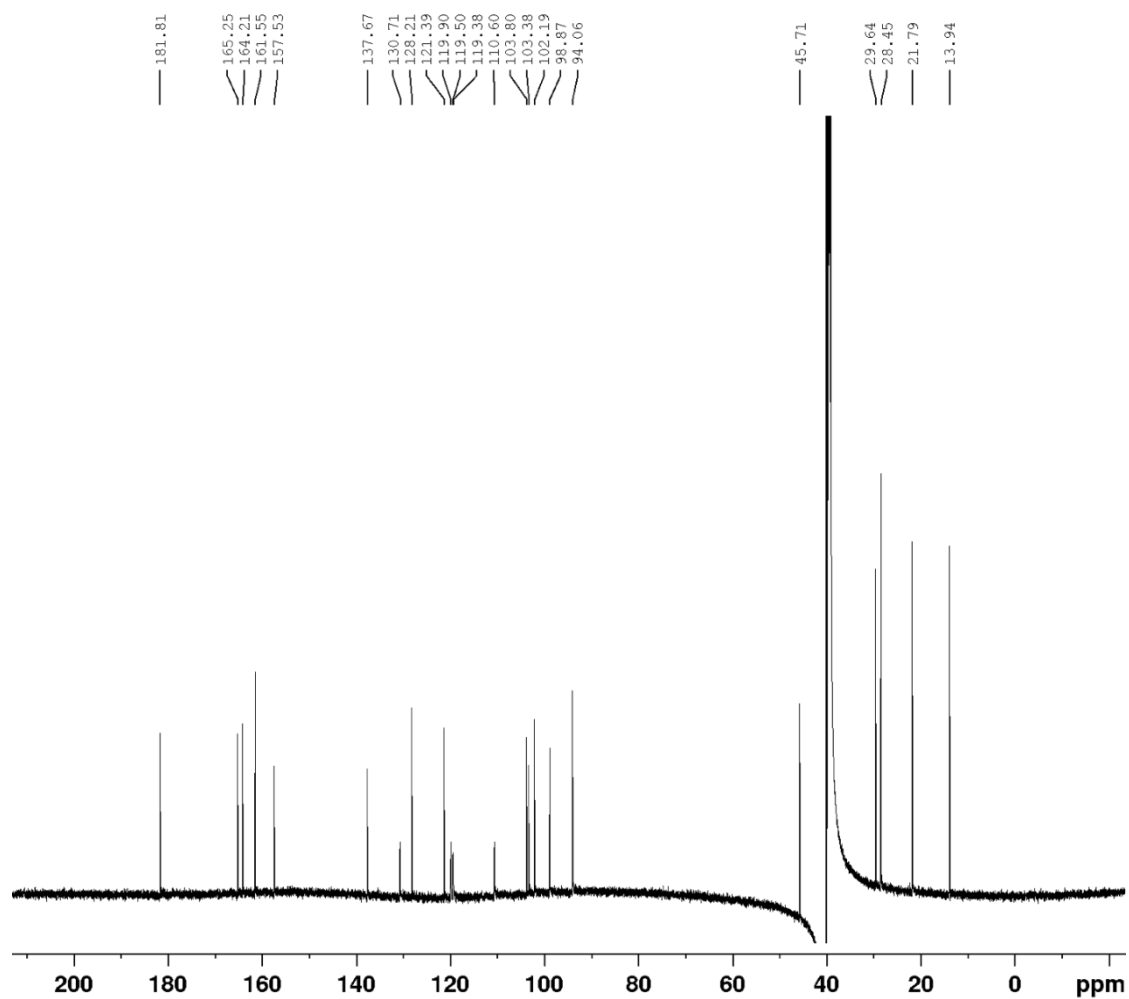
MEY-005



supplementary 15:  $^1\text{H}$  NMR spectra of MEY-005

$^1\text{H}$  NMR (DMSO- $d_6$ , 500 MHz): 10.852 (s, 1H), 8.345 (s, 1H), 7.839 (m, 1H), 7.654 (m, 1H), 7.527 (m, 1H), 6.904 (s, 1H), 6.613 (d, 2H), 6.21 (d, 1H), 4.229 (t, 2H), 1.773 (q, 2H), 1.2364 (m, 4H), 0.831 (m, 3H)

## Supplementary data



supplementary 16:  $^{13}\text{C}$  NMR spectra of MEY-005

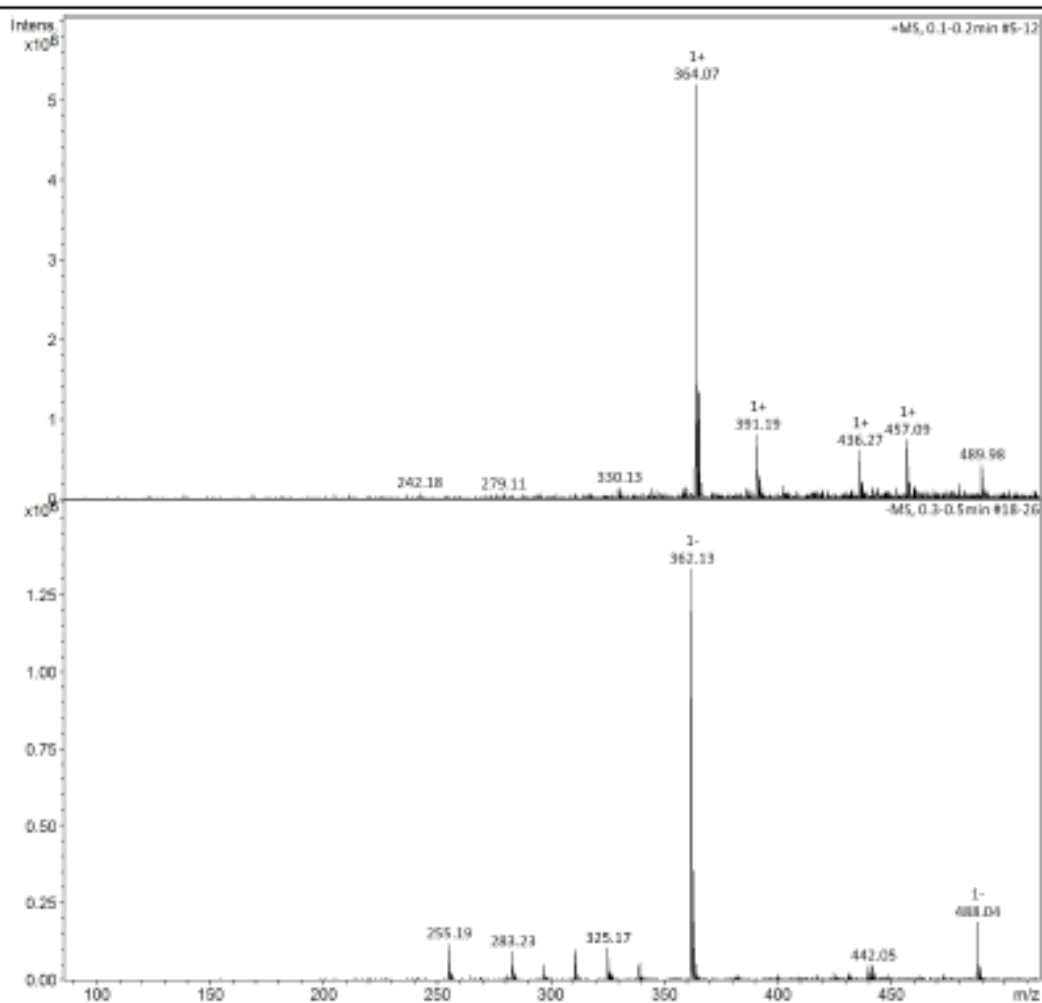
$^{13}\text{C}$  NMR (DMSO- $d_6$ , 126 MHz): 181.809, 165.245, 164.213, 161.545, 157.351, 137.671, 130.7166, 128.206, 121.392, 119.904, 119.5, 119.378, 110.602, 103.801, 103.375, 102.186, 98.874, 94.060, 45.709, 29.638, 28.445, 21.791, 13.938

## Display Report

<b>Analysis Info</b>		<b>Acquisition Date</b>	9/15/2022 4:49:17 PM
<b>Analysis Name</b>	D:\Data\2022\LRB\IS_22258_11.d	<b>Operator</b>	cgueret
<b>Method</b>	MS_600.m	<b>Instrument</b>	amazon speed
<b>Sample Name</b>	boumendjel		
<b>Comment</b>	MEY-003		
	5.10e-5 M CH3OH		

## Acquisition Parameter

<b>Ion Source Type</b>	ESI	<b>Ion Polarity</b>	Positive	<b>Alternating Ion Polarity</b>	off
<b>Mass Range Mode</b>	UltraScan	<b>Scan Begin</b>	50 m/z	<b>Scan End</b>	1300 m/z
<b>Accumulation Time</b>	244 $\mu$ s	<b>RF Level</b>	83 %	<b>Trap Drive</b>	49.0
<b>SPS Target Mass</b>	400 m/z	<b>Averages</b>	20 Spectra	<b>Trap Drive</b>	n/a



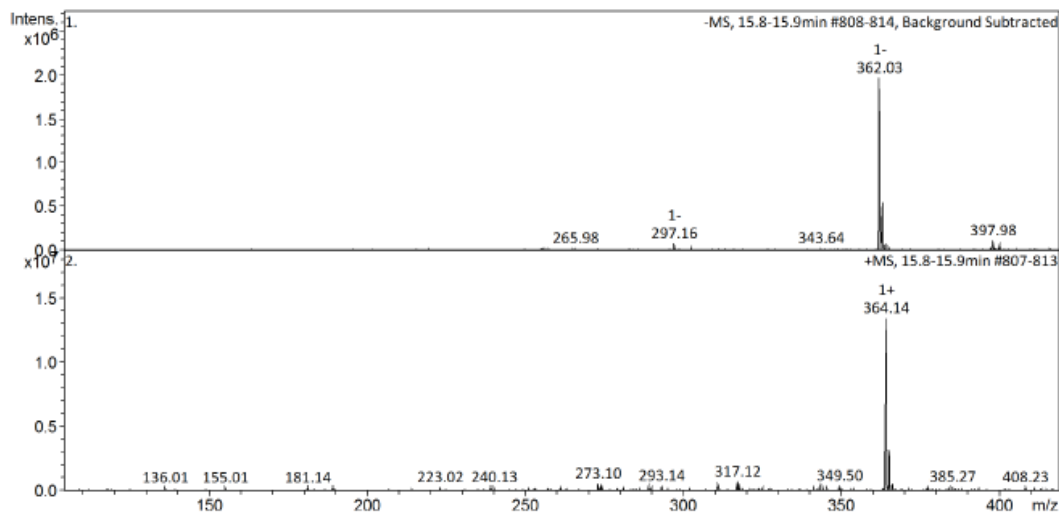
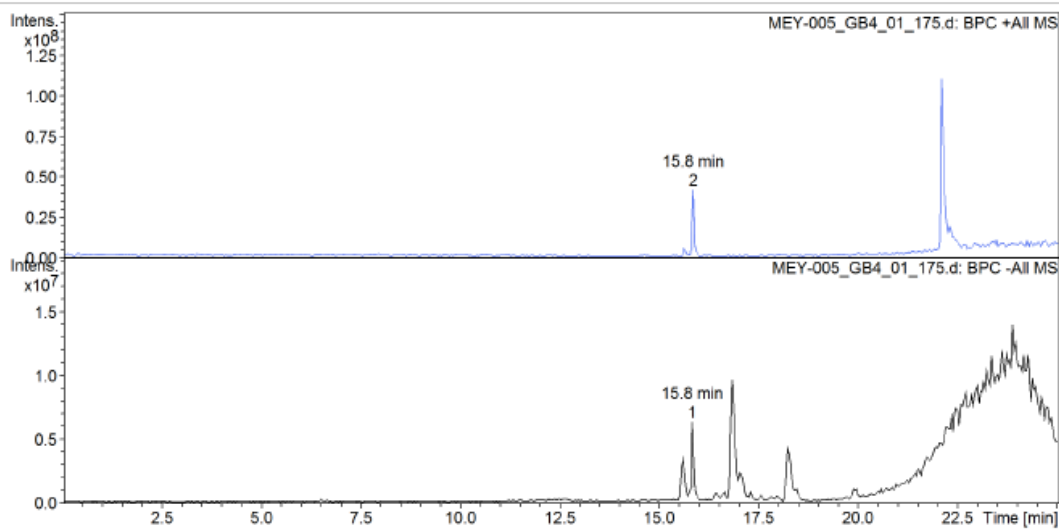
supplementary 17: ESI of MEY-005

LRMS (ESI+) m/z 364 [M+H]<sup>+</sup>. LRMS (ESI-) m/z 362 [M-H]<sup>-</sup>. Theoretical MW: 363.41 g/mol

### Display Report

<b>Analysis Info</b>		Acquisition Date	4/6/2023 4:20:54 PM
Analysis Name	D:\Data\2023\DPMMMEY-005_GB4_01_175.d	Operator	cgueret
Method	175.m	Instrument	amaZon speed
Sample Name	MEY-005		
Comment	5 10e-4 M CH2Cl2		

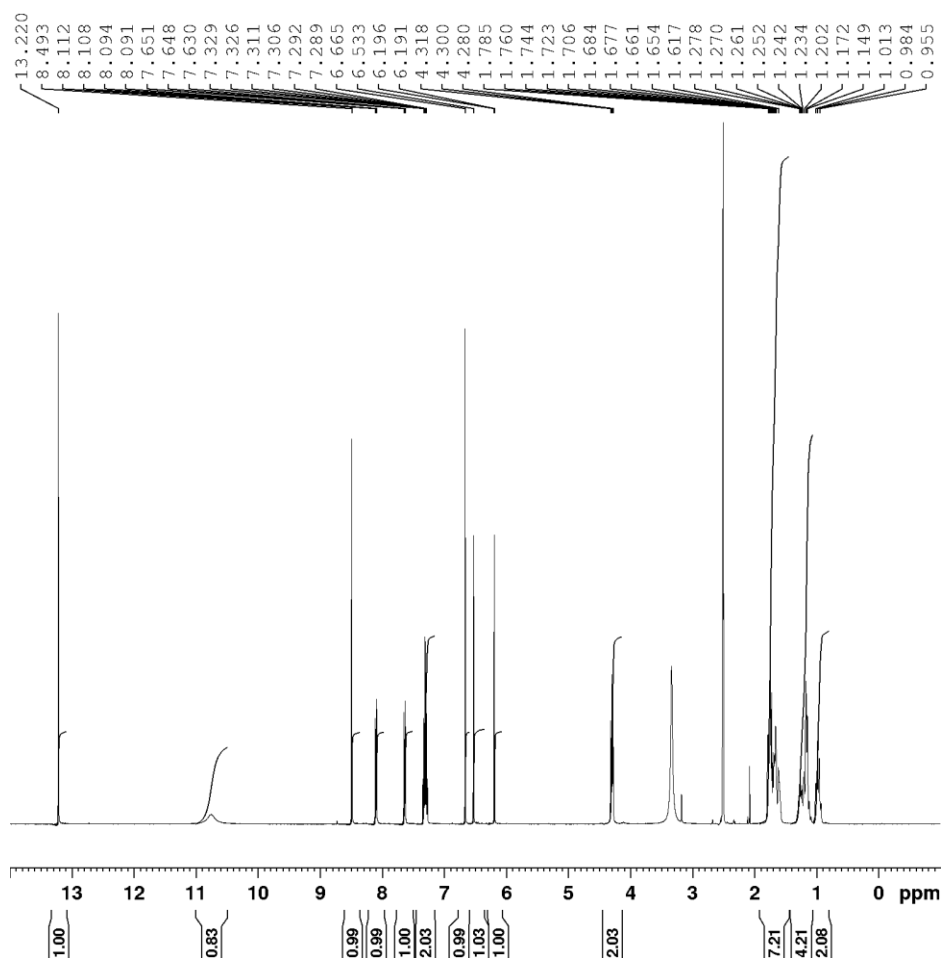
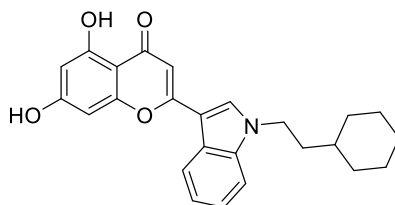
<b>Acquisition Parameter</b>			
Ion Source Type	ESI	Ion Polarity	Positive
Mass Range Mode	UltraScan	Scan Begin	50 m/z
Accumulation Time	638 $\mu$ s	RF Level	63 %
SPS Target Mass	400 m/z	Averages	10 Spectra
		Alternating Ion Polarity	on
		Scan End	1000 m/z
		Trap Drive	49.0
			n/a





Supplementary data

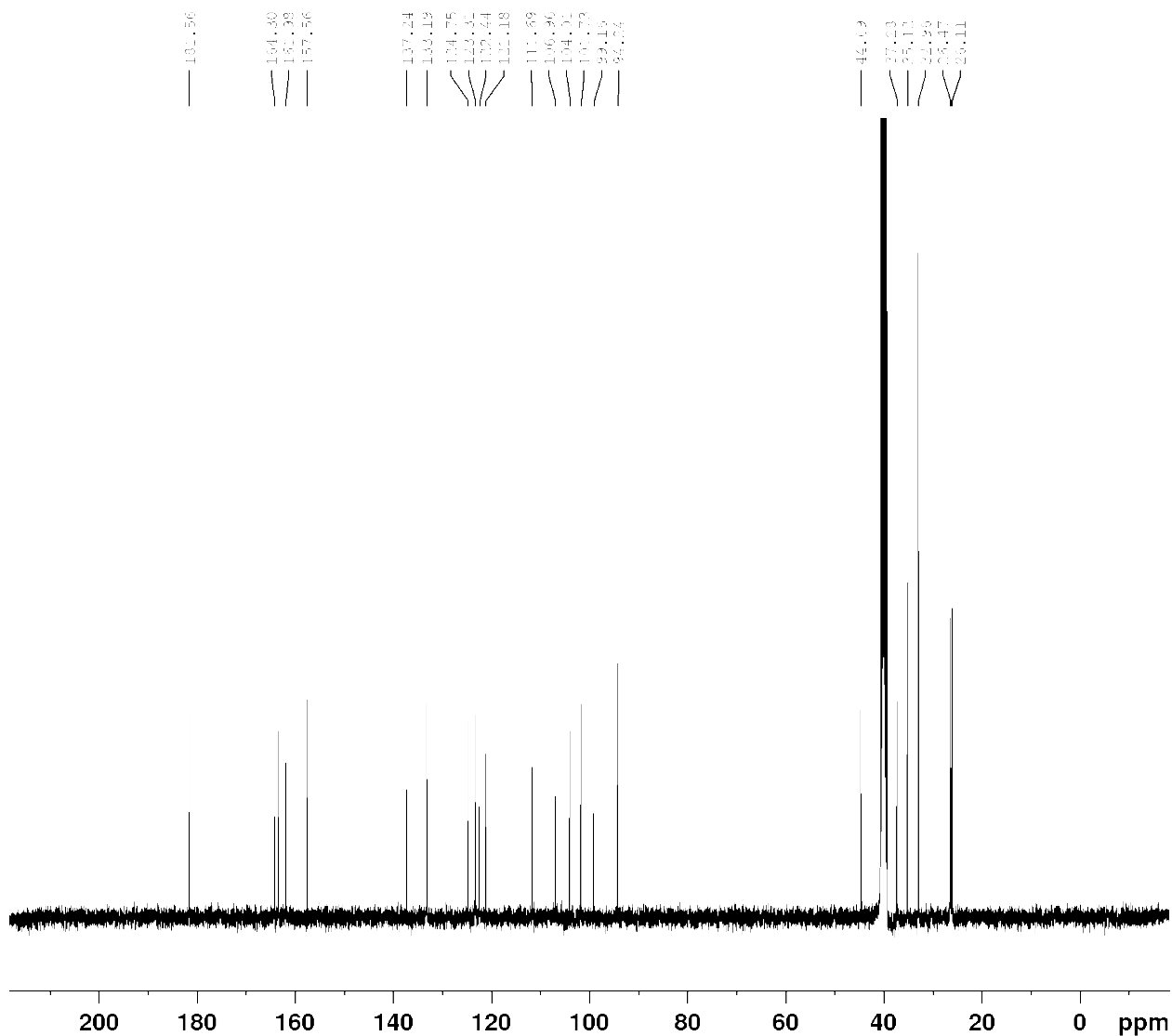
**MEY-007**



supplementary 19: <sup>1</sup>H NMR spectra of MEY-007

<sup>1</sup>H NMR (DMSO-*d*<sub>6</sub>, 400 MHz): 13.22 (s, 1H), 10.75 (s, 1H), 8.50 (m, 1H), 8.1 (m, 1H), 7.66 (m, 1H), 7.32 (m, 2H), 6.68 (m, 1H), 6.54 (m, 1H), 6.18 (m, 1H), 4.33 (m, 2H), 1.72 (m, 7H), 1.17 (m, 4H), 0.97 (m, 2H)

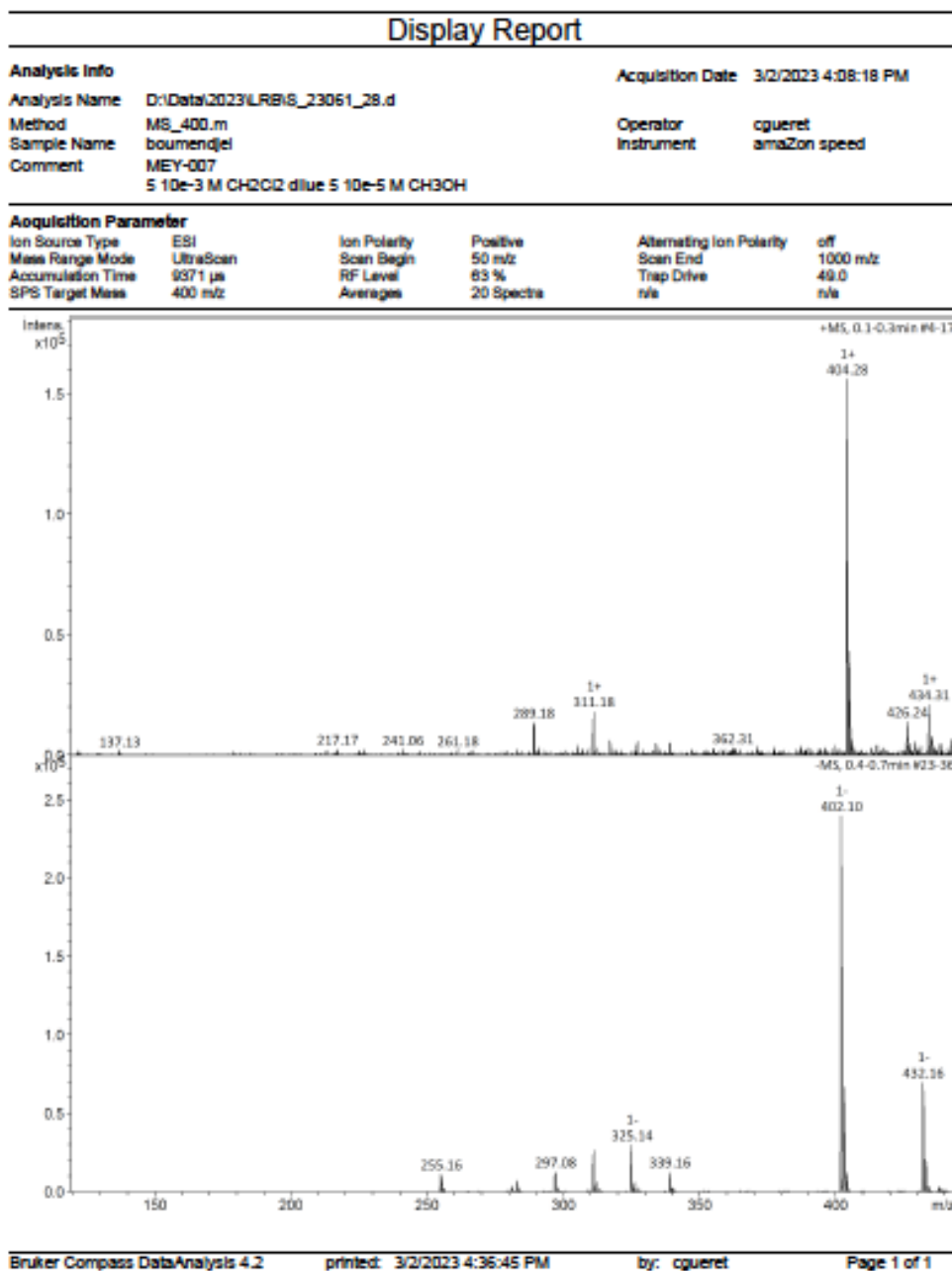
Supplementary data



supplementary 20:  $^{13}\text{C}$  NMR spectra of MEY-007

$^{13}\text{C}$  NMR (DMSO- $d_6$ , 100 MHz): 181.56, 164.30, 161.98, 157.56, 137.24, 133.19, 124.75, 123.31, 122.44, 121.18, 111.69, 106.96, 104.01, 101.73, 99.16, 94.24, 44.69, 37.28, 35.12, 32.96, 26.47, 26.11

Supplementary data



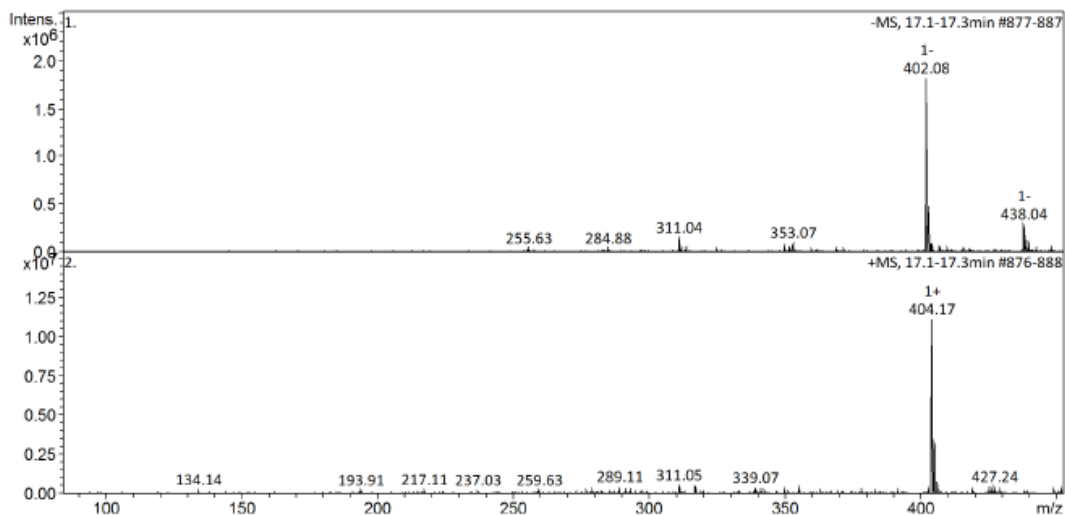
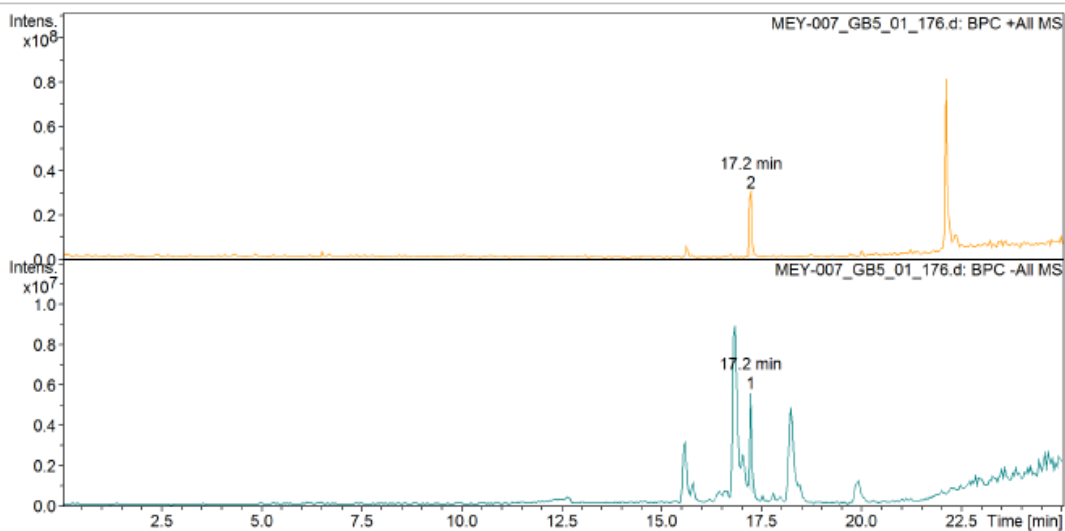
supplementary 21: ESI of MEY-007

LRMS (ESI+) m/z 404.28  $[M+H]^+$ . LRMS (ESI-) m/z 402.10  $[M-H]^-$ . Theoretical MW: 405.49 g/mol

## Display Report

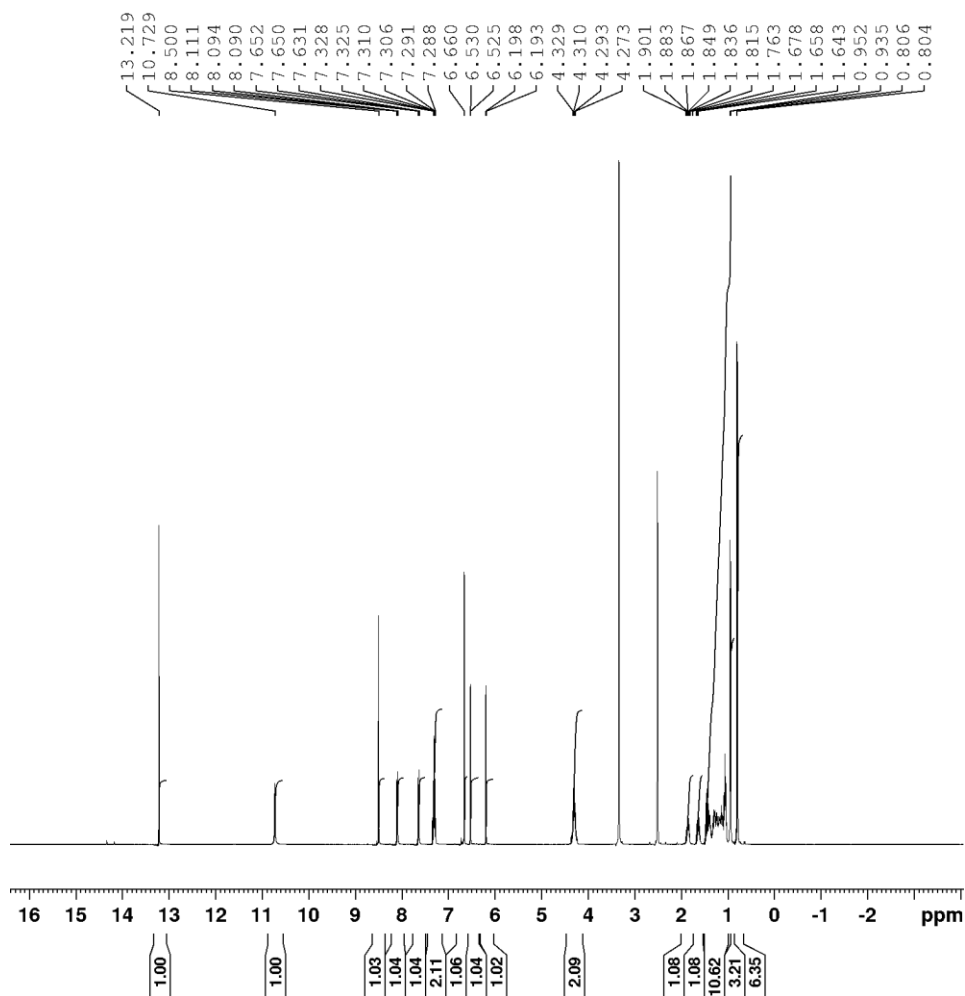
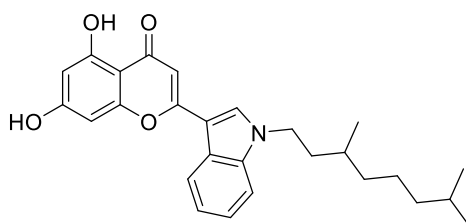
<b>Analysis Info</b>		Acquisition Date	4/6/2023 4:53:47 PM
Analysis Name	D:\Data\2023\DPMMMEY-007_GB5_01_176.d	Operator	cgueret
Method	176.m	Instrument	amaZon speed
Sample Name	MEY-007		
Comment	5 10e-4 M CH2Cl2		

<b>Acquisition Parameter</b>			
Ion Source Type	ESI	Ion Polarity	Negative
Mass Range Mode	UltraScan	Scan Begin	50 m/z
Accumulation Time	5718 µs	RF Level	63 %
SPS Target Mass	400 m/z	Averages	10 Spectra
		Alternating Ion Polarity	on
		Scan End	1000 m/z
		Trap Drive	53.2
			n/a



Supplementary data

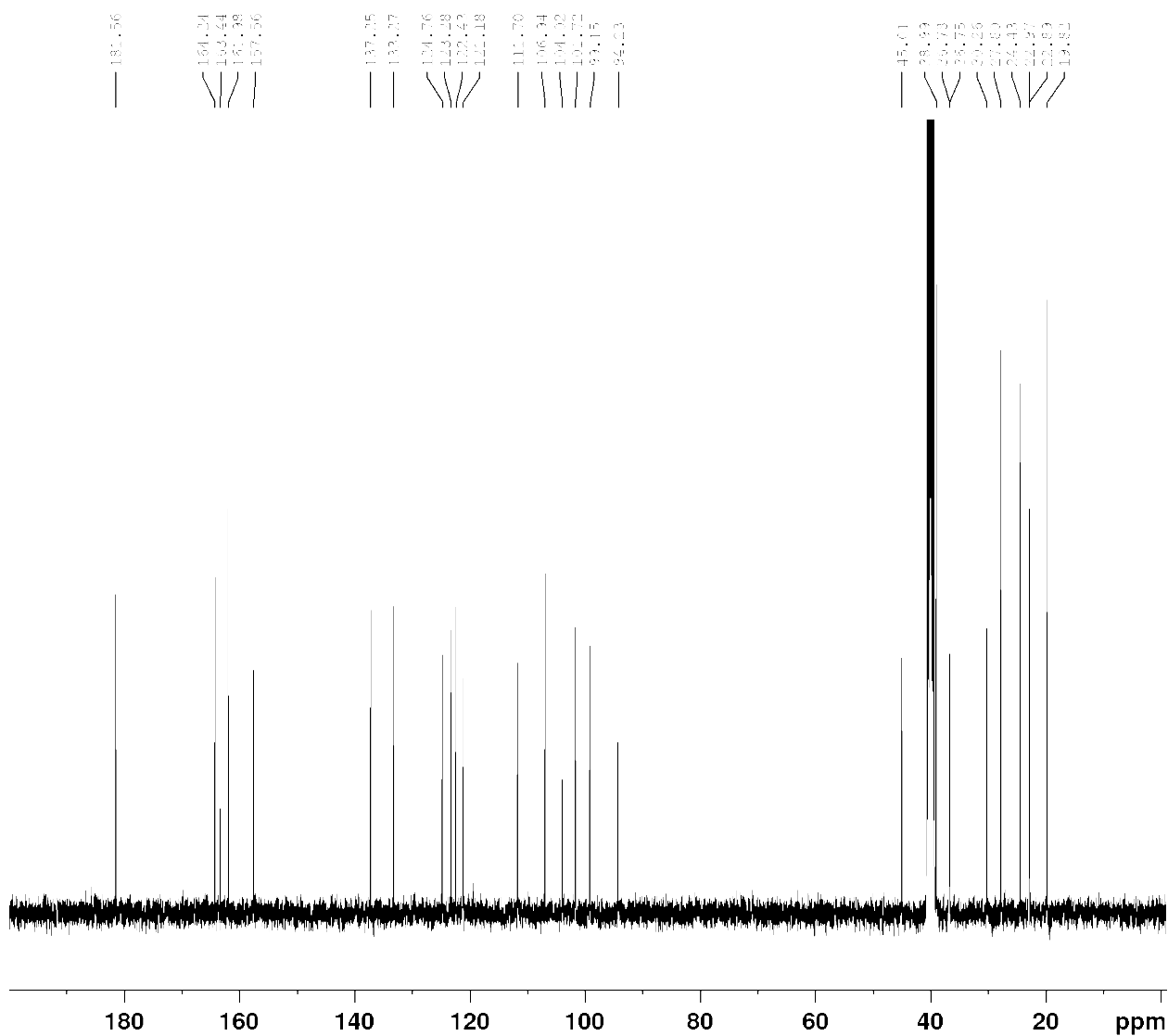
**MEY-008**



*supplementary 23: <sup>1</sup>H NMR spectra of MEY-008*

<sup>1</sup>H NMR (DMSO-*d*<sub>6</sub>, 400 MHz): 13.21 (s, 1H), 10.72 (s, 1H), 8.50(s,1H), 8.1 (d, 1H), 7.76 (d,1H), 7.30 (m, 1H), 6.65 (s, 1H), 6.52 (d, 1H), 6.19 (d, 1H), 4.30 (m, 2H), 1.88 (m, 1H), 1.65 (m, 1H), 1.2 (m, 10H), 0.90 (d, 3H), 0.80 (d, 6H)

## Supplementary data



supplementary 24:  $^{13}\text{C}$  NMR spectra of MEY-008

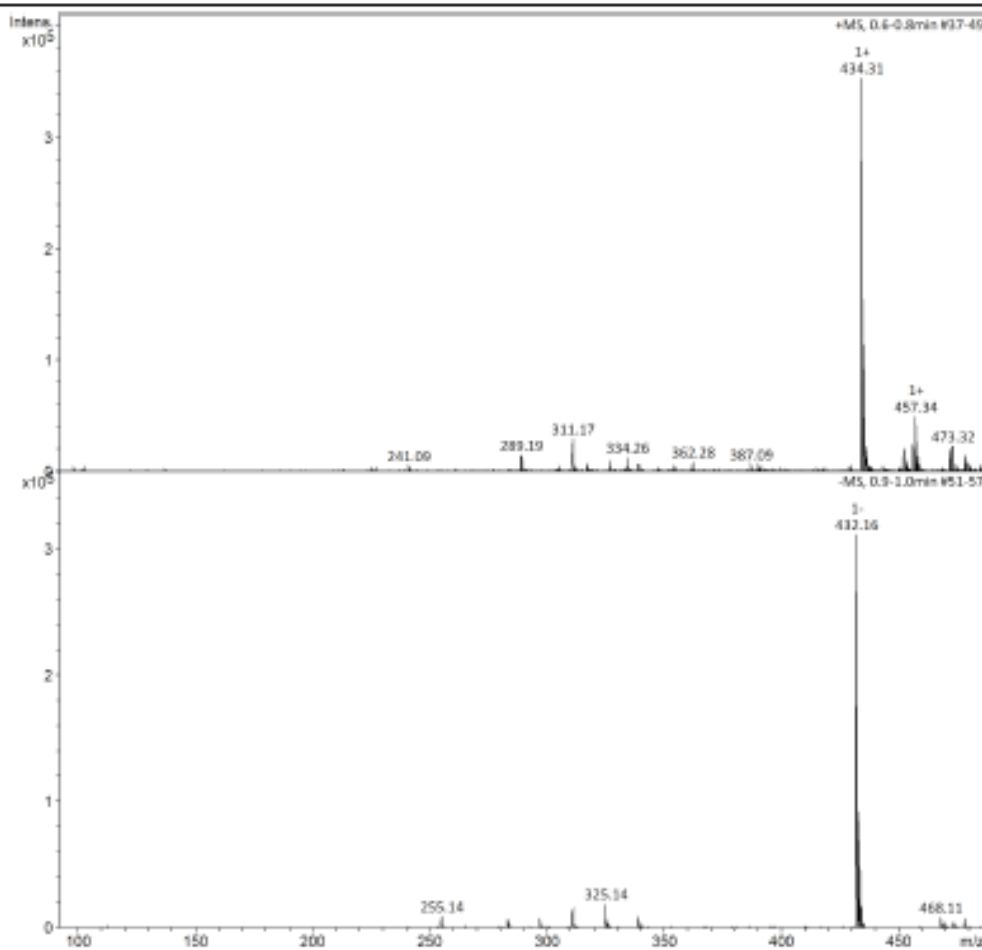
$^{13}\text{C}$  NMR (DMSO- $d_6$ , 100 MHz): 181.56, 164.24, 163.44, 161.98, 157.56, 137.25, 133.27, 124.76, 123.28, 122.43, 121.18, 111.70, 106.94, 104.02, 101.72, 99.15, 94.23, 45.01, 38.99, 36.78, 36.75, 30.26, 27.80, 24.43, 22.97, 22.89, 19.82

# Supplementary data

## Display Report

<b>Analysis Info</b>		<b>Acquisition Date</b>	3/2/2023 4:06:05 PM
<b>Analysis Name</b>	D:\Data\2023\LRBS_23051_27.d		
<b>Method</b>	MS_400.m	<b>Operator</b>	cguret
<b>Sample Name</b>	boumendjel	<b>Instrument</b>	amaZon speed
<b>Comment</b>	MEY-008 5 10e-3 M CH2Cl2 dilue 5 10e-5 M CH3OH		

<b>Acquisition Parameter</b>					
<b>Ion Source Type</b>	ESI	<b>Ion Polarity</b>	Positive	<b>Alternating Ion Polarity</b>	off
<b>Mass Range Mode</b>	UltraScan	<b>Scan Begin</b>	50 m/z	<b>Scan End</b>	1000 m/z
<b>Accumulation Time</b>	3050 $\mu$ s	<b>RF Level</b>	83 %	<b>Trap Drive</b>	49.0
<b>SPS Target Mass</b>	400 m/z	<b>Averages</b>	20 Spectra	<b>n/a</b>	n/a



supplementary 25: ESI of MEY-008

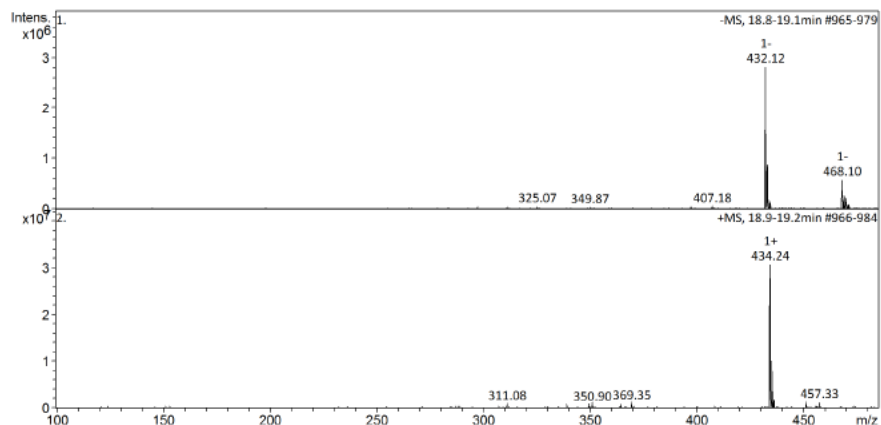
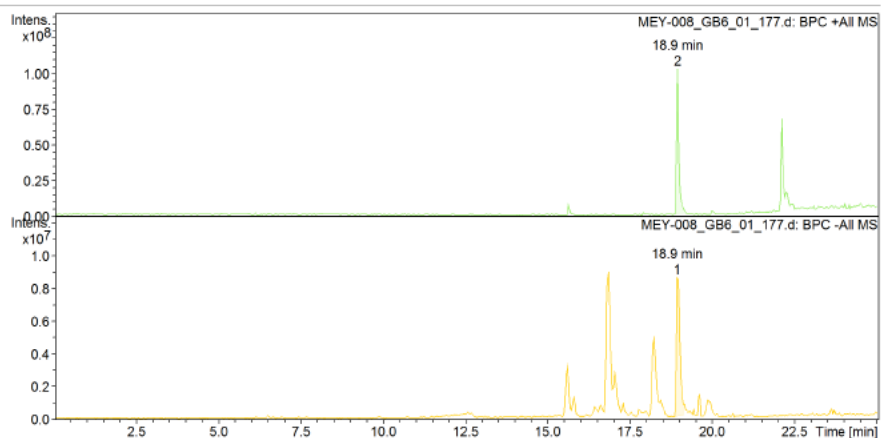
LRMS (ESI+) m/z 434.31  $[M+H]^+$ . LRMS (ESI-) m/z 432.16  $[M-H]^-$ . Theoretical MW:  
435.562g/mol

# Supplementary data

## Display Report

**Analysis Info**  
Analysis Name D:\Data\2023\DPMMMEY-008\_GB6\_01\_177.d Acquisition Date 4/6/2023 5:26:38 PM  
Method 177.m Operator cgueret  
Sample Name MEY-008 Instrument amazon speed  
Comment 5 10e-4 M CH2Cl2

**Acquisition Parameter**  
Ion Source Type ESI Ion Polarity Negative Alternating Ion Polarity on  
Mass Range Mode UltraScan Scan Begin 50 m/z Scan End 1000 m/z  
Accumulation Time 5904  $\mu$ s RF Level 83 % Trap Drive 53.2  
SPS Target Mass 400 m/z Averages 10 Spectra n/a

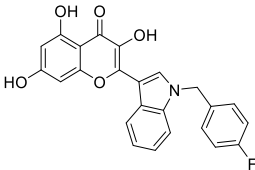
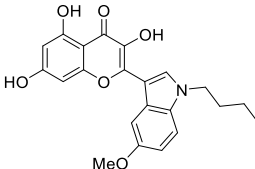
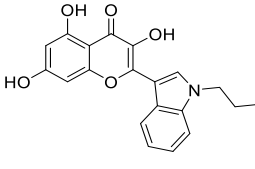
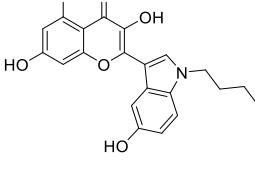
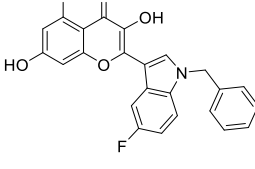


Bruker Compass DataAnalysis 4.2 printed: 4/7/2023 12:30:54 PM by: cgueret Page 1 of 1

supplementary 26: LCMS of MEY-008



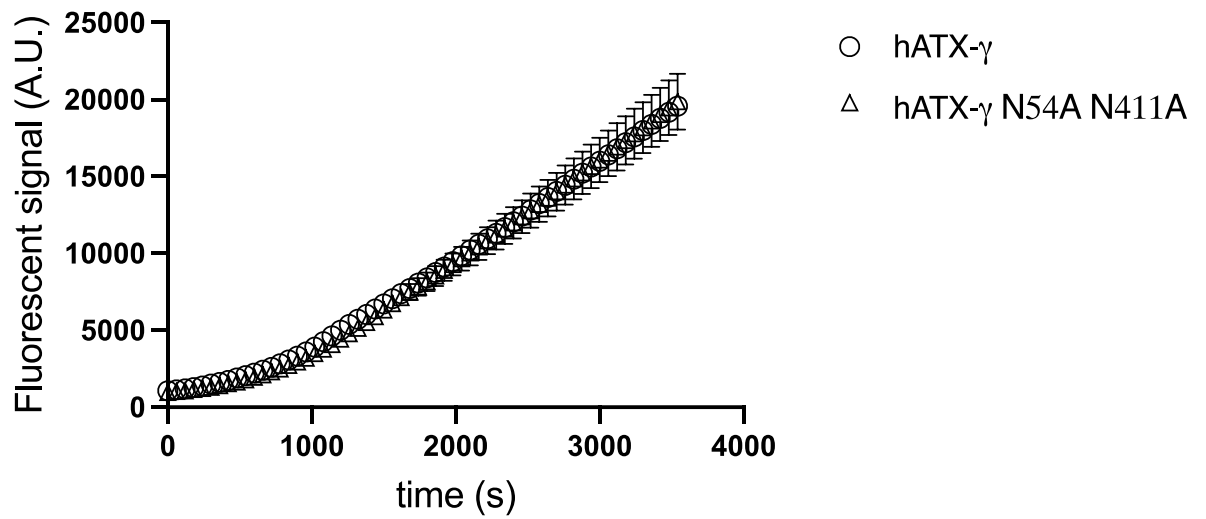
Supplementary data

Reference	Structure	IC <sub>50</sub> hATX (μM)
KAN-VI-115		2.06 (1.15-4.9)
KAN-VI-123		> 5
KAN-VI-125		1.36 (1.1-1.6)
KAN-VI-126		> 5
KAN-VI-127		> 5

supplementary 27: Analogs of MEY-003 bearing an extra hydroxyl group at position 3 of the chromone moiety. are less potent than MEY-003, using the FS3 assay.

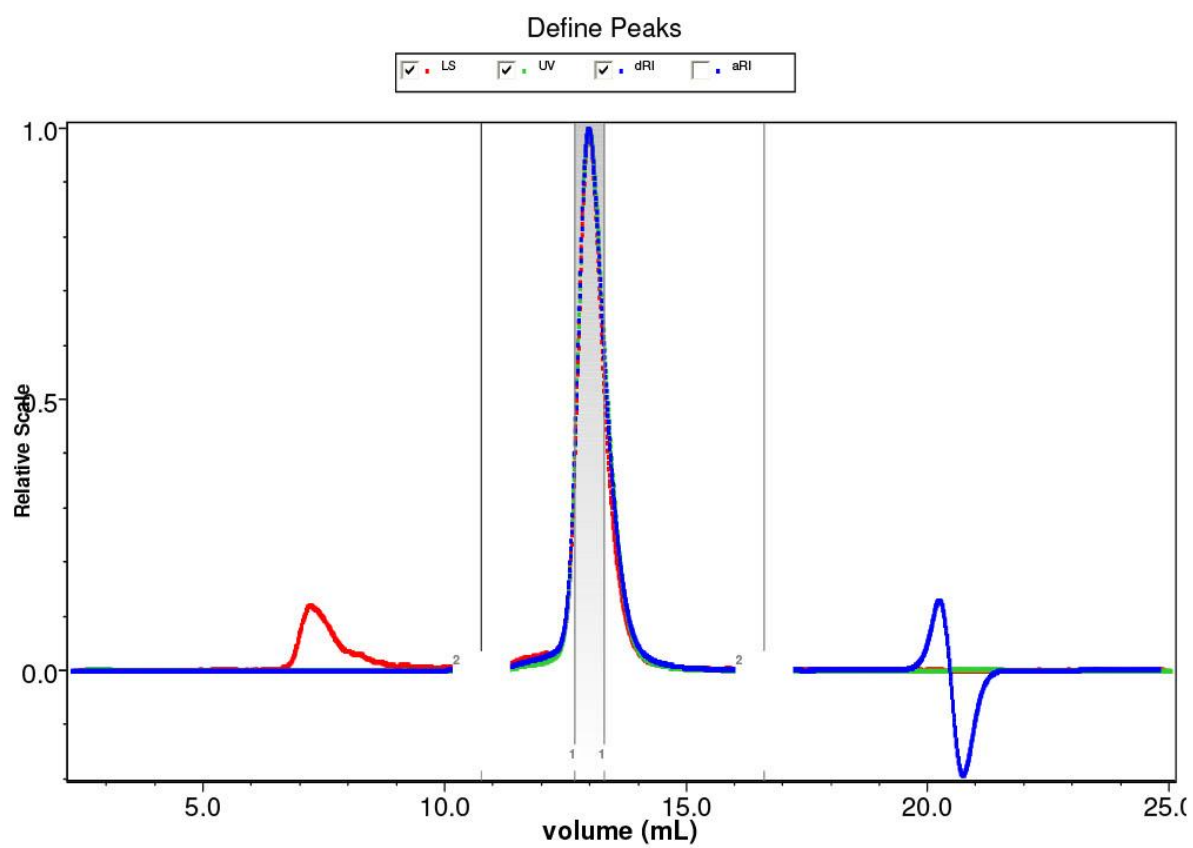
**OH-flavone-derived inhibitors structure and compound characterization using the FS3 assay. IC<sub>50</sub> incertitude are given by 95% CI (profile likelihood).**

Supplementary data



*supplementary 28: hATX- $\gamma$  and hATX- $\gamma$  N54A N411A have the same catalytic activity towards LPC18:1.*

Supplementary data



supplementary 29: SEC-MALL curves of rATX

# Supplementary data

ASTRA 6 Report Exp 1105

ASTRA 6 Report Exp 1105



**File Name:** D:\MALLS-HELEOS\_2022\Exp 1105.afe6  
**Collection Operator:** GRE026565\cibb (GRE026565\cibb (cibb))  
**Processing Operator:** GRE026565\cibb (cibb)

**Sample:**

**Concentration:** 0.000 mg/mL

### Configuration

**Concentration Source:** RI  
**Flow Rate:** 0.500 mL/min

**Light Scattering Instrument:** HELEOS

**Band Broadening Correction:** Yes (Instrumental: 7.895 µL, Mixing: 63.407 µL, Mixing2: 1.000 µL, Relative Amplitude: 1.000)

**Cell Type:** Fused Silica

**Wavelength:** 663.8 nm

**Calibration Constant:**  $3.1531 \times 10^{-5}$  1/(V cm)

Detector	Scattering angle	Gain	Normalization coefficient
1	n/a	n/a	1.000
2	12.9°	n/a	2.643
3	20.6°	n/a	1.881
4	29.6°	n/a	1.997
5	37.4°	n/a	2.659
6	44.8°	n/a	0.754
7	53.0°	n/a	0.845
8	61.1°	n/a	0.923
9	70.1°	n/a	0.932
10	80.1°	n/a	1.030
11	90.0°	n/a	1.000
12	99.9°	n/a	1.004
13	109.9°	n/a	0.925
14	120.1°	n/a	0.934
15	130.5°	n/a	0.788
16	140.1°	n/a	0.731
17	149.1°	n/a	2.318
18	157.8°	n/a	1.973

**RI Instrument:** rEX

**Band Broadening Correction:** n/a

**Wavelength:** 658.0 nm

**UV Instrument:** generic UV

**Band Broadening Correction:** Yes (Instrumental: 29.930 µL, Mixing: 74.543 µL, Mixing2: 1.000 µL, Relative Amplitude: 1.000)

**UV Cell Length:** 1.000 cm

**UV Response Factor:** 1.000 AU/V

**Solvent:** water

**Temperature Correction Enabled:** yes

**Refractive Index:** 1.330

Fluid Connections	Destination Instrument	Delay Volume (mL)
-------------------	------------------------	-------------------

ASTRA 6.1.7.17

14/06/2022 14:41:11

1 of 3

## Supplementary data

### ASTRA 6 Report Exp 1105

Source Instrument	Destination Instrument	Delay Volume (mL)
Generic Pump	Injector	0.000
Injector	Generic UV Instrument	0.000
Generic UV Instrument	DAWN HELEOS	0.108
DAWN HELEOS	Optilab rEX	0.106

Source Instrument	Destination Instrument	Aux Channel	Calibration Constant
Generic UV Instrument	DAWN HELEOS	2	1.000

### Processing

Collection Time: Thursday June 09, 2022 09:52:03 AM Paris, Madrid (heure d'été)  
 Processing Time: Thursday June 09, 2022 10:55:50 AM Paris, Madrid (heure d'été)

#### Basic Collection:

LS Instrument Collection Interval: 1.000 sec

#### Baselines:

Series	Start	Stop	Type
detector 2	(4.317, 0.311)	(22.400, 0.303)	manual x, auto y
detector 3	(4.317, 0.112)	(22.400, 0.103)	manual x, auto y
detector 4	(4.317, 0.048)	(22.400, 0.045)	manual x, auto y
detector 5	(4.317, 0.015)	(22.400, 0.015)	manual x, auto y
detector 6	(4.317, 0.051)	(22.400, 0.049)	manual x, auto y
detector 7	(4.317, 0.035)	(22.400, 0.034)	manual x, auto y
detector 8	(4.317, 0.026)	(22.400, 0.026)	manual x, auto y
detector 9	(4.317, 0.026)	(22.400, 0.026)	manual x, auto y
detector 10	(4.317, 0.021)	(22.400, 0.021)	manual x, auto y
detector 11	(4.317, 0.022)	(22.400, 0.022)	manual x, auto y
detector 12	(4.317, 0.021)	(22.400, 0.021)	manual x, auto y
detector 13	(4.317, 0.026)	(22.400, 0.026)	manual x, auto y
detector 14	(4.317, 0.041)	(22.400, 0.039)	manual x, auto y
detector 15	(4.317, 0.042)	(22.400, 0.042)	manual x, auto y
detector 16	(4.317, 0.065)	(22.400, 0.066)	manual x, auto y
detector 17	(4.317, 0.026)	(22.400, 0.025)	manual x, auto y
detector 18	(4.317, 0.051)	(22.400, 0.050)	manual x, auto y
channel	(4.317, 0.004)	(22.400, 0.001)	manual x, auto y
differential refractive index data	(4.317, -0.000)	(22.400, -0.000)	manual x, auto y

#### Peak settings:

Peak Name	Peak 1	Peak 2
Peak Limits (mL)	12.701 - 13.316	10.770 - 16.607
Light Scattering Model	Zimm	Zimm
Fit Degree	1	1
dn/dc (mL/g)	0.1850	0.1850
A2 (mol mL <sup>2</sup> g <sup>-2</sup> )	0.000	0.000
UV Ext. Coef. (mL/(mg cm))	0.000	0.000

#### Results Fitting Procedure:

Data	Fit Model	Degree	r <sup>2</sup>	Extrapolation
Molar Mass	None	n/a	n/a	none
Rms Radius	None	n/a	n/a	none
Mean Square Radius	None	n/a	n/a	none

### Results

#### Peak Results

	Peak 1	Peak 2
<b>Masses</b>		
Injected Mass (µg)	0.00	0.00
Calculated Mass (µg)	110.69	165.95
Mass Recovery (%)	n/a	n/a

ASTRA 6.1.7.17

14/06/2022 14:41:11

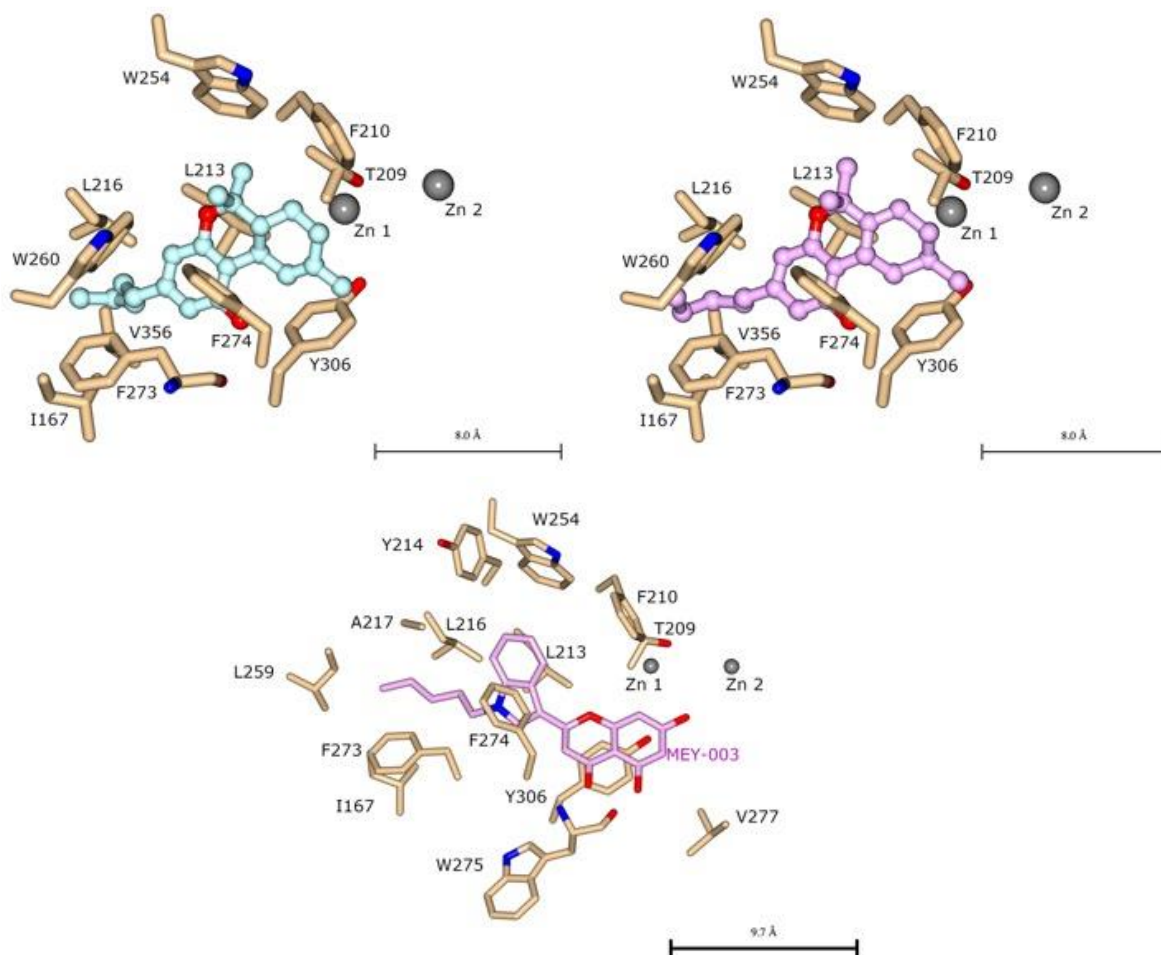
2 of 3

### ASTRA 6 Report Exp 1105

	Peak 1	Peak 2
<b>Mass Fraction (%)</b>	66.7	100.0
<b>Molar mass moments (g/mol)</b>		
Mn	9.884×10 <sup>4</sup> (±1.631%)	9.591×10 <sup>4</sup> (±2.949%)
Mp	1.009×10 <sup>5</sup> (±1.618%)	1.009×10 <sup>5</sup> (±1.618%)
Mv	n/a	n/a
Mw	9.890×10 <sup>4</sup> (±1.631%)	9.827×10 <sup>4</sup> (±4.413%)
Mz	9.895×10 <sup>4</sup> (±3.647%)	1.083×10 <sup>5</sup> (±21.710%)
Mz+1	9.900×10 <sup>4</sup> (±5.878%)	1.760×10 <sup>5</sup> (±63.079%)
M(avg)	9.836×10 <sup>4</sup> (±0.191%)	9.249×10 <sup>4</sup> (±0.144%)
<b>Polydispersity</b>		
Mw/Mn	1.001 (±2.306%)	1.025 (±5.308%)
Mz/Mn	1.001 (±3.995%)	1.129 (±21.909%)
<b>rms radius moments (nm)</b>		
Rn	15.7 (±24.3%)	16.0 (±41.8%)
Rw	15.6 (±24.4%)	17.4 (±39.1%)
Rz	15.6 (±24.5%)	20.2 (±42.8%)
R(avg)	15.7 (±2.8%)	19.0 (±1.5%)

supplementary 30: SEC-MALLS report of rATX

Supplementary data



supplementary 31 : 3D representation of the interaction of THC(a), 6a10aTHC(b) and MEY-003(c) with surrounding amino acids in ATX hydrophobic pocket



# Linking medicinal cannabis to autotaxin–lysophosphatidic acid signaling

Mathias C Eymery<sup>1</sup> , Andrew A McCarthy<sup>1</sup> , Jens Hausmann<sup>1,2</sup>

**Autotaxin is primarily known for the formation of lysophosphatidic acid (LPA) from lysophosphatidylcholine. LPA is an important signaling phospholipid that can bind to six G protein–coupled receptors (LPA<sub>1–6</sub>). The ATX-LPA signaling axis is a critical component in many physiological and pathophysiological conditions. Here, we describe a potent inhibition of  $\Delta^9$ -*trans*-tetrahydrocannabinol (THC), the main psychoactive compound of medicinal cannabis and related cannabinoids, on the catalysis of two isoforms of ATX with nanomolar apparent EC<sub>50</sub> values. Furthermore, we decipher the binding interface of ATX to THC, and its derivative 9(R)- $\Delta$ 6a,10a-THC (6a10aTHC), by X-ray crystallography. Cellular experiments confirm this inhibitory effect, revealing a significant reduction of internalized LPA<sub>1</sub> in the presence of THC with simultaneous ATX and lysophosphatidylcholine stimulation. Our results establish a functional interaction of THC with autotaxin–LPA signaling and highlight novel aspects of medicinal cannabis therapy.**

DOI [10.26508/lsa.202201595](https://doi.org/10.26508/lsa.202201595) | Received 8 July 2022 | Revised 25 November 2022 | Accepted 25 November 2022 | Published online 9 January 2023

## Introduction

Autotaxin (ATX; ENPP2) is an extracellular glycoprotein, which hydrolyzes lysophosphatidylcholine (LPC) into lysophosphatidic acid (LPA) by cleaving off the choline head group (Tokumura et al, 2002; Umezū-Goto et al, 2002; Moolenaar & Perrakis, 2011). LPA is a multifunctional bioactive lipid mediator with six designated G protein–coupled receptors (LPA<sub>1–6</sub>) (Noguchi et al, 2009), forming together with ATX the ATX-LPA signaling axis. ATX is the main producer of LPA in blood, which has been demonstrated by a heterozygous *Enpp2* (ATX) knockout mouse model. These mice show only 50% of the normal LPA levels in serum (van Meeteren et al, 2006). It is widely accepted that the ATX-LPA signaling axis is of crucial importance for lipid homeostasis in humans (Smyth et al, 2014). ATX is present in almost every body fluid and essential for murine embryonic vessel formation, which highlights its importance for life (Aoki, 2004; Boutin & Ferry, 2009; Moolenaar & Perrakis,

2011). Thus, the ATX-LPA axis is linked to numerous physiological and pathological processes, such as vascular and neuronal development, neuropathic pain, fibrosis, and immune-mediated diseases including rheumatoid arthritis, multiple sclerosis, atherosclerosis, and cancer (Moolenaar & Perrakis, 2011). In fact, *Enpp2* (ATX) is among the top 40 most up-regulated genes in metastatic breast cancer (Euer et al, 2002), whereas ATX-LPA signaling is positively correlated with the invasive and metastatic potential of several cancers including melanoma, breast, ovarian, thyroid, renal cell, lung, neuroblastoma, hepatocellular carcinoma, and glioblastoma multiforme (Samadi et al, 2011).

ATX consists of four domains, two repetitive N-terminal somatomedin B-like domains (SMB1 and SMB2), followed by the catalytic phosphodiesterase domain (PDE) and an inactive nuclease domain (Nuc) (Hausmann et al, 2011; Nishimasu et al, 2011). The active site of ATX constitutes a bimetallo zinc coordination center and the active site nucleophile, Thr209, in rodents (Hausmann et al, 2011). A nearby hydrophobic pocket, which extends into the PDE domain, accommodates the lipid substrate aliphatic chain; in addition, there is an allosteric tunnel that is formed between the SMB2 and PDE domains, where an oxysterol and bile acids bind (Hausmann et al, 2011; Keune et al, 2016).

The gene product of ATX can exist in at least three different isoforms, which are ATX- $\alpha$ , ATX- $\beta$ , and ATX- $\gamma$ , as a result of an alternative splicing event (Giganti et al, 2008). ATX- $\alpha$  is characterized by a polybasic insertion of 52 amino acids in the PDE domain, when compared to the canonical plasma isoform ATX- $\beta$ . ATX- $\alpha$  can bind to heparin and cell surface heparan sulfate proteoglycans (Houben et al, 2013), whereas ATX- $\beta$  has been shown to bind to  $\beta_1$  and  $\beta_3$  subunits of integrins (Kanda et al, 2008; Hausmann et al, 2011). ATX- $\gamma$  is the so-called “brain-specific” isoform (Perrakis & Moolenaar, 2014) and has been implicated with neuronal disorders, such as multiple sclerosis, depression, Alzheimer’s disease, and neuropathic pain (Moolenaar & Perrakis, 2011).

Another important signaling system is the well-established endocannabinoid system (Cristino et al, 2020), with its two cannabinoid receptors, the cannabinoid receptor type 1 (CB<sub>1</sub>) and type 2 (CB<sub>2</sub>) (Matsuda et al, 1990; Munro et al, 1993). The human CB<sub>1</sub> is primarily expressed in the central nervous system and also present in the peripheral nervous system and testis (Matsuda et al, 1990), whereas the CB<sub>2</sub> is mainly expressed in the immune system (Munro

<sup>1</sup>European Molecular Biology Laboratory, Grenoble, Grenoble, France <sup>2</sup>European Molecular Biology Laboratory, Chemical Biology Core Facility, Heidelberg, Germany

Correspondence: [andrewmc@embl.fr](mailto:andrewmc@embl.fr); [jens.hausmann@uni-oldenburg.de](mailto:jens.hausmann@uni-oldenburg.de)

Jens Hausmann’s present address is Research Group Anatomy, School of Medicine and Health Sciences, Carl von Ossietzky University of Oldenburg, Oldenburg, Germany

et al, 1993). The endogenous ligands, anandamide (Devane et al, 1992) and 2-arachidonoylglycerol (2-AG) (Sugiura et al, 1995), which were detected in samples of the brain and intestine and shown to activate CB<sub>1</sub> and CB<sub>2</sub> with high affinity and efficacy, were subsequently identified as endocannabinoids (Di Marzo & Fontana, 1995; Cristino et al, 2020). The endocannabinoid system can be further expanded to the endocannabinoidome, a much wider complex network of promiscuous mediators overlapping with other signaling pathways, including LPA and its receptors (Cristino et al, 2020). Interestingly, it has been shown that dephosphorylation of a 2-arachidonoyl species of LPA in the brain of rats leads to the formation of the endocannabinoid 2-AG (Nakane et al, 2002), a process that was later revealed to depend on lipid phosphate phosphatases (Aaltonen et al, 2012). In addition, the two endocannabinoid receptors, CB<sub>1</sub> and CB<sub>2</sub>, show an amino acid sequence identity to LPA<sub>1-3</sub> of around 18–20% (Chun et al, 1999). Moreover, a functional crosstalk between CB<sub>1</sub> and LPA<sub>1</sub> has been revealed, where the absence of the main cerebral receptors for LPA or endocannabinoids is able to induce a modulation

on the other at the levels of both signaling and synthesis of endogenous neurotransmitters (González de San Román et al, 2019).

Pharmacological manipulation of the endocannabinoid system can be achieved by medicinal cannabis. The major psychoactive cannabinoid component of medicinal cannabis from the plant *Cannabis sativa* is  $\Delta^9$ -trans-tetrahydrocannabinol (THC), which can bind to CB<sub>1</sub> and CB<sub>2</sub> in a low nanomolar regime (Pertwee, 2008). Here, we show the potential of THC, and other cannabinoid compounds, to modulate the catalytic activity of ATX, and present results that THC can reduce ATX-mediated LPA signaling in a cellular context.

## Results and Discussion

### Inhibition of ATX by various cannabinoids

We first set out to validate the hypothesis that cannabinoids might bind ATX to modulate its catalytic function. For this, we used various cannabinoids (Fig 1A) at a fixed concentration of 10  $\mu$ M for each

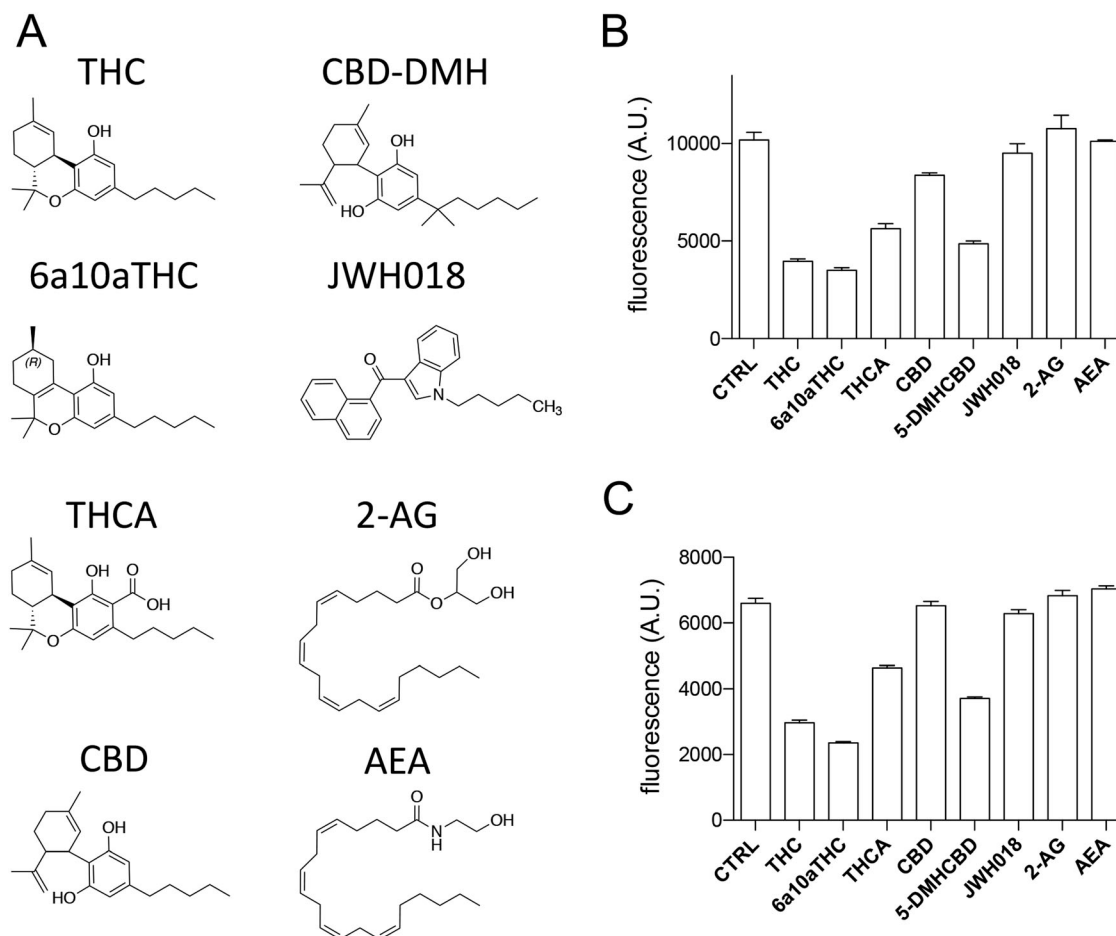


**Figure 1. End-point assays of compounds tested.**

(A) Chemical representation of  $\Delta^9$ -trans-tetrahydrocannabinol (THC), cannabidiol-dimethylheptyl (CBD-DMH), 9(R)- $\Delta^6$ a,10a-THC (6a10aTHC), JWH018, tetrahydrocannabinolic acid, 2-arachidonoylglycerol, cannabidiol (CBD), and anandamide. (B, C) End-point assay for (B) ATX- $\beta$  and (C) ATX- $\gamma$  inhibition with various cannabinoids and endocannabinoids. All error bars represent the SEM (n = 3). (B, C) Activity rate of 99 and 65 mMol end product/mM ATX/min has been found for (B, C), respectively. ANOVA comparison between CTRL and other conditions showed statistically significant differences for THC, 6a10aTHC, tetrahydrocannabinolic acid, CBD, and 5-DMH-CBD for ATX- $\beta$  and ATX- $\gamma$  inhibition ( $P < 0.005$ ). ATX was not significantly inhibited by JWH018, anandamide, and 2-arachidonoylglycerol ( $P > 0.005$ ).



compound in our biochemical validation with LPC 18:1 (200  $\mu$ M) as substrates in an end-point assay for ATX- $\beta$  (UniProt ID: Q13822-1) and ATX- $\gamma$  (UniProt ID: Q13822-3) (Fig 1B and C). The quality of our enzyme assay is confirmed with HA155, a well-documented ATX inhibitor (Fig S1A) (Albers et al, 2011; Hausmann et al, 2011). The obtained  $IC_{50}$  ( $6 \pm 0.8$  nM) for HA155 is similar in our assay conditions compared with previous results (Albers et al, 2011). In addition, we can exclude interference of the cannabinoid compounds in our enzymatically coupled assay, as no difference is detectable in the absence of ATX and LPC (Fig S1B), performed in the presence of choline.

We observe a potent inhibition of THC on the catalysis of both ATX isoforms with more than 50% inhibition (Fig 1B and C). Furthermore, 9(R)- $\Delta$ 6a,10a-THC (for simplicity referred to from here as 6a10aTHC), a derivative of THC that differs only in the position of the double bond in the C-ring compared with THC (Fig 1A), is included in our cannabinoid inhibition screen. Interestingly, this minimal difference causes a further increase in the magnitude of inhibition for both ATX isoforms tested (Fig 1B and C). Tetrahydrocannabinolic acid is a precursor of THC and an active component of medicinal cannabis. It is distinguishable from THC by the presence of a carboxylic group at the A-ring (Fig 1A). Tetrahydrocannabinolic acid also showed an inhibition of the enzymatic activity of both ATX isoforms tested. However, this inhibition is less pronounced, when compared to THC and 6a10aTHC, and did not reach a 50% inhibition magnitude in our assay conditions (Fig 1B and C).

The next compound we tested was cannabidiol (CBD), a non-psychoactive ingredient of medicinal cannabis. CBD is structurally different from THC by an opening of the B-ring. Interestingly, CBD showed only a weak inhibition toward ATX- $\beta$ , and no observable inhibition for ATX- $\gamma$  (Fig 1B and C). CDB-DMH is a synthetic CBD derivative, which is characterized by the addition of two methyl groups at the beginning of the aliphatic chain and an elongation with a single methyl group at the end of the carbon chain (Fig 1A). These structural modifications remarkably increase the magnitude of inhibition for ATX- $\beta$  and ATX- $\gamma$  (Fig 1B and C).

We also analyzed JWH018 (Fig 1A), which is a synthesized compound and full agonist for CB<sub>1</sub> and CB<sub>2</sub> with  $K_i$  values of  $9.0 \pm 8.0$  and  $2.9 \pm 2.7$  nM, respectively (Aung et al, 2000). However, this artificial cannabinoid did not influence the catalytic activity of either ATX- $\beta$  or ATX- $\gamma$  isoforms (Fig 1B and C). To complete our picture of the modulation cannabinoids on the enzymatic activity of ATX, we also used the endocannabinoids 2-AG and anandamide. However, both endocannabinoids did not affect the catalysis of ATX in the applied conditions (Fig 1B and C).

### Biochemical characterization of THC and 6a10aTHC with ATX- $\beta$ and ATX- $\gamma$

We choose THC and 6a10aTHC for our detailed biochemical characterization, as these inhibitors have a maximum magnitude of inhibition of more than 50%, a cutoff criterion selected under the assay conditions used. THC works as a partial inhibitor on the catalysis of both isoforms (Fig 2A and B). The apparent  $EC_{50}$  value of THC with ATX- $\beta$  and LPC 18:1 as a substrate is  $1,026 \pm 138$  nM, as shown in Fig 2A. The magnitude of inhibition is around 60%. A

similar magnitude of inhibition is observed with ATX- $\gamma$ , with an apparent  $EC_{50}$  of  $407 \pm 67$  nM for THC toward this isoform (Fig 2B).

Next, we validate the artificial THC derivative 6a10aTHC. The apparent  $EC_{50}$  value of 6a10aTHC for ATX- $\beta$  is  $844 \pm 178$  nM (Fig 2C) and thus comparable to THC. The maximum inhibition is marginally increased and appears to be around 75%. 6a10aTHC has the highest potency toward ATX- $\gamma$  with a determined apparent  $EC_{50}$  of  $374 \pm 66$  nM (Fig 2D). The magnitude of inhibition is around 70%, which is consistent with ATX- $\beta$ . Overall, 6a10aTHC is the best used cannabinoid inhibitor for both isoforms tested with the classical substrate LPC 18:1, and also with LPC 16:0 (Fig S2).

Both THC and 6a10aTHC are very closely related in structure to each other and show a similar behavior in biochemical assays. Thus, we performed a mode of inhibition analysis with THC only, to understand the inhibition mode of these compounds (Fig 2E). This analysis is carried out with 0, 0.35, 0.7, and 1.4  $\mu$ M of THC with geometrically increasing concentrations of LPC 18:1. It revealed that THC functions as a mixed-type inhibitor, which is demonstrated by the decrease in  $V_{max}$  from 8.5 to 7.3, 6.3, and 5.0, respectively, and an increase in  $K_m$  from 10.1 to 19.6, 29.9, and 31.5  $\mu$ M, respectively.

### Co-crystal structure of ATX-THC

To understand the binding interface between THC and ATX in detail, we expressed and purified the second isoform of ATX from *Rattus norvegicus* (UniProt ID: Q64610-2, rATX- $\beta$ ) and co-crystallized this formerly used ATX construct (Hausmann et al, 2011; Keune et al, 2016) with THC. We determined this ATX-THC structure (PDB ID: 7P4J) to 1.8 Å resolution with an  $R_{free}$  of 23.5% (Table 1). We obtained clear residual electron density close to the active site of ATX. Modeling of THC here resulted in a very good fit to this remaining electron density (Fig 3A). ATX binds to THC at the entrance of the hydrophobic pocket with the aliphatic chain pointing into this pocket. The binding of the THC molecule is driven by hydrophobic interactions of the residues I167, F210, L213, L216, W254, F274, Y306, and V365 (Fig 3B), as analyzed by the PLIP server (Adasme et al, 2021). A superposition of our ATX-THC structure with the ATX-LPA 18:1 structure (PDB ID: 5DLW) (Keune et al, 2016) shows that the THC molecule blocks binding of the LPA 18:1 aliphatic chain, whereas binding to the glycerol backbone and the phosphate group can still occur (Fig 3C).

### Co-crystal structure of ATX-6a10aTHC

We also obtained an ATX-6a10aTHC structure (PDB ID: 7P4O) to 1.7 Å resolution with an  $R_{free}$  of 20.6% (Table 1). In this ATX-6a10aTHC structure, we observed clear residual electron density, which resembles almost perfectly the 6a10aTHC ligand (Fig 4A). The binding of the 6a10aTHC molecule is again mainly accomplished by hydrophobic interactions of the residues I167, F210, L213, W254, F273, F274, and Y306 (Fig 4B), as analyzed by the PLIP server (Adasme et al, 2021). Nevertheless, an additional water bridge between the carbonyl of F273 and the THC derivative can be observed (Fig 4C), which suggests that the binding stability of this ligand is higher compared with THC, and potentially explains the lower apparent  $EC_{50}$  for 6a10aTHC. However, the authors are aware that a comparable water

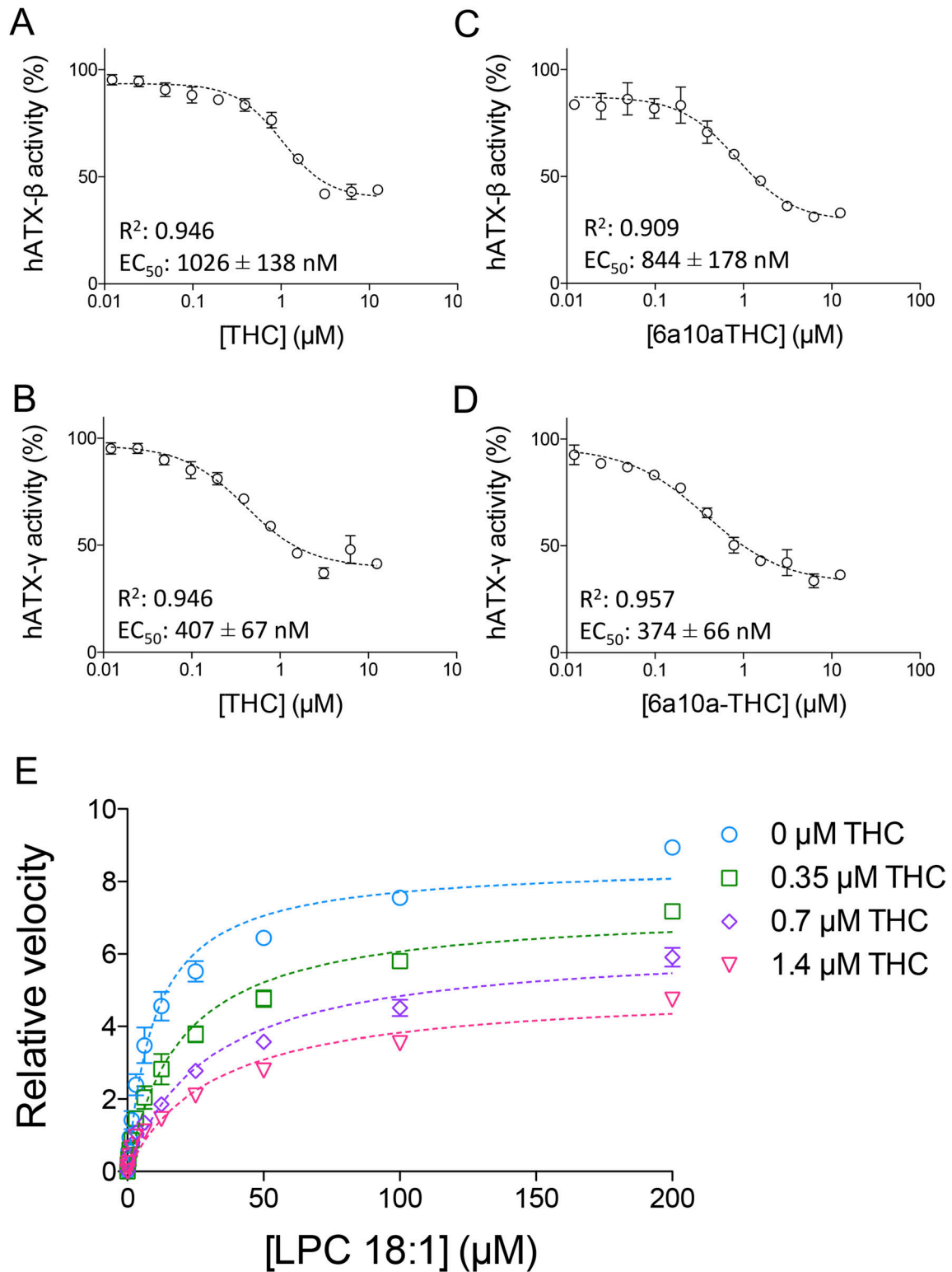


**Figure 2. Inhibition of ATX by plant-derived THC and synthetic 6a10aTHC.**

(A, B, C, D) Dose–response analysis of (A) ATX-β and (B) ATX-γ with THC and LPC 18:1, and of (C) ATX-β and (D) ATX-γ with 6a10aTHC and LPC 18:1. (E) Mode of inhibition of THC with ATX-γ indicates a mixed-type inhibition. All error bars represent the SEM ( $n = 3$ ).

**Table 1. Crystallographic data collection and refinement statistics.**

Crystal	ATX-THC	ATX-9(R)- $\Delta$ 6a,10a-THC
PDB identifier	7P4J	7P4O
Data collection		
Wavelength (Å)	0.976	1.000
Space group	P1	P1
Cell dimensions		
a, b, c (Å)	53.7 61.0 63.6	53.8 62.4 64.4
$\alpha$ , $\beta$ , $\gamma$ (°)	103.2 97.4 94.2	103.7 98.4 93.4
Resolution (Å) <sup>a</sup>	61.2-1.8 (1.9-1.8)	53.0-1.7 (1.75-1.7)
No. of reflections	47,909 (2,395)	85,204 (8,434)
R <sub>pin</sub> (%)	5.8 (64)	7.25 (63.8)
Completeness (%)		
Spherical	65.9 (13.1)	94.8 (94.2)
Ellipsoidal	91.6 (60.4)	—
Redundancy	9.2 (7.0)	3.5 (3.6)
Refinement		
R <sub>work</sub> (%)	18.69(29.1)	17.10 (21.5)
R <sub>free</sub> (%)	23.5(22.8)	20.60 (25.3)
No. of atoms <sup>b</sup>	6,800	6,818
Protein + carbohydrates	6,230	6,244
Ligand + metal ions	163	113
Waters and other ions	407	461
B-factors (Å <sup>2</sup> )		
All	27.5	31.9
Protein + carbohydrates	27.0	31.3
Ligand + metal ions	34.3	42.1
Water and other ions	32.9	36.6
R.m.s. deviations		
Bond lengths (RMS)	0.005	0.007
Bond angles (RMS)	0.86	0.90

<sup>a</sup>Values given in parenthesis refer to reflections in the highest resolution bin. For calculation of R<sub>free</sub>, 5% of all reflections were omitted from refinement. <sup>b</sup>Alternate conformations are counted as multiple atoms.

molecule also exists in the ATX-THC structure, where the distance between the THC oxygen and carbonyl oxygen of F273 is 4.5 Å, thus above the PLIP server threshold for such an interaction (Fig S3).

The 6a10aTHC ligand in ATX adopts an overall similar binding position to the cannabinoid in our ATX-THC structure. However, the aliphatic chain of the ligand points in a slightly different direction when compared to THC. Also noteworthy is that the cyclohexene (C-ring) appears to adopt a different stereoisomeric configuration (Fig S4) because of the alternate localization of the double bond (Fig 1A).

### Inhibition of LPA<sub>1</sub> internalization in HeLa cells by THC

To validate THC can act as an inhibitor in the production of LPA and thus ATX-LPA signaling in a cellular context, we used an agonist-

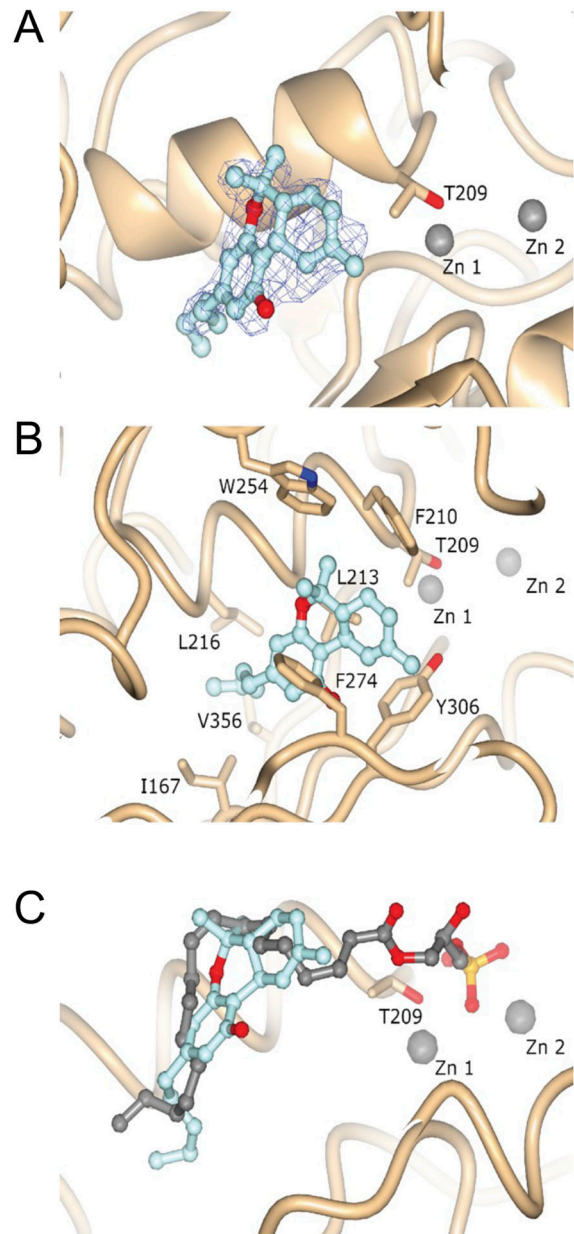


**Figure 3. Structure and electron density of ATX-THC.**

(A) Feature-enhanced electron density map before THC placement, contoured at 1 RMSD and represented as a blue wireframe model. (B) Molecular interactions of THC with ATX. (C) Superposition of ATX binding to THC (PDB ID: 7P4J) and LPA 18:1 (PDB ID: 5DLW).

induced LPA<sub>1</sub> receptor internalization as a readout in cultured cell assays (Murph et al, 2003; Lee et al, 2006, 2007). As shown in Fig 5, stimulation of HA/LPA<sub>1</sub>-transfected HeLa cells with 30 nM ATX, 150 μM LPC 18:1, and 1 μM THC significantly reduced LPA<sub>1</sub> internalization. This observation was only detectable in the presence of ATX and not in control conditions (Fig S5). This is an indirect response to blocking LPA production, which inhibits receptor activation and endocytosis, confirming a more physiological role of THC as a potent inhibitor.

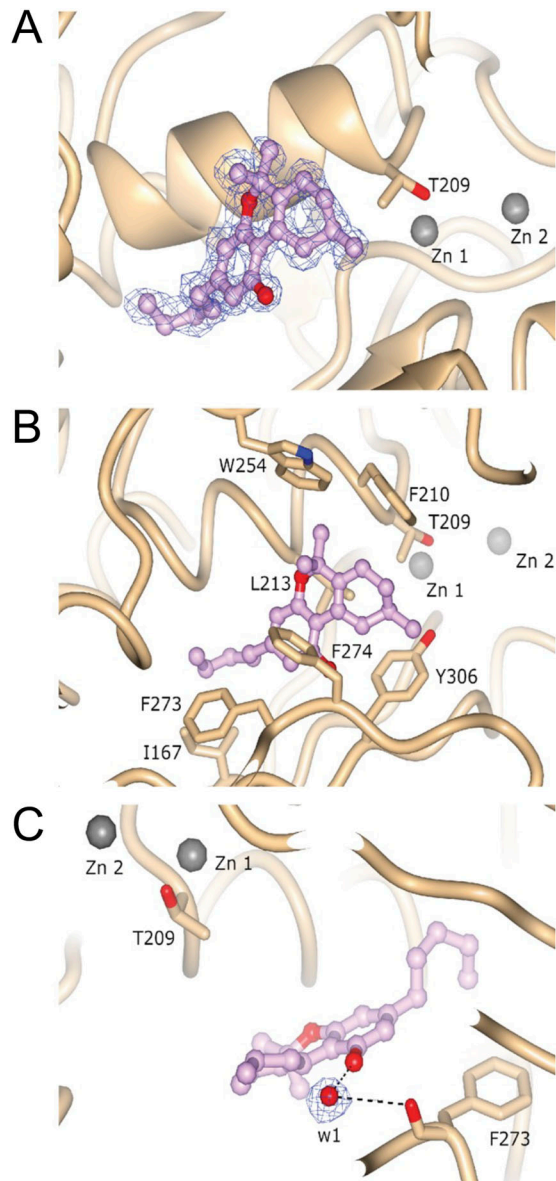


**Figure 4. Structure and electron density of ATX-6a10aTHC.** (A) Featured-enhanced electron density map before 6a10aTHC placement, contoured at 1 RMSD and represented as a blue wireframe model. (B) Molecular interactions of 6a10aTHC with ATX. (C) Bridging water molecule interaction between 6a10aTHC and carbonyl oxygen of F273.

## Discussion

Medicinal cannabis has been approved as a therapeutic agent by local authorities in an increasing number of states all over the world. Even though great progress in the molecular basis of medicinal cannabis therapy has been achieved over the last decades, the pleiotropic effects have been insufficiently characterized to date. We establish here a potent *in vitro* inhibition of various cannabinoids, such as THC, on the catalysis of ATX with different substrates (LPC 16:0 and LPC 18:1) and isoforms. Based on our investigations, we provide evidence that THC can potently modulate LPA signaling.

In most studies that try to address the pharmacological aspects of medicinal cannabis, the administration has been performed via smoking. In this context, the first body fluid that encounters THC is the saliva. The mean concentration of THC in this oral fluid has been detected with up to 4,167 ng/ml (13  $\mu$ M) in a radioimmunoassay (Huestis & Cone, 2004). Interestingly, LPA is present in saliva (Sugiura et al, 2002) and ATX expression can be detected in salivary gland tissue (Maruya et al, 2004), suggesting that ATX-LPA signaling may be reduced by THC *in vivo*. Furthermore, the deposition of THC in oral fluid reflects a similar time course in plasma after smoked cannabis administration (Huestis & Cone, 2004). Serum concentrations of THC show a wide inter-individual difference, between 59 and 421 ng/ml after a 49.1-mg THC dose, which equals 190 nM to 1.3  $\mu$ M of THC (Hunault et al, 2008). The observed mean THC peak in this study for a 69.4-mg THC dose was 190.4 ng/ml (SD = 106.8), which is in the range of the apparent  $EC_{50}$  determined during our studies.

95–97% of THC is bound to plasma proteins, and our data suggest that ATX might function as a carrier for THC in plasma. The authors extensively tried to determine the binding affinity of ATX for THC with various techniques, such as isothermal titration calorimetry and nuclear magnetic resonance; however, these approaches were unsuccessful because of the hydrophobic nature of the cannabinoid ligand.

Recently, the potential use of medicinal cannabis in tissue fibrosis has been proposed (Pryimak et al, 2021). In this regard, it is noteworthy to mention the role of ATX in idiopathic pulmonary fibrosis. Several inhibitors targeting ATX are under clinical investigations for their therapeutic use against idiopathic pulmonary fibrosis (Zulfikar et al, 2020). However, the ISABELA study (clinical phase 3 investigation) of the most advanced molecule targeting ATX, Ziritaxestat (Glp1690) from Galapagos N.V, was discontinued because of risk–benefit concerns. It is tempting to speculate that a full ATX inhibitor, which reduces LPA levels to almost zero, causes many systemic unwanted side effects, as the ATX-LPA signaling axis is pivotal under physiological conditions. In this context, our observation that THC is a partial inhibitor of ATX is of great interest, because this molecule is an FDA-approved drug, which could reduce LPA levels incompletely. Moreover, the fact that THC can cross the blood–brain barrier makes it an attractive candidate to manipulate neuronal diseases, where the brain-specific isoform of ATX is involved.

In addition, glaucoma is the leading cause of irreversible blindness worldwide (Tham et al, 2014). Glaucoma is characterized by elevated intraocular pressure levels, and medicinal cannabis is being used to treat this pathology; however, the therapeutic mechanism is not completely known. Interestingly, in recent years it has been discovered that aqueous humor samples of patients suffering from primary open-angle glaucoma have elevated levels of ATX, LPC, and LPA (Ho et al, 2020). Moreover, pharmacological inhibition of ATX lowered intraocular pressure in rabbits (Iyer et al, 2012). Our data may explain the molecular basis for the therapeutic effect of medical cannabis in glaucoma patients, as THC could feasibly reduce the formation of LPA by inhibiting the enzymatic activity of ATX.

In conclusion, our study warrants further research into the pleiotropic effects of medicinal cannabis in the context of ATX-LPA

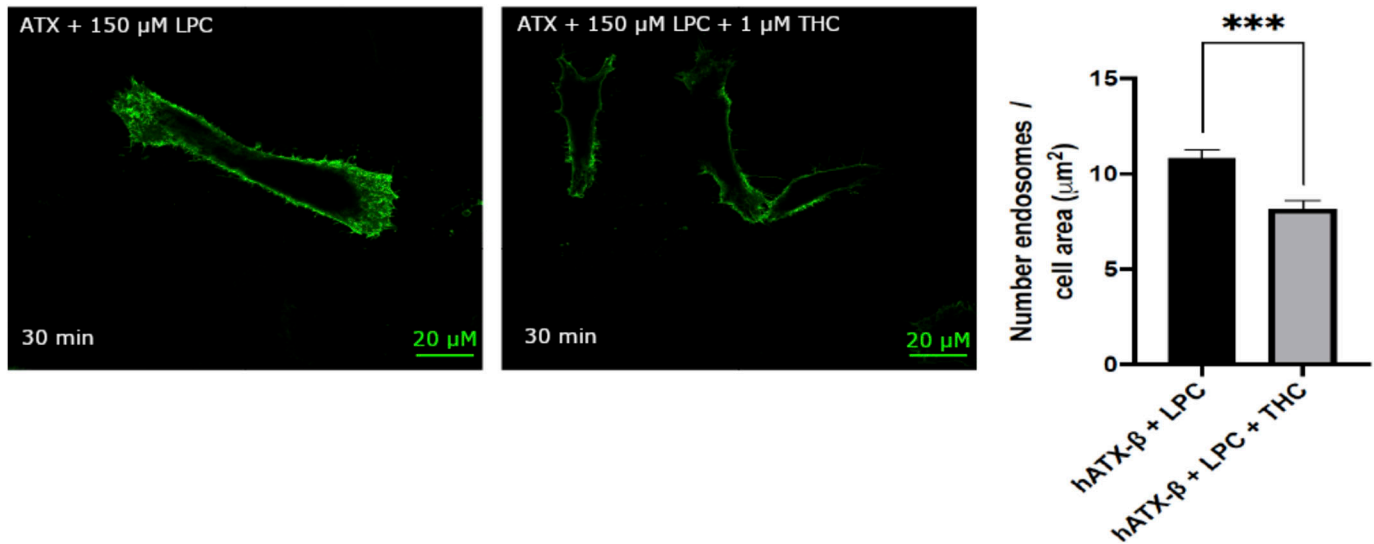


**Figure 5. Physiological effect of THC on LPA<sub>1</sub> receptor internalization.**

Quantification of LPA<sub>1</sub> receptor internalization revealed that THC reduced the number of endosomes internalized when compared to untreated condition, paired t test,  $P = 0.0008$ . All error bars represent the SEM, calculated from 11 images per condition in biological triplicate experiments.

signaling, while also providing a promising starting point for such research lines. Furthermore, this work also provides a scaffold for the design of new inhibitors for further studies of the ATX-LPA signaling axis, and suggests a new way to intervene in ATX-LPA signaling-mediated pathologies with THC.

## Materials and Methods

### Materials

We obtained T300 tissue culture flasks (#90301) from TPP and roller bottles (#681070) from Greiner Bio-One; DMEM (#12491023; Gibco), Opti-MEM (#31985062; Gibco), FBS (#10270106; Gibco), fatty acid-free FBS (#A3382101; Gibco), L-glutamine (#25030-123; Gibco), POROS-20 MC column (#1542906; Thermo Fisher Scientific), Lipofectamine 3000 (#L3000001; Thermo Fisher Scientific), Alexa Fluor 594 conjugate (#W11262; Invitrogen), and SDS precast gel (#XP04205BOX; Invitrogen) from Thermo Fisher Scientific; CELLSTAR 12-well culture plates (#665180; Greiner) and Fluoroshield (#F6182-20 ml) from Sigma-Aldrich; Amicon ultra 15-ml 10-kD (#UFC901008) and ultra 0.5-ml 10-kD (#UFC501008) concentrators from Merck; Superose 6 (10/300) column (#17-5172-01) and Superdex 200 Increase 3.2/300 column (#28-9909-46) from GE Healthcare; Trans-Blot Turbo transfer pack (#1704158) from Bio-Rad; LPC 18:1 (#845875P), LPC 16:0 (#855675C), and LPA 18:1 (#857130C) from Avanti Polar Lipids; choline quantification kits (#40007) from AAT Bioquest; THC (#LGCAMP1088.00-05) from LGC Standards, France; 9(R)-Δ6a,10a-THC (#33013) from Cayman; CBN (#C-046-1ML) from Cerilliant; 5-DMH-CBD (#1481) from Tocris; CBD (#HB2785) from HelloBio; NH<sub>4</sub>I (#AB202711) from Abcr; NaSCN (#HR2-693) from Hampton Research; and InstantBlue Coomassie protein stain (#ab119211), anti-HA tag primary antibody (#ab18181), anti-mouse antibody (#ab150113), anti-ATX antibody (#ab77104), anti-mouse HRP

secondary antibody (#ab6728), and ECL substrate kit (#ab133406) from Abcam.

### Methods

#### ATX expression and purification

Recombinant ATX proteins were essentially produced as previously described (Hausmann et al, 2010). HEK293-Flp-In cells were cultivated in complete DMEM supplemented with 10% FBS with minor differences. The cells were grown to 80–90% confluence, washed twice with preheated PBS, and trypsinized for 5 min with 5 ml of trypsin. Inactivation was accomplished by adding 45 ml of complete medium. Cells were resuspended in complete medium and inoculated into roller bottles. 10 T300 flasks were used to inoculate eight roller bottles, and the cells were cultured for 4 d after transfer into 125 ml DMEM containing 10% FBS and 2 mM glutamine. The medium was then replaced by 125 ml DMEM containing 2% FBS and 2 mM glutamine. The cells were then left to express protein for 4–5 d before collection. Fresh expression medium was added for a further round of recombinant expression.

HEK293 medium from eight roller bottles was pooled together, and the recombinant ATX proteins were purified using a POROS-20 MC column preloaded with Cu<sup>2+</sup>. Equilibration was achieved by washing with 10 column volumes of buffer A (20 mM Hepes and 150 mM NaCl, pH 7.4). ATX was eluted with a linear gradient of buffer B consisting of buffer A supplemented with 500 mM imidazole. Reasonably, pure fractions were pooled after SDS-PAGE analysis. The fraction volume was reduced with an Amicon ultra 15-ml 10-kD concentrator to a volume of 500 μl. 5 mg/ml concentrated protein was injected into a Superose 6 (10/300) gel filtration column using buffer A. The purity of the peak fractions was analyzed by SDS-PAGE. The recombinant protein concentration was determined by the ratio of the optical density at 260/280 nm using a NanoDrop 2000

spectrophotometer (Thermo Fisher Scientific). The ATX construct from *Rattus Norvegicus* (UniProt ID: Q64610-2) was concentrated to 3–3.5 mg/ml using an Amicon ultra 0.5-ml 10-kD concentrator. Human ATX (UniProt ID: Q13822-1 and Q13822-3) was concentrated to 1.3 mg/ml. Purity was assessed using SDS-PAGE, Western blot, and SEC analysis (Fig S6A–C). For the SDS-PAGE, 25  $\mu$ g of purified protein in reducing conditions was loaded on a precast gel, run for 1 h at 225 V, and imaged after InstantBlue Coomassie protein staining following the manufacturer's instructions. For Western blot, proteins were transferred using the Trans-Blot Turbo transfer system (Bio-Rad). Membrane staining with the primary antibody was performed overnight using an anti-ATX antibody. Anti-mouse HRP secondary antibody was incubated for 1 h, and detection was then performed using an ECL substrate kit. Analytical SEC was performed by injecting 25  $\mu$ l of rATX on a Superdex 200 Increase 3.2/300 column equilibrated with a 50 mM Tris-HCl (pH 8) and 150 mM NaCl buffer. hATX- $\beta$  and hATX- $\gamma$  activity was controlled using the choline release assay described below (Fig S6D). hATX- $\gamma$  activity was slightly lower than hATX- $\beta$  activity, which is in accordance with published comparison of the different ATX isoforms (Giganti et al, 2008). ATX- $\beta$  and ATX- $\gamma$  activity was monitored in the presence and absence of 0.5 mg/ml albumin (Fig S6E and F).

#### End-point assays

ATX lysophospholipase D activity was measured using choline release from LPC 18:1 and LPC 16:0 with a choline quantification kit (Hausmann et al, 2016) (Fig S6D). 30 nM ATX- $\beta$  or ATX- $\gamma$  was incubated with 200  $\mu$ M LPC 18:1 or LPC 16:0 in a final volume of 100  $\mu$ l buffer, which contained 50 mM Tris-HCl (pH 8.5) and 150 mM NaCl. The LPC solution was obtained by evaporating a commercial LPC chloroform solution directly in a 1.5-ml Eppendorf tube under vacuum. The dried LPC was then resuspended in water to obtain the mentioned concentration and incubated at 37°C on a shaker for 5–10 min before addition to the microplate. The cannabinoid solutions were prepared from a stock solution in ethanol or other organic solvents. After initial evaporation and/or dilution to obtain the highest concentration mentioned in the assay figure, a twofold dilution was performed in Eppendorf tubes. All the compounds were dissolved in 100% ethanol as a vehicle.

The experiments for determining relative inhibition for various cannabinoids were performed at 37°C by adding 10  $\mu$ M of the cannabinoid or endocannabinoid mentioned. Released choline was detected, and the enzyme activity was determined by measuring fluorescence at  $\lambda_{ex}/\lambda_{em} = 540/590$  nm in 96-well plates, every 60 s for 50 min minimum using a CLARIOstar plate reader (BMG Labtech). Absolute values were taken at 25 min after visual inspection, and the 0-min baselines were subtracted to account for compound differences. The relative inhibition values were determined using the normalize method in GraphPad Prism (GraphPad Software, Inc.). Measurements have been performed in triplicate with three different protein preparations. All the compounds were controlled for interference of fluorescence and inhibition in the same assay conditions but in the absence of ATX and replacing LPC with choline.

#### Dose-response assay for cannabinoids

ATX lysophospholipase D activity was measured using choline release from LPC 18:1 and LPC 16:0 with a choline quantification kit

(Hausmann et al, 2016). 30 nM ATX- $\beta$  or ATX- $\gamma$  was incubated with 200  $\mu$ M LPC 18:1 or LPC 16:0 in a final volume of 100  $\mu$ l buffer, which contained 50 mM Tris-HCl (pH 8.5) and 150 mM NaCl. The LPC solution was obtained by evaporating a commercial LPC chloroform solution directly in a 1.5-ml Eppendorf tube under vacuum. The dried LPC was then resuspended in water to obtain the mentioned concentration and incubated at 37°C on a shaker for 5–10 min before addition to the microplate.

The experiment for determining apparent EC<sub>50</sub> for various cannabinoids was performed at 37°C by adding the cannabinoid in a serial twofold dilution for each concentration. The cannabinoid solutions were prepared from a stock solution in ethanol or other organic solvents. After initial evaporation and/or dilution to obtain the highest concentration mentioned in the assay figure, a twofold dilution was performed in Eppendorf tubes. All the compounds were dissolved in 100% ethanol as a vehicle. For THC and 6a10aTHC, the retained twofold dilution started at 12.5  $\mu$ M. For CBN, 5-DMH-CBD, and CBD, the starting concentration was 50  $\mu$ M, 150  $\mu$ M, and 2 mM, respectively. Released choline was detected, and the enzyme activity was determined by measuring fluorescence at  $\lambda_{ex}/\lambda_{em} = 540/590$  nm in 96-well plates, every 60 s for 50 min minimum using a CLARIOstar plate reader (BMG Labtech). Initial velocities were taken between 19 and 31 min after visual inspection. The apparent EC<sub>50</sub> values were determined using the non-linear regression analysis method (fit: [inhibitor] versus response [three parameter]) in GraphPad Prism (GraphPad Software, Inc.). However, it should be mentioned that the relative concentrations of the different lipids/inhibitors in their physical form as micelles, liposomes, protein-bound, or aggregates are unknown (Carman et al, 1995). These uncertainties are widely known, and we provide here an apparent EC<sub>50</sub> for consideration. Measurements have been performed in triplicate with three different protein preparations.

#### Biochemical data analysis

The data analysis was performed with GraphPad (9.4.1). For apparent EC<sub>50</sub> determination, fluorescent time points are subtracted from the baseline. From the subtracted results, a linear regression analysis was run on the linear part of the fluorescent curve, between 10 min and 25 min. The linear regression slopes were then plotted and normalized for each inhibitor concentration. A non-linear regression analysis using the following equation was performed with GraphPad to calculate the apparent EC<sub>50</sub>:

$$Y = \text{Bottom} + (\text{top} - \text{bottom}) / \left(1 + [\text{EC}_{50}/X]^{\text{hillslope}}\right).$$

The apparent EC<sub>50</sub> was calculated as the concentration of inhibitor that gives a response halfway between maximal and minimal ATX activity. The S.E.M. of the apparent EC<sub>50</sub> was determined by GraphPad Prism as the 95% confidence interval of the mean.

#### Choline standard

The assay was run as mentioned in the previous dose-response material and methods above, apart from the replacement of LPC by the choline standard, as mentioned in the manufacturer's instructions. The obtained curve is linear allowing extrapolation of the enzyme activity.

### Crystallization, structure determination, and model building

Crystallization experiments were performed at 303 K using the hanging-drop vapor diffusion method as previously published (Day et al, 2010). The best crystals were obtained with the rATX construct (3–3.5 mg/ml) after 30-min RT preincubation with 5 mM THC or 5 mM 6a10aTHC dissolved in ethanol. 1  $\mu$ l of the protein solution was then mixed with 1  $\mu$ l of the reservoir solution containing 18–22% (m/v) PEG3350, 0.1–0.3 M  $\text{NH}_4\text{I}$ , and 0.3 M NaSCN. All the crystals were cryoprotected with the addition of 20% (vol/vol) glycerol.

X-ray data for THC and 6a10aTHC ATX complexes were collected at 100 K on EMBL PETRA III beamlines P14 and P13 (Cianci et al, 2017), respectively. Crystallographic ATX-THC complex data were acquired using the Global Phasing WFs data collection workflow to maximize the completeness of the P1 dataset. Authorization to collect sample containing THC was granted by the BfArM in Germany. All data were processed with autoPROC (Vonrhein et al, 2011)/STARANISO, which includes XDS (Kabsch, 2010). Structures were determined by molecular replacement using MRage (Adams et al, 2010) with the structure of ATX (PDB: 2XR9) as a model (Hausmann et al, 2011). Model building was performed using Coot (Emsley & Cowtan, 2004), phenix.refine (Afonine et al, 2012), REFMAC5 (Murshudov et al, 2011), and PDB-REDO (Joosten et al, 2009). Ligands were drawn with ELBOW (Moriarty et al, 2009). Validation of the model was performed with phenix PDB deposition tools, using MolProbity (Williams et al, 2018). Maps were generated using phenix.refine and feature-enhanced map (Afonine et al, 2015). The crystallographic parameters and model quality indicators are shown in Table 1. Structural figures were generated using CCP4mg (McNicholas et al, 2011). Structural biology applications used in this project were compiled and configured by SBGrid (Morin et al, 2013).

### hLPA1 receptor internalization assay

The hLPA<sub>1</sub> receptor internalization assay was essentially performed as previously described (Lee et al, 2007). A pRP[Exp]-Puro-CMV > HA/hLPA<sub>1</sub> vector coding for full-length human LPA<sub>1</sub> receptor (UniProt ID: Q92633) with a human influenza HA sequence epitope tag at the 5'-end of the extracellular domain was designed, and maxiprep plasmid DNA was produced commercially (VectorBuilder). Vector quality control was done by restriction enzyme analysis and Sanger sequencing.

HeLa cells were grown on coverslips in a 12-well plate format and transfected with HA/hLPA<sub>1</sub> vector in DMEM complete medium with Lipofectamine 3000 using 1  $\mu$ g of plasmid DNA, and 3  $\mu$ l of Lipofectamine 3000 per well after complexation in 50  $\mu$ l Opti-MEM, as per the manufacturer's instructions, 48 h before fixation. 8 h before treatment and fixation, the cells were starved in fatty acid-free DMEM to avoid hLPA<sub>1</sub> activation by serum lipids. Several assays were performed in different conditions before fixation: 30 nM ATX + 150  $\mu$ M LPC 18:1; 30 nM ATX + 150  $\mu$ M LPC 18:1 + 1  $\mu$ M THC; 1  $\mu$ M THC; 1  $\mu$ M LPA 18:1; untreated (vehicle only); and untransfected, to control specificity of the antibody towards HA-tagged hLPA<sub>1</sub> receptor. LPC 18:1 and LPA 18:1 were dissolved in fatty acid-free FBS with a final concentration in the media of 1%. THC was dissolved in DMSO to a final concentration in the media of 0.025% (vol/vol) DMSO.

Fixation was carried out by adding paraformaldehyde directly into the media to a final concentration of 3%, and incubating at 37°C for 10 min. Cells were washed three times in PBS, and membranes

were labeled using wheat germ agglutinin, and Alexa Fluor 594 conjugate for 10 min at 5  $\mu$ g/ml in PBS, as per the manufacturer's instructions. Cells were washed three times in PBS, permeabilized using 0.2% Tween for 10 min, washed in PBS, and finally blocked with 10% goat serum for 30 min. HA tag was labeled using an anti-HA tag primary antibody at 1/200 dilution in 10% FBS for 1 h at room temperature followed by PBS wash, and secondary staining was done with an anti-mouse antibody, with 30-min incubation at 1/500 dilution in 10% FBS. Cells were washed three times and mounted using Fluoroshield mounting medium. Imaging was performed using a Leica SP5 ( $\times$  63 objective). Endosome quantification was done using Fiji Analyze Particle tools after image thresholding. The number of counted endosomes was normalized over the measuring area to calculate the density per  $\mu\text{m}^2$ . Statistical analysis was performed using a paired *t* test over 11 images for each condition of ATX-THC-LPC and ATX-LPC in biological triplicate.

## Supplementary Information

Supplementary Information is available at <https://doi.org/10.26508/lsa.202201595>

## Acknowledgements

The authors are grateful for the initial in silico work of Dr. Ulrike Uhrig of the Chemical Biology Core Facility, EMBL, who demonstrated a potential inhibition of THC towards ATX, which was fundamental to apply for an initial THC license. The authors are also grateful to Dr. Corinna Gorny for her support to obtain a license for Dronabinol experiments at EMBL Germany under BfArM authorization. We are thankful for the kind gift of ATX-expressing cell lines from the Perrakis laboratory in Amsterdam. We thank beamline staff from the EMBL-Hamburg beamlines at the PETRA III storage ring (DESY, Hamburg, Germany) for beamtime (proposal number MX-661). In particular, we thank Drs. G Bourenkov, and G Bricogne and R Fogh at Global Phasing Limited who provided valuable assistance with multi-orientation data collection strategies on P14. The authors also wish to express their gratitude to the Eukaryotic Expression Facility in Grenoble for infrastructure access, especially Alice Aubert and Martin Pelosse for excellent technical support and fruitful discussions. Lastly, we thank L Gutierrez for her technical support with biochemical assays. MC Eymery has been funded by the EMBL International PhD program. AA McCarthy has been funded by EMBL. J Hausmann was supported by a fellowship from the EMBL Interdisciplinary Postdoc (EI3POD) program under Marie Skłodowska-Curie Actions COFUND (grant number: 664726).

### Author Contributions

MC Eymery: data curation, formal analysis, investigation, visualization, methodology, and writing—review and editing. AA McCarthy: resources, supervision, funding acquisition, validation, project administration, and writing—review and editing. J Hausmann: conceptualization, resources, formal analysis, supervision, validation, and writing—original draft.

### Conflict of Interest Statement

The authors declare that they have no conflict of interest.

## References

- Aaltonen N, Lehtonen M, Varonen K, Gotteris GA, Laitinen JT (2012) Lipid phosphate phosphatase inhibitors locally amplify lysophosphatidic acid LPA1 receptor signalling in rat brain cryosections without affecting global LPA degradation. *BMC Pharmacol* 12: 7. doi:10.1186/1471-2210-12-7
- Adams PD, Afonine PV, Bunkóczi G, Chen VB, Davis IW, Echols N, Headd JJ, Hung L-W, Kapral GJ, Grosse-Kunstleve RW, et al (2010) PHENIX: A comprehensive python-based system for macromolecular structure solution. *Acta Crystallogr D Biol Crystallogr* 66: 213–221. doi:10.1107/S0907444909052925
- Adasme MF, Linnemann KL, Bolz SN, Kaiser F, Salentin S, Haupt VJ, Schroeder M (2021) PLIP 2021: Expanding the scope of the protein–ligand interaction profiler to DNA and RNA. *Nucleic Acids Res* 49: W530–W534. doi:10.1093/nar/gkab294
- Afonine PV, Grosse-Kunstleve RW, Echols N, Headd JJ, Moriarty NW, Mustyakimov M, Terwilliger TC, Urzhumtsev A, Zwart PH, Adams PD (2012) Towards automated crystallographic structure refinement with phenix.refine. *Acta Crystallogr D Biol Crystallogr* 68: 352–367. doi:10.1107/s0907444912001308
- Afonine PV, Moriarty NW, Mustyakimov M, Sobolev OV, Terwilliger TC, Turk D, Urzhumtsev A, Adams PD (2015) FEM: Feature-enhanced map. *Acta Crystallogr D Biol Crystallogr* 71: 646–666. doi:10.1107/S1399004714028132
- Albers HMHG, Hendrickx LJD, van Tol RJP, Hausmann J, Perrakis A, Ovaia H (2011) Structure-based design of novel boronic acid-based inhibitors of autotaxin. *J Med Chem* 54: 4619–4626. doi:10.1021/jm200310q
- Aoki J (2004) Mechanisms of lysophosphatidic acid production. *Semin Cell Dev Biol* 15: 477–489. doi:10.1016/j.semcdb.2004.05.001
- Aung MM, Griffin G, Huffman JW, Wu MJ, Keel C, Yang B, Showalter VM, Abood ME, Martin BR (2000) Influence of the N-1 alkyl chain length of cannabimimetic indoles upon CB(1) and CB(2) receptor binding. *Drug Alcohol Depend* 60: 133–140. doi:10.1016/s0376-8716(99)00152-0
- Boutin JA, Ferry G (2009) Autotaxin. *Cell Mol Life Sci* 66: 3009–3021. doi:10.1007/s00018-009-0056-9
- Carman GM, Deems RA, Dennis EA (1995) Lipid signaling enzymes and surface dilution kinetics. *J Biol Chem* 270: 18711–18714. doi:10.1074/jbc.270.32.18711
- Chun J, Contos JJA, Munroe D (1999) A growing family of receptor genes for lysophosphatidic acid (LPA) and other lysophospholipids (LPs). *Cell Biochem Biophys* 30: 213–242. doi:10.1007/bf02738068
- Cianci M, Bourenkov G, Pompidor G, Karpics I, Kallio J, Bento I, Roesle M, Cipriani F, Fiedler S, Schneider TR (2017) P13, the EMBL macromolecular crystallography beamline at the low-emittance PETRA III ring for high- and low-energy phasing with variable beam focusing. *J Synchrotron Radiat* 24: 323–332. doi:10.1107/s1600577516016465
- Cristino L, Bisogno T, Di Marzo V (2020) Cannabinoids and the expanded endocannabinoid system in neurological disorders. *Nat Rev Neurol* 16: 9–29. doi:10.1038/s41582-019-0284-z
- Day JE, Hall T, Pegg LE, Benson TE, Hausmann J, Kamtekar S (2010) Crystallization and preliminary X-ray diffraction analysis of rat autotaxin. *Acta Crystallogr Sect F Struct Biol Cryst Commun* 66: 1127–1129. doi:10.1107/s1744309110030228
- Devane WA, Hanus L, Breuer A, Pertwee RG, Stevenson LA, Griffin G, Gibson D, Mandelbaum A, Etinger A, Mechoulam R (1992) Isolation and structure of a brain constituent that binds to the cannabinoid receptor. *Science* 258: 1946–1949. doi:10.1126/science.1470919
- Di Marzo V, Fontana A (1995) Anandamide, an endogenous cannabinomimetic eicosanoid: ‘Killing two birds with one stone’.
- Prostaglandins Leukot Essent Fatty Acids* 53: 1–11. doi:10.1016/0952-3278(95)90077-2
- Emsley P, Cowtan K (2004) Coot: Model-building tools for molecular graphics. *Acta Crystallogr D Biol Crystallogr* 60: 2126–2132. doi:10.1107/s0907444904019158
- Euer N, Schwirzke M, Evtimova V, Burtscher H, Jarsch M, Tarin D, Weidle UH (2002) Identification of genes associated with metastasis of mammary carcinoma in metastatic versus non-metastatic cell lines. *Anticancer Res* 22: 733–740.
- Giganti A, Rodríguez M, Fould B, Moulharat N, Cogé F, Chomarat P, Galizzi J-P, Valet P, Saulnier-Blache J-S, Boutin JA, et al (2008) Murine and human autotaxin  $\alpha$ ,  $\beta$ , and  $\gamma$  isoforms. *J Biol Chem* 283: 7776–7789. doi:10.1074/jbc.m708705200
- González de San Román E, Manuel I, Ledent C, Chun J, Rodríguez de Fonseca F, Estivill-Torrús G, Santín LJ, Rodríguez Puertas R (2019) CB1 and LPA1 receptors relationship in the mouse central nervous system. *Front Mol Neurosci* 12: 223. doi:10.3389/fnmol.2019.00223
- Hausmann J, Christodoulou E, Kasim M, De Marco V, van Meeteren LA, Moolenaar WH, Axford D, Owen RL, Evans G, Perrakis A (2010) Mammalian cell expression, purification, crystallization and microcrystal data collection of autotaxin/ENPP2, a secreted mammalian glycoprotein. *Acta Crystallogr Sect F Struct Biol Cryst Commun* 66: 1130–1135. doi:10.1107/s1744309110032938
- Hausmann J, Kamtekar S, Christodoulou E, Day JE, Wu T, Fulkerson Z, Albers HMHG, van Meeteren LA, Houben AJS, van Zeijl L, et al (2011) Structural basis of substrate discrimination and integrin binding by autotaxin. *Nat Struct Mol Biol* 18: 198–204. doi:10.1038/nsmb.1980
- Hausmann J, Keune W-J, Hipgrave Ederveen AL, van Zeijl L, Joosten RP, Perrakis A (2016) Structural snapshots of the catalytic cycle of the phosphodiesterase Autotaxin. *J Struct Biol* 195: 199–206. doi:10.1016/j.jsb.2016.06.002
- Ho LTY, Osterwald A, Ruf I, Hunziker D, Mattei P, Challa P, Vann R, Ullmer C, Rao PV (2020) Role of the autotaxin-lysophosphatidic acid axis in glaucoma, aqueous humor drainage and fibrogenic activity. *Biochim Biophys Acta Mol Basis Dis* 1866: 165560. doi:10.1016/j.bbadis.2019.165560
- Houben AJS, van Wijk XMR, van Meeteren LA, van Zeijl L, van de Westerloo EMA, Hausmann J, Fish A, Perrakis A, van Kuppevelt TH, Moolenaar WH (2013) The polybasic insertion in autotaxin  $\alpha$  confers specific binding to heparin and cell surface heparan sulfate proteoglycans. *J Biol Chem* 288: 510–519. doi:10.1074/jbc.m112.358416
- Huestis MA, Cone EJ (2004) Relationship of Delta 9-tetrahydrocannabinol concentrations in oral fluid and plasma after controlled administration of smoked cannabis. *J Anal Toxicol* 28: 394–399. doi:10.1093/jat/28.6.394
- Hunault CC, Mensinga TT, de Vries I, Kelholt-Dijkman HH, Hoek J, Kruidenier M, Leenders MEC, Meulenbelt J (2008) Delta-9-tetrahydrocannabinol (THC) serum concentrations and pharmacological effects in males after smoking a combination of tobacco and cannabis containing up to 69 mg THC. *Psychopharmacology (Berl)* 201: 171–181. doi:10.1007/s00213-008-1260-2
- Iyer P, Lalane R, Morris C, Challa P, Vann R, Rao PV (2012) Autotaxin-lysophosphatidic acid axis is a novel molecular target for lowering intraocular pressure. *PLoS One* 7: e42627. doi:10.1371/journal.pone.0042627
- Joosten RP, Salzemann J, Bloch V, Stockinger H, Berglund A-C, Blanchet C, Bongcam-Rudloff E, Combet C, Da Costa AL, Deleage G, et al (2009) PDB\_REDO: Automated re-refinement of X-ray structure models in the PDB. *J Appl Crystallogr* 42: 376–384. doi:10.1107/s0021889809008784
- Kabsch W (2010) XDS. *Acta Crystallogr D Biol Crystallogr* 66: 125–132. doi:10.1107/s0907444909047337
- Kanda H, Newton R, Klein R, Morita Y, Gunn MD, Rosen SD (2008) Autotaxin, an ectoenzyme that produces lysophosphatidic acid, promotes the entry



- of lymphocytes into secondary lymphoid organs. *Nat Immunol* 9: 415–423. doi:10.1038/ni1573
- Keune W-J, Hausmann J, Bolier R, Tolenaars D, Kremer A, Heidebrecht T, Joosten RP, Sunkara M, Morris AJ, Matas-Rico E, et al (2016) Steroid binding to Autotaxin links bile salts and lysophosphatidic acid signalling. *Nat Commun* 7: 11248. doi:10.1038/ncomms11248
- Lee C-W, Rivera R, Gardell S, Dubin AE, Chun J (2006) GPR92 as a new G12/13- and Gq-coupled lysophosphatidic acid receptor that increases cAMP, LPA5. *J Biol Chem* 281: 23589–23597. doi:10.1074/jbc.m603670200
- Lee C-W, Rivera R, Dubin AE, Chun J (2007) LPA(4)/GPR23 is a lysophosphatidic acid (LPA) receptor utilizing G(s)-G(q)/G(i)-mediated calcium signaling and G(12/13)-mediated Rho activation. *J Biol Chem* 282: 4310–4317. doi:10.1074/jbc.m610826200
- Maruya S-I, Kim H-W, Weber RS, Lee JJ, Kies M, Luna MA, Batsakis JG, El-Naggar AK (2004) Gene expression screening of salivary gland neoplasms: Molecular markers of potential histogenetic and clinical significance. *J Mol Diagn JMD* 6: 180–190. doi:10.1016/s1525-1578(10)60508-9
- Matsuda LA, Lolait SJ, Brownstein MJ, Young AC, Bonner TI (1990) Structure of a cannabinoid receptor and functional expression of the cloned cDNA. *Nature* 346: 561–564. doi:10.1038/346561a0
- McNicholas S, Potterton E, Wilson KS, Noble MEM (2011) Presenting your structures: The CCP4mg molecular-graphics software. *Acta Crystallogr D Biol Crystallogr* 67: 386–394. doi:10.1107/s0907444911007281
- Moolenaar WH, Perrakis A (2011) Insights into autotaxin: How to produce and present a lipid mediator. *Nat Rev Mol Cell Biol* 12: 674–679. doi:10.1038/nrm3188
- Moriarty NW, Grosse-Kunstleve RW, Adams PD (2009) electronic Ligand Builder and Optimization Workbench (eLBOW): A tool for ligand coordinate and restraint generation. *Acta Crystallogr D Biol Crystallogr* 65: 1074–1080. doi:10.1107/s0907444909029436
- Morin A, Eisenbraun B, Key J, Sanschagrin PC, Timony MA, Ottaviano M, Sliz P (2013) Collaboration gets the most out of software. *Elife* 2: e01456. doi:10.7554/elife.01456
- Munro S, Thomas KL, Abu-Shaar M (1993) Molecular characterization of a peripheral receptor for cannabinoids. *Nature* 365: 61–65. doi:10.1038/365061a0
- Murph MM, Scaccia LA, Volpicelli LA, Radhakrishna H (2003) Agonist-induced endocytosis of lysophosphatidic acid-coupled LPA1/EDG-2 receptors via a dynamin2- and Rab5-dependent pathway. *J Cell Sci* 116: 1969–1980. doi:10.1242/jcs.00397
- Murshudov GN, Skubák P, Lebedev AA, Pannu NS, Steiner RA, Nicholls RA, Winn MD, Long F, Vagin AA (2011) REFMAC5 for the refinement of macromolecular crystal structures. *Acta Crystallogr D Biol Crystallogr* 67: 355–367. doi:10.1107/s0907444911001314
- Nakane S, Oka S, Arai S, Waku K, Ishima Y, Tokumura A, Sugiura T (2002) 2-Arachidonoyl-sn-glycero-3-phosphate, an arachidonic acid-containing lysophosphatidic acid: Occurrence and rapid enzymatic conversion to 2-arachidonoyl-sn-glycerol, a cannabinoid receptor ligand, in rat brain. *Arch Biochem Biophys* 402: 51–58. doi:10.1016/s0003-9861(02)00038-3
- Nishimasu H, Okudaira S, Hama K, Mihara E, Dohmae N, Inoue A, Ishitani R, Takagi J, Aoki J, Nureki O (2011) Crystal structure of autotaxin and insight into GPCR activation by lipid mediators. *Nat Struct Mol Biol* 18: 205–212. doi:10.1038/nsmb.1998
- Noguchi K, Herr D, Mutoh T, Chun J (2009) Lysophosphatidic acid (LPA) and its receptors. *Curr Opin Pharmacol* 9: 15–23. doi:10.1016/j.coph.2008.11.010
- Perrakis A, Moolenaar WH (2014) Autotaxin: Structure-function and signaling. *J Lipid Res* 55: 1010–1018. doi:10.1194/jlr.R046391
- Pertwee RG (2008) The diverse CB<sub>1</sub> and CB<sub>2</sub> receptor pharmacology of three plant cannabinoids: Δ<sup>9</sup>-tetrahydrocannabinol, cannabidiol and Δ<sup>9</sup>-tetrahydrocannabivarin. *Br J Pharmacol* 153: 199–215. doi:10.1038/sj.bjp.0707442
- Pryimak N, Zaiachuk M, Kovalchuk O, Kovalchuk I (2021) The potential use of cannabis in tissue fibrosis. *Front Cell Dev Biol* 9: 715380. doi:10.3389/fcell.2021.715380
- Samadi N, Bekele R, Capatos D, Venkatraman G, Sariahmetoglu M, Brindley DN (2011) Regulation of lysophosphatidate signaling by autotaxin and lipid phosphate phosphatases with respect to tumor progression, angiogenesis, metastasis and chemo-resistance. *Biochimie* 93: 61–70. doi:10.1016/j.biochi.2010.08.002
- Smyth SS, Mueller P, Yang F, Brandon JA, Morris AJ (2014) Arguing the case for the autotaxin-lysophosphatidic acid-lipid phosphate phosphatase 3-signaling nexus in the development and complications of atherosclerosis. *Arterioscler Thromb Vasc Biol* 34: 479–486. doi:10.1161/atvbaha.113.302737
- Sugiura T, Kondo S, Sukagawa A, Nakane S, Shinoda A, Itoh K, Yamashita A, Waku K (1995) 2-Arachidonoylglycerol: A possible endogenous cannabinoid receptor ligand in brain. *Biochem Biophys Res Commun* 215: 89–97. doi:10.1006/bbrc.1995.2437
- Sugiura T, Nakane S, Kishimoto S, Waku K, Yoshioka Y, Tokumura A (2002) Lysophosphatidic acid, a growth factor-like lipid, in the saliva. *J Lipid Res* 43: 2049–2055. doi:10.1194/jlr.m200242-jlr200
- Tham Y-C, Li X, Wong TY, Quigley HA, Aung T, Cheng C-Y (2014) Global prevalence of glaucoma and projections of glaucoma burden through 2040. *Ophthalmology* 121: 2081–2090. doi:10.1016/j.ophtha.2014.05.013
- Tokumura A, Majima E, Kariya Y, Tominaga K, Kogure K, Yasuda K, Fukuzawa K (2002) Identification of human plasma lysophospholipase D, a lysophosphatidic acid-producing enzyme, as autotaxin, a multifunctional phosphodiesterase. *J Biol Chem* 277: 39436–39442. doi:10.1074/jbc.m205623200
- Umezū-Goto M, Kishi Y, Taira A, Hama K, Dohmae N, Takio K, Yamori T, Mills GB, Inoue K, Aoki J, et al (2002) Autotaxin has lysophospholipase D activity leading to tumor cell growth and motility by lysophosphatidic acid production. *J Cell Biol* 158: 227–233. doi:10.1083/jcb.200204026
- van Meeteren LA, Ruurs P, Stortelers C, Bouwman P, van Rooijen MA, Pradère JP, Pettit TR, Wakelam MJO, Saulnier-Blache JS, Mummery CL, et al (2006) Autotaxin, a secreted lysophospholipase D, is essential for blood vessel formation during development. *Mol Cell Biol* 26: 5015–5022. doi:10.1128/mcb.02419-05
- Vonrhein C, Flensburg C, Keller P, Sharff A, Smart O, Paciorek W, Womack T, Bricogne G (2011) Data processing and analysis with the autoPROC toolbox. *Acta Crystallogr D Biol Crystallogr* 67: 293–302. doi:10.1107/s0907444911007773
- Williams CJ, Headd JJ, Moriarty NW, Prisant MG, Videau LL, Deis LN, Verma V, Keedy DA, Hintze BJ, Chen VB, et al (2018) MolProbity: More and better reference data for improved all-atom structure validation: PROTEIN SCIENCE.ORG. *Protein Sci* 27: 293–315. doi:10.1002/pro.3330
- Zulfikar S, Mulholland S, Adamali H, Barratt SL (2020) Inhibitors of the autotaxin-lysophosphatidic acid Axis and their potential in the treatment of interstitial lung disease: Current perspectives. *Clin Pharmacol* 12: 97–108. doi:10.2147/CPAA.S228362



**License:** This article is available under a Creative Commons License (Attribution 4.0 International, as described at <https://creativecommons.org/licenses/by/4.0/>).

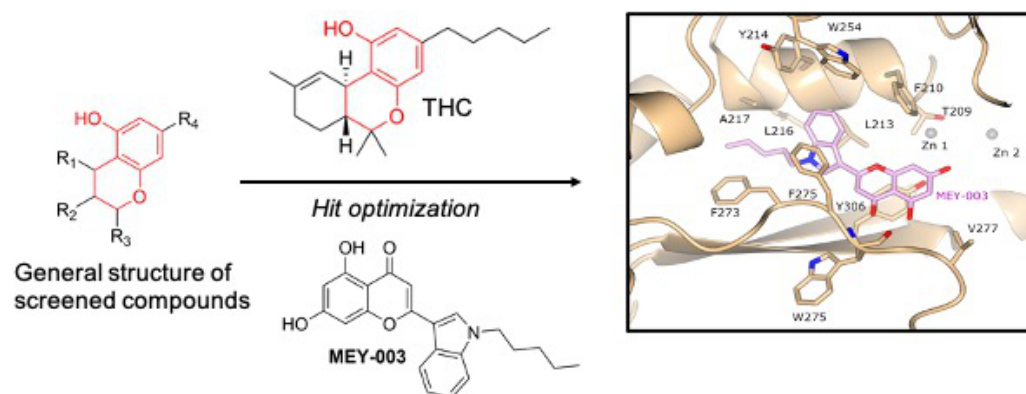
## Cannabinoid-inspired Inhibitors of Autotaxin

Mathias Christophe Eymery, Kim-Anh Nguyen, Shibom Basu, Jens Hausmann, Viet-Khoa Tran Nguyen, Hans Peter Seidel, Lola Gutierrez, Ahcène Boumendjel,\* and Andrew Aloysius McCarthy\*

---

**ABSTRACT:** Autotaxin (ATX) is an enzyme primarily known for the production of lysophosphatidic acid. Being involved in the development of major human diseases, such as cancer and neurodegenerative diseases, the enzyme has been featured in multiple studies as a pharmacological target. We previously found that the cannabinoid tetrahydrocannabinol (THC) could bind and act as an excellent inhibitor of ATX. This study aims to use the cannabinoid scaffold as a starting point to find cannabinoid-unrelated ATX inhibitors, following a funnel down approach in which large chemical libraries sharing chemical similarities with THC were screened to identify lead scaffold types for optimization. This approach allowed us to identify compounds bearing chromone and indole scaffolds as promising ATX inhibitors. Further optimization led to MEY-003, which is characterized by the direct linkage of an *N*-pentyl indole to the 5,7-dihydroxychromone moiety. This molecule has potent inhibitory activity towards ATX- $\beta$  and ATX- $\gamma$  as evidenced by enzymatic studies and its mode of action was rationalized by structural biology studies.

## Graphical Abstract



## ■ INTRODUCTION

Autotaxin (ATX) is a 115-125 kDa lysophospholipase D involved in a large range of physiological and pathological processes.<sup>1</sup> This enzyme is part of the ectonucleotide pyrophosphatase/phosphodiesterase family and is also referred to as ENPP2. ATX is mainly involved in the phospholipidic metabolism and the production of extracellular lysophosphatidic acid (LPA) from lysophosphatidylcholine (LPC).<sup>2</sup> At least five human isoforms have been discovered so far.<sup>3</sup> The  $\beta$  isoform is the most abundant, expressed in many parts of the body and accounting for the majority of ATX activity. The  $\alpha$  and  $\varepsilon$  isoforms are less abundant and differ from ATX- $\beta$  by a 52 amino acid (aa) polybasic insertion.<sup>4</sup> The ATX delta isoform is missing an exon of 19 tetrapeptides with unknown function.<sup>5</sup> ATX- $\gamma$  is brain-specific and differs from ATX- $\beta$  by a 25 aa insertion, while its activity is similar to the  $\beta$  isoform (Figure 1).<sup>3</sup> The ATX structure has been widely studied with 51 experimental entries in the Protein Data Bank to date.<sup>6</sup> It relies on (i) two flexible somatomedin B (SMB)-like domains, involved in protein-protein interactions, (ii) a conserved phosphodiesterase domain responsible for catalytic activity, and (iii) an inactive nuclease domain (Figure 1).<sup>7</sup> Structural insights into ATX show that the active site contains two zinc ions, allowing lysophosphatidylcholine binding and cleavage. A major point of substrate recognition by the ATX active site is the presence of a hydrophobic pocket, allowing the accommodation of both LPA and LPC.<sup>7</sup>

The implication of ATX in a large range of human diseases can be highlighted by both fundamental research and clinical trials.<sup>2,3,8-10</sup> Firstly, it has been shown that ATX is important for cancer progression and metastasis as this enzyme is responsible for LPA generation.<sup>8,9,11</sup> LPA is a growth factor, regulating many different cellular functions, some of which are important for malignant cells. Notably, it has been shown that LPA is a cell motility factor and that inhibiting ATX results in a decrease of *in vitro* cellular invasion through a decrease of LPA concentration in the surrounding fluids.<sup>10</sup> *In vivo* experiments and clinical trials showed that ovarian cancer cells produce high levels of LPA, as well as other conditions like during pregnancy,<sup>12</sup> stroke<sup>13</sup>, bone diseases<sup>14</sup> and acute coronary syndrome.<sup>15</sup> Recently, the confirmation of ATX's implication in neurological diseases was reported.<sup>11,16</sup> Further studies showed that ATX

levels are related to metabolism disorders in Alzheimer's disease, highlighting ATX as an interesting biomarker for this devastating pathology.<sup>17</sup> ATX levels in the serum were compared to MRI data of patients suffering from this disease, showing that some features of the latter were correlated with the former.<sup>17</sup> Serum levels of ATX also vary in other diseases and physiological conditions, which strengthens the need for fine-tuning of ATX catalysis.<sup>8</sup> However, while systemic LPA generation by ATX can be used as a biomarker it is not freely available in the blood, and unable to cross physiological compartments. In addition, LPA levels are not necessarily elevated in patients with cancer as the secretion and binding is mostly limited to tumor sites.<sup>3</sup> Also, LPA binds to receptors expressed at the cell surface. These receptors have many functions, e.g. regulating cell survival, apoptosis, cell differentiation, malignant transformation and many other processes through their G protein-coupled receptor activity.<sup>18</sup> More precisely, LPA receptors from the EDG family (LPA1 to LPA3) have been widely studied and are major pharmacological targets. Non-EDG family LPA receptors (LPA4-LPA6) were reported and recent studies allowed LPA6 structure determination and described this receptor family as important drug targets<sup>19</sup>. In recent years, it has been hypothesized and demonstrated that ATX may act not only as an enzyme but also as a chaperone presenting LPA to its receptors.<sup>7,20</sup> In this setting, it is of great interest to develop drugs that could selectively inhibit ATX in its pathological environment, without decreasing the overall levels of LPA in the blood.

Various ATX inhibitors have already been developed and some are now in clinical trials.<sup>2,21-23</sup> However, compounds with satisfactory pharmacokinetics parameters and low toxicity are limited. There is still no approved drug for ATX brain-related diseases. Moreover, ATX distribution is tissue-specific and most of the research has been focused on the  $\alpha$  and  $\beta$  isoforms. For ATX- $\gamma$ , plausibly related to many neurological diseases, a deeper understanding is needed to design and develop more specific inhibitors of this isoform and to fully understand its pathophysiological role.

Recently, we discovered that ATX was inhibited by various cannabinoids. In particular, THC and delta 6a,10a-THC inhibited ATX as mixed-type inhibitors at nanomolar concentrations.<sup>24</sup> Pharmacokinetic parameters for cannabinoids are widely studied and there is a consensus that they cross the blood brain

barrier and bind to CB1 and CB2 receptors, making them an ideal starting point to specifically inhibit ATX in the brain. Although cannabinoids were revealed as excellent ATX inhibitors, their major drawbacks relate to regulations, legislation and acceptance by patients, making them less desirable for development.

In this study, we used the results obtained with cannabinoids for the identification and development of new inhibitors devoid of potential side effects. Here, we identified a new family of potent ATX inhibitors through the screening of chemical libraries sharing structural similarities with THC. We also report the human ATX- $\gamma$  structure bound to the most active inhibitor (namely here MEY-003), a novel ATX inhibitor bearing both chromone and indole scaffolds, and LPA at atomic resolutions using X-ray crystallography.

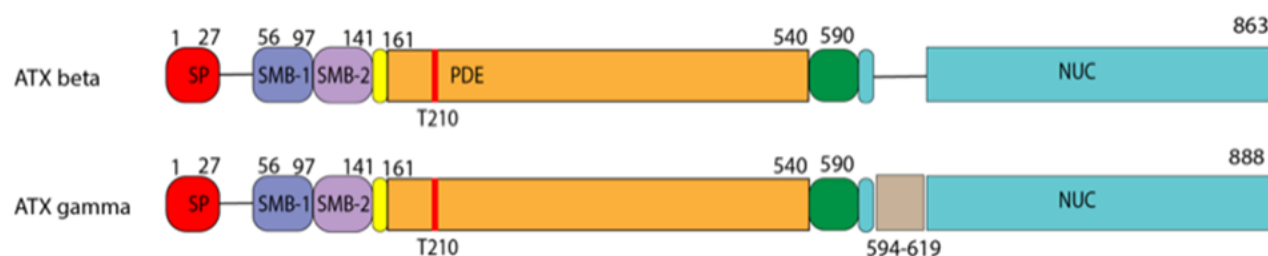


**Figure 1.** Schematic comparison of the ATX- $\beta$  and ATX- $\gamma$  isoforms.

## ■ RESULTS

**Identification of hits by the screening of compounds sharing structural similarities with cannabinoid.** Our strategy was based on the structural similarity between the benzopyran moiety of THC and THC-unrelated molecules bearing this chemical entity. Among these compounds, we targeted chromone-bearing derivatives (Figure 2). This druggable scaffold is known for its therapeutic potential and safety. The therapeutic potential of chromone was recently highlighted in two major reports.<sup>25,26</sup> Herewith, 80 compounds bearing a chromone and chromone-like moieties were tested for their inhibitory potential at 1  $\mu$ M. The most important representatives of the screened compounds are available in supplementary information section II. The screening revealed that molecules bearing an indole linked to a chromone

moiety presented the highest inhibition against ATX (Figure 2). Following further structure-activity relationship (SAR) studies and optimization, we found that compounds having the following substitution pattern tended to exert a high inhibitory effect: (a) the presence of a linear hydrophobic substituent at the indole nitrogen, (b) the presence of two hydroxyls at positions 5/7 of the chromone moiety (Figure 2), (c) the addition of a hydroxyl group at position 3 of chromone was harmful for the inhibition activity (Table S1), (d) the site of linkage of chromone and indole moieties is crucial since when the linkage was done through the phenyl ring of the indole moiety (MEY-005), the inhibition activity was decreased (Table 1), (e) the benzopyranone moiety of chromone is important as its shift to a benzofuran led to drop of activity. Interestingly, the length of hydrophobic carbon chain inducing the highest inhibition activity correlates with the one found in THC. Branched chains, and chains bearing aromatic or saturated rings were disadvantageous for the inhibition activity as shown by the lower activity of MEY-001, MEY-002, MEY-007 and MEY-008 compounds. Based on these structural requirements, we followed a funnel down synthetic and SAR approach that led to the identification of MEY-003 as the most inhibitory compound (Table 1).

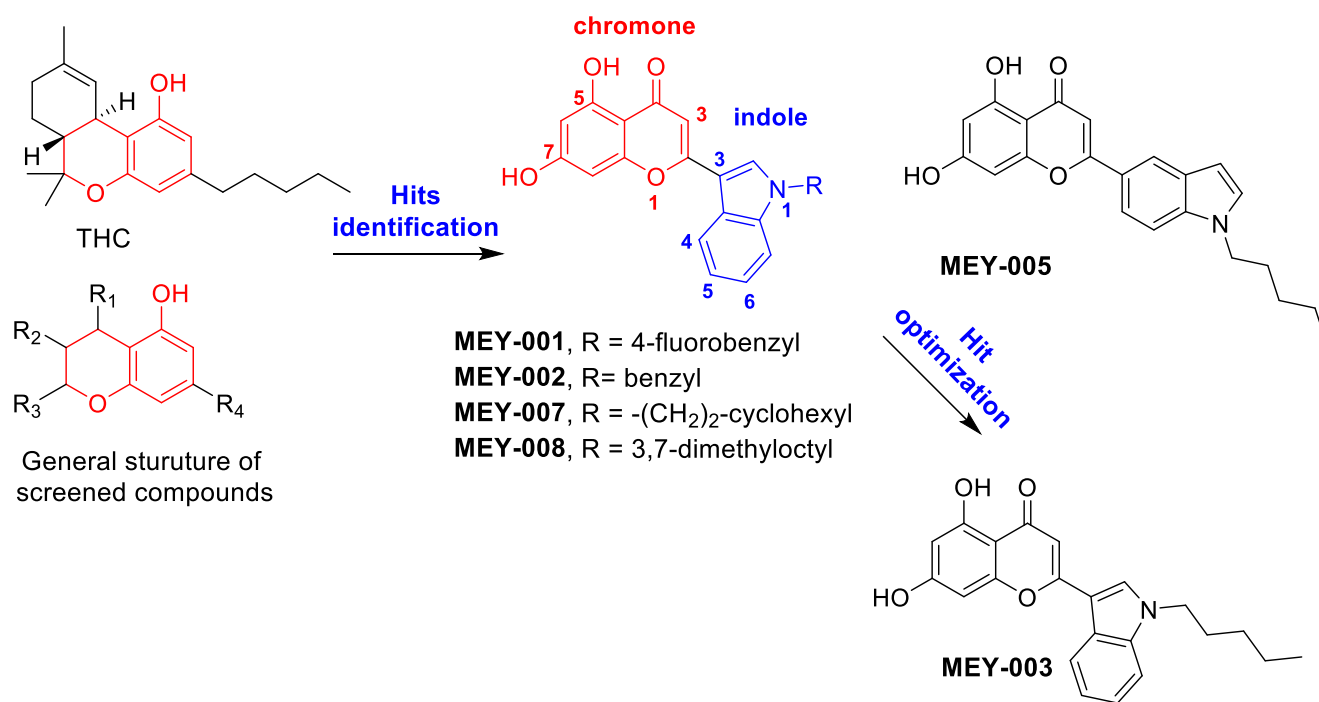


**Figure 2.** Discovery process of ATX inhibitors through screening and optimization of compounds sharing cannabinoid structural similarity.

**Table 1.** Inhibition activity of lead hits on hATX- $\beta$  and hATX- $\gamma$ .

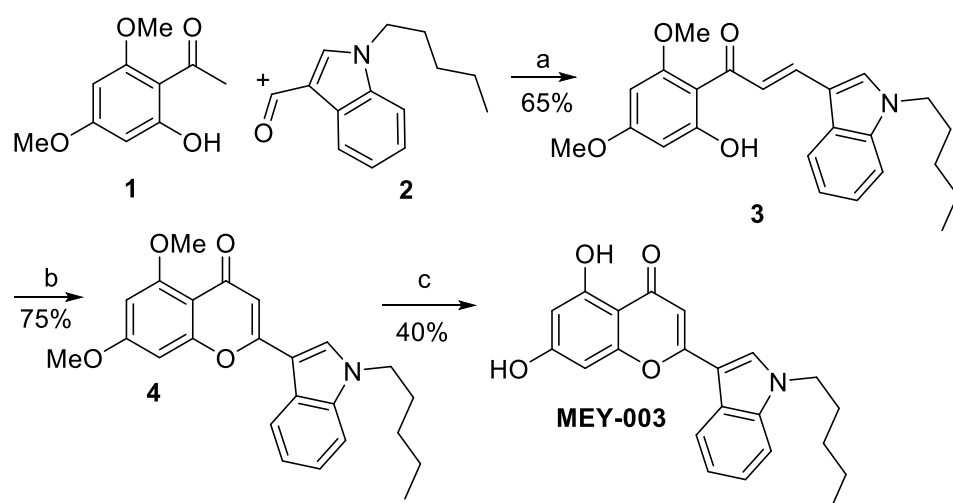
Compound	IC <sub>50</sub> hATX- $\beta$ ( $\mu$ M)		IC <sub>50</sub> hATX- $\gamma$ ( $\mu$ M)	
	LPC18:1	LPC16:0	LPC18:1	LPC16:0
MEY-001	1.40 (0.9-1.8)	1.20 (0.31-1.970)	3.8(2.2-9.3)	2.4 (1.9-2.3)
MEY-002	0.82 (0.7-0.96)	0.88 (0.6-1.08)	1.25 (0.99-1.65)	0.81 (0.61-1)
MEY-003	0.46 (0.35-0.61)	0.384 (0.36-0.4)	1.099 (0.925-1.317)	0.38 (0.3-4.6)
MEY-005	> 5	> 5	> 5	> 5
MEY-007	< 20%*	< 20%*	-	-
MEY-008	NA**	NA**	-	-

\* at 1 micromolar concentration; \*\* Not Active. Value shows 95% CI (profile likelihood)

Hits shown above (Figure 2) can be synthesized in three steps according to the same synthetic sequence as exemplified by the synthesis of MEY-003 shown in scheme 1. MEY-003 was synthesized starting from the commercially available 2,4-dimethoxy-6-hydroxyacetophenone (**1**) and *N*-pentylindol-3-carboxaldehyde (**2**). The latter can be very easily prepared by the *N*-alkylation of indol-3-carboxaldehyde. Starting materials (**1**) and (**2**) were subjected to a condensation reaction in the presence of potassium hydroxide in methanol to yield diarylpropenone (**3**) with 65% yield. The latter was submitted to an oxidative-cyclization reaction with iodine at 150 °C with DMSO as the solvent to provide chromone derivative (**4**) with 75% yield. Finally, compound (**4**) was subjected to boron tribromide-mediated demethylation to provide the desired compound, MEY-003, with 40% yield. The purity and authenticity of MEY-003 and its analogs shown in Figure 2 were attested by NMR (<sup>1</sup>H and <sup>13</sup>C), MS (ESI+) and LCMS.



### Scheme 1. Synthesis of MEY-003.



(a) KOH, MeOH, reflux, (b) I<sub>2</sub>, DMSO, 150 °C, (c) BBr<sub>3</sub>, CH<sub>2</sub>Cl<sub>2</sub>, room temperature.

As outlined above, emphasis has been focused on MEY-003 since it produced the highest inhibition level (Figure 3a, b, c, d). EC<sub>50</sub> measurements are described in the supplemental experimental section and were adapted from our previous work using the choline-release assay.<sup>24</sup> The apparent EC<sub>50</sub> with human ATX-β and LPC18:1 was 0.46 μM with an inhibition slope of 68% (Figure 3a). The apparent EC<sub>50</sub> with human ATX-β and LPC16:0 was 0.38 μM with an inhibition slope of 83% (Figure 3c). In order to demonstrate the potency with the cerebral isoform of ATX, the apparent EC<sub>50</sub> measurements were repeated using human ATX-γ under similar assay conditions. Interestingly, the apparent EC<sub>50</sub> was slightly higher with LPC18:1, at 1.1 μM (Figure 3b), but similar to that previously obtained for hATX-β and LPC16:0, with an apparent EC<sub>50</sub> of 0.38 μM, showing the ability of this compound to inhibit both ATX isoforms at different levels. Additionally, the span of inhibition ranged from 66% to 72% for LPC18:1 and LPC16:0, respectively.

**MEY-003 acts as a non-competitive ATX inhibitor.** In order to better understand the mode of action of MEY-003, an inhibition assay was run in similar assay conditions using hATX-β and LPC18:1 (Figure 3e). It shows that MEY-003 behaves as a non-competitive inhibitor (apparent K<sub>i</sub> was 432 nM), which is in agreement with structural data (shown later). The non-competitive inhibition for MEY-003 reported

here with an Alpha value  $>1$  can also be considered as a special case of mixed inhibition with preferential binding to the free enzyme<sup>27</sup>.

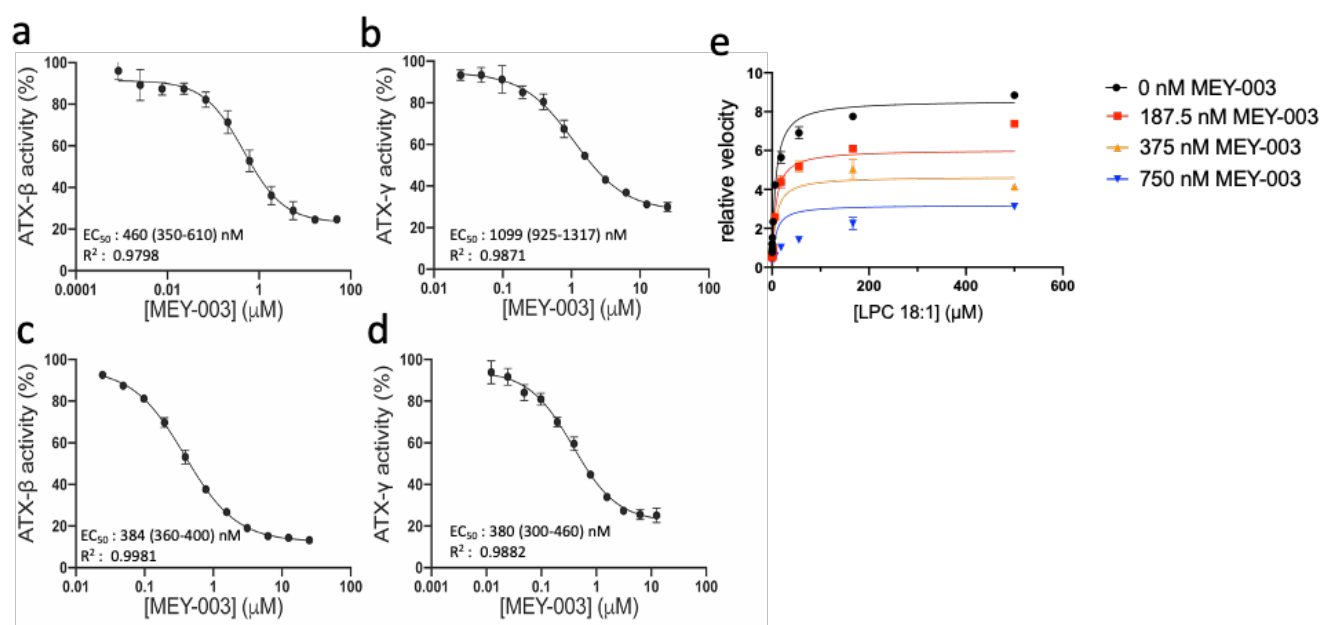


**Figure 3. Inhibition of autotaxin (ATX) by MEY-003.** Dose-response analysis of (a) hATX- $\beta$  and (b) hATX- $\gamma$  with LPC18:1 and MEY-003, (c) hATX- $\beta$  and (d) hATX- $\gamma$  with LPC16:0 and MEY-003. (e) The mode of inhibition of MEY-003 with hATX- $\beta$  and LPC18:1 indicates a non-competitive inhibitory activity. All error bars represent the S.E.M. ( $n=3$ ).  $EC_{50}$  values are computed with a 95% CI (profile likelihood).

**MEY-003 binds in the hydrophobic pocket of ATX- $\gamma$ .** Human ATX- $\gamma$  has been co-crystallized with MEY-003 and LPA (Table S3, Figure 4 and S1). A recombinant N54A/N411A hATX- $\gamma$  mutant was used for crystallization as previously reported for other isoforms.<sup>24,28</sup> Interestingly, the enzyme crystallized in the same conditions as rat ATX- $\beta$  (Supplemental experimental section), with two molecules in the asymmetric unit. The ATX-MEY-003 complex structure allowed the identification of important protein-ligand interactions in the ATX hydrophobic binding pocket using the PLIP (Protein-Ligand Interaction Profiler) server (Figure 4c and S2). Most of the interactions are hydrophobic, similar to those observed with THC and rATX- $\beta$ . However, we observed two hydrogen bonds between the main chain carbonyl of W276 and

a MEY-003 hydroxy, as well as  $\pi$  stacking interactions between MEY-003 and residues F275 and Y307. The additional  $\pi$  stacking and hydrogen bonds most likely explain the difference in binding between MEY-003 and THC in the ATX hydrophobic pocket. Indeed, EC50 comparisons showed that the apparent EC50 of THC is 1.026  $\mu\text{M}$  and that of MEY-003 with hATX- $\beta$  and LPC18:1 is 0.46  $\mu\text{M}$ . A further superposition of hATX- $\gamma$ -MEY-003 and hATX- $\gamma$ -LPA18:1 was carried out (Figure 4d), showing that the LPA lipophilic tail is bounded in a similar position to MEY-003 in hATX- $\gamma$ . Additionally, a superposition with the rATX- $\beta$ -THC structure from previous work shows that MEY-003 binds in a similar position, but with a slightly different conformation, to THC (Figure 4e). Interestingly, other ATX inhibitors do not seem to share a similar binding interface. For example, PAT-078, which retains an indole in its structure, does not adopt a similar conformation, at least, for the indolic part of the inhibitor (Figure 5c) (PDB: 4ZG6)<sup>27</sup>.

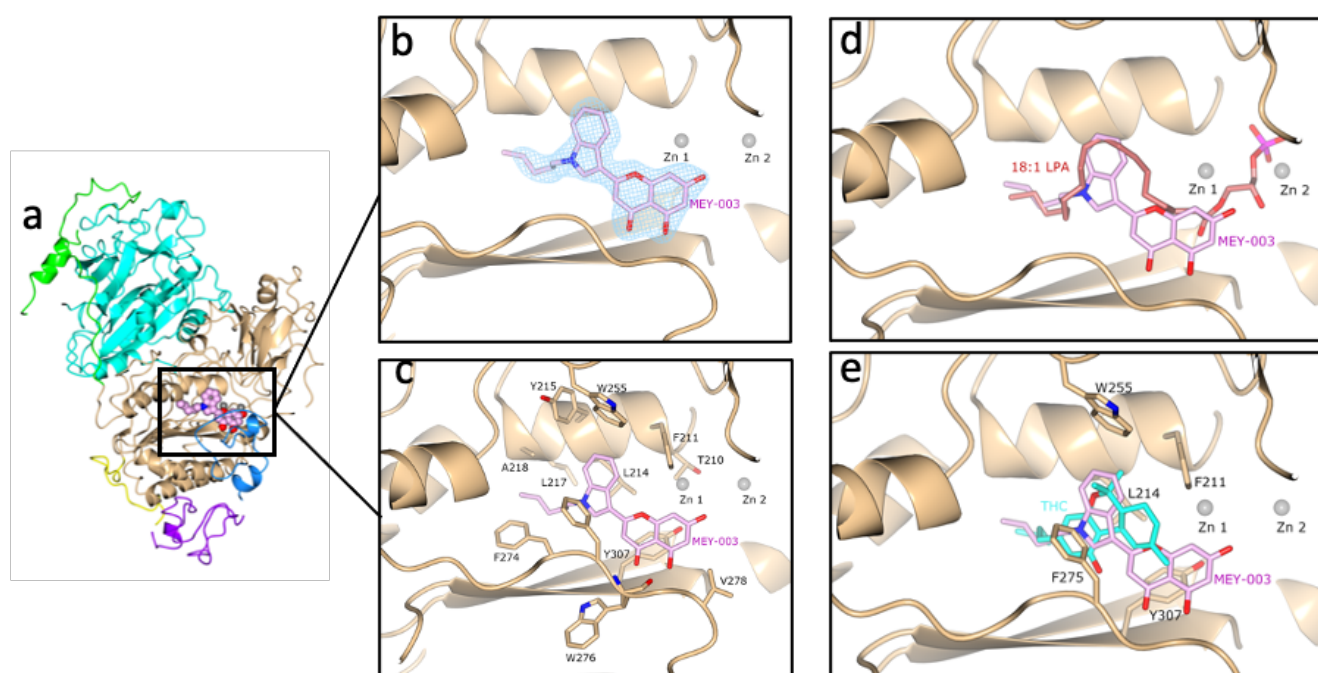


**Figure 4. MEY-003 binding to hATX- $\gamma$  hydrophobic pocket.** (a) hATX- $\gamma$  overall structure bound with MEY-003 (PDB: 8C3O). Domains are colored according to Figure 1. (b) MEY-003 2F<sub>o</sub>-F<sub>c</sub> density at 1 sigma after refinement (PDB: 8C3O). (c) MEY-003 binding interface with hATX- $\gamma$  (PDB: 83CO). (d) Superposition of hATX- $\gamma$ -MEY-003 and hATX- $\gamma$ -LPA (PDB: 8C3O and 8C3P). (e) Superposition of hATX- $\gamma$ -MEY-003 and rATX-THC with main interactions displayed (PDB: 8C3O and 7P4J).

To obtain a higher structural resolution, rATX- $\beta$  was co-crystallized with both MEY-003 and MEY-002 (Table S3 and Figure 5). Superpositions of both structures showed that the indole can adopt a slightly different conformation in the hydrophobic pocket, relying on the ability of L213 to adopt two different conformations (Figure 5 d,e,f). In the MEY-003 bound structure, L213 makes a side-on interaction with the indole while adopting a face-to-face conformation with MEY-002. The MEY-002 bound structure also revealed an important water bridge in the binding interface, linking the ligand with important residues, T209 and D171, to indirectly interact with the active site Zn ions (Figure 5d). We can expect this water bridge to be relevant for MEY-003 as well, but this is probably only visible in the MEY-002-rATX- $\beta$  co-structure due to the higher resolution obtained (1.9 vs 2.5 Å) (PDB: 8C4W). This might explain the non-competitive inhibition of hATX- $\gamma$  of MEY-003 (Figure 3e). Therefore, MEY-003 could be classified as a type 2 inhibitor since it binds in the hydrophobic pocket. However, it does not completely overlap with corresponding type 2 inhibitors like PAT-078 (Figure 5c) (PDB: 4ZG6). Partial overlap with type 1 inhibitors such as HA-155 (Figure 5c) (PDB: 2XRG) shows that chromone-indol hybrid inhibitors can be classified as type 2-like inhibitors, with indirect interactions with the active site through a water bridge.

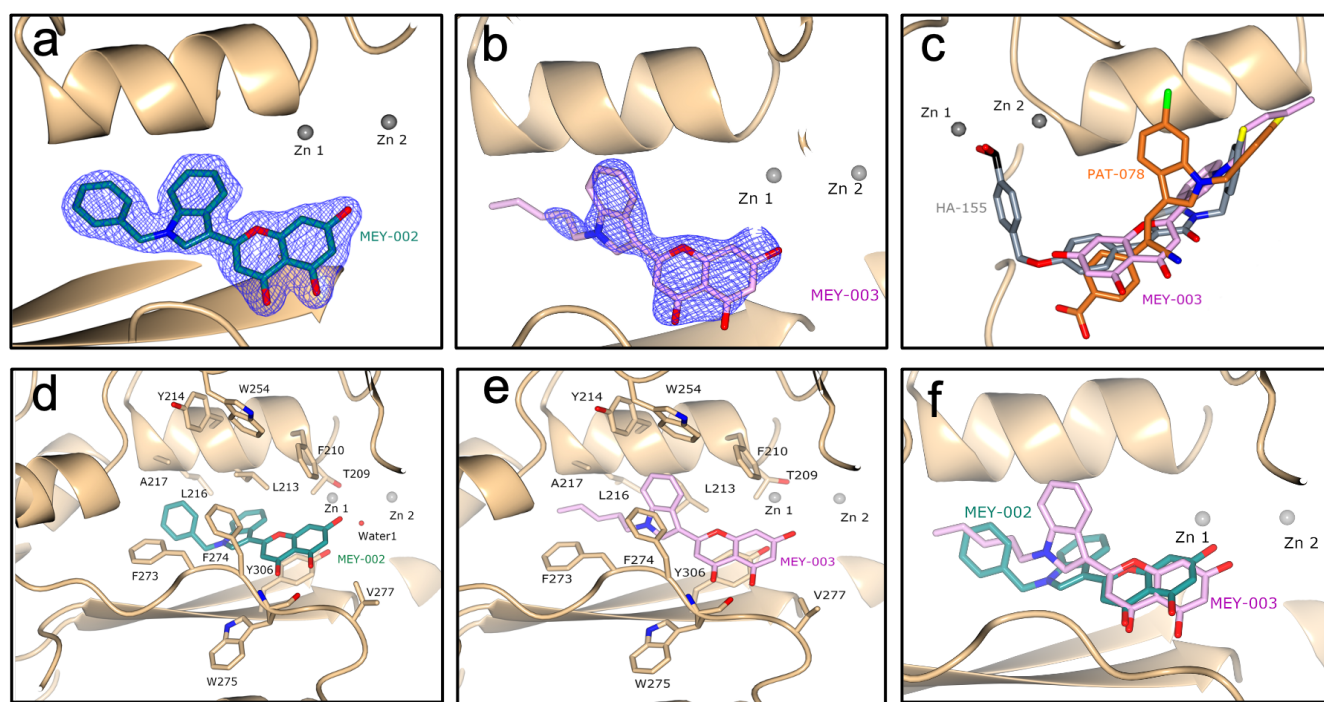


**Figure 5. MEY-002 and MEY-003 binding to the rATX- $\beta$  hydrophobic pocket.** (a) MEY-002 2F<sub>o</sub>-F<sub>c</sub> density at 1 sigma after refinement (PDB: 8C4W). (b) MEY-003 2F<sub>o</sub>-F<sub>c</sub> density at 1 sigma after refinement (PDB: 8C7R). (c) Superposition of inhibitors HA-155, PAT-078 and MEY-003 (PDB: 2XRG, 4ZG6 and 8C7R). (d) MEY-002 binding interface with rATX- $\beta$  (PDB:8C4W). (e) MEY-003 binding interface with rATX- $\beta$  (PDB: 8C7R). (f) Superposition of rATX- $\beta$ -MEY-002 and rATX- $\beta$ -MEY-003 (PDB: 8C4W and 8C7R).

**MEY-003 reduces hLPA1 internalization and is not cytotoxic to HeLa cells.** ATX regulates various physiological and pathological processes in cells. One of the key roles of ATX is to produce LPA, a major lipid cell signaling component. Previous studies showed that the ATX-LPA axis is highly regulated and dependent on ATX activity in order to trigger LPA receptor internalization.<sup>8</sup> It has been recently demonstrated that ATX is responsible for LPA presentation towards receptors by acting as a chaperone.<sup>20</sup> In this study, we confirmed that MEY-003 is able to reduce LPA1 receptor internalization in HeLa cells after treatment with LPC and hATX- $\beta$ . LPA1 internalization was reduced by approximately 47% (Figure 6a), showing that MEY-003 significantly blocks LPA signaling through ATX inhibition. Moreover, further *in*

*in vitro* assays showed that MEY-003 is non-cytotoxic after prolonged treatment (up to 8 hours) at 100  $\mu$ M. The same assay performed on MEY-002 also showed no cytotoxicity effects (Figure 6b).

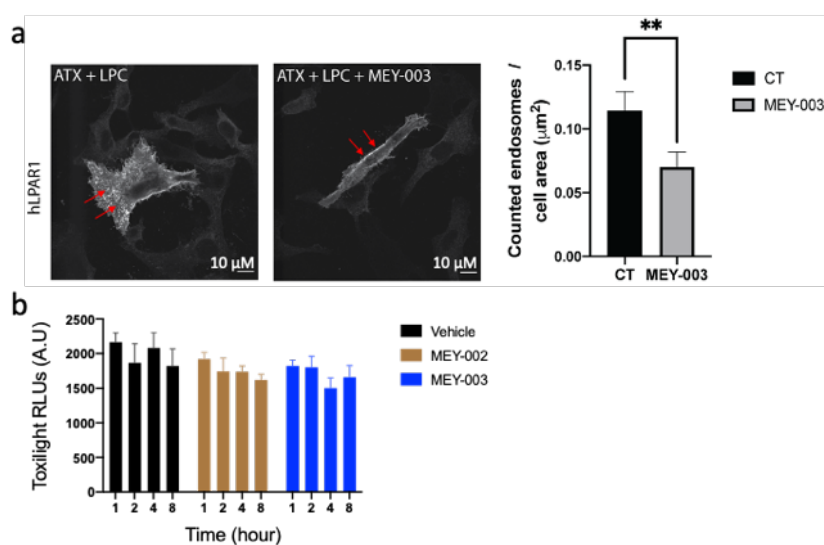


**Figure 6. MEY-003 reduces LPA1 receptor internalization and is not cytotoxic to HeLa cells. (a)**

Cells were treated with hATX- $\beta$  and LPC with or without MEY-003 addition. After treatment, cells were fixed and stained using an anti-HA tag antibody. 17 and 15 images were acquired in biological triplicate for hATX- $\beta$  + LPC + MEY-003 and hATX- $\beta$  + LPC, respectively, using a LEICA microscope at 63X magnification. Red arrows are pointing at LPA1 receptor hypersignal. Receptor internalization was quantified with Fiji with a paired t-test p-value = 0.0078. (b) Cells were incubated with 100  $\mu$ M of MEY-003 or MEY-002 for 1 to 8 hours. Cytotoxicity detection was performed using Toxilight assay. All error bars represent S.E.M. (n=3) in biological triplicate.

## ■ DISCUSSION

The plant *Cannabis sativa* (Marijuana) has been used in medicine for a long time and still attracts interest due to the biological activity of its metabolites, known as cannabinoids (a group of C21 terpenophenolic compounds). The most abundant among them is  $\Delta$ 9-tetrahydrocannabinol (THC). Marijuana-derived drugs, and especially those derived from THC, have been developed but their therapeutic/psychotropic balance was frequently criticized. In this study, we have used the general chemical structure of THC that

showed an inhibitory activity against ATX as a basis to screen chemical libraries sharing some structural similarities with THC, but derived from different secondary metabolites. Hence, following the screening of a chemical library of compounds bearing the benzopyranone moiety (Supplemental section II) and the optimization of the obtained selected hits (Figure 2 and Table 1), we identified the compound MEY-003, which is derived from a hybrid system bearing both chromone and indole scaffolds as a potent inhibitor of ATX (Figure 3).

Here, we also describe the structure of hATX- $\gamma$  in complex with its natural end-product LPA18:1 and MEY-003 at a resolution of 2.4 and 2.3 Å, respectively (Figure 4). Our results highlight that hATX- $\gamma$  shares a very similar structural organization with hATX- $\beta$ , as deduced from superposition with the PDB: 4ZG7,<sup>27</sup> resulting in an RMSD of 0.56 Å for 775 aligned C $\alpha$  atoms. The deglycosylated mutant used for crystallization did not lead to a significant activity difference when compared to wild-type hATX- $\gamma$  (Figure S3). One major difference between the brain-specific hATX- $\gamma$  and hATX- $\beta$  is the presence of a 25 aa insertion at position 593 (EAETRKFRGSRNENKENINGNFEPK), leading to a flexible loop at the surface of hATX- $\gamma$ . The function of this modification is unknown and specific to the brain isoform. Up to now, there is no evidence that proteolytic cleavage of this loop is related to neurological, psychiatric and neoplastic diseases.<sup>16,17,29</sup> In this study, we also observed that hATX- $\gamma$  can be cleaved (Figure S4), resulting in a fragment of ~34 kDa that corresponds to a C-terminal region cleavage at this insertion. Further experiments would be needed to understand which enzyme is responsible for cleaving hATX- $\gamma$  and if this is biologically relevant.

Chromones and indoles are two prominent scaffolds largely investigated for their therapeutic potential in the management of major chronic diseases, including neurodegenerative diseases, cancer, diabetes, infection and inflammation.<sup>25,30</sup> The physicochemical properties of MEY-003 are promising, with a calculated logP of 3.7, a MW of 363.41 Da, as well as 2 and 5 hydrogen bond donors and acceptors, respectively (Table S2). MEY-003 respects the Lipinski's rule for oral bioavailability and fits most of the properties described by Pajouhesh *et al.* for successful central nervous system drugs, with a calculated PSA of 70 Å and previously described properties<sup>31</sup>. Concerning the metabolic liability of the chromone, a good *in vivo*

stability of this scaffold has previously been reported<sup>32</sup>. In addition, Cromolyn, a drug used for allergies and composed of a chromone scaffold has also been shown to have good metabolic stability, with most of the compound excreted without modifications<sup>33</sup>. In latter contexts, many clinically approved drugs contain one of these two entities.<sup>25</sup> Therefore, the combination of a chromone and an indole, two druggable scaffolds, in the same entity may offer diverse advantages for the development of MEY-003 as a drug candidate that targets ATX-related diseases.

## ■ CONCLUSION

We recently reported that THC is a potent ATX inhibitor.<sup>24</sup> Due to its psychotropic effect, legislation, and non-acceptance by society, this marijuana-derived compound is unlikely to be used in clinical settings for the management of ATX-related disorders. Therefore, we used THC as a basis to explore diverse molecules with partial chemical and structural similarity, particularly those sharing a benzopyrane moiety such as naturally occurring chromones and flavones. The process of screening, hit identification and hit optimization allowed us to identify MEY-003 as a potent and safe inhibitor of ATX. The inhibition profile of MEY-003 was rationalized through advanced structural biology drug discovery studies. MEY-003 has a unique structure compared to previously published ATX inhibitors that could potentially lead to the development of new drugs targeting the ATX-LPA axis with fewer side effects.

## ■ ASSOCIATED CONTENT

### SUPPORTING INFORMATION

The Supporting Information is available free of charge at <https://pubs.acs.org>

Synthesis methods and characterization of MEY-003 analogs. Spectral data, inhibitor summary, biochemical reagents and crystallographic data.



PDB accession codes for the presented structures: atomic coordinates and experimental data will be released upon article publication (see table S3 for PDB codes).

## ■ AUTHOR INFORMATION

### Corresponding Authors

**Andrew A. McCarthy** - *European Molecular Biology Laboratory, EMBL Grenoble, 71 avenue des Martyrs, 38000 Grenoble, France*

**Ahcène Boumendjel** – *Univ. Grenoble Alpes, INSERM, LRB, 38000 Grenoble, France*

### Authors

**Mathias Christophe Eymery** - *European Molecular Biology Laboratory, EMBL Grenoble, 71 avenue des Martyrs, 38000 Grenoble, France*

**Kim-Anh Nguyen** - *Univ. Grenoble Alpes, INSERM, LRB, 38000 Grenoble, France*

**Shibom Basu** - *European Molecular Biology Laboratory, EMBL Grenoble, 71 avenue des Martyrs, 38000 Grenoble, France*

**Jens Hausmann** - *European Molecular Biology Laboratory, EMBL Grenoble, 71 avenue des Martyrs, 38000 Grenoble, France. Current address: School of Medicine and Health Sciences, Carl von Ossietzky University of Oldenburg, Oldenburg, Germany.*

**Viet-Khoa Tran-Nguyen** - *Centre de Recherche en Cancérologie de Marseille (CRCM), Inserm, U1068, Marseille, F-13009, France*

**Hans Peter Seidel** - *European Molecular Biology Laboratory, EMBL Grenoble, 71 avenue des Martyrs, 38000 Grenoble, France*

**Lola Gutierrez** - *European Molecular Biology Laboratory, EMBL Grenoble, 71 avenue des Martyrs, 38000 Grenoble, France*

## Author Contributions

M.C.E. Development of methodology, acquisition of data, analysis and interpretation of results. K.A.N. Organic synthesis of hits and MEY-003. S.B., J.H., H.P.S and L.G. Structural biology studies and interpretation of results. V.K.T.N. Molecular modelling and docking studies. A.B. and A.A.M. Conception, design and study supervision. The manuscript was written through the contributions of all authors. All authors read and approved the final version of the manuscript.

## Notes

Findings regarding the potential applications of MEY-003 and analogs are the subject of E.U. patent application EP22215403.1, filed on December 21, 2022, owned by European Molecular Biology Laboratory, and Université Grenoble Alpes, and lists M.C.E., A.B., and A.A.M as inventors.

## ■ ACKNOWLEDGMENT

We are thankful for the kind gift of ATX-expressing cell lines from the Perrakis laboratory at NKI in Amsterdam. We thank the beamline staff from the EMBL-ESRF Joint Structural Biology Group for beamtime at the European Synchrotron Radiation Facility (ESRF), Grenoble, France. The authors also wish to express their gratitude to the Eukaryotic Expression Facility in Grenoble for infrastructure access, especially Alice Aubert and Martin Pelosse for excellent technical support and fruitful discussions. MC Eymery has been funded by the EMBL International PhD program. AA McCarthy has been funded by EMBL. J Hausmann was supported by a fellowship from the EMBL Interdisciplinary Postdoc (EI3POD) program under Marie Skłodowska-Curie Actions COFUND (grant number: 664726).

## ■ ABBREVIATIONS

ATX, autotaxin; FCS, fetal calf serum; HRP, horseradish peroxidase; LPA, lysophosphatidic acid; LPC, lysophosphatidyl choline; MTBE, methyl tert-butyl ether; NUC, nuclease; PDB, protein data bank; PDE, phosphodiesterase; SEM, standard error of the mean; SMB, somatomedin  $\beta$ -like.

## ■ REFERENCES

- (1) Ninou, I.; Magkrioti, C.; Aidinis, V. Autotaxin in Pathophysiology and Pulmonary Fibrosis. *Front. Med.* **2018**, *5*, 180. <https://doi.org/10.3389/fmed.2018.00180>.
- (2) Castagna, D.; Budd, D. C.; Macdonald, S. J. F.; Jamieson, C.; Watson, A. J. B. Development of Autotaxin Inhibitors: An Overview of the Patent and Primary Literature: Miniperspective. *Journal of Medicinal Chemistry* **2016**, *59* (12), 5604–5621. <https://doi.org/10.1021/acs.jmedchem.5b01599>.
- (3) Ninou, I.; Magkrioti, C.; Aidinis, V. Autotaxin in Pathophysiology and Pulmonary Fibrosis. *Frontiers in Medicine* **2018**, *5*. <https://doi.org/10.3389/fmed.2018.00180>.
- (4) Giganti, A.; Rodriguez, M.; Fould, B.; Moulharat, N.; Cogé, F.; Chomarat, P.; Galizzi, J.-P.; Valet, P.; Saulnier-Blache, J.-S.; Boutin, J. A.; Ferry, G. Murine and Human Autotaxin  $\alpha$ ,  $\beta$ , and  $\gamma$  Isoforms. *Journal of Biological Chemistry* **2008**, *283* (12), 7776–7789. <https://doi.org/10.1074/jbc.M708705200>.
- (5) Hashimoto, T.; Okudaira, S.; Igarashi, K.; Hama, K.; Yatomi, Y.; Aoki, J. Identification and Biochemical Characterization of a Novel Autotaxin Isoform, ATX , with a Four-Amino Acid Deletion. *Journal of Biochemistry* **2012**, *151* (1), 89–97. <https://doi.org/10.1093/jb/mvr126>.
- (6) *RCSB Protein Data Bank - RCSB PDB*. <http://www.rcsb.org/pdb/home/home.do> (accessed 2017-12-09).
- (7) Moolenaar, W. H.; Perrakis, A. Insights into Autotaxin: How to Produce and Present a Lipid Mediator. *Nat Rev Mol Cell Biol* **2011**, *12* (10), 674–679. <https://doi.org/10.1038/nrm3188>.
- (8) Gotoh, M.; Fujiwara, Y.; Yue, J.; Liu, J.; Lee, S.; Fells, J.; Uchiyama, A.; Murakami-Murofushi, K.; Kennel, S.; Wall, J.; Patil, R.; Gupte, R.; Balazs, L.; Miller, D. D.; Tigyi, G. J. Controlling Cancer through the Autotaxin–Lysophosphatidic Acid Receptor Axis. *Biochemical Society Transactions* **2012**, *40* (1), 31–36. <https://doi.org/10.1042/BST20110608>.
- (9) Lee, D.; Suh, D.-S.; Lee, S. C.; Tigyi, G. J.; Kim, J. H. Role of Autotaxin in Cancer Stem Cells. *Cancer and Metastasis Reviews* **2018**, *37* (2–3), 509–518. <https://doi.org/10.1007/s10555-018-9745-x>.
- (10) Umezū-Goto, M.; Kishi, Y.; Taira, A.; Hama, K.; Dohmae, N.; Takio, K.; Yamori, T.; Mills, G. B.; Inoue, K.; Aoki, J.; Arai, H. Autotaxin Has Lysophospholipase D Activity Leading to Tumor Cell Growth and Motility by Lysophosphatidic Acid Production. *The Journal of Cell Biology* **2002**, *158* (2), 227–233. <https://doi.org/10.1083/jcb.200204026>.
- (11) Valdés-Rives, S. A.; González-Arenas, A. Autotaxin-Lysophosphatidic Acid: From Inflammation to Cancer Development. *Mediators of Inflammation* **2017**, *2017*, 1–15. <https://doi.org/10.1155/2017/9173090>.
- (12) Willier, S.; Butt, E.; Grunewald, T. G. P. Lysophosphatidic Acid (LPA) Signalling in Cell Migration and Cancer Invasion: A Focussed Review and Analysis of LPA Receptor Gene Expression on the Basis of More than 1700 Cancer Microarrays: Role of LPA in Cell Migration and Cancer Metastasis. *Biol. Cell* **2013**, *105* (8), 317–333. <https://doi.org/10.1111/boc.201300011>.

- (13) Achón Buil, B.; Rust, R. Preserving Stroke Penumbra by Targeting Lipid Signalling. *Journal of Cerebral Blood Flow & Metabolism* **2023**, *43* (1), 167–169. <https://doi.org/10.1177/0271678X221121853>.
- (14) Alioli, C.; Demesmay, L.; Peyruchaud, O.; Machuca-Gayet, I. Autotaxin/Lysophosphatidic Acid Axis: From Bone Biology to Bone Disorders. *IJMS* **2022**, *23* (7), 3427. <https://doi.org/10.3390/ijms23073427>.
- (15) Dohi, T.; Miyauchi, K.; Ohkawa, R.; Nakamura, K.; Kishimoto, T.; Miyazaki, T.; Nishino, A.; Nakajima, N.; Yaginuma, K.; Tamura, H.; Kojima, T.; Yokoyama, K.; Kurata, T.; Shimada, K.; Yatomi, Y.; Daida, H. Increased Circulating Plasma Lysophosphatidic Acid in Patients with Acute Coronary Syndrome. *Clinica Chimica Acta* **2012**, *413* (1), 207–212. <https://doi.org/10.1016/j.cca.2011.09.027>.
- (16) Herr, D. R.; Chew, W. S.; Satish, R. L.; Ong, W.-Y. Pleotropic Roles of Autotaxin in the Nervous System Present Opportunities for the Development of Novel Therapeutics for Neurological Diseases. *Molecular Neurobiology* **2020**, *57* (1), 372–392. <https://doi.org/10.1007/s12035-019-01719-1>.
- (17) for the Alzheimer’s Disease Neuroimaging Initiative; McLimans, K. E.; Willette, A. A. Autotaxin Is Related to Metabolic Dysfunction and Predicts Alzheimer’s Disease Outcomes. *JAD* **2017**, *56* (1), 403–413. <https://doi.org/10.3233/JAD-160891>.
- (18) Tigyi, G. Aiming Drug Discovery at Lysophosphatidic Acid Targets: Novel LPA Targets. *British Journal of Pharmacology* **2010**, *161* (2), 241–270. <https://doi.org/10.1111/j.1476-5381.2010.00815.x>.
- (19) Taniguchi, R.; Inoue, A.; Sayama, M.; Uwamizu, A.; Yamashita, K.; Hirata, K.; Yoshida, M.; Tanaka, Y.; Kato, H. E.; Nakada-Nakura, Y.; Otani, Y.; Nishizawa, T.; Doi, T.; Ohwada, T.; Ishitani, R.; Aoki, J.; Nureki, O. Structural Insights into Ligand Recognition by the Lysophosphatidic Acid Receptor LPA6. *Nature* **2017**, *548* (7667), 356–360. <https://doi.org/10.1038/nature23448>.
- (20) Salgado-Polo, F.; Borza, R.; Matsoukas, M.-T.; Marsais, F.; Jagerschmidt, C.; Waeckel, L.; Moolenaar, W. H.; Ford, P.; Heckmann, B.; Perrakis, A. Autotaxin Facilitates Selective LPA Receptor Signaling. *Cell Chemical Biology* **2023**, *30* (1), 69–84.e14. <https://doi.org/10.1016/j.chembiol.2022.12.006>.
- (21) Albers, H. M. H. G.; Hendrickx, L. J. D.; van Tol, R. J. P.; Hausmann, J.; Perrakis, A.; Ovaa, H. Structure-Based Design of Novel Boronic Acid-Based Inhibitors of Autotaxin. *Journal of Medicinal Chemistry* **2011**, *54* (13), 4619–4626. <https://doi.org/10.1021/jm200310q>.
- (22) Keune, W.-J.; Potjewyd, F.; Heidebrecht, T.; Salgado-Polo, F.; Macdonald, S. J. F.; Chelvarajan, L.; Abdel Latif, A.; Soman, S.; Morris, A. J.; Watson, A. J. B.; Jamieson, C.; Perrakis, A. Rational Design of Autotaxin Inhibitors by Structural Evolution of Endogenous Modulators. *Journal of Medicinal Chemistry* **2017**, *60* (5), 2006–2017. <https://doi.org/10.1021/acs.jmedchem.6b01743>.
- (23) Miller, L. M.; Keune, W.-J.; Castagna, D.; Young, L. C.; Duffy, E. L.; Potjewyd, F.; Salgado-Polo, F.; Engel García, P.; Semaan, D.; Pritchard, J. M.; Perrakis, A.; Macdonald, S. J. F.; Jamieson, C.; Watson, A. J. B. Structure–Activity Relationships of Small Molecule Autotaxin Inhibitors with a Discrete Binding Mode. *Journal of Medicinal Chemistry* **2017**, *60* (2), 722–748. <https://doi.org/10.1021/acs.jmedchem.6b01597>.
- (24) Eymery, M. C.; McCarthy, A. A.; Hausmann, J. Linking Medicinal Cannabis to Autotaxin–Lysophosphatidic Acid Signaling. *Life Science Alliance* **2023**, *6* (2), e202201595. <https://doi.org/10.26508/lsa.202201595>.
- (25) Reis, J.; Gaspar, A.; Milhazes, N.; Borges, F. Chromone as a Privileged Scaffold in Drug Discovery: Recent Advances: Miniperspective. *Journal of Medicinal Chemistry* **2017**, *60* (19), 7941–7957. <https://doi.org/10.1021/acs.jmedchem.6b01720>.
- (26) Gaspar, A.; Matos, M. J.; Garrido, J.; Uriarte, E.; Borges, F. Chromone: A Valid Scaffold in Medicinal Chemistry. *Chemical Reviews* **2014**, *114* (9), 4960–4992. <https://doi.org/10.1021/cr400265z>.

- (27) Stein, A. J.; Bain, G.; Prodanovich, P.; Santini, A. M.; Darlington, J.; Stelzer, N. M. P.; Sidhu, R. S.; Schaub, J.; Goulet, L.; Lonergan, D.; Calderon, I.; Evans, J. F.; Hutchinson, J. H. Structural Basis for Inhibition of Human Autotaxin by Four Potent Compounds with Distinct Modes of Binding. *Molecular Pharmacology* **2015**, *88* (6), 982–992. <https://doi.org/10.1124/mol.115.100404>.
- (28) Hausmann, J.; Kamtekar, S.; Christodoulou, E.; Day, J. E.; Wu, T.; Fulkerson, Z.; Albers, H. M. H. G.; van Meeteren, L. A.; Houben, A. J. S.; van Zeijl, L.; Jansen, S.; Andries, M.; Hall, T.; Pegg, L. E.; Benson, T. E.; Kasiem, M.; Harlos, K.; Kooi, C. W. V.; Smyth, S. S.; Ovaa, H.; Bollen, M.; Morris, A. J.; Moolenaar, W. H.; Perrakis, A. Structural Basis of Substrate Discrimination and Integrin Binding by Autotaxin. *Nature Structural & Molecular Biology* **2011**, *18* (2), 198–204. <https://doi.org/10.1038/nsmb.1980>.
- (29) Herr, D. R.; Ong, J. H.-J.; Ong, W.-Y. Potential Therapeutic Applications for Inhibitors of Autotaxin, a Bioactive Lipid-Producing Lysophospholipase D, in Disorders Affecting the Nervous System. *ACS Chemical Neuroscience* **2018**, *9* (3), 398–400. <https://doi.org/10.1021/acscchemneuro.8b00057>.
- (30) Eymery, M.; Tran-Nguyen, V.-K.; Boumendjel, A. Diversity-Oriented Synthesis: Amino Acetophenones as Building Blocks for the Synthesis of Natural Product Analogs. *Pharmaceuticals* **2021**, *14* (11), 1127. <https://doi.org/10.3390/ph14111127>.
- (31) Pajouhesh, H.; Lenz, G. R. Medicinal Chemical Properties of Successful Central Nervous System Drugs. *Neurotherapeutics* **2005**, *2* (4), 541–553. <https://doi.org/10.1602/neurorx.2.4.541>.
- (32) Csepanyi, E.; Szabados-Furjesi, P.; Kiss-Szikszai, A.; Frensemeier, L. M.; Karst, U.; Lekli, I.; Haines, D. D.; Tosaki, A.; Bak, I. Antioxidant Properties and Oxidative Transformation of Different Chromone Derivatives. *Molecules* **2017**, *22* (4), 588. <https://doi.org/10.3390/molecules22040588>.
- (33) Ashton, M. J.; Clark, B.; Jones, K. M.; Moss, G. F.; Neale, M. G.; Ritchie, J. T. The Absorption, Metabolism and Excretion of Disodium Cromoglycate in Nine Animal Species. *Toxicology and Applied Pharmacology* **1973**, *26* (3), 319–328. [https://doi.org/10.1016/0041-008X\(73\)90268-8](https://doi.org/10.1016/0041-008X(73)90268-8).